

Improvements in Monitoring the CTBT in the Middle East by the Israel Seismic Network

Approved for public release; distribution is unlimited.

October 2003



Prepared for:
Defense Threat Reduction Agency
8725 John J. Kingman Road, MS-6201
Fort Belvoir, VA 22060-6201

DSWA01-97-C-0151

Yefim Gitterman,
Vladimir Pinsky and
Avi Shapira

Prepared by:

The Geophysical Institute of Israel
Seismology Division
PO Box 182
Lod 71100, Israel

20040324 100

Best Available Copy

Technical Report

DESTRUCTION NOTICE:

Destroy this report when it is no longer needed.
Do not return to sender.

PLEASE NOTIFY THE DEFENSE THREAT REDUCTION
AGENCY, ATTN: BDMI, 8725 JOHN J. KINGMAN ROAD,
MS-6201, FT BELVOIR, VA 22060-6201, IF YOUR ADDRESS
IS INCORRECT, IF YOU WISH IT DELETED FROM THE
DISTRIBUTION LIST, OR IF THE ADDRESSEE IS NO
LONGER EMPLOYED BY YOUR ORGANIZATION.

REPORT DOCUMENTATION PAGE		Form Approved OMB NO. 0704.0188	
Public reporting burden for this collection of information is estimated to average 1 hour per response, including the time for reviewing instructions, searching existing data sources, gathering and maintaining the data needed, and completing and reviewing the collection of information. Send comments regarding this burden estimate or any other aspect of collection of information, including suggestions of reducing this burden, to Washington Headquarters Services, Directorate for Information Operations and Reports, 1215 Jefferson Davis Highway, suite 1204, Arlington, VA 22202-4302, and to the Office of Management and Budget, Paperwork Reduction Project (0704-0188), Washington, DC 20503.			
1. AGENCY USE ONLY (Leave Blank)	2. REPORT DATE October 2003	3. REPORT TYPE AND DATES COVERED Technical 970918 - 010331	
4. TITLE AND SUBTITLE Improvements in monitoring the CTBT in the Middle East by the Israel Seismic Network		5. FUNDING NUMBERS C - DSWA01-97-C-0151 PE - 463D PR - CD TA - CD WU - DH00356	
6. AUTHORS Yefim Gitterman, Vladimir Pinsky and Avi Shapira			
7. PERFORMING ORGANIZATION NAME(S) AND ADDRESS(ES) Geophysical Institute of Israel Seismology Division PO Box 182, Lod 71100, Israel		8. PERFORMING ORGANIZATION REPORT NUMBER	
9. SPONSORING/MONITORING AGENCY NAME(S) AND ADDRESS(ES) Defense Threat Reduction Agency 8725 John J. Kingman Road, MS 6201 Fort Belvoir, VA 22060 - 6201 TDANS/Dainty		10. SPONSORING/MONITORING AGENCY REPORT NUMBER DTRA-TR-01-35	
11. SUPPLEMENTARY NOTES This work was sponsored by the Defense Threat Reduction Agency under RDT & E RMC Code B 463D D CD CD 4RSV C340 25904D.			
12a. DISTRIBUTION/AVAILABILITY STATEMENT Approved for public release; distribution is unlimited.		12b. DISTRIBUTION CODE	
13. ABSTRACT (<i>Maximum 200 words</i>) This report presents a comprehensive effort to compile reliable seismic information, primarily obtained by the operation of the ISN, that improves event detection, location and discrimination in the Middle East. For the sake of IMS calibration more accurate information is now available for 61 earthquakes (GT2-GT5) and 26 explosions (GT0), including five controlled quarry blasts and three large-scale Dead Sea underwater calibration tests, and three India and Pakistan nuclear tests recorded by the Israel IMS stations. Several $M_L > 4$ earthquakes from Lebanon and Cyprus were used to characterize different propagation paths. The highlight of this project was the detonation of a 5-ton explosion in the Dead Sea that is used in the process of travel time calibration of IMS stations in the Middle East and farther. The experiment provided important information that characterizes phenomenology of underwater explosions. We estimated the threshold magnitudes of detection by the ISN system for different seismic zones in the Middle East and evaluated the efficiency of the detection methods: STA/LTA, Murdock & Hutt and the Statistically Optimal Detector. Improvements in location were provided by development of the new automatic location method, based on a combination of the optimal statistical time series analysis and robust statistical phase identification. Spectral semblance and ratio discriminants, applied to the India and Pakistan nuclear tests recordings, showed good performance. The same methods proved reliable for identifying the Dead Sea calibration explosions, and controlled quarry blasts.			
14. SUBJECT TERMS Ground Truth Database (GT) Comprehensive Nuclear Test-Ban Treaty (CTBT) Seismic Event Automatic Location Israel Seismic Network (ISN) Spectral Discrimination International Monitoring System Stations (IMS) Calibration Dead Sea Explosions Israel Seismic Network Detectability			15. NUMBER OF PAGES 196
			16. PRICE CODE
17. SECURITY CLASSIFICATION OF REPORT UNCLASSIFIED	18. SECURITY CLASSIFICATION OF THIS PAGE UNCLASSIFIED	19. SECURITY CLASSIFICATION OF ABSTRACT UNCLASSIFIED	20. LIMITATION OF ABSTRACT SAR

NSN 7540-01-280-5500

Standard Form 298 (Rev. 2-89)

Prescribed by ANSI Std. Z39-18, 298-102

CONVERSION TABLE

Conversion Factors for U.S. Customary to metric (SI) units of measurement.

MULTIPLY \longrightarrow BY \longrightarrow TO GET
 TO GET \longleftarrow BY \longleftarrow DIVIDE

angstrom	1.000 000 x E -10	meters (m)
atmosphere (normal)	1.013 25 x E +2	kilo pascal (kPa)
bar	1.000 000 x E +2	kilo pascal (kPa)
barn	1.000 000 x E -28	meter ² (m ²)
British thermal unit (thermochemical)	1.054 350 x E +3	joule (J)
calorie (thermochemical)	4.184 000	joule (J)
cal (thermochemical/cm ²)	4.184 000 x E -2	mega joule/m ² (MJ/m ²)
curie	3.700 000 x E +1	*giga bacquerel (GBq)
degree (angle)	1.745 329 x E -2	radian (rad)
degree Fahrenheit	$t_k = (t^{\circ}f + 459.67)/1.8$	degree kelvin (K)
electron volt	1.602 19 x E -19	joule (J)
erg	1.000 000 x E -7	joule (J)
erg/second	1.000 000 x E -7	watt (W)
foot	3.048 000 x E -1	meter (m)
foot-pound-force	1.355 818	joule (J)
gallon (U.S. liquid)	3.785 412 x E -3	meter ³ (m ³)
inch	2.540 000 x E -2	meter (m)
jerk	1.000 000 x E +9	joule (J)
joule/kilogram (J/kg) radiation dose absorbed	1.000 000	Gray (Gy)
kilotons	4.183	terajoules
kip (1000 lbf)	4.448 222 x E +3	newton (N)
kip/inch ² (ksi)	6.894 757 x E +3	kilo pascal (kPa)
ktap	1.000 000 x E +2	newton-second/m ² (N-s/m ²)
micron	1.000 000 x E -6	meter (m)
mil	2.540 000 x E -5	meter (m)
mile (international)	1.609 344 x E +3	meter (m)
ounce	2.834 952 x E -2	kilogram (kg)
pound-force (lbs avoirdupois)	4.448 222	newton (N)
pound-force inch	1.129 848 x E -1	newton-meter (N-m)
pound-force/inch	1.751 268 x E +2	newton/meter (N/m)
pound-force/foot ²	4.788 026 x E -2	kilo pascal (kPa)
pound-force/inch ² (psi)	6.894 757	kilo pascal (kPa)
pound-mass (lbm avoirdupois)	4.535 924 x E -1	kilogram (kg)
pound-mass-foot ² (moment of inertia)	4.214 011 x E -2	kilogram-meter ² (kg-m ²)
pound-mass/foot ³	1.601 846 x E +1	kilogram-meter ³ (kg/m ³)
rad (radiation dose absorbed)	1.000 000 x E -2	**Gray (Gy)
roentgen	2.579 760 x E -4	coulomb/kilogram (C/kg)
shake	1.000 000 x E -8	second (s)
slug	1.459 390 x E +1	kilogram (kg)
torr (mm Hg, 0° C)	1.333 22 x E -1	kilo pascal (kPa)

*The bacquerel (Bq) is the SI unit of radioactivity; 1 Bq = 1 event/s.

**The Gray (GY) is the SI unit of absorbed radiation.

Table of Contents

Section	Page
Conversion	ii
Figures	vi
Tables	xii
1 Executive Summary.....	1
2 Introduction	2
3 Task 1 Waveform Data Set for the Middle East.....	4
3.1 Collecting the GTI Explosion Database	4
3.1.1 Controlled ripple-Fired Quarry Blasts.....	4
3.1.2 Land Surface Single Explosions.....	7
3.1.3 Dead Sea Underwater Explosions	7
3.1.4 Nuclear Tests in India and Pakistan	8
3.2 Moderate Earthquakes in Israel and Adjacent Areas	8
4 Task 2 Characterization of the Middle East Areas	10
4.1 Evaluation of the Travel Time Models Using the Dead Sea Explosions Data.....	10
4.1.1 Initial Data Analysis.....	10
4.1.2 Looking for the Best-Fit ISN Model	10
4.1.3 Application of the ISN Model to the JSN Data	14
4.1.4 Looking for a JSN Model.....	21
4.1.5 Building the Composite ISN+JSN+CNN Model	22
4.1.6 Analysis of the Travel Time Deviations.....	25
4.1.7 Location of the Dead Sea Explosions, using Different Velocity Models	28
4.1.8 Evaluation of S Wave Travel Time Model.....	30
4.1.9 Comparison of the Controlled Arad Quarry Explosions Travel Times with the New Velocity Model.....	33
4.1.10 Locations of Arad Quarry Explosions using New Velocity Model.....	37
4.2 Excitation and Attenuation of Various Seismic Phases for Different Paths	38
4.2.1 Events from the East Mediterranean	38
4.2.2 Attenuation of Peak amplitudes for Land Blasts and Underwater Explosions.....	42
4.3 Threshold Magnitude of Detection by the Israel Seismic Network	45
4.4 Conclusions	51
5 Task 3 Direct Improvements in Monitoring the CTBT	52

Table of Contents (Continued)

Section	Page
5.1 Improvements in Location-Case Study: ISN Detection of the India and Pakistan Nuclear Tests and Chemical Calibration Explosions in Kazakhstan.....	52
5.1.1 Summary	52
5.1.2 Data	52
5.1.3 Travel Times and Peak Amplitudes	55
5.1.4 Characterization of Noise and Signals at Stations EIL, MRNI and JER.....	56
5.1.5 Comparison of Different Detectors: Murdock-Hutt, Johnson (STA/LTA) and SOD.....	59
5.2 Analysis of ISN Subarrays Detectability	69
5.3 Improvements in Location: Precise Automatic Location of Regional Events	72
5.3.1 Background and Data	72
5.3.2 Method	74
5.3.3 Results.....	80
5.4 Characterizations and Identification of Seismic Sources	82
5.4.1 Spectral features of seismic waves and waveform characterization for controlled quarry blasts, correlation between parameters and signal characteristics, and discrimination analysis	82
5.4.2 Waveform Characterization of Surface Single Explosions	94
5.4.3 Spectral features and discrimination analysis for recent nuclear tests, recorded by Israel station.....	98
5.5 Conclusions and Recommendations	103
6 Task 4 Field Experiments: Land Explosions	105
6.1 Collection of Detailed Information about Mining Practices and Blasting Patterns in Israeli Quarries	105
6.2 Measurements of Ground Truth Data (Location and Origin Time).....	108
7 Task 4 Dead Sea Calibration Experiment.....	109
7.1 Introduction	109
7.2 Preliminary Test Small Explosions	109
7.3 Observers and Public Relations	116
7.4 Explosion Design.....	119
7.5 Measuring Origin Times and Coordinates.....	124
7.6 Audio-Visual Records of the Explosions.....	125
7.7 Hydroacoustic Measurements.....	128
7.7.1 Recording System; Estimation of Travel Times and Shock Wave Speed.....	128
7.7.2 Types of Water Shock Waves	129
7.7.3 Verification of Distance and Depths	131

Table of Contents (Continued)

Section	Page
7.7.4 Enhanced Peak Pressures	134
7.7.5 Estimation of the Shock Wave Energy.....	136
7.7.6 Estimation of the TNT Equivalent	137
7.8 Seismic Observations	137
7.8.1 Accelerograph Records	137
7.8.2 Ground Motions in the Hotel Area.....	144
7.8.3 Observations at Local Distances and Seismic Efficiency.....	146
7.8.4 Signal Features: Spectral Modulation	155
7.8.5 Discrimination Analysis.....	158
7.8.6 Calibration of TT Models at Regional and Teleseismic Distances	164
7.9 Geophysical Observations	170
7.10 Conclusions	172
8 References	173
DL	DL-1

Figures

Figure	Page
1 Local Ground Truth events and Israel seismic stations.....	5
2 Regional stations reporting detection of the Dead Sea explosions.....	12
3 Seismograms of the first 0.5 ton Dead Sea explosion exhibit.....	13
4 P travel times for the two stratified models.....	14
5 Comparison of the first arrival pickings from the selected JSN seismograms.....	16
6 Signal arrival from explosions 2 and 3 to the JSN station LISJ.....	17
7 Signal arrival from explosions 2 and 3 the JSN station SALJ.....	18
8 Signal arrival from explosions 2 and 3 to the JSN station QTRJ.....	19
9 Signal arrival from explosions 2 and 3 to the JSN station JDRJ.....	20
10 JSN fixed velocity model.....	21
11 Unified model using ISN, JSN, CSN P pickings for the three Dead Sea explosions.....	23
12 SNR vs. distance R for the three explosions.....	26
13 Deviation $ dt $ of the travel time measurements Tobs from the model.....	26
14 Deviation $ dt $ of the travel time measurements Tobs from the model.....	27
15 Scatter of P travel times between the three explosions vs. distance.....	27
16 S phase travel time measurements for the three Dead Sea explosions.....	32
17 Travel time residuals for the four Arad calibration events using the new velocity model.....	36
18 Selected earthquakes from Eastern Mediterranean, recording stations and waves paths.....	39
19 Crustal structure for the propagation paths of the selected events.....	40
20 Recordings of the selected East Mediterranean events at 3-C stations HAF and MKT.....	41
21 Observation of the Cyprus Oct 29, 1996 event at ISN 3-C stations.....	42
22 Attenuation of seismic waves for different data sets of explosions.....	43

Figures (Cont.)

Figure	Page
23 Comparison of attenuation data for different data sets of explosions.....	44
24 PDE and ISN detections of the ME events in the magnitude ranges.....	46
25 Upper most mantle Pn velocity according Hearn & Ni, 1994.....	49
26 Magnitude threshold vs. distance for Israel Seismic Network	49
27 Relative location of short period and broadband stations of the ISN used in the analysis.	53
28 Location of short period and broadband stations of the ISN used in the analysis.	53
29 Filtered broadband vertical records of the three nuclear tests	56
30 Velocity spectral density of noise at the EIL station	58
31 Application of the Murdock-Hutt detector algorithm to the BB EIL seismograms.....	61
32 Detection of the Indian test at EIL station.....	63
33 Detection of the first Pakistan test on May 28, 1998.	64
34 Detection of the second Pakistan test on May 30, 1998.....	66
35 Detection trial of the Kazakh chemical explosion at EIL BB station.....	68
36 Location of the three analyzed ISN subnetworks and the associated telemetry network	70
37 Rate of detection vs. magnitude for the ABT (AOGF) and standard STA/LTA procedure	71
38 Map showing earthquake epicenters, quarry blasts and the ISN stations.....	73
39 Example of typical earthquake recording by different ISN stations.....	74
40 Initial epicenter location.....	76
41 Final automatic hypocenter location for a local earthquake.....	78
42 Automatic location results for 61 local earthquakes.	81
43 Seismograms (in the same scale) of Example 3 and 4 at BB stations EIL.....	84
44 Expected arrival of P-waves from Example 3 at the BB station CSS	85

Figures (Cont.)

Figure	Page
45 Comparison of amplitudes of the recorded blasts at the BB EIL station.....	86
46 Comparison of waveform (normalized) at the short-period ISN station YTIR.....	87
47 Spectral modulation and the main maximum feature for Example 4 at ISN stations.....	89
48 Spectral modulation and the first spectral null feature for Example 1 at ISN stations.....	90
49 3-component accelerograms of near-field observations of the blasts.....	91
50 Spectral analysis of accelerograms.....	93
51 Seismograms of Example 16, recorded at ISN stations.....	95
52 Seismograms of Example 3.....	96
53 Seismograms of Example 13.....	97
54 Sample seismograms of different of types of seismic events.....	99
55 Spectra of the first Pakistan test.....	100
56 Application of semblance and energy ratio discriminants to the recent nuclear tests and nearby earthquakes.....	102
57 Field measurements at the Arad quarry.....	105
58 Detonation of Example 3 on 26.01.99.....	106
59 Detonation of Example 4 on 27.01.99.....	107
60 Measurement of Origin Time for Example 3.....	108
61 Classic shock wave shape recorded by a Geospace hydrophone near the ship from Example 1t.....	113
62 Recordings of the successful Example 3t.....	113
63 Photocopy of the weight certificate of the 5000kg charge.....	116
64 An article in the daily newspaper "Maariv" on 9.11.99 about the Dead Sea explosions.....	117
65 Information about the Dead Sea experiment on the Website NEWS24.....	118
66 Details of marine operations and experiment configuration.....	119

Figures (Cont.)

Figure	Page
67 Design of charge unit	120
68 Sample photographs of the charges of the three explosions	121
69 Bathymetric chart of the Dead Sea near the shot point	122
70 Sample photographs of marine activities during the experiment	123
71 Measurements of the origin time for the 500 kg shot	124
72 Sample video snapshots of the 2060 kg explosion.....	126
73 Sample video snapshots of the 5-ton explosion	127
74 Spectrogram of the video-recording soundtrack for the 5-ton explosion	128
75 Water pressure-time history of the 2-ton explosion	130
76 Water pressure-time history of the largest explosion	130
77 Measuring the absolute GPS time of the shock waves.....	131
78 Complex form of the P3 phase for the shot 5000 kg.....	133
79 Peak water pressure vs. distance	135
80 Primary and surface-reflected shock waves and the curve-fit equation	136
81 Location of nearby stations recorded the explosions.....	138
82 Accelerograms and power spectra observed at the closest station at Mineral Beach.....	140
83 Accelerograms and power spectra observed at Mineral Beach.....	141
84 Seismometer and hydrophone recording of the 2060 kg explosion at Mineral Beach	142
85 Cumulative Sum of the normalized squared acceleration and Power Spectra Density	143
86 Seismometer recordings of the 2060 kg explosion.....	144
87 Smoothed spectra of the whole seismogram of the Dead Sea explosion 2060 kg.....	145
88 ISN recording of the largest explosion.....	146

Figures (Cont.)

Figure	Page
89	Records of the three explosions at IMS station MRNI..... 147
90	Records of the two explosions at IMS station EIL..... 148
91	Records of the three explosions at IMS station BB station JER..... 149
92	Records of the largest explosion at EILESA array..... 150
93	Records of the largest explosion at CNF station AMZI 151
94	Seismograms (normalized) of the Jordanian station ASFJ (vertical component) 152
95	Magnitude vs. charge weight for the Dead Sea explosions 154
96	Seismic efficiency of the Dead Sea explosions 155
97	Amplitude spectra for the three explosions at the microarray 156
98	Amplitude spectra at short-period ISN stations..... 157
99	Dead Sea explosions, earthquakes and recorded stations used for the discrimination analysis 160
100	Sample seismogram and spectral patterns at ISN stations for the 2-ton shot..... 161
101	Sample seismogram and spectral patterns at different ISN stations..... 162
102	Discrimination results for the Dead Sea explosions and nearby earthquakes 163
103	IMS stations and national/international stations reported observations of the Dead Sea explosions 165
104	Seismograms of the explosions recorded at the BB station CSS..... 166
105	Seismograms of the 5-ton explosion recorded by the Cyprus Seismic Network..... 166
106	Seismograms of the 5-ton explosion recorded by the German operated stations 167
107	Seismograms of the 5-ton explosion recorded at the Swiss operated stations..... 167
108	Recording of the 5-ton explosion at the IMS primary station 168
109	Information of the IDC about the 5-ton Dead Sea explosion 169

Figures (Cont.)

Figure	Page
110 GPS stations of Israel.....	170
111 Observations of the Total Electronic component during the Dead Sea experiment	171

Tables

Table	Page
1 Different types of Ground Truth explosions.	4
2 Parameters of controlled ripple-fired quarry blasts in Jordan and Israel.....	6
3 Data for surface single explosions.....	7
4 Source parameters of the Dead Sea explosions.....	8
5 Local GT5 earthquakes used in the study (location, origin time and magnitude estimated by GII)	9
6 Parameters of calibration underwater explosions in the Dead Sea.....	10
7 Present velocity model.....	11
8 Least-Square velocity model.....	11
9 Best-fit model with fixed velocities	11
10 Deviation of measured first arrival time from the best-fit model.....	15
11 Unified velocity model.....	22
12 Residuals for the ISN+JSN+CSN data Least-Square model.....	24
13 Robust Location of the three Dead Sea explosions	29
14 Travel times for S phase.....	31
15 "Best-Fit model with S velocities varied.....	31
16 Unified model with S velocities varied.....	32
17 Residuals for the 1 st Arad blast.....	34
18 Residuals for the 2 nd Arad blast.....	34
19 Residuals for the 3 rd Arad blast.....	35
20 Residuals for the 4 th Arad blast	36
21 Location of the Arad quarry explosions using manual and automatic pickings.....	37
22 Source parameters from ISN and NEIC bulletins	38

Tables (Cont.)

Table	Page
23	ISN detectability vs. NEIC..... 50
24	Source parameters of nuclear tests and earthquakes 54
25	Travel times (IASPEI9) and P-wave peak amplitudes 57
26	Local magnitudes and peak amplitudes of the analyzed quarry blasts 83
27	Waveform correlation of the quarry blasts 83
28	Calibration and ground motion measurements..... 92
29	Discrimination results for the controlled ripple-fired quarry blasts 94
30	Average spectral discrimination results for India and Pakistan.....101
31	Design parameters and details of the test explosions110
32	Comparison of predicted and observed Peak Ground Velocity.....111
33	Comparison of predicted and observed local magnitudes and fundamental frequencies111
34	Measurement systems and on-site data analysis at the Command Center.....115
35	Parameters of calibration underwater explosions in the Dead Sea.....120
36	Measured arrival times of different water shock waves132
37	Shot configuration parameters and bubble periods133
38	Measured peak pressures in the shock waves.....135
39	Coordinates of the accelerograph stations.....137
40	Recorded Peak Ground Accelerations.....139
41	Peak-to-peak amplitudes144
42	Comparison of predicted and observed local magnitudes and fundamental frequencies153
43	List of earthquakes of October-November 1999159
44	Observations of the Dead Sea calibration165

Section 1

Executive Summary

The Israel Seismic Network, ISN, operated by the Geophysical Institute of Israel, is continuously monitoring the seismicity of the Middle East, and in that capacity provides useful, and sometimes crucial, information that contributes to the enhancing the capabilities of the IMS to monitor the Comprehensive Nuclear Test Ban Treaty (CTBT). This report presents a comprehensive effort to compile reliable seismic information, primarily obtained by the operation of the ISN, that improves event detection, location and discrimination in the Middle East. We are confident that the tasks set forth in our original project proposal have been completed successfully.

1. A data set of 61 accurately located (GT2-GT5) earthquakes and explosions is compiled (GTx = Ground Truth within x km). More accurate (GT0) information is now available for 23 chemical explosions, including five controlled quarry blasts and three large-scale Dead Sea underwater calibration tests. For the sake of IMS calibration we collected in addition 5 relatively large earthquakes with $M_L > 4$ from the GT5 category and the ISN recordings (including IMS stations EIL and MRNI) of the India and Pakistan nuclear tests which occurred during the project period. Several $M_L > 4$ earthquakes from Lebanon and Cyprus were used to characterize different propagation paths. The highlight of this project was the detonation of a 5-ton explosion in the Dead Sea that is used in the process of travel time calibration of IMS stations in the Middle East and farther.
2. The selected data base and other data is used to validate the currently used travel time model by the ISN and develop a unified one dimensional travel time model for the whole area within a 500 km radius of the ISN.
3. The threshold magnitudes of detection by the ISN system for different seismic zones in the Middle East are estimated. We also evaluated the efficiency of the detection methods (STA/LTA (by Johnson, 1979), Murdock&Hutt and the Statistically Optimal Detector (SOD) (by Kushnir et al., 1990)) by extracting the extremely weak signal from a 100-ton calibration shot in Kazakhstan.
4. We utilized the ISN recordings of the India and Pakistan nuclear tests to compare the signal and noise spectral characteristics of the IMS stations EIL and MRNI.
5. A new automatic location method is developed by Pinsky (2000). It is based on combining the optimal statistical time series analysis and robust statistical phase identification. The results often show locations better than those by a skilled analyst.
6. We applied semblance and spectral ratio methods developed by Gitterman et al., 1996 to identify the India and Pakistan nuclear tests. The same methods proved reliable for identifying the Dead Sea calibration explosions, and controlled industrial blasts at the Arad phosphate quarry in the Negev desert.
7. The Dead Sea calibration experiment provided important information that characterizes the phenomenology of underwater explosions in the Dead Sea. It also provided unique information that facilitated assessments and validation of safety parameters for underwater explosions.

Section 2

Introduction

Confidence in the ability to monitor small and moderate sized seismic events in areas of special interest, such as the Middle East, is crucial for CTBT. However, the task of event detection, location and discrimination in the region is complicated due to the large variety of geophysical conditions (Sandvol et al., 2000), scarcity of high-quality stations from which data are readily available, problematic access to waveform data and too few data of controlled sources. Much data from the low seismicity and aseismic areas in the Middle East are available from the Israel Seismic Network (ISN), operated by the Seismology Division of the Geophysical Institute of Israel.

The objectives of this project were to collect appropriate ground truth (GT) data using ISN recordings of seismic events and develop and implement improved techniques for location, detection and discrimination of seismic activity in the Middle East. The project was split into four interrelated tasks.

Task1 - Waveform Data Set for the Middle East- consisted of collecting the bulletin and waveform data set by scanning ISN records to select ground truth characteristics and high-quality seismograms of explosions and earthquakes. The task was carried out (Paragraph 3.) through the compilation of 61 accurately located small local earthquakes with magnitude $M_L < 3$, 23 GT0-EPI and GT0-HYP chemical explosions, including five controlled quarry blasts and three Dead Sea underwater calibration tests (GTx = GT to x km). For the sake of IMS calibration we also collected five relatively large earthquakes with $M_L > 4$ from the GT5 category and the ISN recordings (including IMS stations EIL and MRNI) of the India and Pakistan nuclear tests which occurred during the project period. Several $M_L > 4$ earthquakes from Lebanon and Cyprus were used to characterize different propagation paths. The selected data base and other data were used to complete:

Task 2 – Characterization of Middle East Areas - in terms of:

- travel time models for P and S crustal phases (Section 4.1). This was provided mostly on the basis of the Dead Sea calibration explosions data and indicated serious lateral heterogeneity in the source area.

- excitation and attenuation of Sg and Lg for the ocean and land propagation paths using earthquakes from the Lebanon and Cyprus area (Section 4.2).

- measuring threshold magnitude of detection by the ISN system. for the Middle East. The task was carried out by comparing the ISN and NEIC catalogs showing significant variations in the threshold for different seismic zones.

Task 3 – Direct Improvements in Monitoring the CTBT was devoted to the improvement of **detection, location and discrimination** methods and application to the ISN (Section 5). For this purpose we utilized the ISN recordings (including IMS stations EIL and MRNI) of the India and Pakistan nuclear tests (Section 5.1). Using these data we compared signal and noise spectral characteristics for the IMS stations EIL and MRNI performing within the ISN. We then compared efficiency of the two conventional methods STA/LTA (by Johnson, 1979) and the one by Murdock&Hutt and Statistically Optimal Detector (SOD) (by Kushnir, 1990) and tried to evaluate the detection threshold for the best of them by extracting the extremely weak signal from the 100 tonn Kazach calibration shot. Next, the ISN detectability was investigated by comparing the number of events detected by the ISN subarrays with those detected by the whole network. For this research we compared performance of the SOD with the conventional STA/LTA (Section 5.2) and proved the essential advantage of the first.

Improvements in location (Section 5.3 and Section 4.1) were provided by development of the new automatic location method, based on a combination of optimal statistical time series analysis and robust statistical phase identification. The locator is realized as a grid search procedure. The new travel time models resulting from the Dead Sea experiment were used by the locator, which was applied to a number of local and regional events. The resulting locations were often better than those calculated by a skilled analyst.

In the task of identification (Section 5.4) we limited ourselves to comparison of the ISN spectral characteristics of the India and Pakistan nuclear tests with several earthquakes from the corresponding seismic regions as well as comparison of the Dead Sea underwater explosions with earthquakes from adjacent areas. For this purpose we applied spectral semblance and spectral ratio methods developed by Gitterman et al., 1996.

In Task 4 we carried out a wide range field experiment program (Section 6), including conducting a series of 13 single surface explosions (Israel jointly with the USA), five ripple-fired quarry blasts of different configurations, two preliminary test underwater explosions in the Dead Sea and, finally, three successful large-scale calibration shots in the Dead Sea: 0.5, 2 and 5 tons (Section 7). The first two calibration shots were registered all over the ISN and even in Cyprus. The main third explosion was detected almost everywhere in the Middle East and as far as Germany and Great Britain. All of the experimental data was analyzed in the project and used for calibration purposes.

Section 3

Task 1 Waveform Data Set for the Middle East

3.1 Collecting the GTI Explosion Database.

The database includes seismic events with source information provided by GPS measurements for location and Origin Time. The Origin Time is obtained from the output of a sensor located at the shot point (see details in Section 6.2). The GTI also includes detailed information regarding the explosion design (except for the nuclear tests). The database comprises four datasets of explosions (see Table 1) recorded by short-period stations of the Israel Seismic Network (ISN), auxiliary stations of the International Monitoring System (IMS) and the Contributing National Facility (CNF) stations in Israel (see the map in Figure 1).

Table 1. Different types of Ground Truth explosions used in the study.

Data set #	Description	GTI rank	Conducted during	Number of events
1	Controlled ripple-fired quarry blasts	GT0-EPI	1998-1999	5
2	Single land surface explosions	GT0-EPI	1998	13
3	Underwater explosions in the Dead Sea	GT0-HYP	1999	5
4	Nuclear tests in India and Pakistan recorded by Israel stations	GT0-HYP	1998	3

3.1.1 Controlled Ripple-Fired Quarry Blasts.

Four routine quarry blasts at the Arad phosphate quarry in the Negev desert were measured for GTI. A total charge weight of about 12-15 tons was large enough to provide clear P-wave arrivals at local network stations and the CTBT related stations (i.e., IMS and CNF, [see Table 2]).

After obtaining the appropriate permits to enter the blasting areas, we used GPS to measure the coordinates of a relevant explosion (namely, coordinates of an initial detonation point) and the detonation time with accuracy better than 50 m and 0.02 sec, respectively. We also collected the accurate blast design parameters (Table 2,[see Sections 6.1, 6.2]).

The blasts were well recorded by most ISN stations (including the remotest HRI at a distance of about 250 km) and by both IMS stations EIL (161 km) and MRNI (212 km). Blast No.3 was recorded by an A-800 accelerograph located 340 m away (Section 6.3).

A quarry blast at Al-Shydiah mine, Jordan, was also included in the dataset. The blast parameters were provided by the Jordanian Seismological Observatory (JSO).

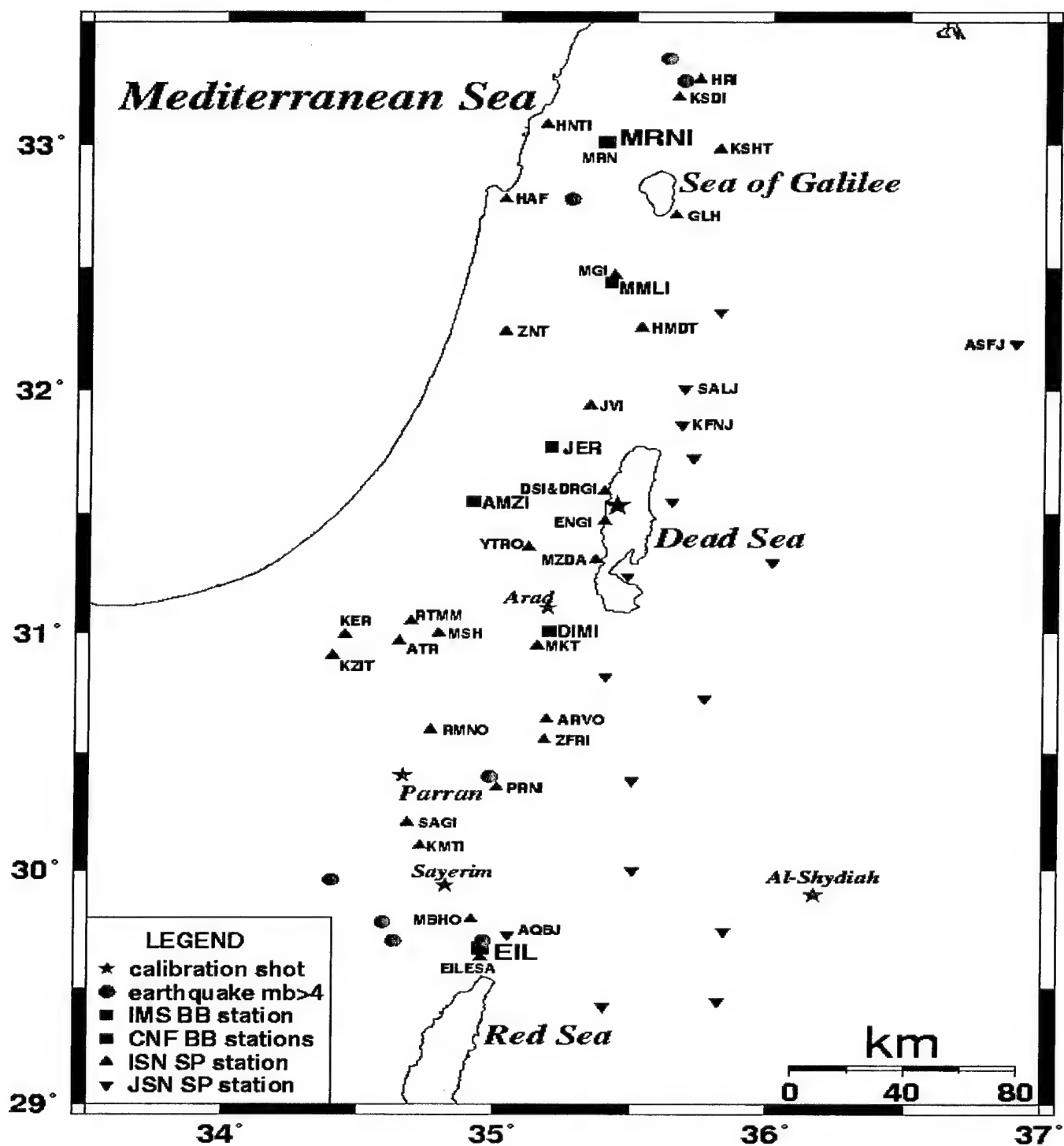


Figure 1. Local Ground Truth events and Israel seismic stations. Jordanian Seismic Network stations (JSN) are also shown.

Table 2. Parameters of controlled ripple-fired quarry blasts in Jordan and Israel

No.	Date	Quarry	Origin time (O.T.), GMT Magnitude M_L^+	Coordi- nates	Total charge, tons	Delay, msec	No. of del.	No. of rows	No. of holes	Hole depth, m	Hole diam., mm	Blast pattern
1	30.071 998	Arad, Israel consolidated clays	08:18:51.911* 2.6	31.10439N* 35.18801E*	8 ANFO	40	5	6	70	8.5	200	Regular blast pattern, about equal rows (9, 13, 14, 13, 13, 8 holes)
2	09.091 998	Arad, consolidated clays	10:00:03.221* 2.7	31.10416N* 35.18880E*	10.5 ANFO	40	8	9	75	8.5-9	200	Non-regular pattern with variable row length (1-15 holes)
3	26.011 999	Arad, marl (chalk+clay, consolid.)	11:46:02.410* 2.9	31.10968N* 35.18914E*	14.34 ANFO	12	10	11	120	8.5	200	Non-regular pattern with variable row length (4-13 holes)
4	27.011 999	Arad, marl (chalk+clay, consolid.)	10:01:00.641* 2.7	31.10894N* 35.18936E*	12.0 ANFO	80	9	10	76	8.5	200	Non-regular pattern with variable row length (3-9 holes)
5	14.061 998	Al-Shydiah Jordan	17:31:49.57† 2.7	29.896N†† 36.169E††	35	45	-	-	-	-	-	32.5 tons Gelatine and 2.5 tons ANFO

* - Local magnitude M_L is estimated from ISN records.

† - Location and origin time data provided by GPS measurements. O.T. refers to the detonation time of the first hole.

†† - Estimation given by the Jordanian Seismological Observatory (estimation by GII: 17:31:48.2).

††† - Coordinates of the quarry as informed by the JSO.

3.1.2 Land Surface Single Explosions.

Data of thirteen co-located controlled single shots on the ground (215-2200 kg) were collected in 1998 during a series of joint Israel/US blast experiments at the Sayerim military site north-west of Eilat. The blast design information was made available through the kind assistance of Dr. R. Reinke, and the kind permission of Dr. G.Y. Baladi (DSWA Test Directorate). Valuable help was provided by Mr. R.J. Dinan and his team (U.S. Army Corps of Engineers), and by Mr. A. Rozen (personal communication). The charges of different configurations and explosive composition were detonated on the surface. We measured exact detonation time for seven shots. The Ground Truth Information and the full database of different seismic recording systems are presented in Table 3. The shots were well recorded by the IMS station EIL (32 km), and the Eilat Experimental Seismic Array, the EILESA microarray, located near the EIL station. Some shots triggered the ISN. Near-source (2-10 km) observations of seismic and acoustic waves by portable stations are also carried out.

Table 3. Data for surface (contact) single explosions.

No.	Date	Origin time (GMT)	Weight W, kg	Explosives	Records
Sayerim site - GPS coordinates: 29.9378°N, 34.8185°E; local: x=132.245 km, y= -72.24 km					
1	20.05.98	~11:37:47.5*	830	TNT	BB EIL (80 Hz), EILESA
2	24.05.98	14:37:13.700	830	TNT	ISN, EILESA, BB EIL (80 Hz),
3	26.05.98	14:44:02:693	1000	ANFO	ISN, EILESA, BB EIL (80 Hz), portable stations
4	28.05.98	~12:25:29*	1000	ANFO	BB EIL (20 Hz)
5	02.06.98	9:18:46.672	480	TNT	BB EIL (20 Hz), EILESA, portable
6	02.06.98	~16:30:18*	480	TNT	BB EIL (20 Hz), EILESA
7	03.06.98	~09:08:57*	480	TNT	BB EIL (20 Hz), EILESA, portable
8	03.06.98	15:50:35.677	480	TNT	BB EIL (20 Hz), EILESA
9	03.06.98	16:31:06.159	480	TNT	BB EIL (20 Hz), EILESA
10	04.06.98	16:43:58.902	1000	ANFO	BB EIL (20 Hz)
11	07.06.98	12:02:11.672	830	TNT	ISN, EILESA
12	07.06.98	~15:16:56.8*	~215	TNT	BB EIL (20 Hz), EILESA
13	08.06.98	09:49:07.9**	830+195	TNT+ANFO	ISN, EILESA, BB EIL (80 Hz),
14	08.06.98	16:15:58*	~2200	TNT+khanit	ISN, EILESA, BB EIL (80 Hz)
Parran site - coordinates: 30.405°N, 34.659°E local: x = 117.1 km, y = -20.1 km					
15	11.05.90	13:41:54.68	1000	TNT	ISN
16	14.05.90	12:56:19.40	10000	TNT	ISN

* - O.T. is estimated from BB records, ** - O.T. is estimated from ISN records.

To extend the observation range, we also included two old military shots in the Parran region, about 50 km to the north of the Sayerim site (shown on the map, Figure 1), conducted for engineering purposes.

3.1.3 Dead Sea Underwater Explosions.

Three large-scale chemical calibration explosions were detonated in November, 1999 in the Dead Sea at water depth of about 70 m (about 485 m below the sea level). The main objective of the experiment was to calibrate the seismic travel times at local and regional distances. Two small test shots, detonated two weeks before the main series at the same location and depth, are also considered in the analysis.

Using a specially designed recording system and GPS measurements, it was possible to provide an accuracy of about 5 milliseconds for detonation time and a few meters for location. However, the actual location accuracy was reduced to 50 meters due to strong variable undercurrents and winds in the Dead Sea during the experiment. The source parameters of the explosions are shown in Table 4. Detailed information about charge design and detonation technique is presented in Section 7.4.

Table 4. Source parameters of the Dead Sea explosions.

Date	Origin Time (GMT)	Coordinates	Charge, kg	Magnitude	
				M _L	m _b
29.10.99	09:35:01.471	31°32'09.6"N 35°26'27.6"E	25	1.9	-
29.10.99	11:55:01.842	31°32'09.6"N 35°26'27.6"E	25	1.7	-
08.11.99	13:00:00.330	31°31'58.804"N 35°26'26.242"E	500	3.1	-
10.11.99	13:59:58.210	31°32'01.800"N 35°26'24.000"E	2060	3.6	-
11.11.99	15:00:00.795	31°32'00.995"N 35°26'28.760"E	5000	3.9	4.1

Regional phases Pn, Sn and Lg are clearly recorded in Israel at both IMS stations EIL (212km) and MRNI (164km), and CNF stations DIMI, MMLI and AMZI deployed temporarily for the experiment. More details about collected regional and teleseismic recordings are presented in Section 7.8. Acoustic shock wave recordings were made for the two largest explosions, at a distance of about 700 m.

3.1.4 Nuclear Tests in India and Pakistan.

Three recent 1998 underground nuclear explosions, one in India and two in Pakistan, were also registered in Israel by ISN and IMS stations EIL and MRNI, located at teleseismic distances from the explosions. The small chemical 100-ton calibration explosion of magnitude 3.7, conducted in 1998 at the Semipalatinsk nuclear Test Site (STS), Kazakhstan, was also included in the project database. These data were used for detection, location and discrimination analysis. The source parameters, the map of epicenters and recording stations, and the analysis of results are presented in Section 5.1.

3.2 Moderate Earthquakes in Israel and Adjacent Areas.

The earthquake subset includes local events with $m_b > 4$ (green circles on Figure 1), recorded by the ISN and some of the Jordan stations (Table 5). The epicenter uncertainty is estimated to be less than 5 km at 90% confidence level. In the bulk the events are shallow (with hypocenter depth not exceeding 20 km) and are characterized by a more tightly constrained epicenter location.

For the discrimination analysis of the Dead Sea calibration explosions we used data of four earthquakes similar in magnitude, location and time, to the explosions. The earthquake parameters and the analysis are presented in Section 7.8 (Table 43).

Several regional earthquakes from the Eastern Mediterranean, recorded by Israel 3-component network stations, were also included in the database for analysis of excitation of different regional phases, in particular, Lg phase. Source parameters and a map are presented in Section 4.2 (Table 20 and Figure 18).

Table 5. Local GT5 earthquakes used in the study (location, origin time and magnitude estimated by GII).

Date	Origin Time	Magnitude		Local coord.		Depth km	Latit. N	Long. E	Area
		M _L	m _b	X, km	Y, km				
1995/11/22	15:12:24.1	4.3	4.4	93.1	-69.4	13	29.96	34.40	Sinai
1997/5/18	19:46:56.5	3.6	4.1	174.3	242.4	10	32.78	35.27	Galilee
1997/5/29	7:6:27.4	3.7	4.1	206.7	306.3	8	33.35	35.62	Golan
1997/8/4	11:29:46.5	4.0	4.2	216.5	295.9	10	33.26	35.73	Golan
1998/4/25	12:93:5.4	4.1	4.2	111.0	-89.0	18	29.78	34.59	Uvda
1998/11/19	12:9:32.9	4.4	4.5	115.2	-98.2	16	29.70	34.63	Uvda
1999/10/28	15:39:15.5	4.6	4.6	148.8	-20.9	9	30.40	34.98	Parran
1999/12/19	8:42:49.0	4.1	4.2	146.9	-98.4	17	29.70	34.96	Uvda

Section 4

Task 2 Characterization of the Middle East Areas

4.1 Evaluation of the Travel Time Models using the Dead Sea Explosion Data.

4.1.1 Initial Data Analysis.

One of the main goals of the Dead Sea experiment is the calibration of the IMS and other stations in the area. The true known source location and ignition time (see Table 6) provide a unique opportunity for measuring exact travel times. All the explosions' P waves are well observed over the Israel and Jordan seismic networks (ISN, JSN) in the distance range 8 – 240 km (see Figure 3) and also in Cyprus (CSN) up to 500 km. We measured P travel times for the available seismograms of the ISN, JSN and CSN and noted that the travel time for the three explosions differs significantly, yielding a scatter of 0.26 sec (one standard deviation). This deviation of the travel time is mainly due to the difficulty associated with identifying the first arrivals, because all three sources were placed within 160 m and have the same path. In addition, information about the P arrival was available from some of the Saudi Arabian stations (see Figure 2 and Tables 9 and 11). The picks were then compared to the travel times (see Figure 4) corresponding to the 3-layer velocity model (see Table 7), presently used for the ISN routine source location. For most of the ISN and CSN readings the model predictions are quite good. However, many of the readings to the JSN stations deviate significantly from the model travel time.

Table 6. Parameters of calibration underwater explosions in the Dead Sea.

No.	Date	Origin time (O.T.), GMT	Local coordinates (GPS measured)	
			X, km	Y, km
CE1	08.11.99	13:00:00.33	192.33	104.67
CE2	10.11.99	13:59:58.21	192.27	104.76
CE3	11.11.99	15:00:00.795	192.39	104.74

For the travel time evaluations we used the GPS origin time and source coordinates according to Table 6.

4.1.2 Looking for the Best-Fit ISN Model.

We first tried to find the model that best matches the ISN P pickings. Thus, the outliers were excluded and only those matching the ISN and CSN observations ($N = 80$) well were selected. A four layer stratified media was chosen from visual inspection of the data. The velocity model was derived by non-linear Least-Square fit via the Levenberg-Marquardt optimization procedure.

The residuals $dt_j = T_{obs,j} - T_{calc,j}$, $j = 1, \dots, N$ reached $RMS = 0.201$ sec (Table 8) compared to $RMS = 0.25$ obtained from the initial (Table 7) model.

Table 7. Present velocity model.

Thickness, km	Vp, km/sec	Vs, km/sec
2.56	4.36	2.45
7.2	5.51	3.10
21.64	6.23	3.50
∞	7.95	4.46
RMS=0.25		

Table 8. Least-Square velocity model.

Thickness, km	Vp, km/sec	Vs, km/sec
3.35	3.77	2.12
3.18	6.00	3.37
12.16	6.11	3.43
13.77	6.73	3.78
∞	7.88	4.43
RMS=0.201		

Table 9. Best-fit model with fixed velocities.

Thickness, km	Vp, km/sec	Vs, km/sec
2.79	3.83	2.15
3.86	5.71	3.21
13.06	6.11	3.43
14.97	6.78	3.80
∞	7.97	4.48
RMS=0.207		

However, the model parameters appear to be poorly constrained, requiring manual intervention. Visual inspection of the data indicated five linear segments of the travel time curve, suggesting a four layer stratified velocity model for the data description. The best-fit inclinations of the straight lines for each of the first four segments, determine the corresponding four velocities (see Table 9). They were estimated separately, using linear Least-Square fit approximation. The fifth segment (highest) velocity we use is $V_p=7.97$ km/sec - from previous experience. The thickness of the layers (Table 9) was estimated by applying the Levenberg-Marquardt optimization procedure keeping fixed velocities of the layers. The new model (Table 9) yields $RMS=0.207$ seconds. We shall refer to this model as the "ISN model". The corresponding P travel time versus distance R is presented in Figure 4. Residuals $dt_j = T_{obs,j} - T_{calc,j}$, $j=1, \dots, N$ are presented in Table 10. In the velocity models of Tables 7, 8 and 9, S waves velocity is $V_s = V_p/k$, where $k=1.78$ is an empirical coefficient.

Regional Observing Stations

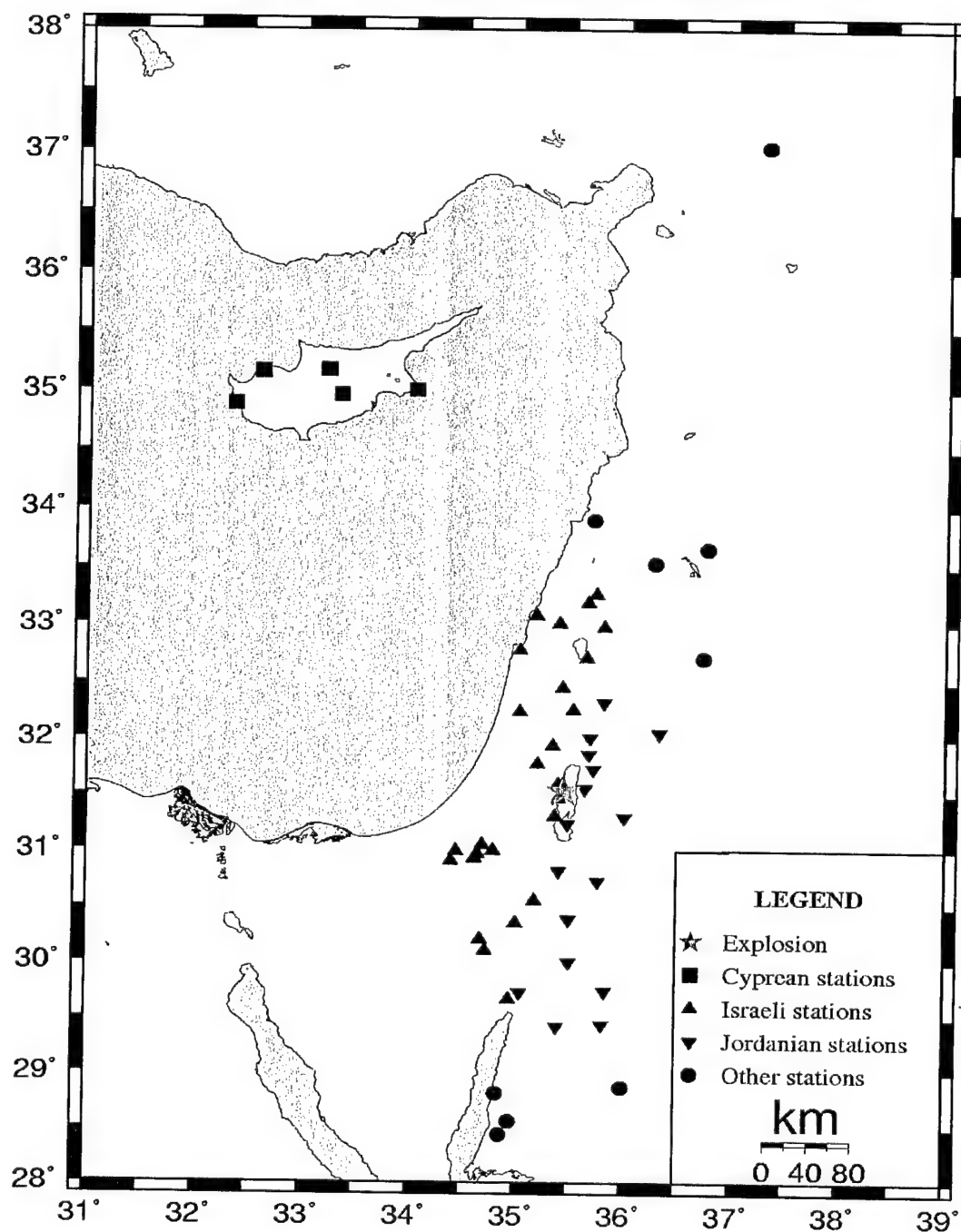


Figure 2. Regional stations reporting detection of the Dead Sea explosions.

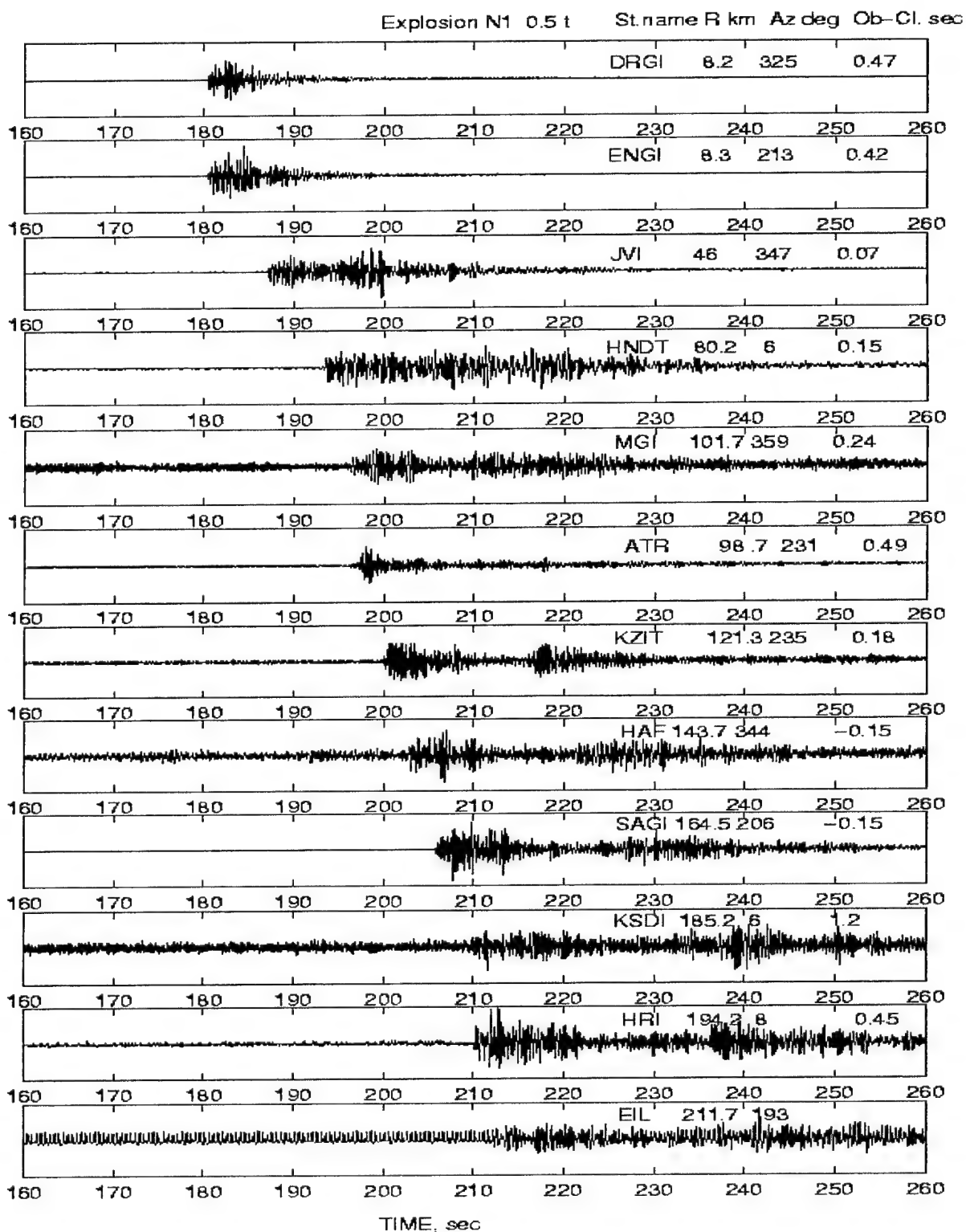


Figure 3. Seismograms of the first 0.5 ton Dead Sea explosion exhibit relatively worse SNR for some remote stations (vertical scale is arbitrary).

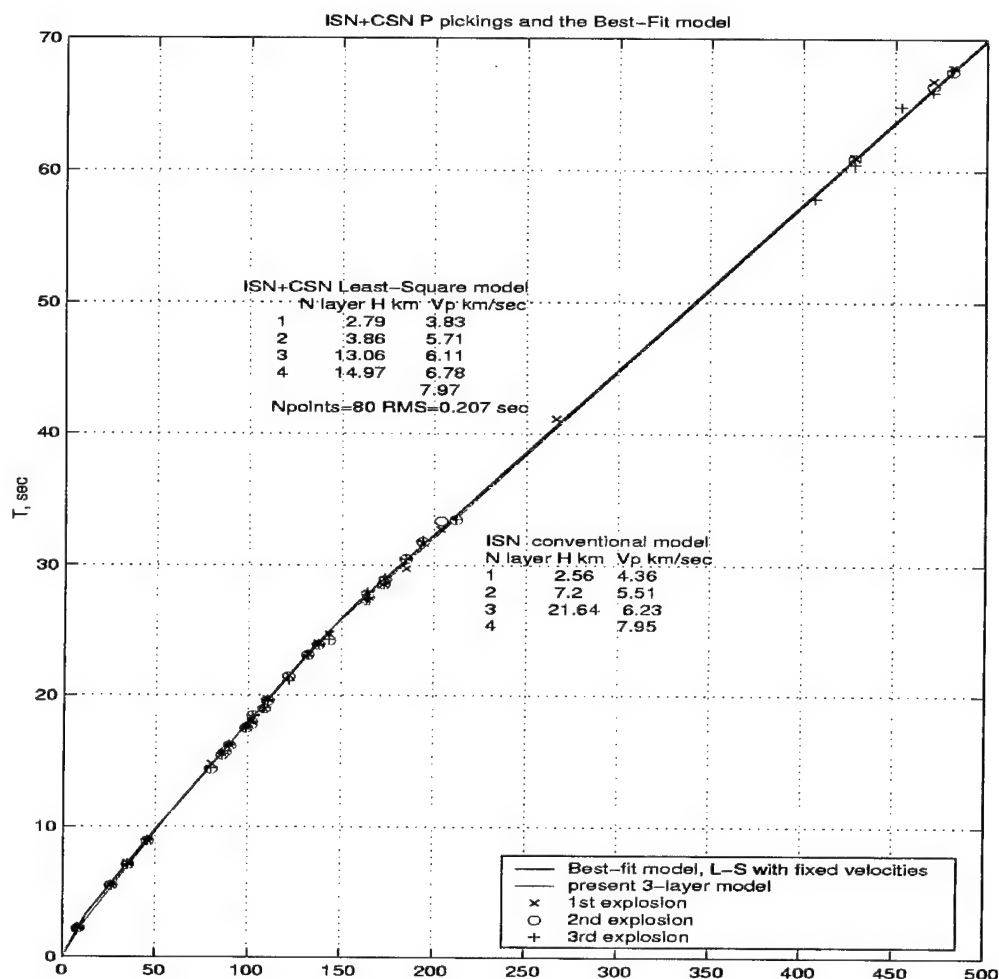


Figure 4. P travel times for the two stratified models: best fit (Table 9) and conventional (Table 7) and the P picks for the three explosions (source depth $H=0.5$ km).

4.1.3 Application of the ISN Model to the JSN Data.

Most Jordanian stations (see Figure 4 and Table 10) (letter J at the end of the stations name) show delays of ~ 0.7 sec from the ISN travel times model. The reason has still to be clarified. It was assumed that this is simply a clock problem, but this assumption was soon rejected, since at least one station during each of the explosions was recorded on both the ISN and JSN acquisition systems. Subsequently, we considered the outliers as arrivals of the later refracted phases, assuming the first arrivals were masked by noise or degenerated. As shown in Figure 5, we associated the JSN readings with predicted arrival times using the ISN model. The total error, obtained from such a comparison is $\text{RMS}=0.215$. However, direct observations and filtering of the seismograms do not show preceding arrivals (see Figures 4-9). Consequently, we may refer to the time discrepancies as "station corrections". Significant ($|dt_j| > 0.5$ sec) residuals $dt_j = T_{\text{obs},j} - T_{\text{calc},j}$, $j=1, \dots, N$ of the first arrivals are highlighted (by orange color) in Table 10. The IMS BB stations EIL and MRNI (yellow color) fit the theoretical model well and probably don't require time correction.

Table 10. Deviation of measured first arrival time from the best-fit model (Table 9).

N station	Station NAME	Distance R, km	Azimuth, deg	Dt=T _{obs} -T _{calc} , sec			
1	DRGI	8.3	322.	0.10	0.052	0.10	0.08
2	MZDA	26.2	197.	0.075	0.048	0.049	0.06
4	JER	35.2	318.	0.16	0.065	0.11	0.11
5	JVI	45.9	347.	0.070	0.020	0.064	0.05
9	HMDT	80.	5.	0.3	-0.05	0.03	0.09
10	MSH	86.0	227.	0.070	0.02	0.082	0.06
11	ZNT	87.5	333.		0.014	0.041	0.03
12	RTMM	90.0	234.	0.12	0.058	0.08	0.09
13	ANJJ	94.	22.	(0.35)*		-0.23	0.06
15	ATR	99.0	231.	0.029	-0.06	-0.02	-0.02
16	MGI	101.5	359.	0.00	-0.22	-0.08	-0.1
17	HMRJ	102.	56.	0.46	0.075	-0.24	0.098
18	SVTA	102.6	230.	0.080	0.29	0.23	0.20
19	KER	108.6	237.	-0.16	-0.16	-0.12	-0.15
20	ZFRI	110.5	193.	0.27	0.15	0.22	0.21
21	KZIT	121.8	235.	0.23	0.15	-0.14	0.08
23	GLH	132.1	8.	0.10	0.1	0.087	0.10
24	SHMJ	137.	13.	-0.006		-0.49	-0.25
25	PRNI	137.6	198.	0.16	0.021	0.073	0.08
26	MRNI	163.8	358.	-0.24	-0.27	-0.22	-0.24
27	SAGI	164.8	207.	-0.14	-0.25	-0.19	-0.19
29	KMTI	172.8	204.	-0.15	-0.17	-0.14	-0.15
30	HNTI	173.6	351.	0.17	0.10	0.254	0.17
31	KSDI	184.8	6.	-0.45	0.28	0.25	0.026
33	EIL	211.8	193.		-0.12	-0.09	-0.1
35	MRSJ	205.	183.	(1.5)*	(1.85)*	-0.26	*
36	HSJH	234.	181.		(1.29)*	0.37	*
38	BHL*	263.6	5.			1.0	*
39	KOOC*	266.2	27.			3.3	*
40	AYN*	300.	169.		-0.10	0.85	*
42	BADA*	333.	188.		-1.24	-0.95	-1.1
44	PHNC	406.7	341.			-0.18	
45	CSS	428.2	333.	0.28	0.20	-0.28	0.07
46	MAMC	453.5	333.			0.94	
47	PPCY	470.7	323.	0.7	0.35	-0.12	0.11 (2.3)
48	ALFC	481.2	327.	0.42	0.14	0.25	0.27
	RMS** (Npt)			0.26 (25)	0.17 (27)	0.19 (32)	0.207 (84)

* -Non reliable data or absence of seismogram.

** RMS is computed for all dt < 0.5 sec.

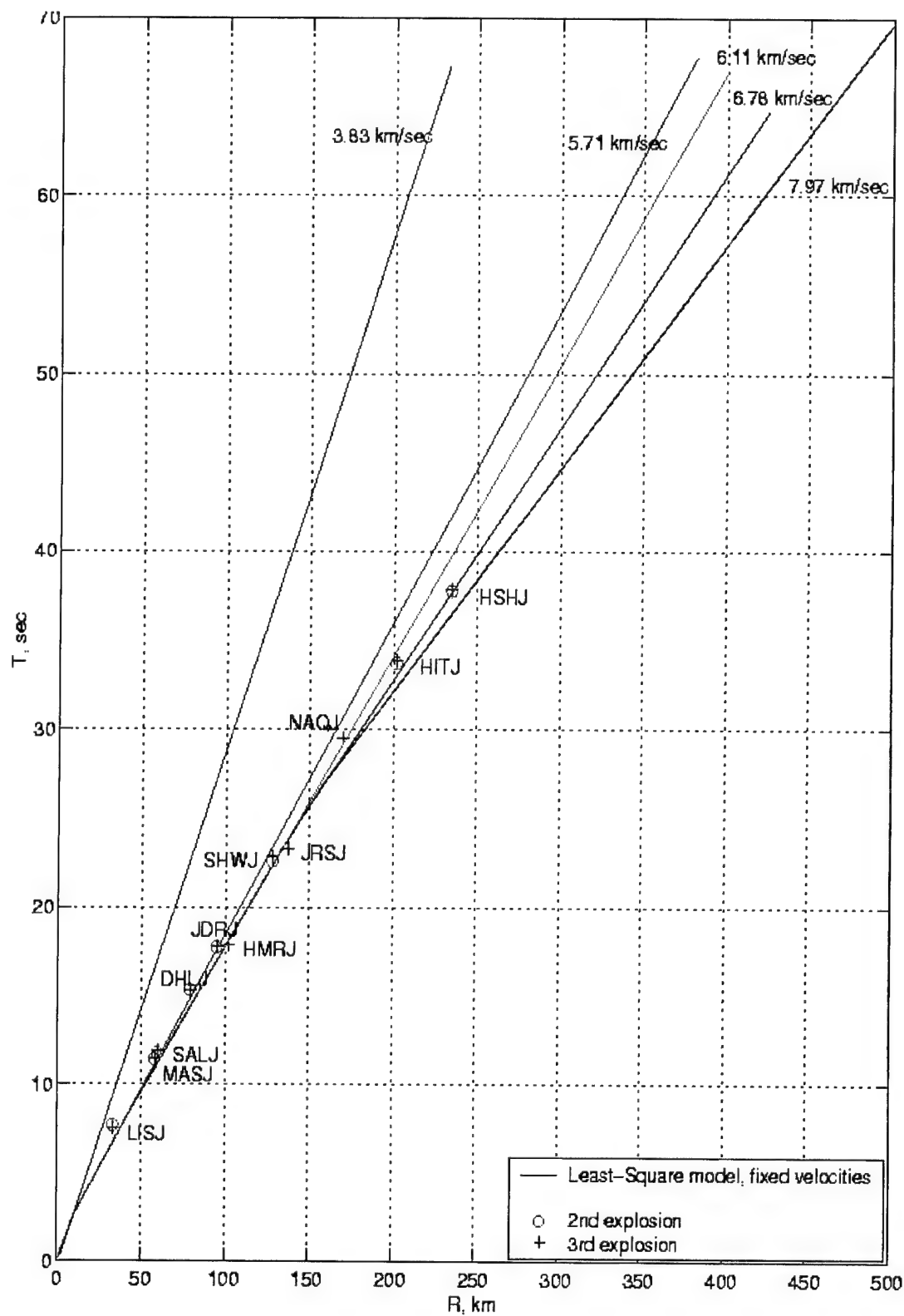


Figure 5. Comparison of the first arrival pickings from the selected JSN seismograms with the theoretical arrivals (given by the Table 9 model) of the refracted waves.

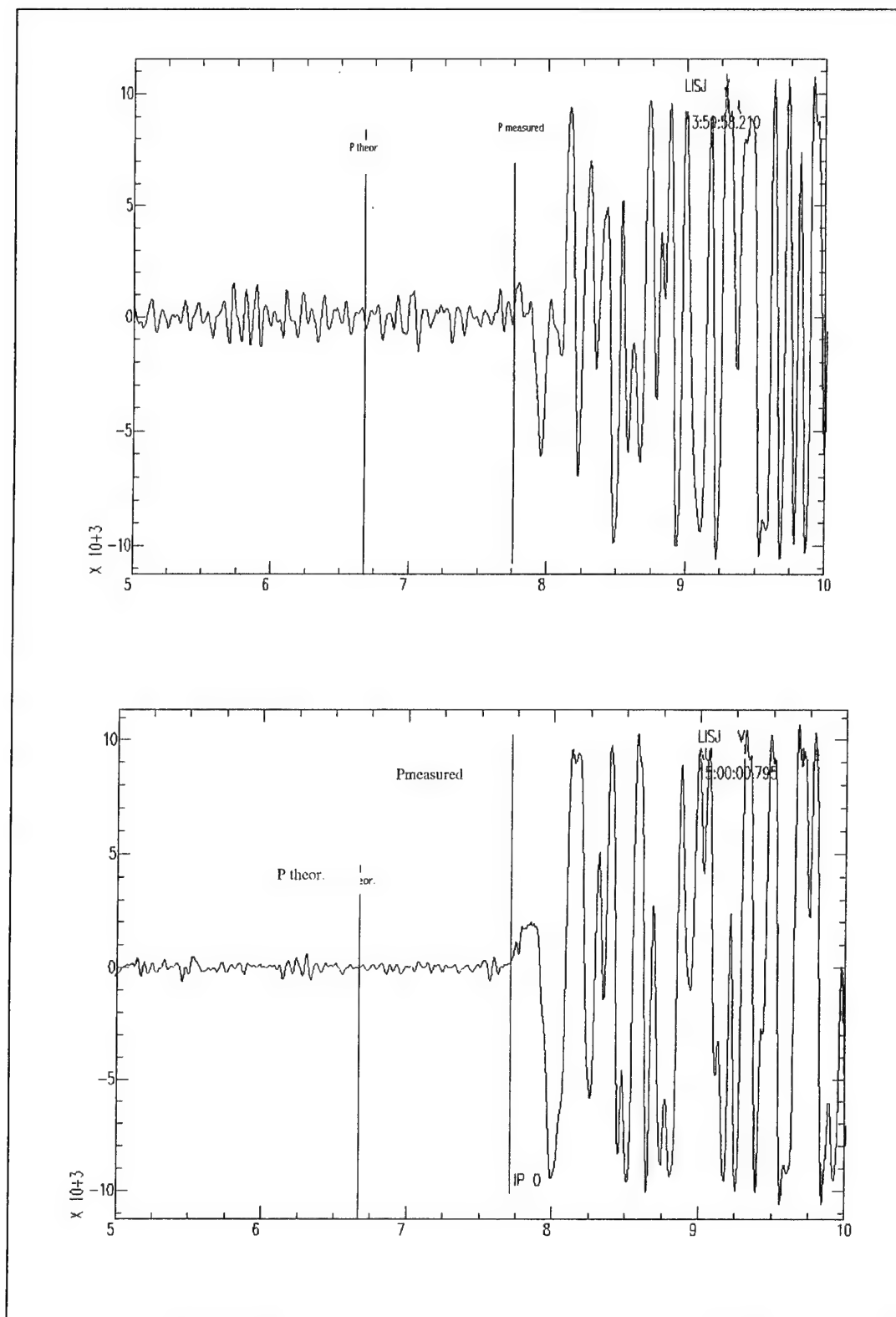


Figure 6. Signal arrival from explosions 2 and 3 to the JSN station LISJ, 33 km.

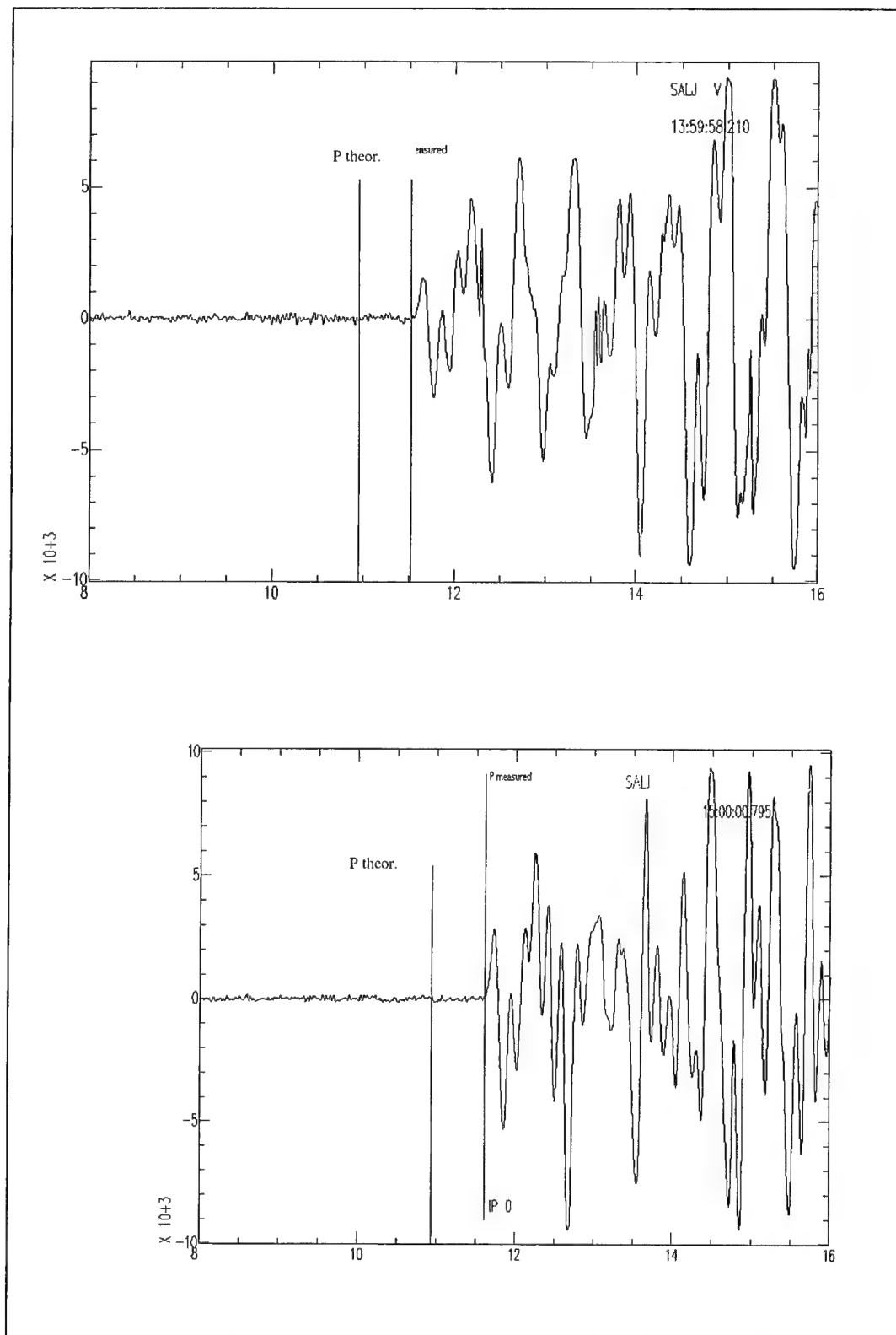


Figure 7. Signal arrival from explosions 2 and 3 to the JSN station SALJ, 58 km.

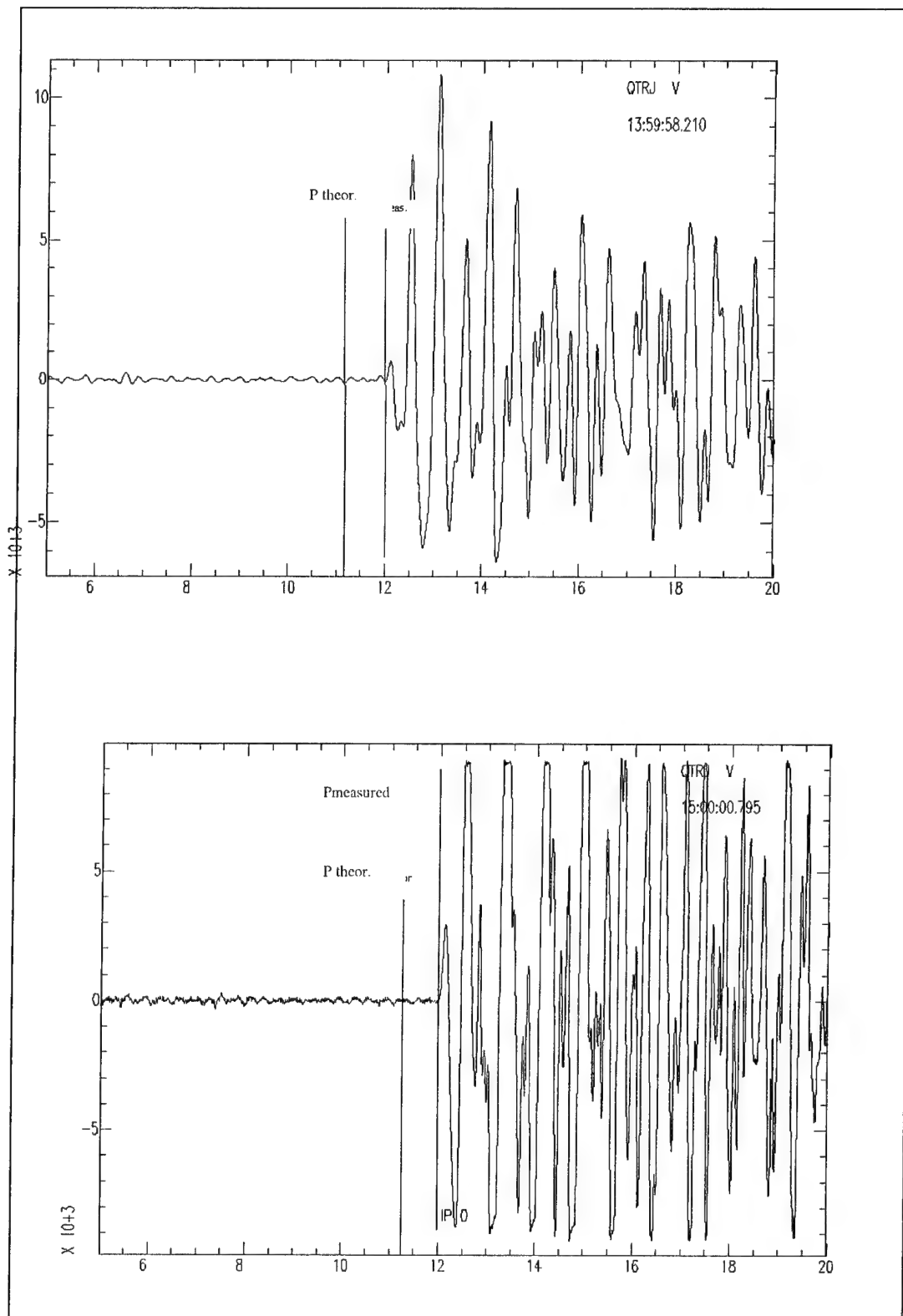


Figure 8. Signal arrival from explosions 2 and 3 to the JSN station QTRJ, 60 km.

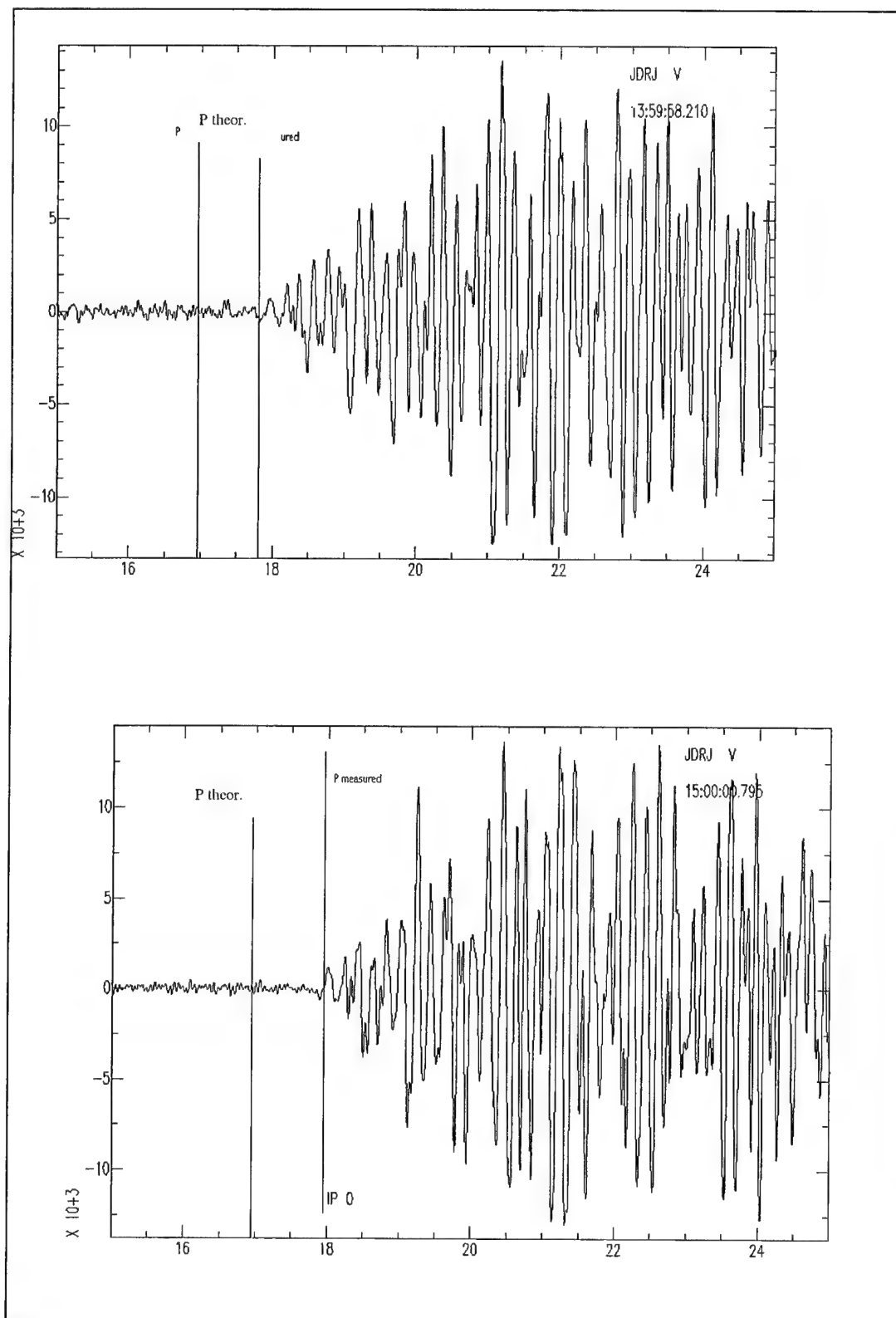


Figure 9. Signal arrival from explosions 2 and 3 to the JSN station JDRJ, 95 km.

4.1.4 Looking for a JSN Model.

Based on previous studies (Ginzburg et. al., 1979, 1980, 1981, Makris et al., 1983, El-Isa et. al., 1987 and El-Isa, 1990) we should expect different crustal models at the two sides of the Dead Sea Transform. Using the 17 most reliable 1st arrival P wave readings to the JSN stations and assuming a 4 layer model with P wave velocities as in the ISN model we obtain the result shown in Figure 10. This JSN model yields RMS=0.17. The delays are explained here by 2 km increases in the sedimentary first layer.

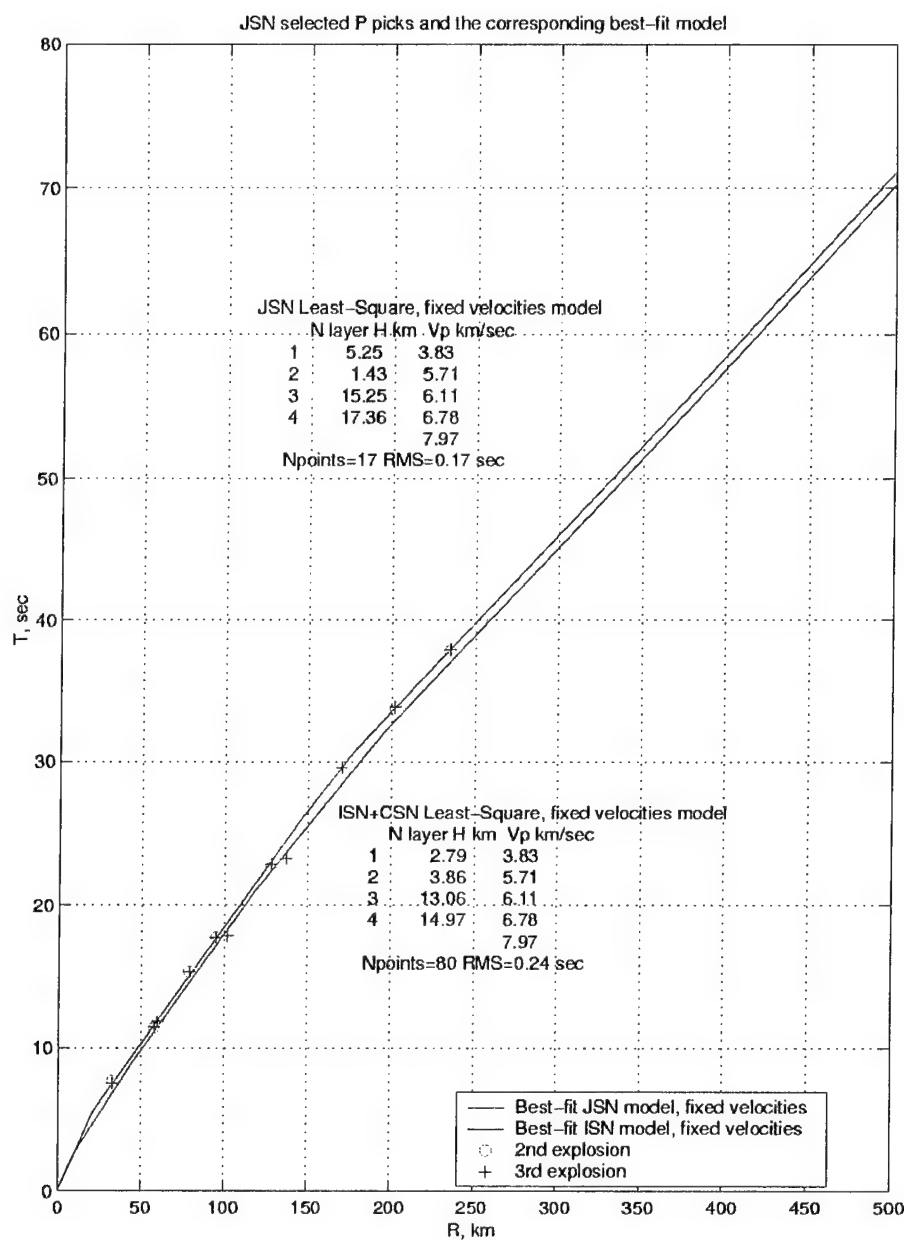


Figure 10. JSN fixed velocity model resulting from the selected P picks from the Dead Sea Explosions.

4.1.5 Building the Composite ISN+JSN+CSN Model.

We took all available data including Saudi Arabian readings and fitted a four-layer model. The “unified velocity model” is presented in Table 11. This model is based on 95 P-wave readings out of the 120 initial acquired by the ISN, JSN, CSN and Saudi Arabian stations. These data yields an RMS of 0.25 sec. The residuals are shown in Table 12, where bold letters mark stations participating in the fitting. For each station, having three data points in the table we computed average residual and standard deviation. The latter represent the scatter in the measurement. From the table we see that six JSN stations remain in the final fitting for some of explosions (often with one or two observations). The final model P travel time is shown in Figure 11.

Table 11. Unified velocity model.

Thickness, km	Vp, km/sec	Vs=Vp/1.78, km/sec
3.52	3.81	2.14
5.47	5.79	3.25
10.48	6.27	3.52
13.91	6.61	3.71
	7.97	4.48

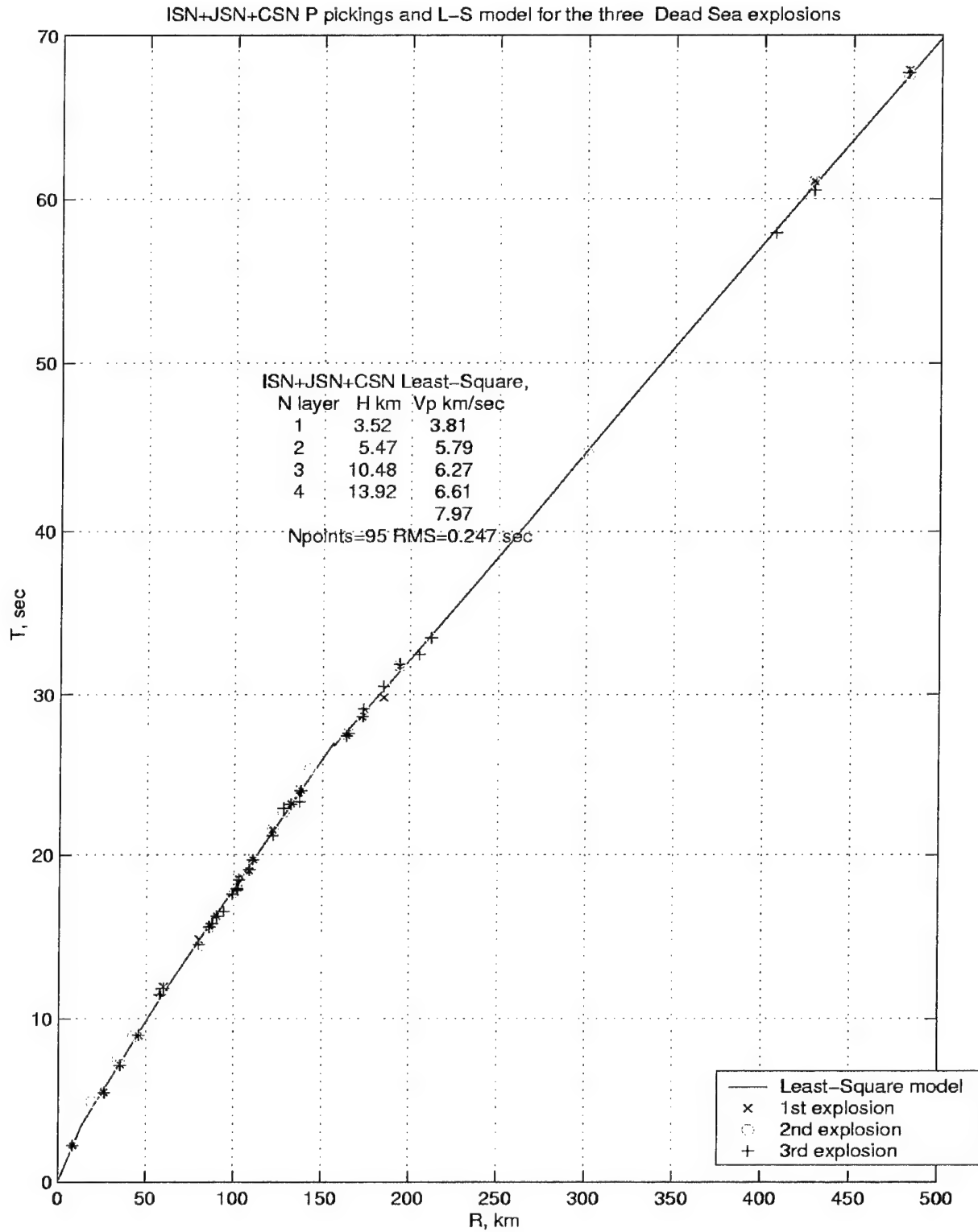


Figure 11. Unified model using ISN, JSN, CSN P pickings for the three Dead Sea explosions.

Table 12. Residuals for the ISN +JSN+CSN (Table 11) data Least-Square model.

N	St.name	R km	Az, deg	dt1,sec	dt2, sec	dt3,sec	AVER	STDEV	SNR1	SNR2	SNR3
1	DRGI	8.30	322.00	0.09	0.04	0.10	0.08	0.03	1075.90	1952.	1910.60
2	ENGI	8.60	214.00	0.05	-0.03	*			321.37	1217.	*
3	MZDA	26.20	197.00	-0.17	-0.20	-0.20	-0.19	0.02	4.15	27.56	101.74
4	LISJ	33.00	173.00	0.79	0.84	0.65	0.76	0.10	11.57	8.25	32.63
5	JVI	45.90	347.00	-0.13	-0.18	-0.12	-0.15	0.03	41.73	80.42	122.47
6	SALJ	58.00	24.00	0.40	0.22	0.28	0.30	0.09	6.19	23.96	40.17
7	QTRJ	60.00	115.00	0.41	*	0.31			30.99	40.84	68.93
8	DHLJ	79.00	183.00	1.10		0.73			5.90	11.41	9.09
9	HMDT	80.00	5.00	0.08	-0.29	-0.20	-0.14	0.20	21.70	40.70	24.20
10	MSH	86.10	227.00	-0.20	-0.14	-0.19	-0.18	0.03	3.71	5.03	6.37
11	ZNT	87.60	333.00	-0.19	-0.16	*			*	44.97	33.26
12	RTMM	90.10	234.00	-0.07	-0.14	-0.11	-0.11	0.03	11.11	11.56	13.85
13	ANJJ	94.00	22.00	0.18	?	-0.42			6.02	5.84	7.19
14	JDRJ	95.00	161.00	1.21	0.63	0.60	0.81	0.34	6.21	6.38	9.23
15	ATR	99.10	231.00	-0.13	-0.22	-0.18	-0.18	0.05	31.88	21.38	53.69
16	MGI	101.50	359.00	-0.15	-0.38	-0.23	-0.25	0.12	3.00	9.59	25.36
17	HMRJ	102.00	56.00	0.32	-0.07	-0.39	-0.04	0.36	4.76	7.40	9.20
18	SVTA	102.70	230.00	-0.06	0.15	0.10	0.06	0.11	32.67	4.34	4.51
19	KER	108.70	237.00	-0.28	-0.28	-0.24	-0.27	0.02	71.48	50.41	50.77
20	ZFRI	110.50	193.00	0.16	0.05	0.11	0.11	0.06	10.70	45.30	30.36
21	KZIT	121.80	235.00	0.17	0.10	-0.21	0.02	0.20	11.84	14.26	13.52
22	SHWJ	128.00	177.00	*	0.26	0.46			3.08	*	29.48
23	GLH	132.10	8.00	0.09	0.09	0.07	0.08	0.01	14.41	6.63	22.19
24	PRNI	137.70	198.00	0.11	-0.04	0.02	0.03	0.07	152.79	178.9	323.41
25	HAF	143.60	344.00	-0.14	-0.61	-0.52	-0.42	0.25	2.86	7.61	9.42
26	KSHT	164.20	12.00	0.23	0.17	0.30	0.23	0.07	16.61	15.61	43.46
27	SAGI	164.80	207.00	-0.19	-0.30	-0.24	-0.24	0.06	87.29	42.52	68.85
28	NAQJ	170.00	178.00	1.39	0.67	1.12	1.06	0.36	4.54	5.32	17.29
29	KMTI	172.90	204.00	-0.19	-0.22	-0.19	-0.20	0.01	25.89	35.26	71.09
30	HNTI	173.60	351.00	0.14	0.07	0.21	0.14	0.07	6.62	19.98	24.48
31	KSDI	184.90	6.00	-0.49	0.24	0.21	-0.01	0.42	2.89	4.41	7.98
32	HRI	193.90	8.00	0.31	0.43	0.48	0.41	0.09	10.87	46.07	45.47
33	HITJ	202.00	169.00	*	1.32	1.39			5.25	9.13	10.39
34	MRSJ	205.00	183.00	1.53	1.82	-0.31	1.01	1.15	0.68	2.31	1.82
35	EIL	211.90	193.00	*	-0.17	-0.14			1.71	6.20	4.39
36	HSIJ	234.00	181.00	*	1.25	0.33			1.27	3.05	1.81
37	MDRJ	235.00	171.00	3.32	1.24	1.33	1.96	1.18	4.38	1.84	14.35
38	BHL	263.6	5			0.76					
39	KOOC	266.2	27			*					
40	AYN	300	169		-0.15	0.81					
41	BMSH	307	191		-1.78	-1.31					
42	BADA	333	188		-1.29	-0.99					
43	MKNA	347	189		-1.64	-1.08					
44	PHNC	406.7	341			-1.16					
45	CSS	428.2	333	0.32	0.16	-0.24	0.08	0.17			
46	MAMC	453.5	333			0.90					
47	PPCY	470.7	0.69	0.75	0.4	-0.18					
48	ALFC	481.30	327	0.38	0.10	0.21	0.23	0.14			
	RMS*(Npt)			0.27 (26)	0.22 (30)	0.246 (30)	0.245 (86)				
	AVERAGE(Npt)							0.194 (27)			

* RMS is computed for all dt < 0.5 sec.

4.1.6 Analysis of the Travel Time Deviations.

The travel time residual $dt = T_{obs} - T_{calc}$ consists as a first approximation of two parts $dt = dt_1 + dt_2$, where dt_1 is a measurement (picking) error, dt_2 is the discrepancy between the model and the real travel time. Both have a random and systematic component. The last three columns of Table 12 contain $SNR = \text{RMS}(\text{Signal}, 2 \text{ seconds}) / \text{RMS}(\text{Noise}, 5 \text{ seconds})$ measured with respect to the P arrival time. The SNR versus distance relation is shown in Figure 12. For simplicity we describe it using a simple asymptotic function.

Noise conditions differ significantly between the stations. This explains the cases of large scatter in the data. The several very quiet ISN stations (tagged in Figure 12) exhibit outstandingly high SNR at significant distances.

The influence of the SNR on the time discrepancy, dt , is demonstrated in Figure 13. In general, dt decreases as SNR increases. However, at stations with a large SNR as well as a large time discrepancy, the difference is most likely due to modeling. The role of measurement error, dt_1 , can be estimated by examining the scatter between the three events for each station. Time residuals and their corresponding scatter are shown in Figures 14 and 15, respectively. These do not suggest any distance dependency, however, they do emphasize the high scatter in the data of stations. Having a scatter of ~ 0.2 sec. (see column STDEV in Table 12), in P wave travel time measurements implies that there is no real physical preference for any of the travel time (TT) models discussed above. We may fairly state that the controlling parameter in TT modeling in the investigated region is the capability to identify accurately and measure the arrival time. True model variations seem to be of marginal influence.

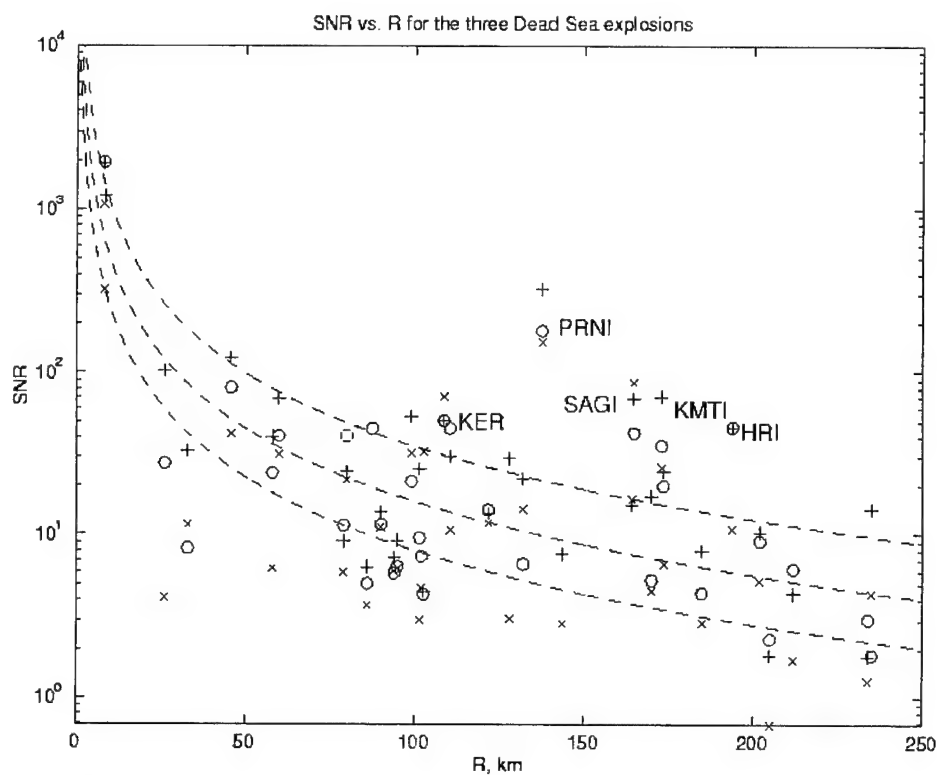


Figure 12. SNR vs distance R for the three explosions: "x" - first, "o" - second and "+" - third.

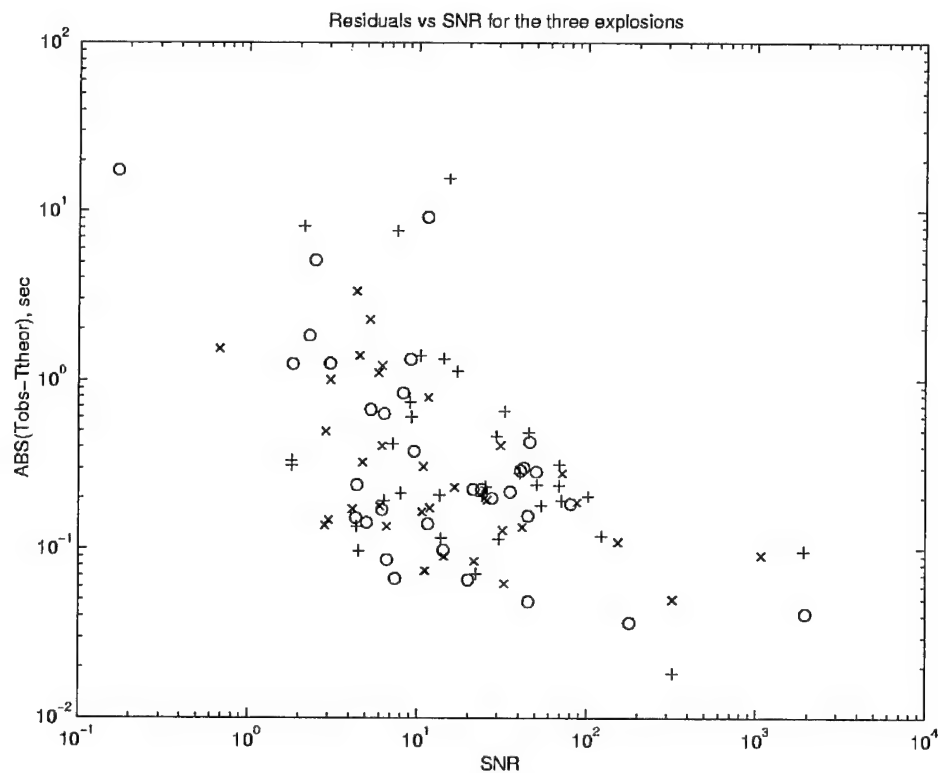


Figure 13. Deviation $|dt|$ of the travel time measurements T_{obs} from the model (Table 11) time T_{calc} vs SNR for the three explosions: "x" - first, "o" - second and "+" - third.

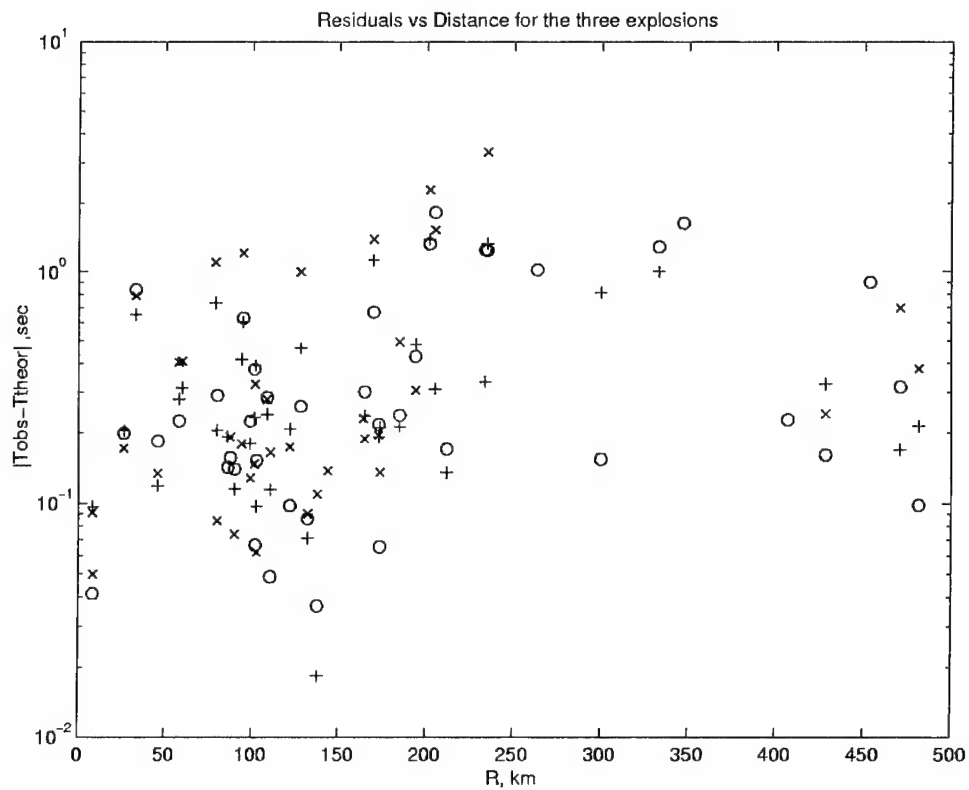


Figure 14. Deviation $|dt|$ of the travel time measurements T_{obs} from the model time T_{calc} (Table 11) vs distance R for the three explosions: “x” - first, “o” - second and “+” - third.

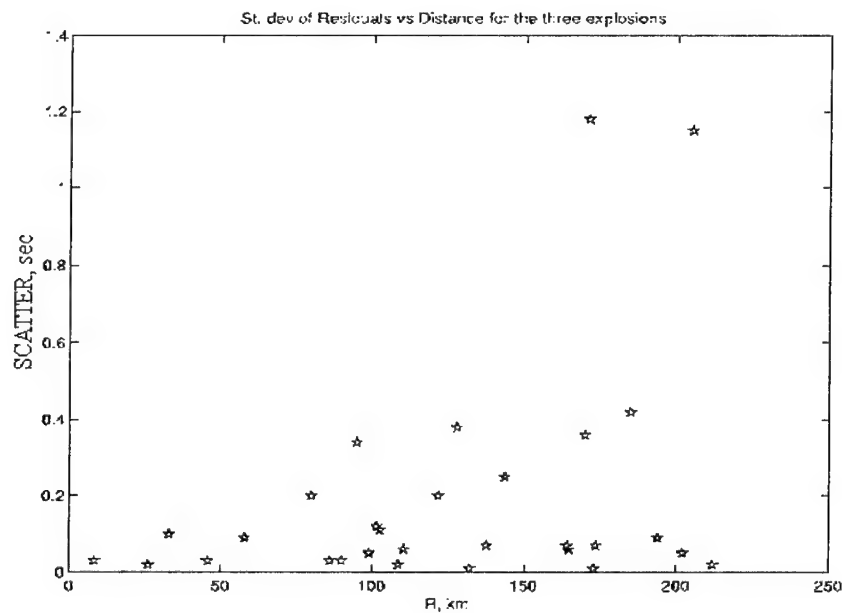


Figure 15. Scatter of P travel times between the three explosions vs. distance R .

4.1.7 Location of the Dead Sea Explosions, using Different Velocity Models.

In order to locate the explosions we applied a robust automatic locator (Pinsky and Shapira, 1999), developed under this contract (see Section 4.2). The procedure was used in two modes: manual picking and automatic picking. We also analyzed the influence of the travel time models: "ISN+CSN" (Table 7), "ISN+CSN+JSN" (Table 11) and the "JSN" (Figure 10), on the location accuracy.

Location results using the three models are shown in Table 13. For each combination of event number, travel time model, observational system (number of stations is shown) and type of locator (manual or automatic), the table shows location results and deviation epicenter and hypocenter. The best location was obtained for the first explosion. Using the "ISN+CSN" (Table 9) velocity model and ISN manual pick the errors are: $dx=0.5$ km, $dy=-0.16$ km, $dh=0.1$ km. From the table we see that locations given by the ISN data only are better than those provided by the ISN + JSN stations, contradicting expectations based on full coverage network configuration. This is due to systematic shifts in the readings of the Jordanian stations discussed above. Adding the JSN stations leads to shifting the epicenter in a western direction (1.9 - 2.5 km) and a little to the north (0.5 - 1.5 km), which yields a delay for the Jordan stations in the prevailing first arrival. It seems that the error in the manual mode does not depend to a great extent on whether the ISN+CSN or the ISN+JSN+CSN velocity model was used.

Comparison of the manual picking mode with the automatic procedure shows that the latter is amazingly accurate, especially when only ISN picks are used. In many cases automatic locations are better than those obtained from manual picks.

When using the JSN model in the location procedure it was expected that the error would be less for the JSN stations only than for a mixture of ISN and JSN or ISN stations alone. In practice there is no evidence of this, probably owing to the smaller number of stations and/or poor configuration of the Jordan stations. The most practical result from this investigation is that for all the models and combinations of stations the total error did not exceed 3.2 km, thus showing that model variations were not in this case crucial for accurate location.

Table 13. Robust Location of the three Dead Sea explosions using different velocity models manual and automatic pickings (Israel Coordinate System is used).

MODEL	ISN+JSN+CSN MODEL								
	MANUAL PICKING					AUTOMATIC PICKING			
EVENT	FIRST EXPL.								
Network	GPS	ISN	ERROR	ISN+JSN	ERROR	ISN	ERROR	ISN+JSN	ERROR
Nst		24		24+6st		24		24+6	
Unit	km	km	km	km		km		km	
X	191.96	192.36	0.4	188.9	-3.06	192.96	1	189.9	-2.06
Y	104.59	104.42	-0.17	105.5	0.91	104.42	-0.17	105.6	1.01
H	0.5	1.2	0.7	0.8	0.3	0.6	0.1	1	0.5
Depicen.			0.43		3.19		1.01		2.29
Dhypo.			0.82		3.20		1.02		2.35
EVENT	SECOND EXPL.								
Nst		24		24+7		24		24+7	
X	191.9	193.7	1.8	189.3	-2.6	191.3	-0.6	190.3	-1.6
Y	104.69	104.62	-0.07	105.3	0.61	105.4	0.71	105.23	0.54
H	0.5	0.8	0.3	1.4	0.9	0.8	0.3	0.8	0.3
Depicen.			1.80		2.67		0.92		1.69
Dhypo.			1.82		2.8		0.97		1.71
EVENT	THIRD EXPL								
Nst		25		25+4		25		25+4	
X	192.02	193.07	1.05	192.9	0.88	192.46	0.44	192.46	0.44
Y	104.66	104.62	-0.07	104.6	-0.06	104.83	0.17	105	0.34
H	0.5	1.2	0.7	1	0.5	1.6	1.1	1.6	1.1
Depicen.			1.05		0.88		0.47		0.55
Dhypo.			1.26		1.01		1.20		1.23
MODEL	ISN+CSN MODEL								
	MANUAL PICKING					AUTOMATIC PICKING			
EVENT	FIRST EXPL.								
Network	GPS	ISN	ERROR	ISN+JSN	ERROR	ISN	ERROR	ISN+JSN	ERROR
Nst		24 st		24st+6st		24st		24+6st	
X	191.96	192.3	0.5	189.3	-2.66	192.46	0.5	190.3	-1.66
Y	104.59	104.59	-0.16	104.6	0.01	104.93	0.34	105	0.41
H	0.5	0.6	0.1	0.4	0.6	0.1	-0.5	0	-0.5
Depicen.			0.52		2.66		0.60		1.70
Dhypo.			0.53		2.66		0.61		1.78
EVENT	SECOND EXPL.								
Nst		24		24+7		24		24+7	
X	191.9	192.66	0.76	189.2	-2.7	192.26	0.36	189.9	-2
Y	104.69	104.62	-0.07	105.3	0.61	105.12	0.43	105	0.31
H	0.5	0.7	0.2	0.6	0.1	0.6	0.1	0.8	0.3
Depicen.			0.76		2.76		0.56		2.02
Dhypo.			0.79		2.77		0.57		2.04
EVENT	THIRD EXPL.								
Nst		25		25+4		25		25+4	
X	192.02	193.06	1.04	189.9	-2.12	192.46	0.44	192.5	0.48
Y	104.66	104.62	-0.07	105.8	1.14	104.82	0.16	104.8	0.14
H	0.5	0.6	0.1	1.1	0.6	3.4	2.9	1	0.5
Depicen.			1.04		2.40		0.47		0.5
Dhypo.			1.05		2.48		2.93		0.70

Table 13. (Cont.) Robust Location of the three Dead Sea explosions using different velocity models manual and automatic pickings (Israel Coordinate System is used)

MODEL	JSN MODEL										
Method	MANUAL PICKING							AUTOMATIC PICKING			
Network	GPS	JSN	ERR.	ISN	ERROR	ISN+JSN	ERR.	ISN	ERR.	ISN+JSN	ERROR
Unit	km	km	km	km		km		km			km
EVENT	FIRST EXPL.										
Nst	12			24		24+6		24		24+6	
X	191.96	194.27	2.31	191.9	-0.06	189.7	-2.26	194.3	2.34	189.9	-2.06
Y	104.59	106.23	1.64	104.6	0.01	104.6	0.01	104.6	0.01	105.8	1.21
H	0.5	1.2	0.7	2.4	1.9	2	1.5	1.6	1.1	2.2	1.7
Depicen			2.83		0.06		2.26		2.34		2.39
Dhypo.			2.91		1.90		2.71		2.58		2.93
EVENT	SECOND EXPL.										
Nst	15			24		24+7		24		24+7	
X	191.9	194.77	2.87	193.7	1.8	189.7	-2.2	193.5	1.6	190.9	-1
Y	104.69	105.53	0.84	104.4	-0.29	105.4	0.71	104.82	0.13	104.8	0.11
H	0.5	0.6	0.1	2	1.5	2.6	2.1	2	1.5	2.4	1.9
Depicen			2.991		1.82		2.31		1.60		1.00
Dhypo.			2.99		2.36		3.12		2.20		2.15
EVENT	THIRD EXPL.										
Nst	12			25		25+4		25		25+4	
X	192.02	192.97	0.95	189.5	-2.52	193.1	1.08	193.3	1.28	189.7	-2.32
Y	104.66	106.23	1.57	104.4	-0.26	105.8	1.14	104.2	-0.46	105.4	0.74
H	0.5	0.2	-0.3	2	1.5	2.8	2.3	2.4	1.9	3.2	2.7
Depicen			1.83		2.53		1.57		1.36		2.43
Dhypo.			1.86		2.94		2.78		2.33		3.63

4.1.8 Evaluation of S Wave Travel Time Model.

Reliable S wave readings are extremely useful for accurate source location. However, excitation of S is often not well identified on explosion seismograms. Moreover, prominent Rg, Lg waves from explosions are often misidentified as S. In underwater explosions many bubble and reverberation pulses in P and P coda and later surface waves mask the S phase. Reliable S readings, therefore, are relatively rare. Travel times of 14 S wave readings of the three Dead Sea explosions are presented in Table 14 and compared to the theoretical travel times, provided by the present ISN model (Table 7) and by the models given in Table 8 "Least-Square velocity model", Table 9 "Best-fit velocity model" and Table 11 "Unified velocity model".

In the models of Tables 7-9 and Table 11, the S velocities V_s are estimated as $V_p = kV_s$, where $k=1.78$ is an empirical coefficient. More accurate values can be obtained by fitting the stratified velocity model to the measured S travel times.

Table 14. Travel times for S phase.

No. of explos.	St. Name	R, km	Travel time, sec	Observed-Calculated travel time, sec					
				Tab.3.2	Tab.3.3	Tab.3.4	Tab.3.6	Tab.3.1 α	Tab.3.11
1	MZD	26.1	8.93	-0.52	-0.9	-0.78	-1.22	-0.269	-0.065
	JVI	45.9	15.67	-0.17	-0.04	-0.21	-0.57	0.069	-0.079
	PRNI	137.6	42.75	0.08	0.29	0.22	0.12	0.069	0.10
	KMTI	172.8	51.13	-0.02	0.25	-0.06	-0.12	0.20	0.40
	RMS1			0.28	0.49	0.42	0.68	0.17	0.21
2	MZD	26.2	8.96	-0.5	-0.9	-0.78	-0.26	-0.04	-0.06
	JVI	45.9	15.91	0.07	0.200	0.029	0.30	0.14	0.16
	ZNT	87.6	28.05	-0.3	0.05	0.003	-0.26	-0.20	-0.29
	ATR	99.1	31.55	-0.1	0.19	0.150	-0.25	-0.10	-0.085
	KMTI	172.99	50.68	-0.5	-0.22	-0.53	-0.28	-0.19	-0.09
	RMS2			0.34	0.43	0.43	0.27	0.15	0.16
3	MZD	26.2	9.02	-0.46	-0.84	-0.72	-1.16	-0.20	-0.009
	ZNT	87.6	28.745	0.36	0.740	0.698	0.32	0.43	0.398
	HNTI	173.6	51.035	-0.3	-0.02	-0.33	-0.39	-0.067	0.129
	CSS	428.2	107.605	-0.8	-0.92	-0.59	-0.65	-0.074	-0.134
	ALFC	481.3	119.705	-0.6	-0.81	0.35	-0.41	0.22	0.112
	RMS3			0.54	0.74	0.56	0.66	0.24	0.20
RMS				0.41	0.58	0.48	0.56	0.191	0.191

Table 15. "Best-Fit" model with S velocities varied.

Thickness, km	V _p , km/sec	V _s , km/sec	k
2.79	3.83	2.14	1.79
3.86	5.71	3.14	1.82
13.06	6.11	3.29	1.86
14.97	6.78	3.78	1.79
∞	7.97	4.45	1.79
RMS=0.20 for N=14 S arrivals			

Table 16. Unified model with S velocities varied.

Thickness, km	Vp, km/sec	Vs, km/sec	k
3.52	3.77	2.92	1.29
5.47	6.00	2.49	2.40
10.48	6.11	3.50	1.75
13.91	6.73	3.64	1.85
∞	7.88	4.48	1.76
RMS=0.20 for N=14 S arrivals			

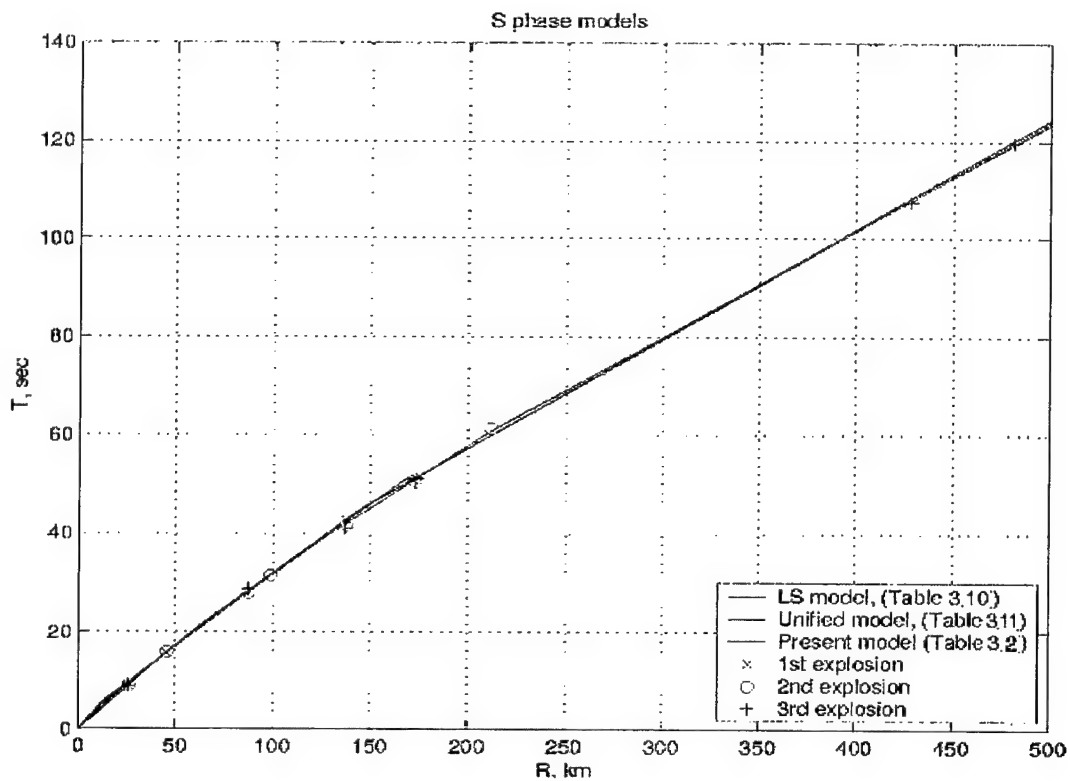


Figure 16. S phase travel time measurements for the three Dead Sea explosions, compared to the three velocity models.

The readings of Table 14 (distance, travel time) pairs are used to fit a velocity model. In the optimization procedure only velocities are varied while depths remain fixed according to the “Best-fit model” (Table 9) and “Unified model” (Table 11). The results are shown in Table 15 and 16 respectively and in Figure 16. Final observation/model discrepancy is presented in Table 14, showing that we managed to reduce the RMS from 0.48 and 0.56 in the initial models of Tables 9 and 11 respectively to 0.2 sec. However, in the final “Unified model” (Table 16) coefficient k is very different from 1.78 for the first two layers, making the result for the model questionable.

4.1.9 Comparison of the Controlled Arad Quarry Explosions Travel Times with the New Velocity Model.

In 1998-1999 four controlled quarry blasts were conducted at the Arad phosphate quarry (Israel) 55 km south-south-west of the Dead Sea explosion site. The general parameters of the explosions are presented in Table 2 (Paragraph 2). It was a challenge to compare the travel times from the two sets of calibration events: Arad and the Dead Sea. The residuals $dt = T_{obs} - T_{model}$ for the Arad quarry blasts are presented in Tables 17-20 for the unified model (Table 11) derived from the Dead Sea shots.

The residuals dt versus distance are also presented in Figure 17. The relatively large travel time differences may be the result of several factors. The first is the long duration of the quarry explosions, $T \approx N_{rows} * Delay$, which varies here from 0.13 to 0.8 sec. The second is a delay of 0.5 sec between the detonation moment and explosion time of each borehole charge in the cases of the 3rd and the 4th explosion. The third is poor phase picking due to the low SNR. The HRI station on Mt. Hermon is a “stable” outlier with a time correction $dt = 1.05$ sec required.

It should be noted that repeating the same analysis while using the “old” velocity model (Table 7), we observed very similar time discrepancies, indicating that the differences between the TT models are negligible.

Table 17. Residuals for the 1st Arad blast.

St. Name	R, km	Az, deg	Dt, sec
MZDA	29.90	35.00	-0.39
YTIR	30.30	348.00	-0.45
LISJ	33.80	59.00	-0.10
DHLJ	36.50	144.00	-0.01
MSH	38.60	255.00	0.44
ATR	53.30	256.00	-0.25
KER	66.20	262.00	-0.22
RMNI	67.40	217.00	0.08
KZIT	77.30	256.00	0.23
PRNI	83.10	192.00	0.44
SAGI	108.80	206.00	-0.13
MBH	145.70	190.00	0.04
EIL	158.40	188.00	0.21
YASH	170.20	190.00	0.15
HRI	247.30	12.00	0.91
RMS			0.35

Table 18. Residuals for the 2nd Arad blast.

St. Name	R, km	Az, deg	Dt, sec
YTIR	28.20	348.00	-0.33
LISJ	32.90	63.00	-0.17
MSH	39.00	252.00	0.28
ENGI	45.30	27.00	-0.06
RTMM	47.80	263.00	-0.08
SVTA	56.20	250.00	0.17
DRGI	57.60	21.00	0.09
ZFRI	60.00	180.00	0.32
SZAF	63.90	249.00	0.03
KER	66.30	260.00	-0.01
RMNI	69.00	216.00	-0.12
MKRJ	66.60	42.00	0.44
PRNI	85.20	191.00	0.15
MASJ	86.40	37.00	0.04
JVI	93.20	10.00	0.11
SAGI	110.60	206.00	0.03
HMDT	131.90	14.00	-0.19
MBH	147.70	190.00	-0.01
AQBJ	153.00	184.00	0.48
YASH	172.30	190.00	0.29
HRI	245.20	12.00	0.86
RMS			0.28

Table 19. Residuals for the 3rd Arad quarry blast.

St. Name	R, km	Az, deg	dt, sec
MZDA	27.90	36.00	-0.53
LISJ	31.80	63.00	0.09
MSH	40.00	253.00	-0.49
DHLJ	38.20	147.00	0.13
ENGI	44.70	26.00	-0.56
RTMM	48.30	263.00	-0.43
ARVI	52.00	180.00	-0.36
ATR	54.70	253.00	-0.35
DRGI	56.90	20.00	-0.32
DSIO	56.90	20.00	-0.28
SVTA	57.30	250.00	-0.34
ZFRI	60.50	181.00	-0.18
SZAF	65.00	249.00	-0.62
KER	67.50	260.00	0.02
RMNI	69.80	216.00	-0.26
JDRJ	69.90	127.00	-0.33
KZIT	78.70	254.00	-0.01
QTRJ	81.50	75.00	0.04
MASJ	85.50	36.00	-0.33
PRNI	85.50	192.00	0.01
JVI	93.30	9.00	-0.50
SHWJ	86.00	159.00	1.07
JRSJ	94.10	177.00	0.65
SALJ	110.50	25.00	-1.22
SAGI	111.40	206.00	-0.76
ZNT	126.50	353.00	0.08
NAQJ	126.70	166.00	0.29
HMDT	131.20	14.00	0.31
MBH	148.10	190.00	-0.37
MGI	150.50	9.00	-0.08
AQBJ	153.60	185.00	0.19
EIL	161.10	188.00	0.12
YASH	171.30	190.00	-0.05
GLH	183.10	14.00	-0.42
HNTI	219.10	360.00	0.18
KSHT	216.10	16.00	0.47
HRI	244.60	12.00	1.02
RMS			0.48

Table 20. Residuals for the 4th Arad quarry blast.

St. Name	R, km	Az, deg	Dt, sec
MZD0	27.90	37.00	-0.36
YTR0	29.20	346.00	-0.57
ARV0	51.90	180.00	-0.42
DSI0	57.00	20.00	-0.05
RMN0	69.70	216.00	0.41
PRN0	85.40	192.00	0.06
SAG0	111.40	206.00	0.51
ZNT0	126.60	353.00	-0.28
MBH0	148.00	190.00	-0.66
YAS0	171.20	190.00	-0.05
RMS			0.40

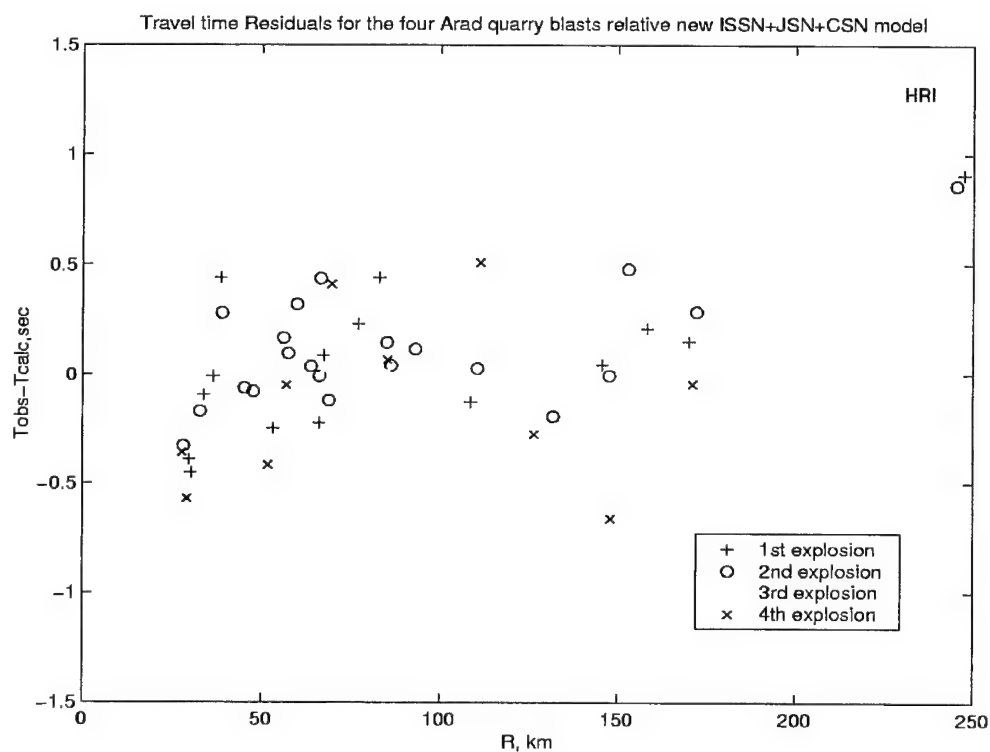


Figure 17. Travel time residuals for the four Arad calibration events using the new (Table 11) velocity model.

4.1.10 Location of Arad Quarry Explosions using New Velocity Model.

The location procedure was applied to the Arad controlled blasts as before. The results are presented in Table 19. In spite of the large scatter of picks mentioned above, the location error for most cases is acceptable. Automatic mode mostly shows slightly worse epicenters and depth but for the last explosion the results are the reverse.

Table 21. Location of the Arad quarry explosions using manual and automatic pickings and Table 11 velocity model.

Event N	GPS	Manual		Automatic	
			ERROR		ERROR
Unit	km	km	km	km	km
A1		First Explosion			
Nst		15		15	
X	167.9	168.2	0.3	168.1	0.2
Y	57	57.9	0.9	58.1	1.1
H	-0.1	0.2	0.3	0.2	0.3
Depic.			0.94		1.12
Dhypoc.			0.99		1.16
A2		Second Explosion			
Nst		21		21	
X	168	167.3	-0.7	166.7	-1.3
Y	57	57.5	0.5	57.9	0.9
H	-0.1	0.2	0.3	2.4	2.5
Depic.			0.86		1.58
Dhypoc.			0.91		2.95
A3		Third Explosion			
Nst		31		31	
X	168	166.9	-1.1	167.19	-0.81
Y	57.6	59.6	2	59.2	1.6
H	-0.1	0.2	0.3	0.4	0.5
Depic.			1.614001		1.79
Dhypoc.			1.32916		1.86
A4		Fourth Explosion			
Nst		10		10	
X	168	170.7	2.7	166.3	-1.7
Y	57.5	58	0.5	58.2	0.7
H	-0.1	0.4	0.5	0.2	0.3
Depic.			2.75		1.84
Dhypoc.			2.79		1.86

4.2 Excitation and Attenuation of Various Seismic Phases for Different Paths.

4.2.1 Events from the East Mediterranean.

Several moderate events of similar magnitudes were selected from the earthquake dataset (mentioned previously in Section 3.2). Source parameters of these are presented in Table 22. Figure 18 shows paths of the waves from the events to recording stations, propagating through different crust structures as presented in Figure 19. We analyzed seismograms observed at 3-component stations of the ISN, including short-period stations MRN and EIL as surrogate for IMS stations MRNI and EIL (see Figures 20, 21).

Table 22. Source parameters from ISN and NEIC (PDE) bulletins.

Date	Agency	Origin Time	Magnitude		Depth km	Latit. N	Long. E	Area
			ML	mb				
1996/06/19	ISN	00:18:05.2	4.7	4.7	2	35.939	35.872	Lattakiya
	PDE	00:18:02.17	4.7	-	10	36.11	35.91	
1996/10/19	ISN	01:20:43.8	4.6	4.6	25	34.417	32.077	Cyprus
	PDE	01:20:43.8	-	4.1	33	34.25	31.89	
1996/10/29	ISN	02:00:24.3	4.9	4.9	25	34.416	32.212	
	PDE	02:00:21.64	4.9	4.5	33	34.50	32.24	

The propagation paths of seismic waves from the events to the ISN stations are very different. The waves from Cyprus cross the Levantine Basin of the Eastern Mediterranean (through the oceanic crust), whereas the Lattakiya event provides paths along the seashore and mainly, inland (through the continental crust). We identified three phases on the waveforms, Pn, Sn and Lg, that are key regional phases for a number of different discriminants. It is known that these phases may have variable amplitudes due to propagation path barriers, and in certain regions Sn and Lg phases are not always observed.

For the Lattakiya event a low frequency Lg phase, associated with the maximum amplitudes is identified. It begins to emerge from the relatively high frequency S-coda quite late at stations HAF and MKT (Figure 20), corresponding to a group velocity of about 3.2 km/sec, also obtained by Baker and Barker (1997) rather than the typical value of 3.5 km/sec used by Baumgardt (1996), for this region. Seismograms of the Cyprus earthquakes show strong Sn waves, whereas the Lg phase is hardly identified on the records, i.e., it is blocked by the sea section of propagation paths. Thus Sn phases tend to be strong for the Lg blockage paths, providing very high Sn/Pn ratios. Similar observations were made at the SP stations EIL and MRN (Figure 21).

In contrast, for the case of strong Lg (the Lattakiya event), Sn phases are lower amplitude, especially at the more distant inland station MKT (Figure 20), showing a strong attenuation and resulting in much lower Sn/Pn ratios.

Similar results (Lg propagation blockage) for Dead Sea transform events observed at KEG station were presented by Baumgardt (1996). The effects are explained by a pinchout of the granitic layer in the Levant basin, where the sediments thicken and the crust thins, according to the Cornell maps of the crustal structure in the Middle East (Barazangi et al., 1995), resulting in a breakdown of the Lg propagation. It is possible that the same factors are responsible for excitation and attenuation features of Lg and Sn from Levant events we observed at Israeli station, where the Moho depth factor is possibly dominant.

We plotted maps of depths to basement and Moho in the area of propagation paths of the selected events to the Israeli stations (Figure 19), based on the Cornell GIS database at the Website: atlas.geo.cornell.edu (Steer et al., 1999). The maps show that the efficient propagation of Lg is observed for paths that do not cross sedimentary basins.

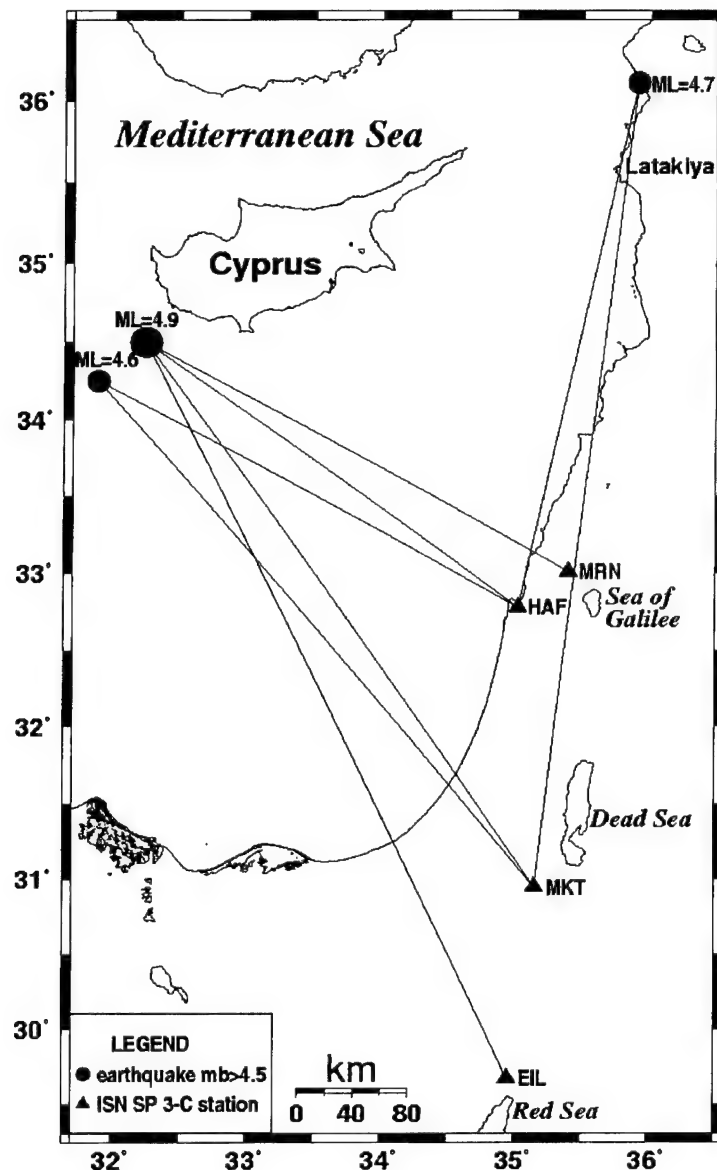
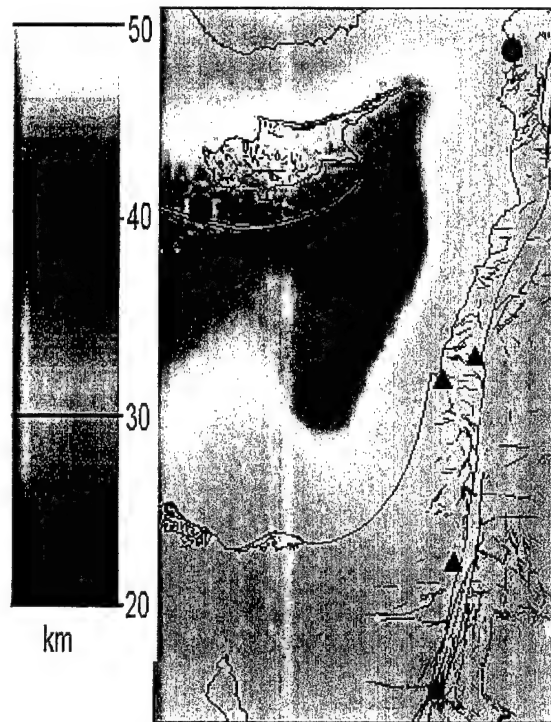
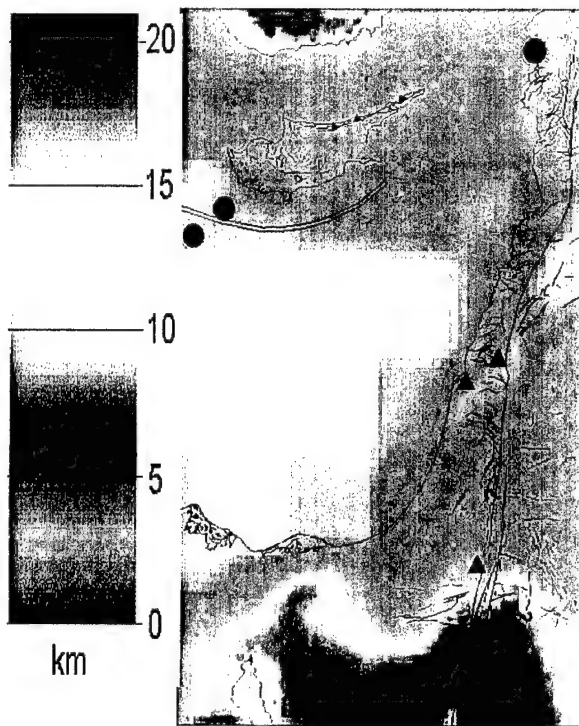


Figure 18. Selected earthquakes from Eastern Mediterranean, recording stations and wave paths.



a – depth to basement

b – Moho depth

Figure 19. Crustal structure for the propagation paths of the selected events (●) to the stations (▲) (from the Cornell GIS database at Website: atlas.geo.cornell.edu).

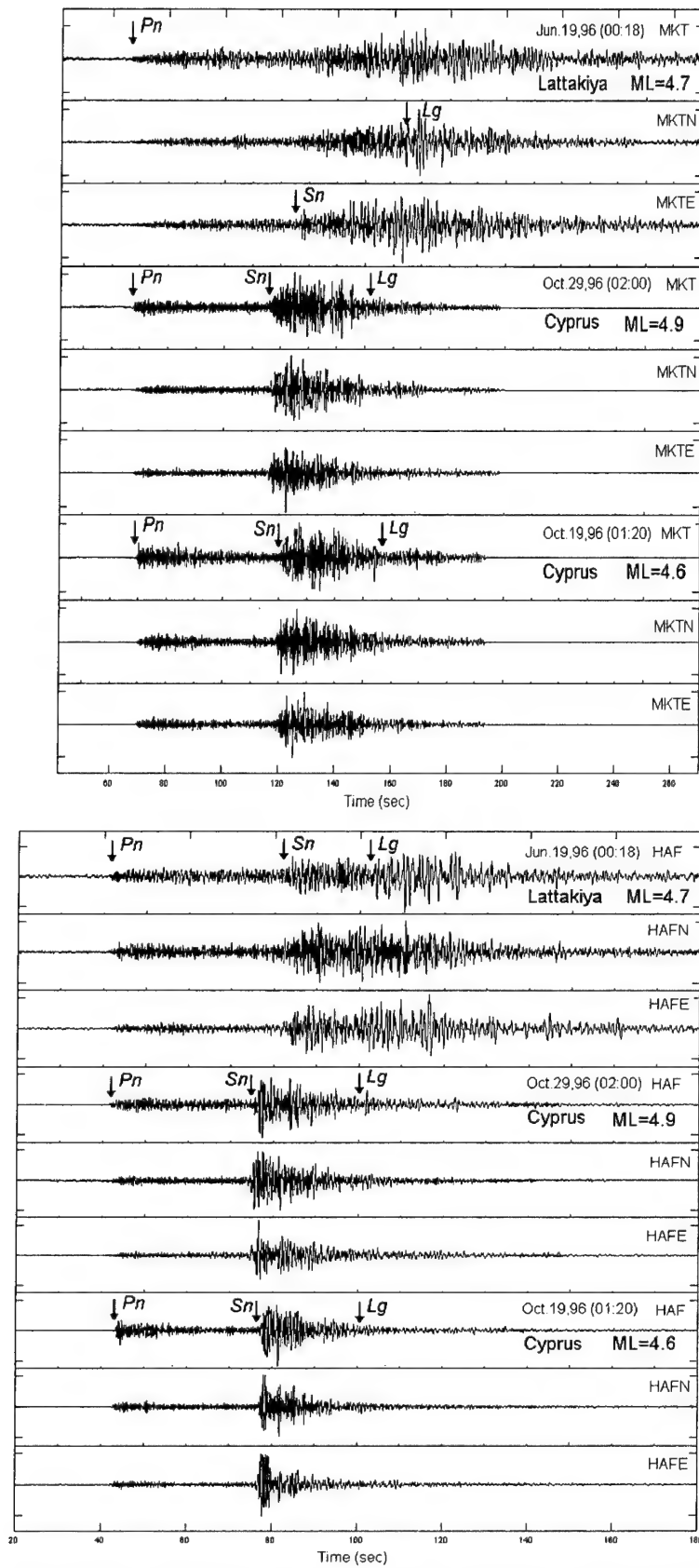


Figure 20. Recordings of the selected East Mediterranean events at 3-C stations HAF and MKT of the ISN (traces are normalized). Arrows show calculated arrival times.

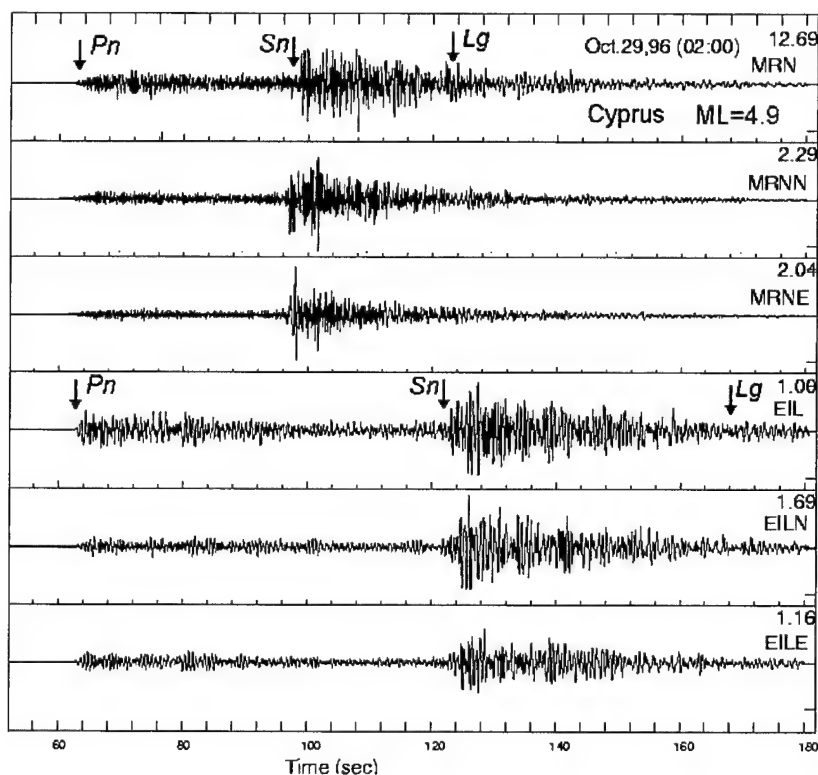


Figure 21. Observation of the Cyprus Oct. 29, 1996 event at ISN 3-C stations which are surrogate for IMS stations MRNI and EIL (traces are normalized). Arrows show calculated arrival times.

4.2.2 Attenuation of Peak Amplitudes for Land Blasts and Underwater Explosions.

We evaluated the attenuation of the vertical Peak Ground Velocity (PGV), using scaled distance $R = r_{(km)}/W_{(kg)}^{1/3}$. Attenuation relations are derived for:

- underwater explosions (UWE) in the Dead Sea in 1993 with charge range $W=16-304$ kg (Gitterman et al., 1998), the calibration shots in the Dead Sea in November 1999 (see Section 3.1.3), UWE in the Mediterranean of 800 kg (Shapira, 1981), and UWE in the Pacific (Willis, 1963);
- experimental (military) single on-surface explosions of 1 and 10 tons (Shapira, 1990), and the Sayerim shot series (Section 3.1.2);
- instantaneous (single) blasts with charge range $W=0.9-2.8$ tons and ripple-fired blasts at Israel quarries $W = 8-15$ tons (Gitterman et al., 1996), as well as controlled quarry blasts in 1998-1999 at the Arad quarry (Section 3.1.3).

Initially we evaluated attenuation of Peak Ground Velocity (PGV) with respect to the epicentral distance r (km). Least-squares fit calculations for the power function $PGV (\mu/sec) = a \cdot r^b$ yields similar values of attenuation parameters for quarry and underwater explosions. The different charge weights are scaled $R = r_{(km)}/W_{(kg)}^{1/3}$.

Similar attenuation laws were found for single and ripple-fired blasts in different areas. Estimations for underwater explosions in the Dead Sea, the Mediterranean (Shapira, 1981) and the Pacific (Willis, 1963) do not show, on average, significant differences (Figure 22).

The following empirical equations were obtained:

$$\text{quarry blasts: PGV}(\mu/\text{sec}) = 5.85 \cdot R^{-1.3} \quad (4.1)$$

$$\text{underwater explosions: PGV}(\mu/\text{sec}) = 67.4 \cdot R^{-1.3} \quad (4.2)$$

$$\text{on-surface explosions: PGV}(\mu/\text{sec}) = 4.23 \cdot R^{-1.71} \quad (4.3)$$

On-surface explosions exhibited differences from instantaneous quarry blasts: the on-surface source amplitudes are, on average, lower, and the attenuation is stronger due to higher frequency content (Figure 23).

The equations developed here were used to estimate the expected efficiency of the planned calibration explosions. Equation 2 was developed prior to the calibration experiment in the Dead Sea (see Section 7). Assuming a detection threshold of $0.1 \mu/\text{sec}$ signal amplitude, according to Equation 2, an underwater shot of 5 ton in the Dead Sea is expected to be detected at $R_{\text{max}} > 2000 \text{ km}$. R_{max} is the greatest distance at which the event might be observed on the seismograms. Quarry blasts with a much larger charge weight of 25 ton, placed in several dozens of spaced holes, are expected to be detected up to 500 km. The high efficiency of a Dead Sea underwater explosion was achieved through enhanced coupling, caused by detonation in water.

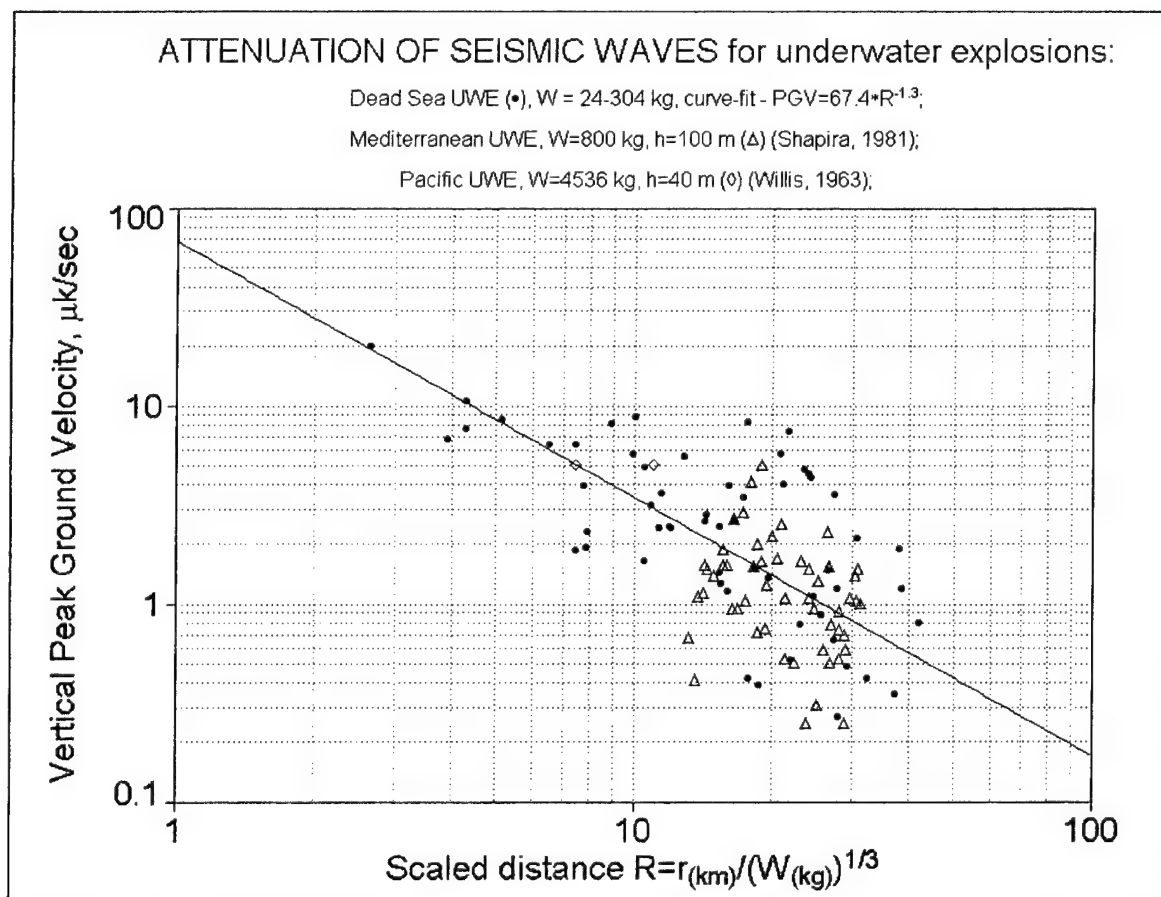


Figure 22. Attenuation of seismic waves for different data sets of underwater explosions.

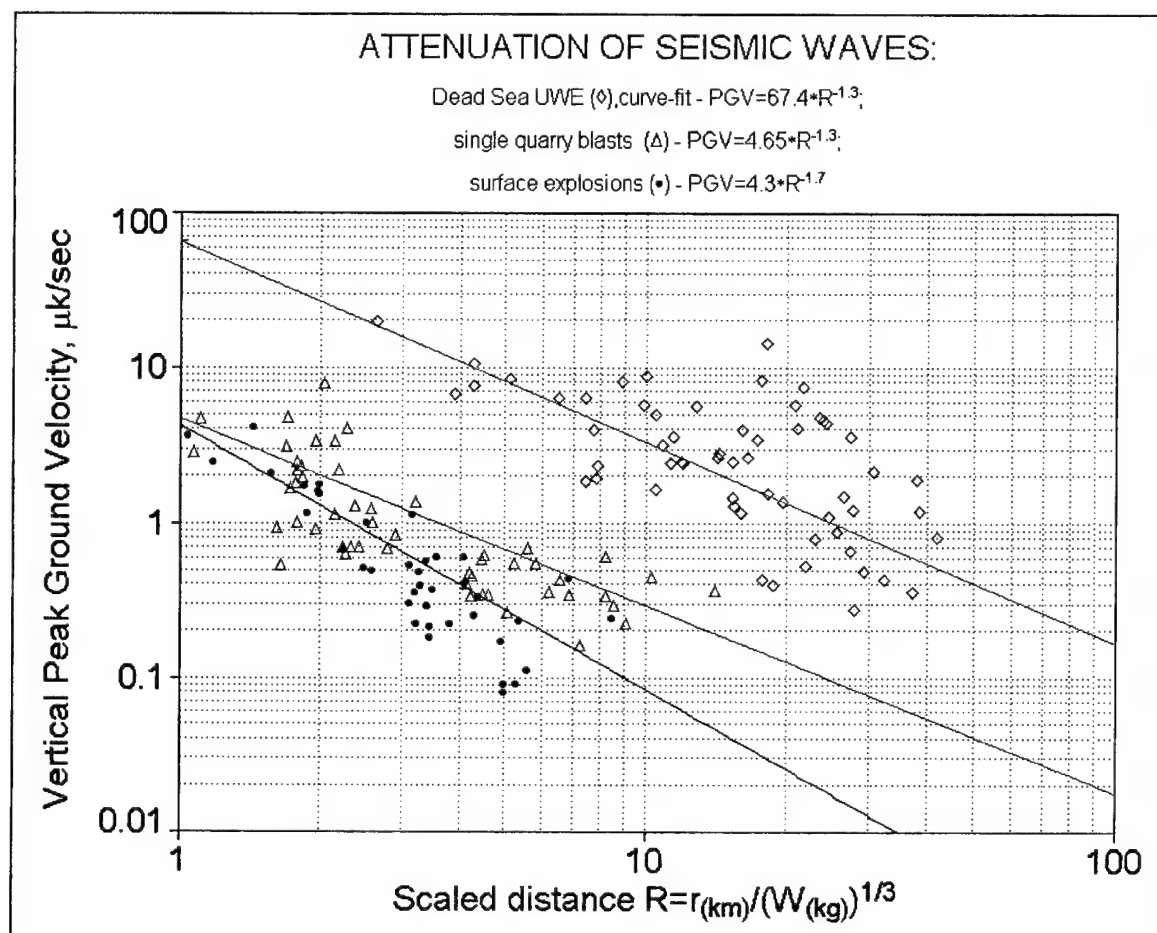


Figure 23. Comparison of attenuation data for different data sets of explosions.

4.3 Threshold Magnitude of Detection by the Israel Seismic Network.

The ISN detects events according to the standard STA/LTA algorithm (Johnson, 1972) ($STA/LTA=1.8$, $STA=1.5$ sec, $LTA=12$ sec), using a simple coincidence criterion requiring that 4 ISN stations trigger within a 12 seconds time interval. The ISN is designed to monitor local seismicity so that all events with $M_L > 2$ within Israel are detectable by the ISN (Shapira, 1992). This detection level is set to avoid recording a multitude of quarry blasts, road excavations and military activities, within the ISN and neighboring countries. For more remote events, detectability of the system degrades gradually. To estimate this detectability we compared lists of events registered by the ISN to those of the National Earthquake Information Center (NEIC) Preliminary Determination of Epicenters (PDE).

We chose a data set of PDE sources within a circular region of $R < 3500$ km centered at the point 32N, 35E (ISN center) and covering a period of 3 years between 1 October 1997 and 31 December 2000. The data set consists of 4100 events. ISN detected 910 of them. Figure 24 shows PDE sources with magnitudes $m_b > 3.4$ (green circles). The ISN detected events are mapped with red stars. Figure 24a depicts 3400 PDE events in the magnitude range $3.4 < m_b < 4.5$ and 590 corresponding ISN detections, Figure 24b depicts 608 PDE and 265 ISN events with $4.5 < m_b < 5.6$, and Figure 24c depicts 37 PDE and 36 ISN events with $5.6 < m_b < 7.8$. From the maps we see that ISN detected all of the events within the 500 km circle, almost all of the events with $m_b > 4.5$ and within the 1000 km circle and all of the strong events with $m_b > 5.6$ (except one remote earthquake in Italy).

From the maps we see that vast areas of the Arabian Peninsula and of the Northeastern Africa are almost aseismic. Most of events come from the Aegean area, however, intensive seismicity is observed in Turkey (to the North) and Iran, Iraq (northeast and east). Many of the events are generated in the Gulf of Aqaba, some in the Red Sea and Indian Ocean (south).

Detectability of the ISN also seems to be azimuth dependant. From the maps we see, for example, that the density of red stars (ISN detections) is higher for events from the East than from the north-north-west. Analysis shows that ISN detects 26% of the PDE detections of events with $3.4 < m_b < 4.5$ for the eastern rectangle shown on the map of Figure 24a and 12% for the symmetric western rectangle.

This can be explained by the considerable difference in geological conditions. Much of the eastern sources are located so that their seismic paths cross in the Mediterranean region. Those to the north and west belong to the Alpine mountain belt. Basalt crust and upper mantle underlying the sea bottom have on average a lower quality factor Q , than granites of the mountain regions, yielding higher attenuation of seismic waves and greater difficulty in detection. This correlates well with the distribution of the P_n upper mantle velocities in the region, presented by the Website atlas.geo.cornell.edu of the Cornell University (Figure 25). Higher P_n velocities correspond to higher Q value. More over, from their tomographic study Hearn and Ni, 1994 claim that the region beneath much of the Turkish-Iranian Plateau corresponds to low velocities (< 7.9 km/s) with exceptionally low P_n (< 7.6 km/s) velocities in the vast area, covering the Turkish-Iranian border. The area coincides with a region of high S_n attenuation (Rodgers et al, 1997, Sandvol et al, 2000) and extensive Neogene volcanism, explained by partial melting.

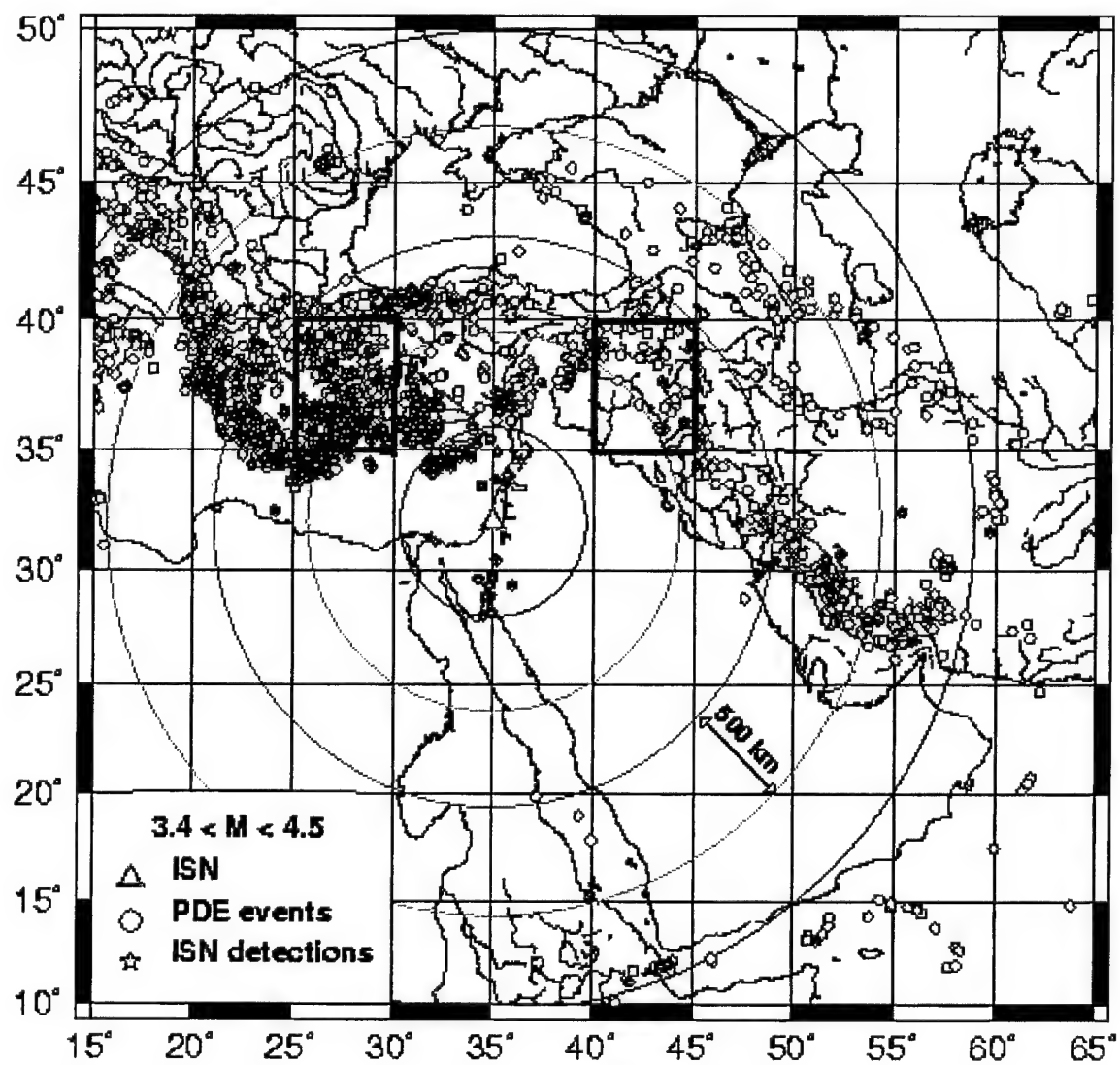


Figure 24. PDE and ISN detections of the ME events in the magnitude ranges: 3.4-4.5, 4.5-5.6 and 5.6-7.8.

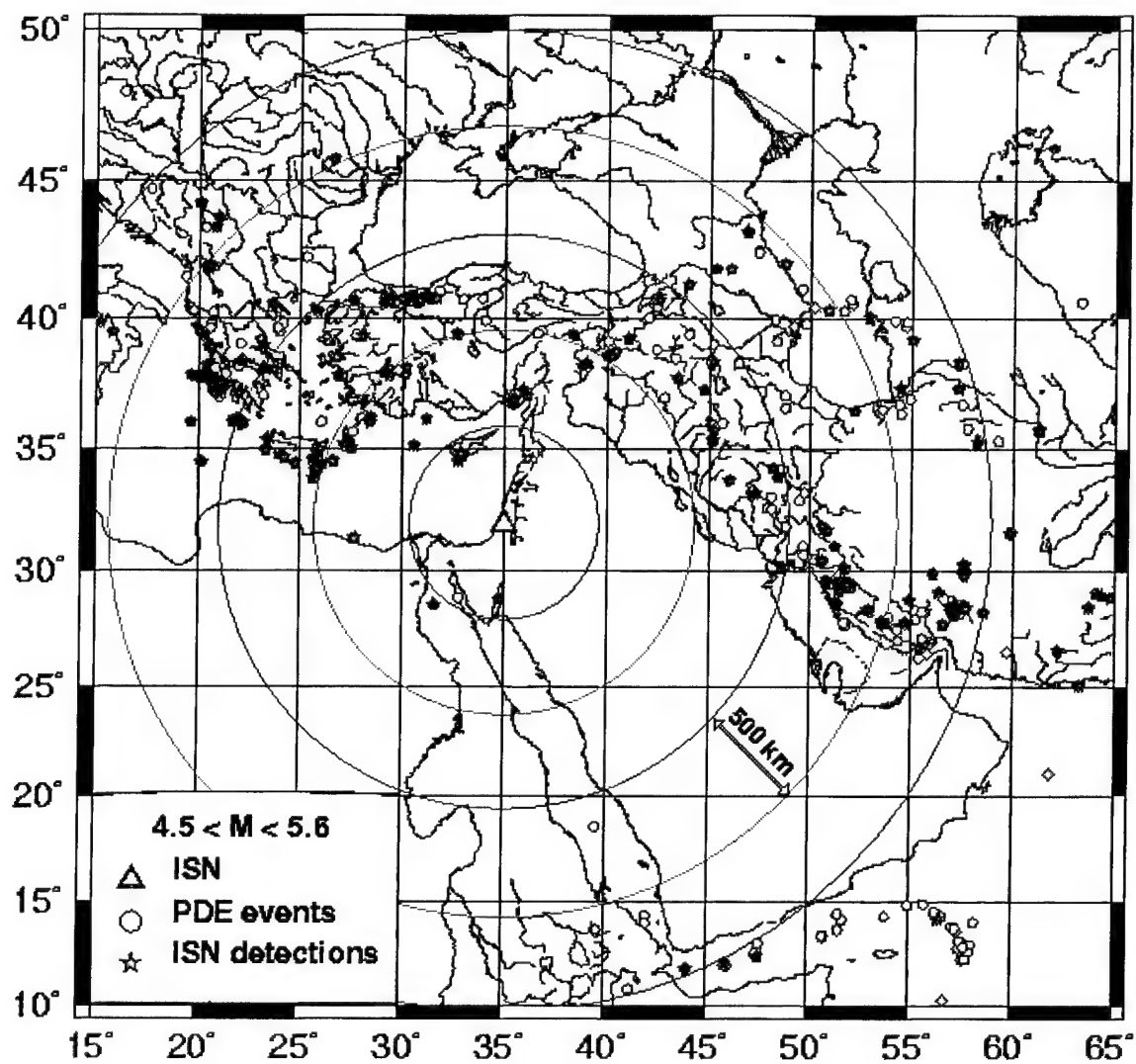


Figure 24. PDE and ISN detections of the ME events in the magnitude ranges: 3.4-4.5, 4.5-5.6 and 5.6-7.8 (continued).

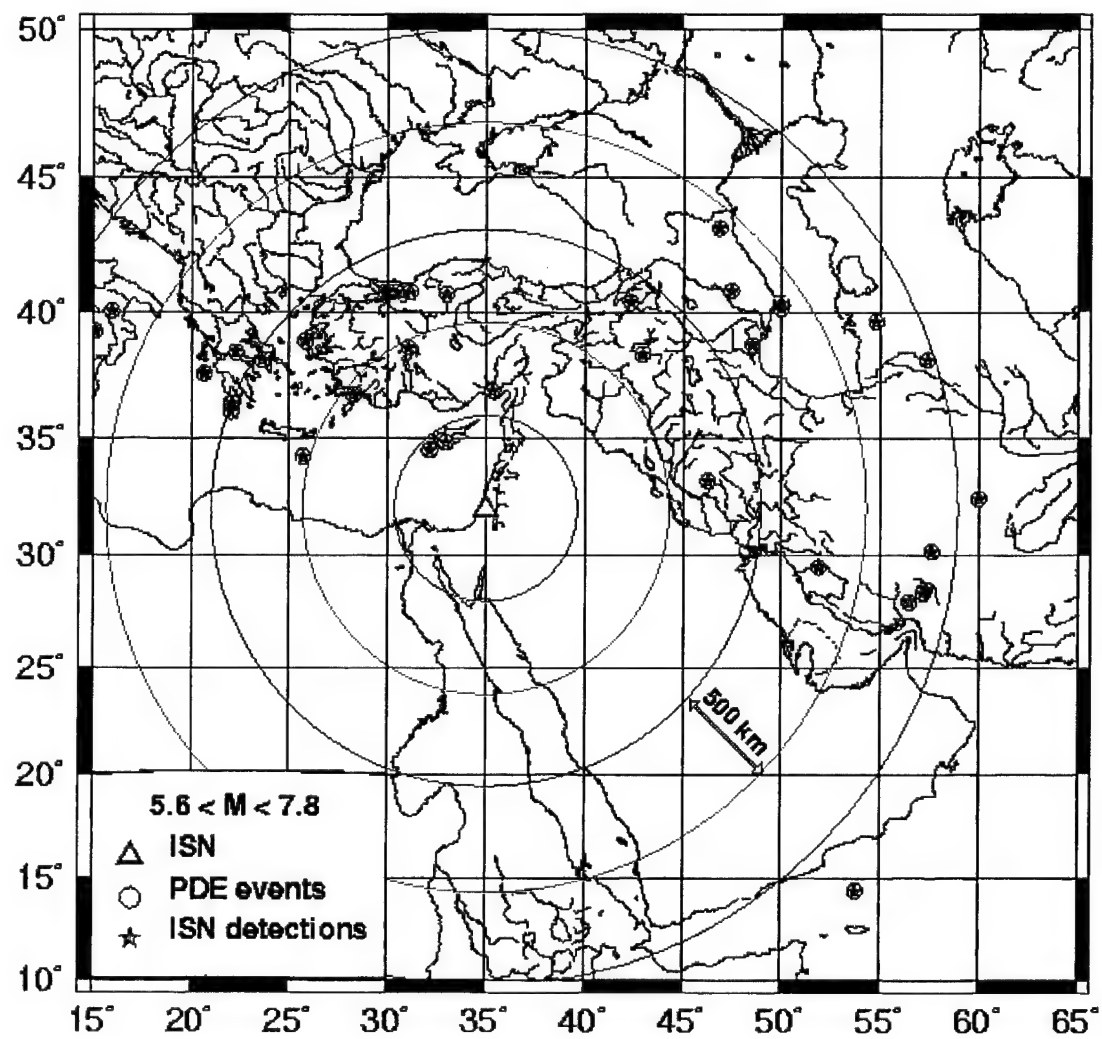


Figure 24. PDE and ISN detections of the ME events in the magnitude ranges: 3.4-4.5, 4.5-5.6 and 5.6-7.8 (continued).



Figure 25. Upper most mantle Pn velocity according Hearn&Ni, 1994

The percentage of the ISN detections versus PDE within a circular area of radius R for different magnitudes is demonstrated in Table 23. The table was used to compute how magnitude threshold depends on distance, as shown on Figure 26. The three curves here are determined for three intervals of the detection rate. For example, the threshold magnitude for a probability of detection of 95-100% are: $m_b = 3.4$ within 500 km, $m_b = 5$ within 1000 km, $m_b = 5.4$ within 1500 km etc. Threshold magnitude of 4.2 associates with detection of 95% of the events within 500 km, 90% within 750 km and 80% within 1000 km, etc.

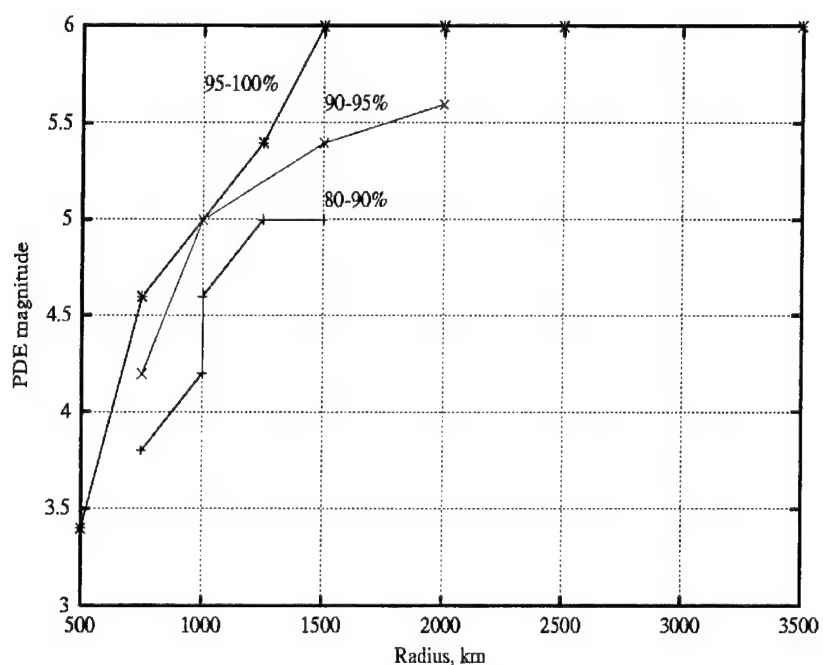


Figure 26. Magnitude threshold versus distance for Israel Seismic Network

Table 23. ISN detectability vs NEIC

M PDE	R km	N PDE	ISN %
3.4	500	20	100
3.8	500	57	100
3.8	750	151	83
4.2	500	31	100
4.2	750	64	93
4.2	1000	191	84
4.4	500	20	100
4.5	500	16	100
4.6	500	8	100
4.6	750	17	100
4.6	1000	54	89
4.6	1250	136	69
5.	1000	18	95
5.	1250	50	82
5.	1500	68	82
5.4	1250	22	100
5.4	1500	28	95
5.4	2000	45	95
5.6	1250	14	95
5.6	1500	18	95
5.6	2000	24	92
6.	1500	10	100
6.	2000	14	100
6.	2500	17	100
6.	3500	28	96

4.4 Conclusions.

1. The three Dead Sea calibration explosions were detonated at almost the same point, thus for all practical purposes the travel time of the P first arrival is the same for all three events and, hence, the error observed is the result of difficulties in accurate arrival time measurements.
The stratified model fitted to the P arrivals of the ISN and CSN stations is the last by 0.7 sec on average relative to the JSN stations. This may indicate that crustal models east and west of the Dead Sea transform are different. These differences should be resolved by 3D modeling.
Comparison of the new and current local model shows that the differences in calculated travel times are small and often insignificant with respect to the observed scatter in the measurements.
Location of the Dead Sea event using the new velocity model is better when only ISN stations are used. When JSN readings are added, the epicenter is shifted to the east. Automatic and manual location yield almost the same results. The new velocity model was used with good results for the location of the four Arad calibration explosions.
2. Three phases, Pn, Sn and Lg, that are key regional phases for a number of different discriminants, were identified on the waveforms of selected earthquakes from the Eastern Mediterranean, recorded by Israel stations, including IMS stations EIL and MRN. Lg-blockage is observed for the Cyprus earthquakes, where the sea-section of propagation paths is significant, whereas Sn phases tend to be strong for the Lg blockage paths, providing very high Sn/Pn ratios.
Peak amplitude attenuation laws were developed for different types of explosions, providing a basis for design of Ground Truth explosions for calibration of remote IMS stations.
3. The threshold magnitude of detection by the Israel Seismic Network was calculated based on comparison of PDE and ISN bulletins.
Detectability of the ISN is azimuth dependant being about twice as high for events from the east than from the north-north-west.
The threshold magnitude for a probability of detection of 95-100% are: $m_b = 3.4$ within 500 km, $m_b = 5$ within 1000 km, $m_b = 5.4$ within 1500 km.

Section 5

Task 3 Direct Improvements in Monitoring the CTBT

5.1 Improvements in Location - Case Study: ISN Detection of the India and Pakistan Nuclear Tests and Chemical Calibration Explosion in Kazakhstan.

5.1.1 Summary.

The study is based on the three most recent (1998) underground nuclear explosions, one in India and two in Pakistan, which provided a Ground Truth test of the existing IMS. These events, having magnitudes of 5.2, 4.8 and 4.6, respectively, were registered by many IMS and other seismic stations. The recently deployed broad band (BB) stations MRNI and EIL are within 3600, 2800 and 2700 km, respectively, of the sources. The Indian and the second Pakistan nuclear test (NT) were not detected by the short period Israel Seismic Network (ISN). As part of this study we examined three detection algorithms and applied them to the BB data of EIL and MRNI. We used the standard STA/LTA detector, the Murdock-Hutt (MH) algorithm and the Statistically Optimal Detector (SOD). The MH and SOD triggered on all three nuclear tests. The signals of the second Pakistan NT arrived at the ISN and its IMS stations in the coda of a strong Afghanistan earthquake and were further disturbed by preceding signals from a local earthquake. Nevertheless, the NT signal was successfully detected at EIL and MRNI using the MH and SOD procedures. We provide comparative analysis of the BB station JER, which has high noise conditions as compared to EIL and MRNI. We demonstrate that SOD can detect events when other algorithms fail. Using the quietest EIL station, the most sensitive SOD and different band-pass filters we also tried to detect the small Kazakh 100-ton chemical calibration explosion of 1998, with magnitude 3.7. This event occurred at a distance of 4000 km from the IMS stations located in Israel. The detector response curve showed some rise in the expected signal time interval, but too low for a reliable detection.

5.1.2 Data.

The recent nuclear test activity in southern Asia (see Figure 27), comprising the announced tests in India (May 11, 1998) and Pakistan (May 28 and 30, 1998), provided new recordings for verification of teleseismic discriminants and for testing new detection and location procedures. It also provided an opportunity to estimate travel time corrections for new stations of the International Monitoring System (IMS). These discriminants and location procedures can serve as a tool for improving the monitoring executed by the Comprehensive Test Ban Treaty. The explosion recordings were analyzed mainly based on the closest station, Nilore (NIL), at near-regional distance range of about 7°-9° (e.g. Walter et al., 1998). In August 1998, a 100 ton chemical explosion was conducted at the former Semipalatinsk Nuclear Test Site (STS), Kazakhstan (Figure 27), as a calibration experiment for the CTBT verification, and was recorded by many stations worldwide (CTBTO, 1998b).

The number of active IMS stations in the Middle East is rather limited, and thus we stress the need to assess, as precisely as possible, the monitoring capabilities of each station. The IMS stations EIL and MRNI were installed in Israel in 1996 and 1998 respectively, when nuclear testing was nearing its end, therefore every chance to analyze Ground Truth explosion data at these stations should be used. Here we analyze and interpret the recordings of the two IMS stations, the cooperating BB station JER and the short period stations of the Israel Seismic Network (ISN; Figure 28). The nuclear and chemical explosions are located at a distance range of 25°-38°. The case of the second Pakistan test is of special interest, because it simulates, to a degree, the scenario of a clandestine test masked by other two events: a strong earthquake in Afghanistan (06:22, $M_S=6.9$), and a local earthquake (06:57, $M_L=2.5$) 20 km south of EIL station.

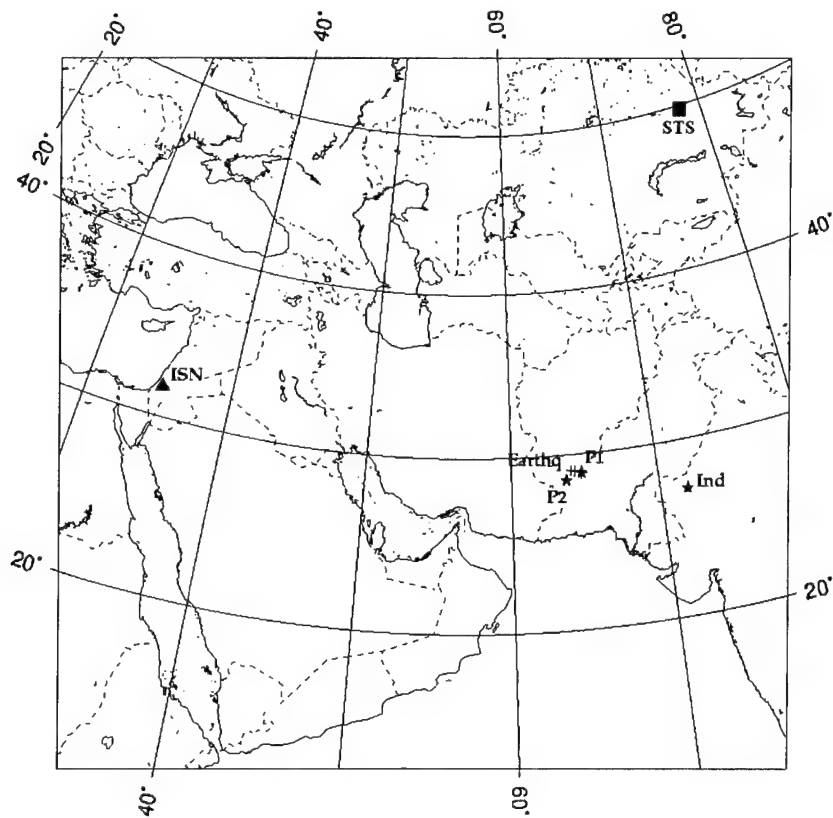


Figure 27. Relative location of short period and broad band stations of the ISN used in the analysis.

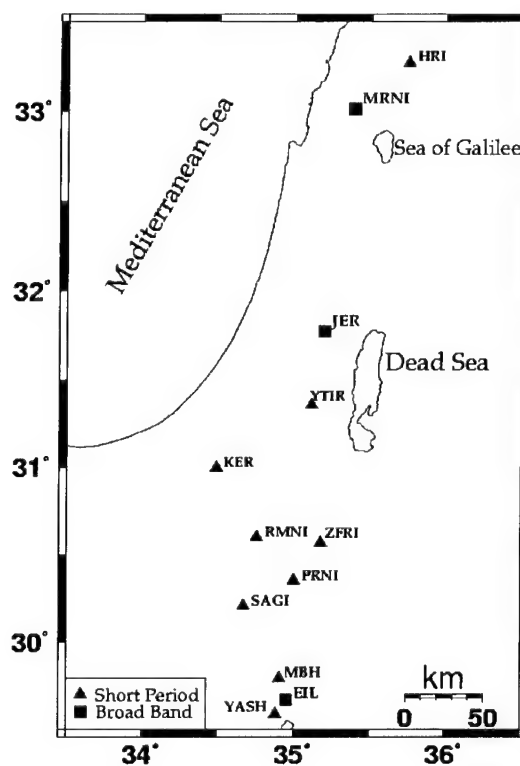


Figure 28. Location of short period and broad band stations of the ISN used in the analysis.

Table 24. Source parameters of nuclear tests and earthquakes used in the study (location, origin time and magnitude are taken from PDE).

#	Date	Origin Time	Lat. N	Lon. E	Depth km	Mag.m b	Dist. to EIL, deg.	Event, Region
New events								
1	1997/12/04	10:17:01.33	29.09	64.11	33	5.0	25.4	Earthquake . Pakistan
2	1998/01/05	16:58:35.29	29.01	64.35	18	4.9	25.6	Earthquake . Pakistan
3	1998/05/11	10:13:41.78	27.10	71.80	0	5.2	32.4	Nucl. expl., India
4	1998/05/28	10:16:15.23	28.90	64.79	0	4.8	26.0	Nucl. expl.,
5	1998/05/28	20:32:46.51	26.58	62.23	47	4.7	24.2	Earthquake . Pakistan
6	1998/05/30	06:54:57.1*	28.50	63.74	0	4.6	25.2	Nucl. expl.,
7	1998/08/22	05:00:18.90	49.77	77.99	0	3.8	38.06	Chem. expl. 100
Old STS nuclear tests								
1	1987/03/12	01:57:17.3	49.93	78.79	0	5.4	38.5	Kazakh- stan
2	1987/04/17	01:03:04.8	49.89	78.69	0	6.0	38.5	
3	1987/05/06	04:02:05.5	49.78	78.09	0	5.5	38.1	
4	1988/04/03	01:33:05.8	49.92	78.95	0	6.1	38.6	
5	1988/11/12	03:30:03.7	50.08	78.99	0	5.3	38.7	
6	1988/12/17	04:18:06.9	49.89	78.93	0	5.9	38.6	
7	1989/01/22	03:57:06.5	49.92	78.86	0	6.0	38.6	
8	1989/02/12	04:15:06.7	49.90	78.76	0	5.9	38.5	

• - JHD solution by Wallace (1998)

There is no ground truth information GT0 for the recent India and Pakistan nuclear tests. Barker et al. (1998) presented location and origin time for these tests, based on the prototype International Data Center (pIDC) Reviewed Event Bulletin (REB), Joint Epicenter Determination and Satellite Imagery. Owing to the use of several nearby Pakistan earthquakes and old Semipalatinsk nuclear tests in our study, we use source parameters taken from the PDE (NEIC) bulletin (see Table 24), in order to retain homogeneity of the data.

The seismograms analyzed comprise observations of the short period stations (1 Hz seismometer, S-13, Geotech) with a sampling rate 50 Hz and broad band stations (STS-2 seismometer and Quanterra data logger) with sampling rates of 0.1, 1, 20, 40 and 80 Hz. The 80 Hz sampling is used in ISN triggering mode. The Pakistan test on May 28, 1998 was the only one to trigger the short-period stations. The explosions on May 11 and 28, 1998 triggered the 80 Hz channel of the broad band station EIL. The second Pakistan nuclear test on May 30, 1998, occurred about 38 minutes after a major $M_s=6.9$ earthquake, and was found on the continuous 20 Hz channel of EIL using a high frequency band filter. In order to conduct discrimination analysis (see Section 5.4.3) we added several recordings of earthquakes occurring near the explosion sites in Pakistan (Figure 27). We also analyzed the EIL recordings of the chemical calibration explosion of 100 ton at the STS, on August 22, 1998 (shown below on Figure 35).

5.1.3 Travel Times and Peak Amplitudes.

The same set of teleseismic events from southern Asia was used to estimate station corrections based on P travel times and NEIC source data. The P-arrivals to the IMS station EIL showed consistent delays with an average of about 4 seconds relative to the IASPEI91 model (see Table 25, Figure 29). Analogous delays of about 3.7 seconds on average were found in the analysis of former nuclear explosions at the Semipalatinsk Test Site (Table 25). The explosions were recorded at the short-period station MBH (EIL was not available at that time) situated 14 km to the north of EIL (Figure 28). Figure 29 also shows similar lags of 3.5-4 sec for the IMS station MRNI and the BB station JER. The similar delays at different stations indicate a path- rather than site-effect.

Based on the corrected arrival time we tried to identify the P-arrival of the recent STS 100-ton chemical explosion using band-pass filtered seismograms at EIL. We tried to estimate P-amplitude for this explosion by extrapolating the dependency between measured P-wave peak amplitudes and magnitude for a series of old STS nuclear explosions (see Table 25), in the m_b range 5.3-6.1. The upper limit of the magnitude-yield relationship for explosions in hard rock (Khalturin et al., 1998) yields for the 100-ton explosion $m_b=3.9$, NEIC reports $m_b=3.8$, and pIDC REB presents $m_b=3.7$. Extrapolation to lower magnitudes of the magnitude-amplitude dependency observed at the MBH station shows that for $m_b=3.7-3.9$ one should expect P-amplitudes much lower than 0.01 micron/sec at EIL station, whereas pre-signal noise level is about 0.01-0.02 micron/sec (in the band 1-3 Hz). A weak phase can be observed on the filtered (2.5-3.5 Hz) vertical component seismogram about 2 seconds after the calculated P-arrival time, corrected for the 3.7 sec average delay (an arrow on Figure 35).

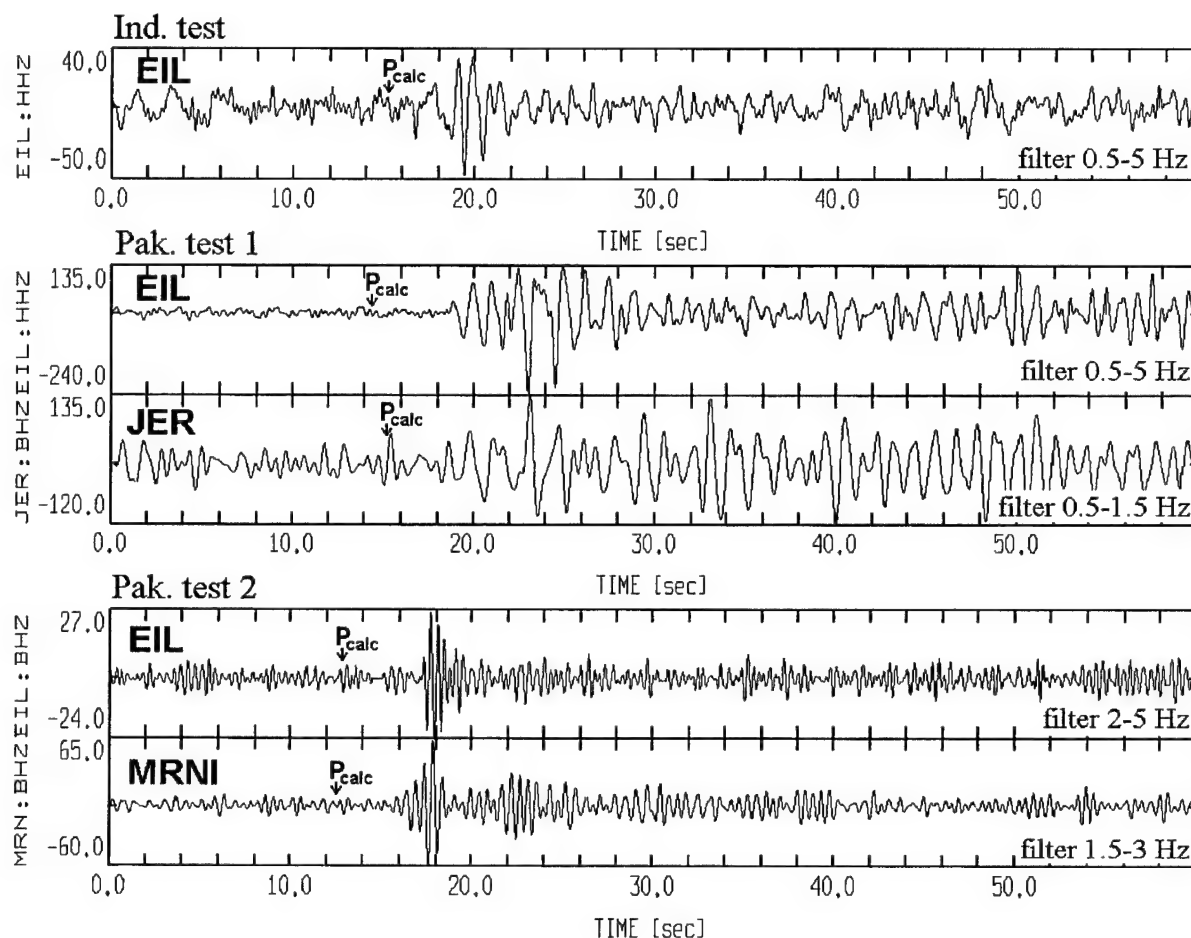


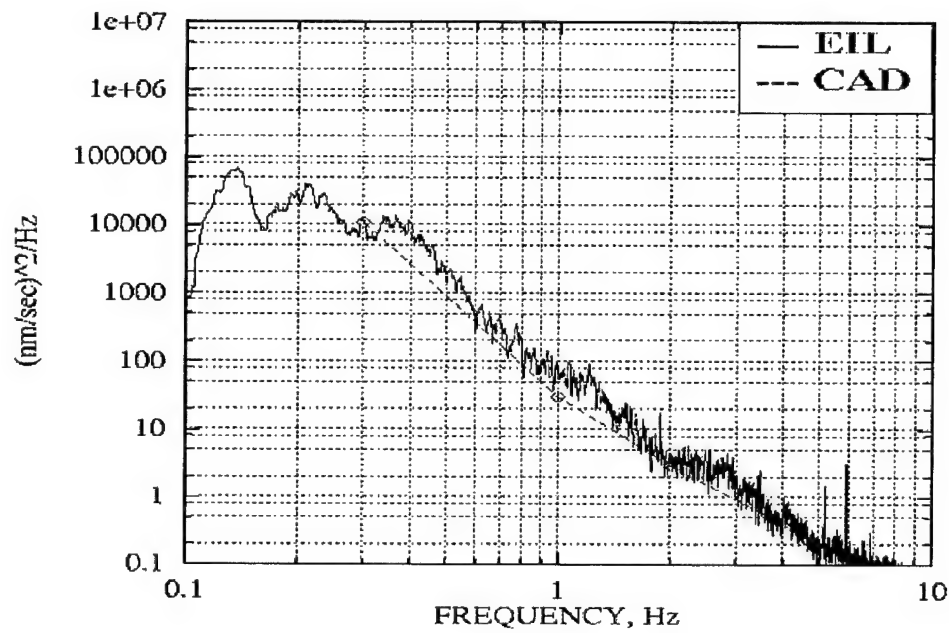
Figure 29. Filtered broad band vertical records of the three nuclear tests. Vertical axis units here are counts (1 count= 1.67×10^{-9} m/s).

5.1.4 Characterization of Noise and Signals at Stations EIL, MRNI and JER.

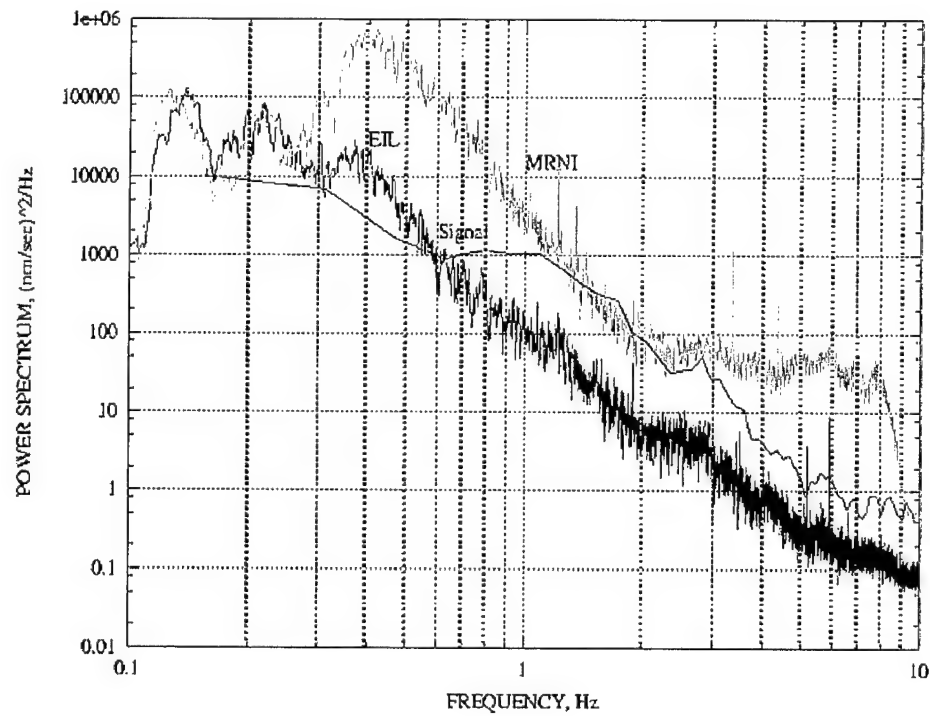
Station EIL, located inside a 200-m long tunnel, carved in granite, is a quiet station. The broad band and short period noise velocity spectral density are presented in Figure 30(a), along with selected noise velocity values of the quiet station CAD in the Pyrenees (Vila, 1998), located in a hard rock tunnel (length of 490 m long, depth of 80 m). In the same frequency range the noise level at MRNI and JER is about 10 and 20 times greater, respectively (see filtered seismograms in Figures 33 and 34). Figure 30 depicts comparison between spectral densities of the EIL and MRNI stations and the spectral density of the EIL record of the Indian nuclear test. From the figure it is clear why the signal is detected by EIL and not detected at MRNI. However, for the EIL station the signals of the explosions under consideration appear much more attenuated than for the remoter GRF, NORES and ARCES stations (CTBTO, 1998a).

Table 25. Travel times (IASPEI91) and P-wave peak amplitudes for the selected events.

#	Date	P-wave arrival time, sec		t_m-t_c , sec	Peak P-ampl. mic/sec	m_b	Filter band, Hz
		calculated t_c	measured t_m				
New events, BB station EIL, vertical component							
1	1997/12/04	10:22:25.6	10:22:30.1	4.5	0.45	5.0	0.5-20
2	1998/01/05	17:04:03.5	17:04:07.5	4.0	0.48	4.9	0.5-20
3	1998/05/11	10:20:13.5	10:20:17.1	3.6	0.08	5.2	0.5-10
4	1998/05/28	10:21:49.8	10:21:54.3	4.6	0.39	4.8	0.5-20
5	1998/05/28	20:37:58.9	20:38:01.6	2.7	0.23	4.7	0.5-20
6	1998/05/30	07:00:24.0	07:00:28.5	4.5	0.043	4.6	2-10
7	1998/08/22	05:07:38.9	?	?	< 0.01	3.8	1-3
Old STS nuclear tests, short period station MBH, vertical component							
1	1987/03/12	02:04:41.4	02:04:44.8	3.4	0.30	5.4	0.5-12
2	1987/04/17	01:10:28.3	01:10:31.3	3.0	1.20	6.0	
3	1987/05/06	04:09:25.6	04:09:28.9	3.3	0.44	5.5	
4	1988/04/03	01:40:30.7	01:40:33.7	3.0	3.60	6.1	
5	1988/11/12	03:37:29.2	03:37:33.9	4.7	0.23	5.3	
6	1988/12/17	04:25:31.6	04:25:35.5	3.9	0.21	5.9	
7	1989/01/22	04:04:30.9	04:04:34.8	3.9	0.77	6.0	
8	1989/02/12	04:22:30.6	04:22:35.0	4.4	0.37	5.9	



a. Noise at CAD BB



b. Noise at MRNI and signal at EIL

Figure 30. Velocity spectral density of noise at the EIL station. The noise power spectra correspond to simultaneous 30 min recordings at EIL and MRNI at night (October 9, 1998). The signal is the 2 second record of the Indian nuclear test.

5.1.5 Comparison of Different Detectors: Murdock-Hutt, Johnson (STA/LTA) and SOD.

We checked the detectability of the EIL BB station using recordings of the India and Pakistan nuclear tests. The 80 Hz channel of the station was used in the Murdock and Hutt (1983) procedure for automatic detection (MH), including the following main stages:

1. The input time series is filtered. For simulation of the detector performance we used a specific ARMA (Auto-Regressive-Moving Average) filter, applied to the 20 Hz channel of the BB station, instead of the built-in WWSSN-SP standard Short Period filter.
2. Relative maxima and minima (peaks and troughs) of the filtered series are found, and successive peaks and troughs are differenced. These differenced values, together with their associated times, are named "P-T" time series.
3. Three thresholds (Th1, Th2 and Th3) are calculated. Detection is declared if P-T amplitude exceeds Th1 and two other P-T values exceed Th2 in a fixed time interval of usually 4 seconds. Th3 is used to search for onsets of detected events. The recommended values of the thresholds are: $Th1=4*s$, and $Th2=3*s$ and $Th3=2*s$. These threshold levels provide high rate of true detections and low rate of false alarms. The parameter s is one standard deviation of the P-T series of noise.

Figure 33 illustrates the P-T curves extracted from the EIL observed seismograms of the three nuclear explosions. The first two nuclear tests pass the stated detection criterion, but the second Pakistan nuclear test (Figure 33c) does not. It would trigger with lower Th1 and Th2, but at the expense of enhanced risk of false alarms. Therefore, two additional different detectors were tested: the first is the STA/LTA detector (based on Johnson, 1979); and the other is the adaptive Statistically Optimal Detector (SOD) by Kushnir et al. (1990).

To extract waveforms from background noise, we manually band-pass filtered all the seismograms of the broad band stations. Spectral analysis of the vertical channel of EIL (Figure 32) shows that the signal of the Indian nuclear test dominates over noise in the frequency band 0.5-2 Hz. To provide less distortion of the signal we used a 0.5-5 Hz filter, yielding peak amplitudes $A_m \sim 0.08$ micron/sec (see Figure 34). We did not extract the signal for MRNI and JER successfully for this explosion.

Though of smaller magnitude (but somewhat closer), the Pakistan nuclear test on May 28, 1998 was well observed by the short period ISN stations (see Figure 30), and the broad band station EIL (Figures 31 and 34), with peak amplitude $A_m \sim 0.4$ micron/sec. A weak signal at JER was observed after a narrow band-pass filtering 0.5-1.5 Hz (Figure 31). We could not detect the signal at MRNI due to a burst of local noise.

The case of the second Pakistan nuclear test on May 30, 1998 is particularly complicated owing to preceding arrivals from the two other events mentioned above: the strong earthquake in Afghanistan, and the local earthquake. Thus the body waves of the explosion are partially masked by the coda waves of these two events (see Figure 35). However, the P-waves of the nuclear test can be identified on the EIL seismogram in the 2-5 Hz frequency range with amplitude $A_m \sim 0.04$ micron/sec. A signal with $A_m \sim 0.1$ micron/sec was obtained at MRNI in the narrow frequency range 1.5-3 Hz (Figure 31), while at JER the signal was masked by noise.

We applied the STA/LTA detector to the seismograms after they had been band-pass filtered in the chosen frequency ranges. The STA/LTA detector depends heavily on the frequency band selected and the background noise.

The performance of the SOD and the STA/LTA, applied to the filtered (0.5-5 Hz) BB records (20 Hz) of the explosions, is presented in Figures 34-36. Both detectors were successful at EIL records of the Indian and the first Pakistan tests (Figures 34 and 35). Detection of the second Pakistan NT at EIL was complicated by the close local earthquake, which blurs NT triggering. Here, the SOD demonstrates better performance. Records of the Pakistan explosions at JER (Figure 35) and MRNI (Figure 35b) show a poor SNR, resulting in a failure of the STA/LTA, whereas the SOD provides reliable detections.

Using the records of the quietest station EIL, the sensitive SOD algorithm and different band-pass filters we also tried to detect the Kazakh chemical explosion. The detector output showed some rise at the expected arrival time of the signal, but too low for reliable detection (Figure 37).

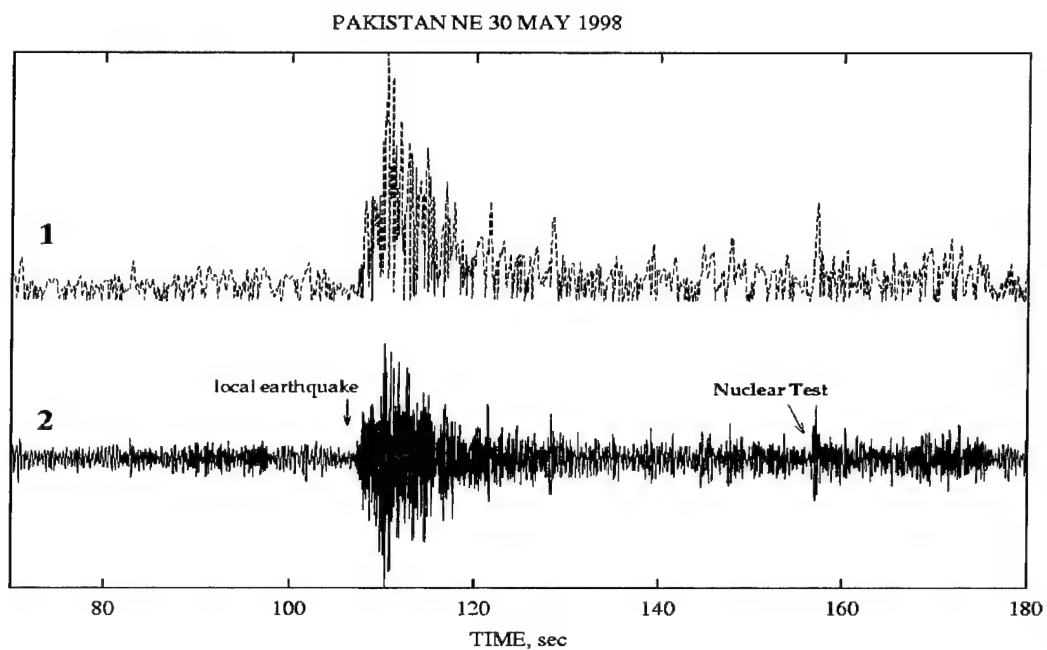
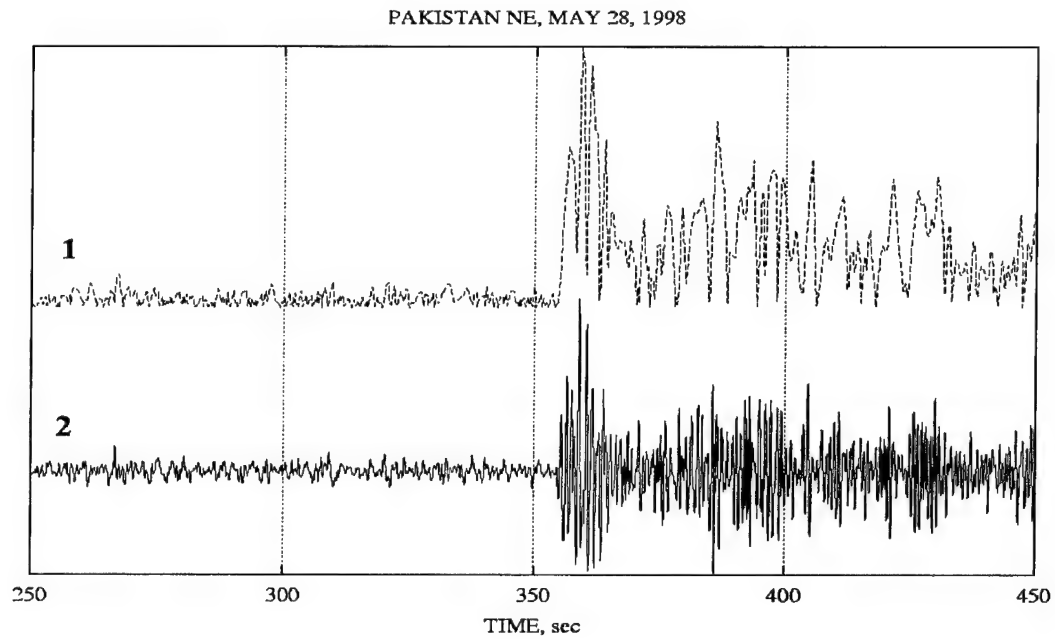


Figure 31. Application of the Murdock-Hutt detector algorithm to the BB EIL seismograms for the three nuclear explosions. P-T curves (1) are obtained using output (2) of the WWSSN_SP filter.

INDIAN NE 11 MAY 1998

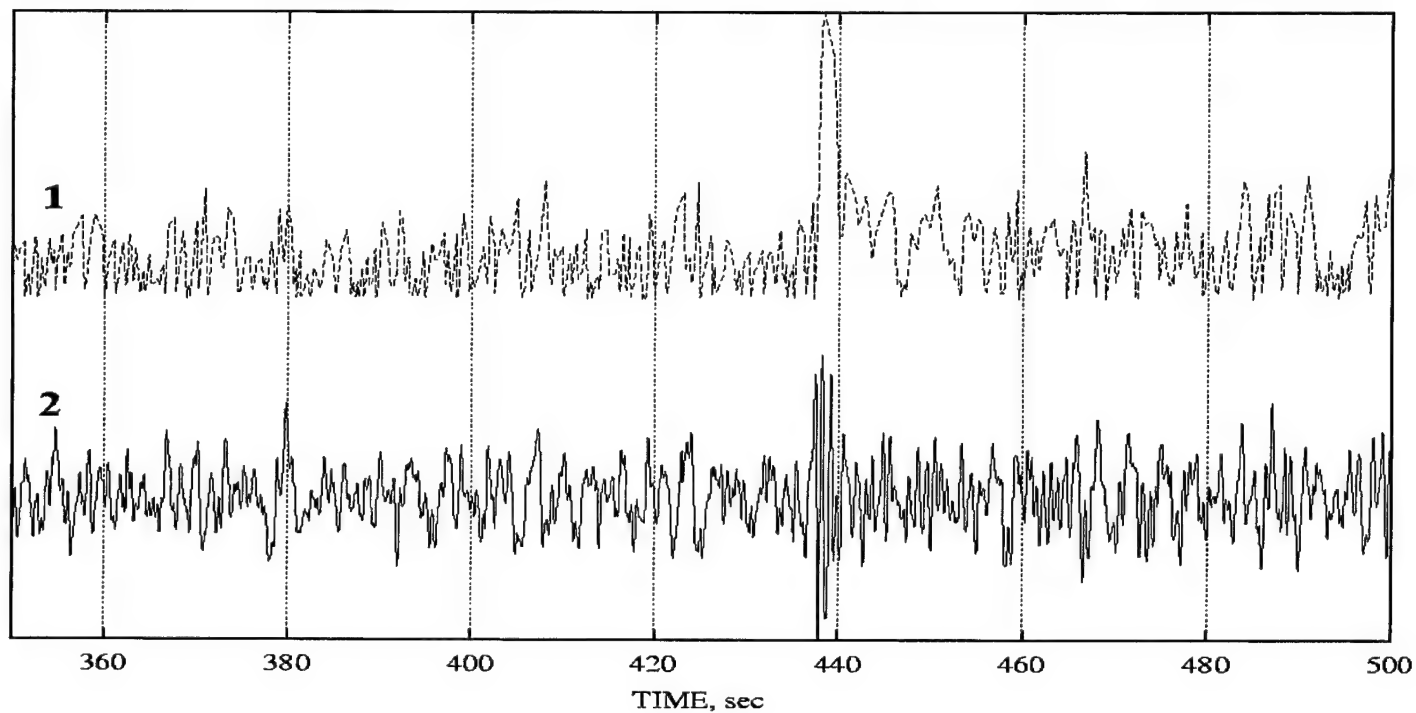


Figure 31. Application of the Mudrock-Hutt detector algorithm to the BB EIL seismograms for the three nuclear explosions. P-T curves (1) are obtained using output (2) of the WWSSN_SP filter (continued).

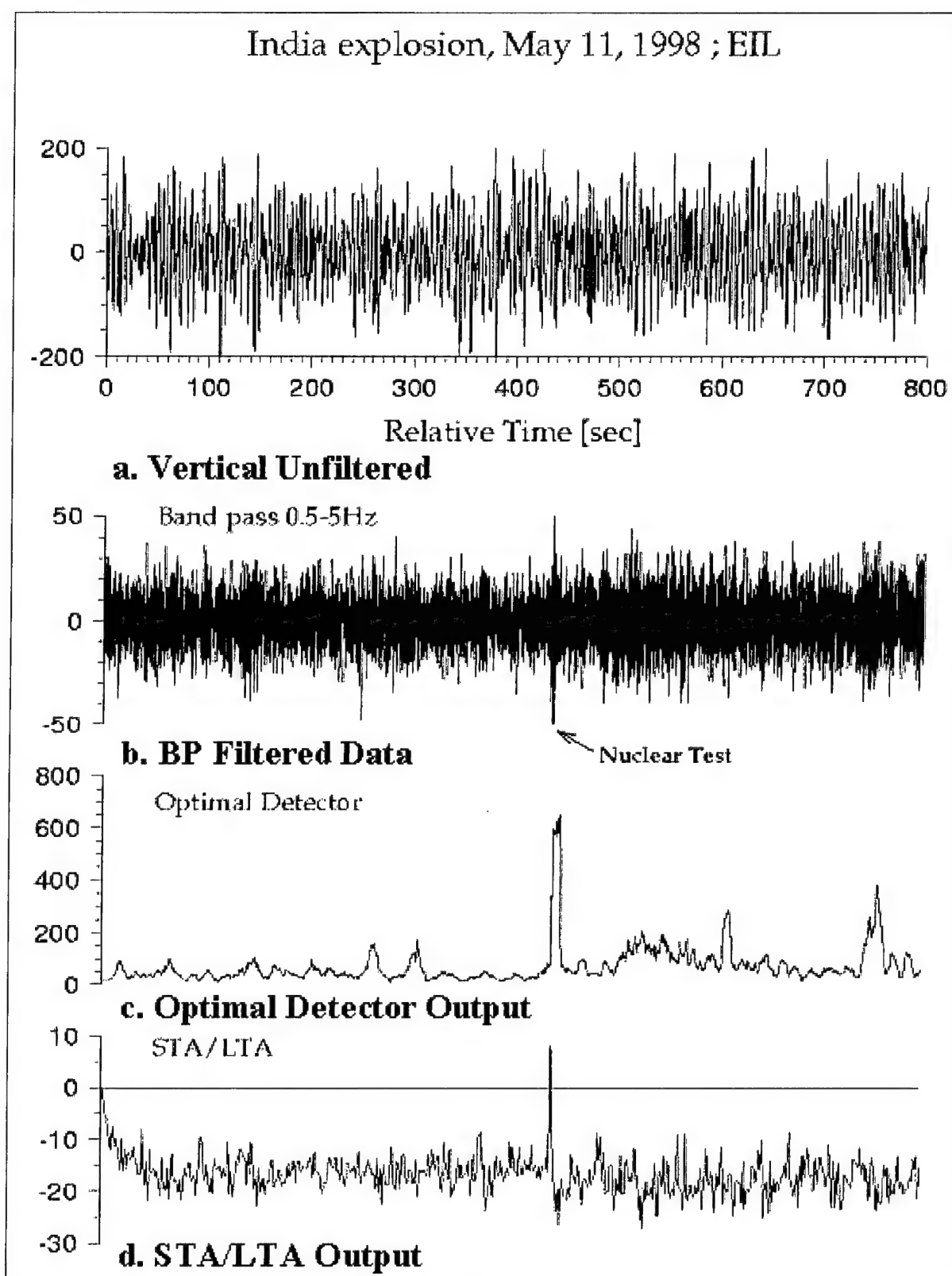
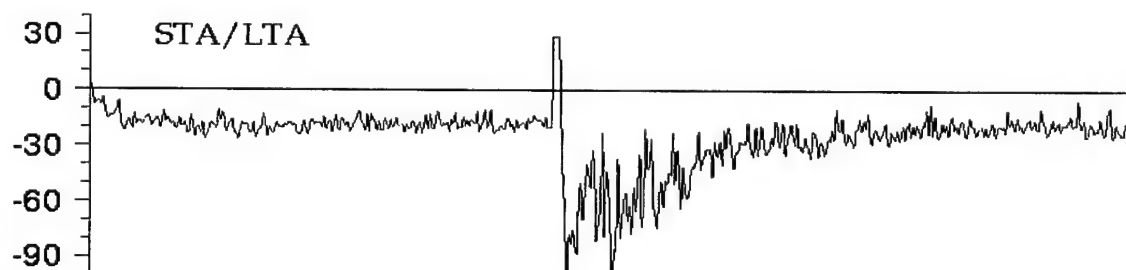
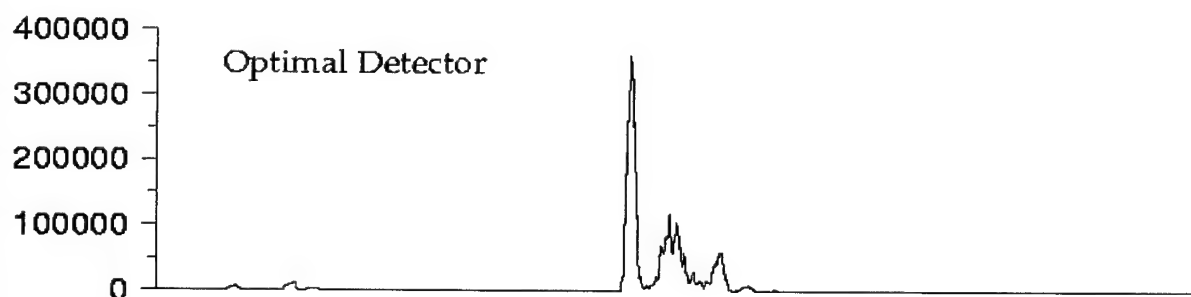
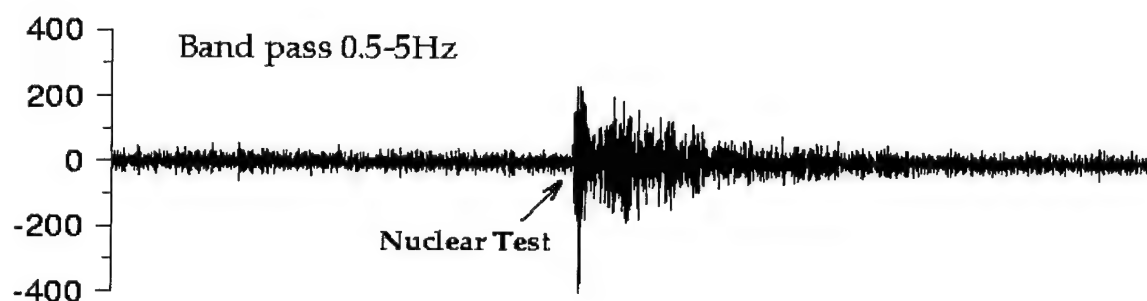
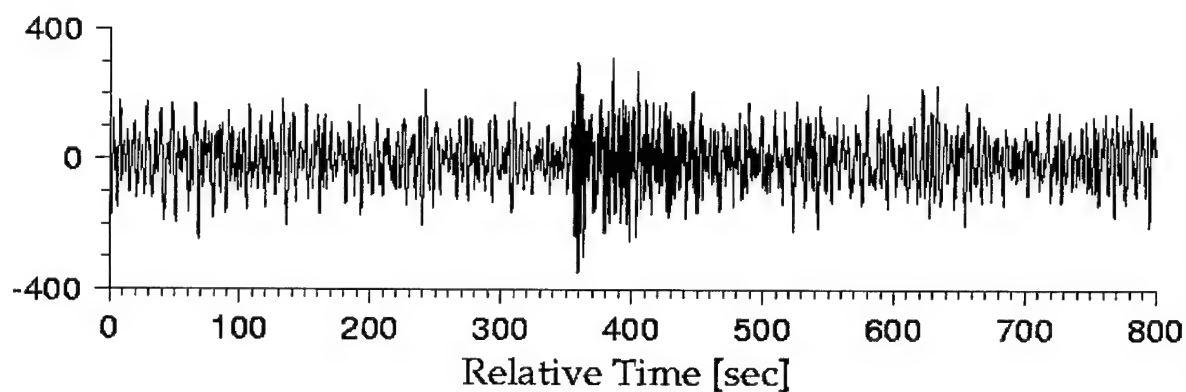


Figure 32. Detection of the Indian test at EIL station.

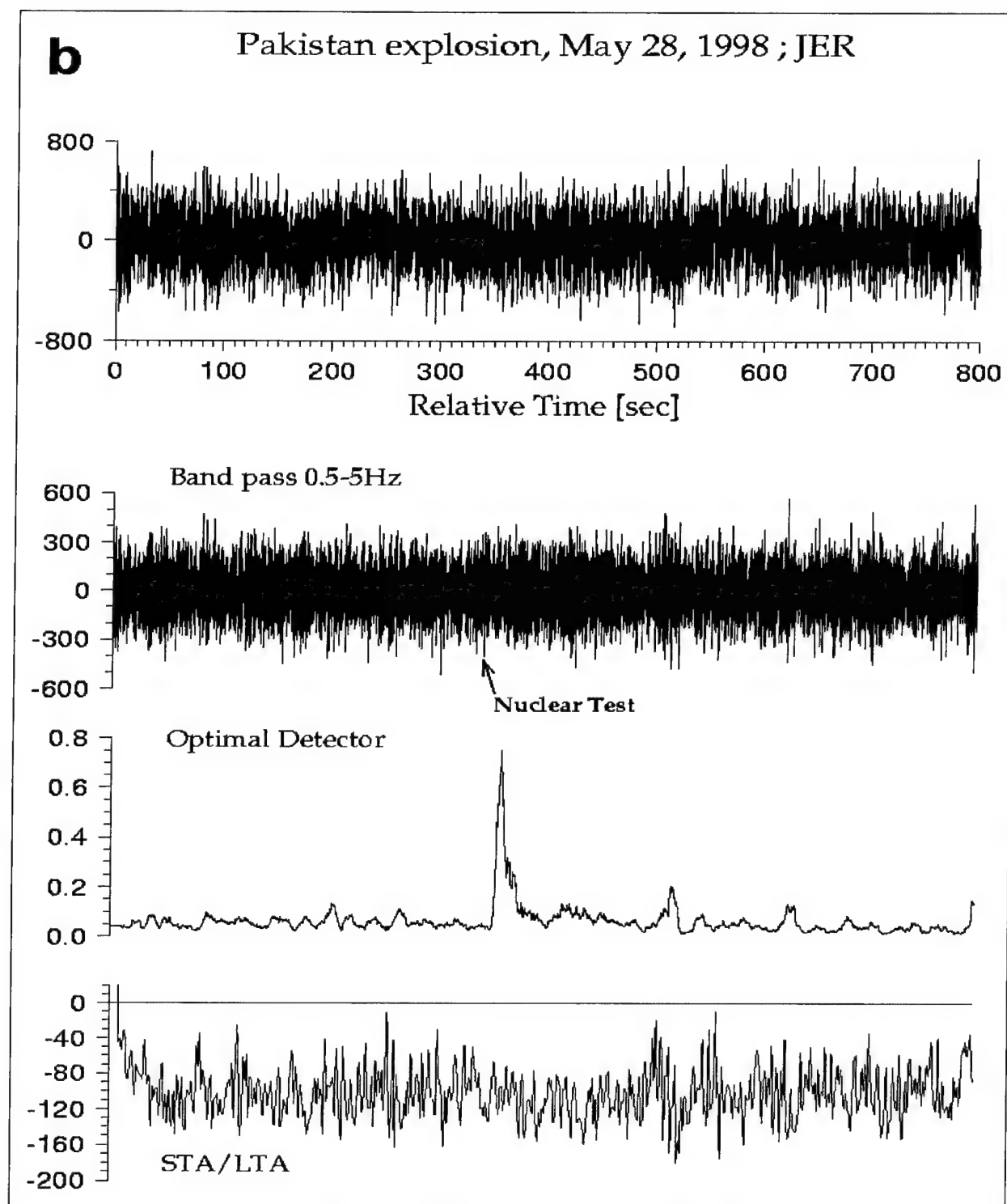
a

Pakistan explosion, May 28, 1998 ; EIL



a. EIL BB Station

Figure 33. Detection of the first Pakistan test on May 28, 1998.

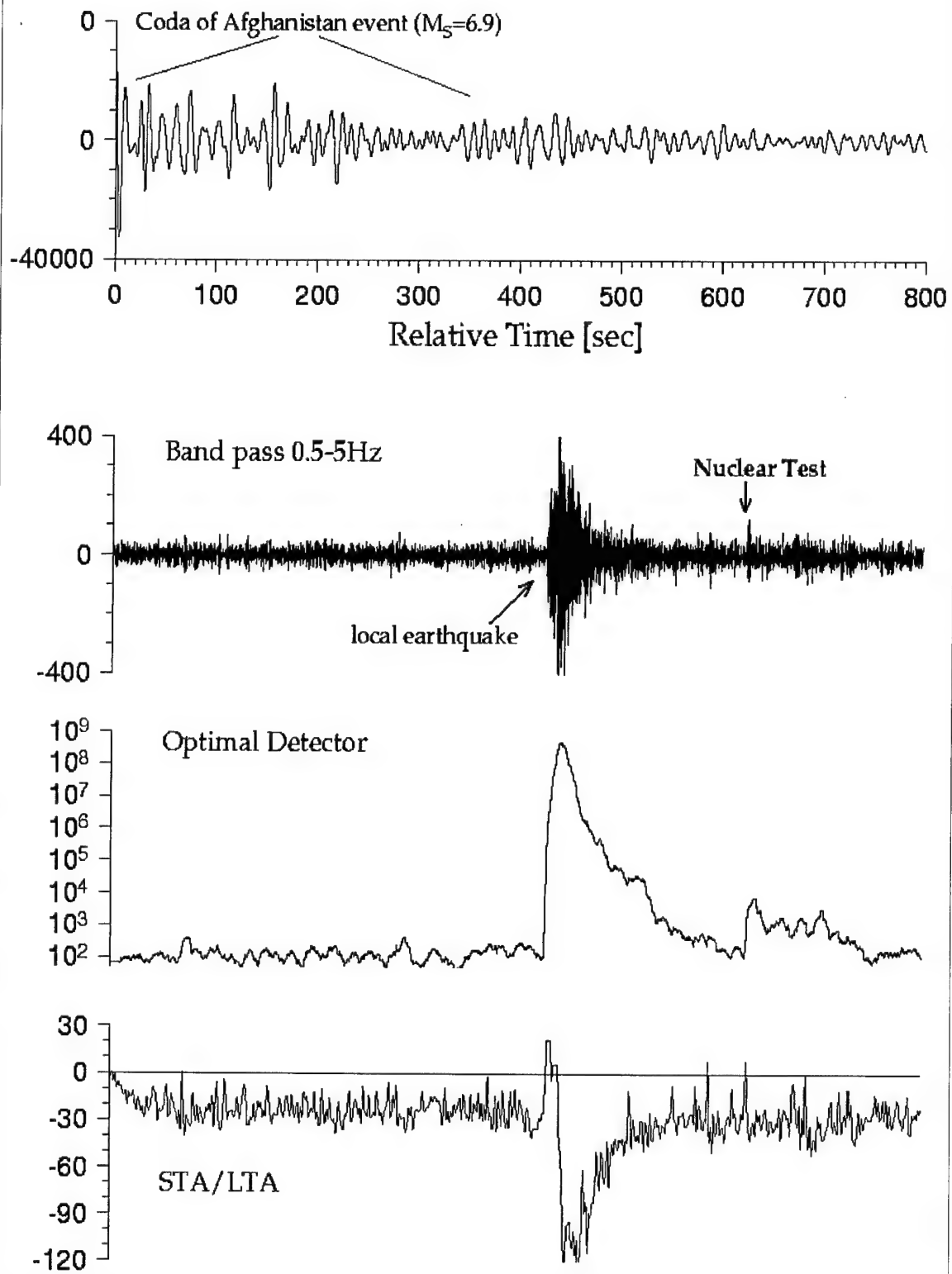


b. JER BB Station

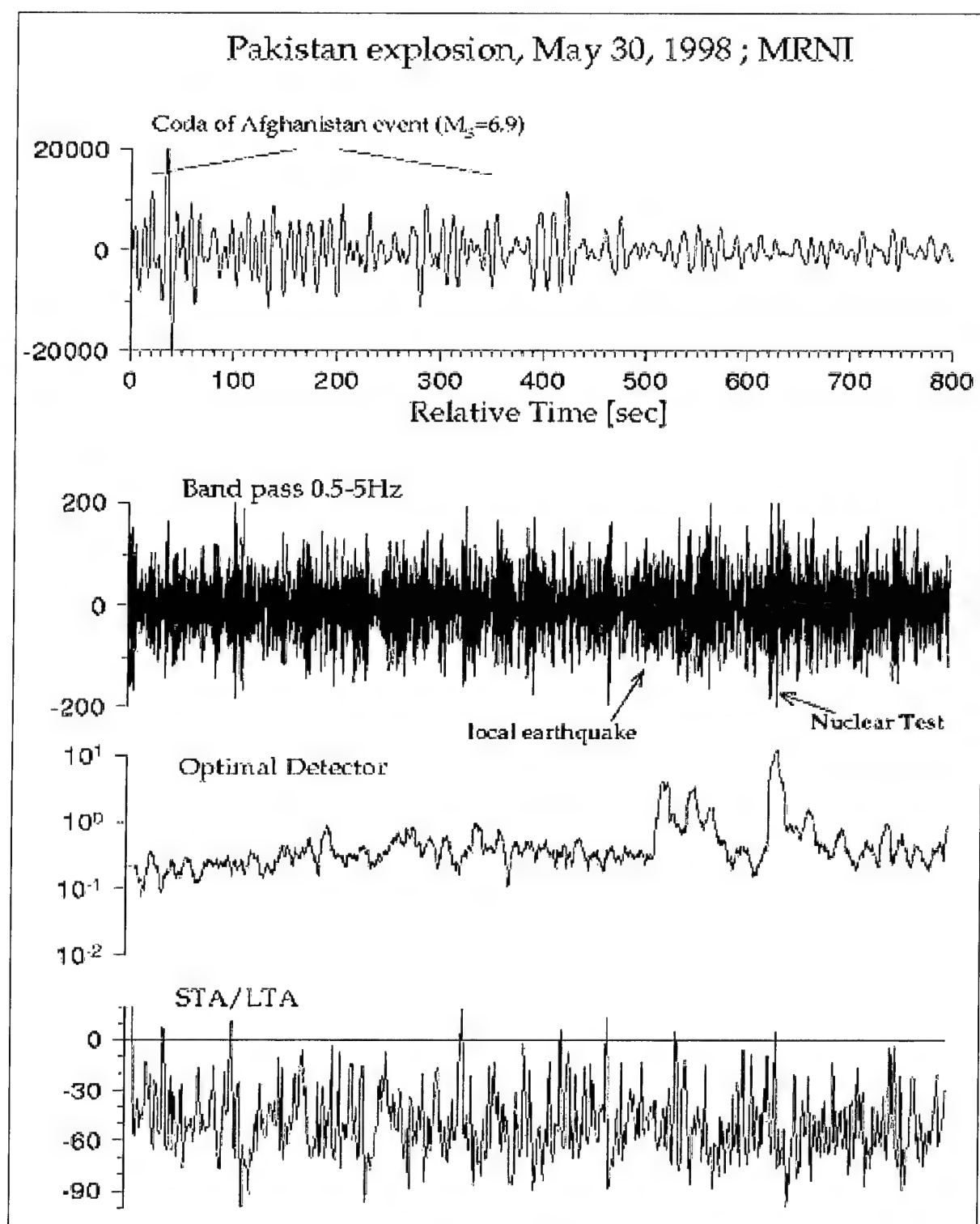
Figure 33. Detection of the first Pakistan test on May 28, 1998 (continued).

a

Pakistan explosion, May 30, 1998 ; EIL



a. Figure 34. Detection of the second Pakistan test on May 30, 1998.



b. MRNI BB Station

Figure 34. Detection of the second Pakistan test on May 30, 1998 (continued).

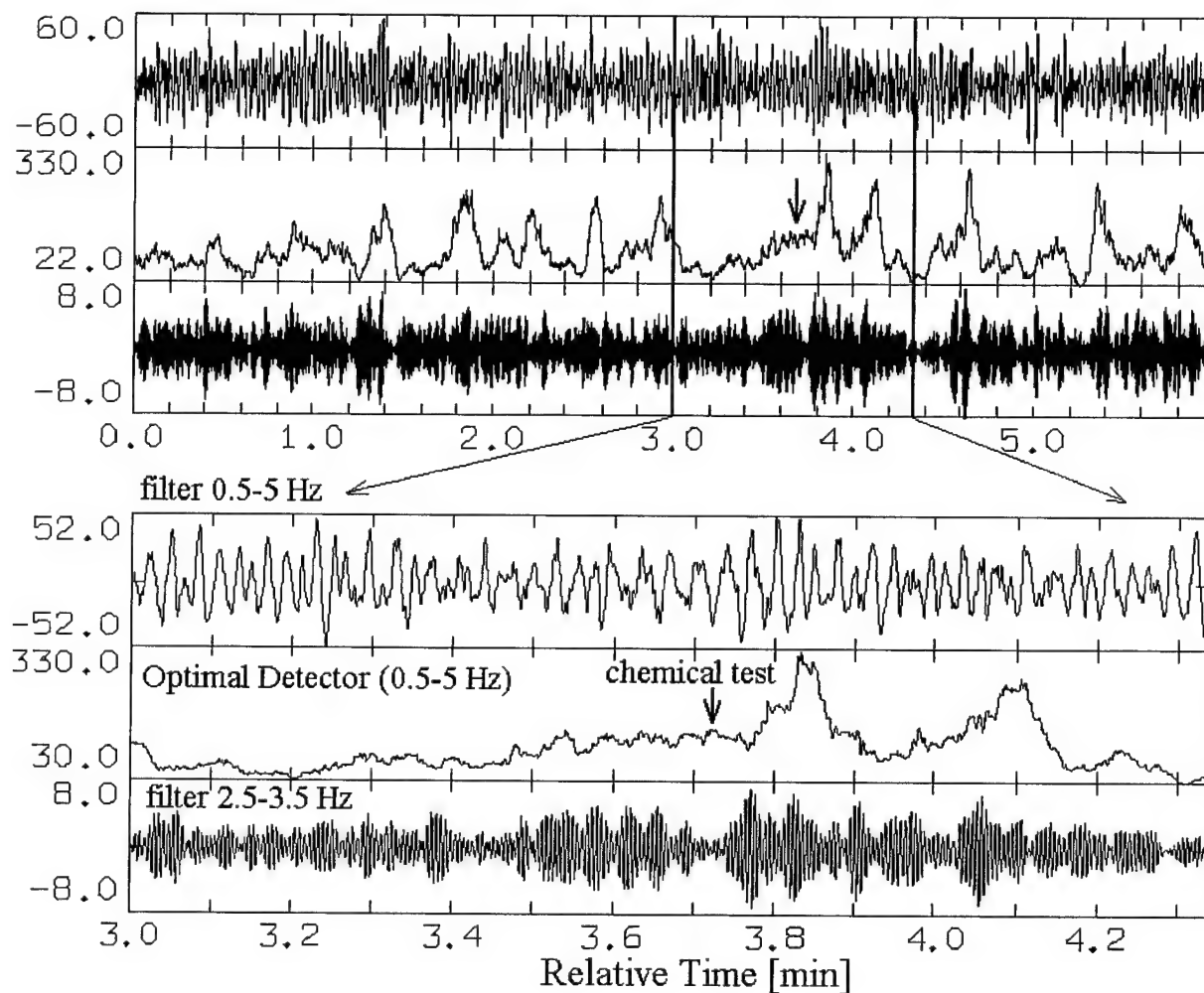


Figure 35. Detection trial of the Kazakh chemical explosion at EIL BB station.

5.2 Analysis of the ISN Subarrays Detectability.

The current configuration of the ISN has been divided into 3 subnetworks: A - northern array, 10 stations, aperture 80 km, B – central 8 stations, aperture about 30 km, and C – southern 4 stations, aperture 20 km, shown on Figure 36.

We formed a database of 232 East Mediterranean and Middle East events triggered and located by the entire ISN network during the period between 01.10.97 and 30.10.97 at a distance range $R < 3200$ km and evaluated the apparent detection capability of the 3 different ISN subnetworks by applying the Statistically Optimal Detector (SOD) and STA/LTA algorithms on the beams that the array stations performed. Unfortunately, there is no continuous recording in the ISN. Thus, only relative (relative ISN bulletin) detectability of the subarrays is available. Using this database we evaluated how the number of events detected by the SOD and the STA/LTA procedure depends on distance and magnitude. We applied the algorithms to the raw data collected, comprising signals from the events and the respective background noise and trigger thresholds tuned so that the rate of false alarm was less than 0.9. The results showed that at distances less than 3200 km and for the magnitude range $M_L = 3.5-5.0$, application of the SOD to the A, B, C arrays enhances detectability (probability of true detection) by a factor of 1.2-2 depending on magnitude and the subnetwork chosen.

The results are shown in Figure 37. The results of detection show that using only 4 stations of subnetwork C and the SOD technique we can detect more than 98% of all the ISN (36 stations) detections, while STA/LTA detects only 60%. For the A and B arrays SOD detects more than 85% (A) and 90% (B), compared to 20% (A) and 70% (B) for the STA/LTA. Thus the results show considerable detection capability of the ISN using the SOD technique.

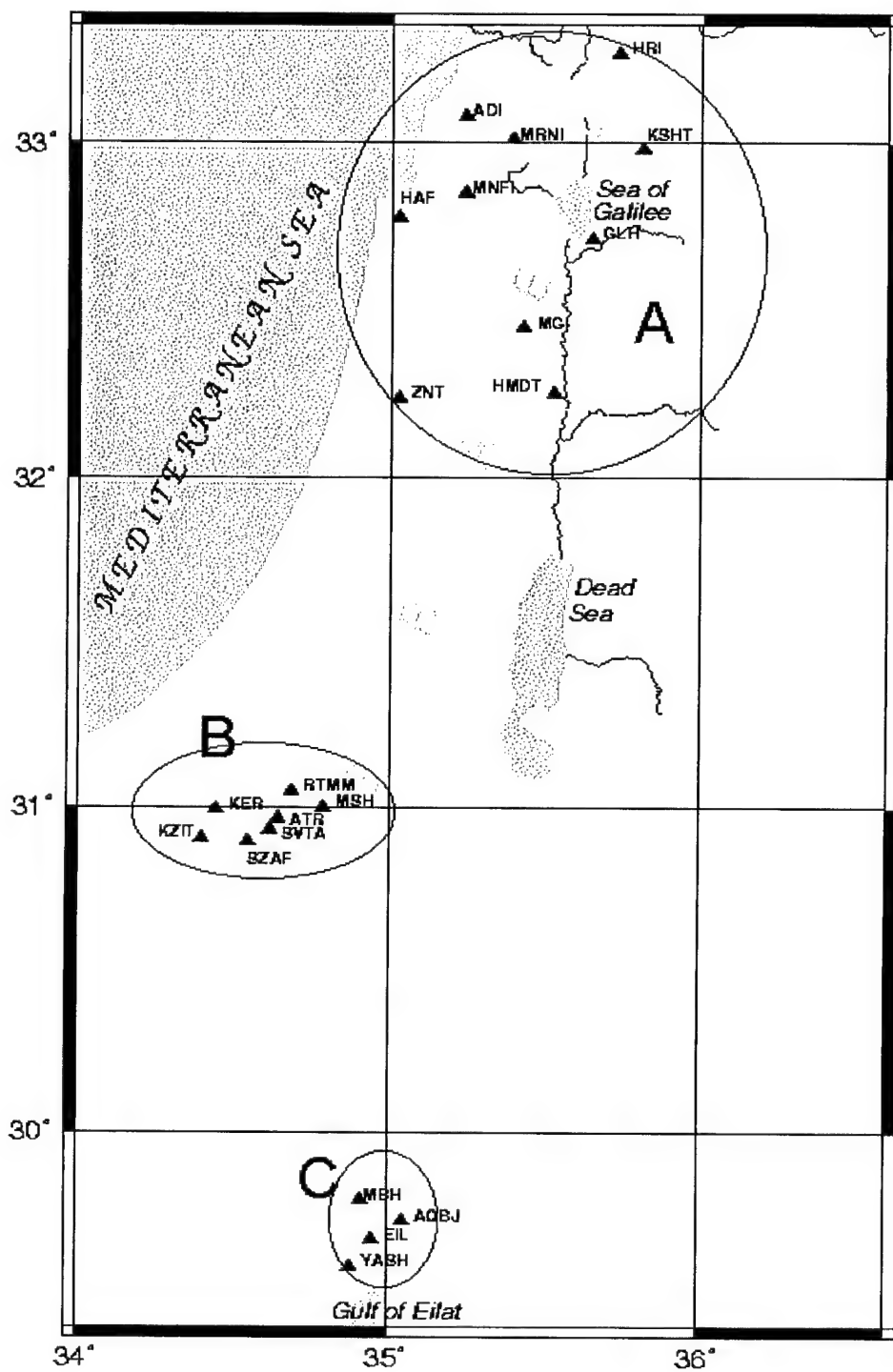
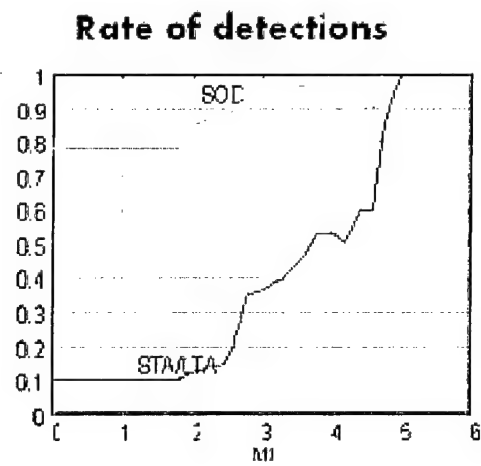
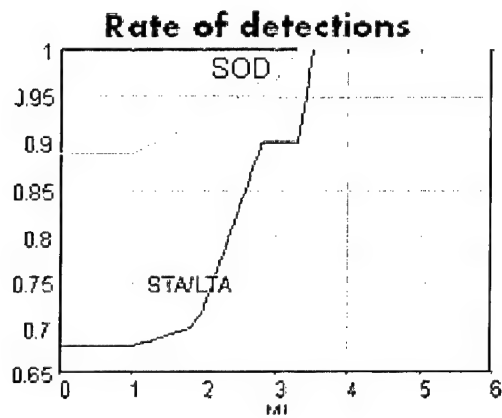


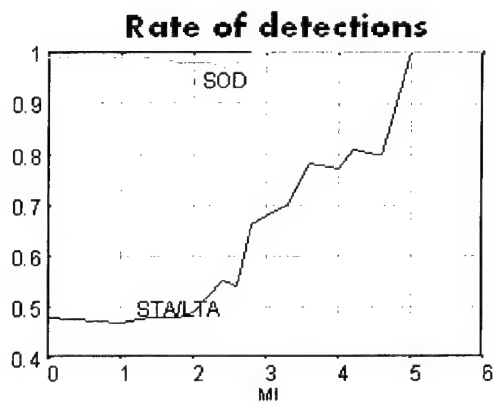
Figure 36. Location of the three analyzed ISN subnetworks and the associated telemetry network.



a. Sub-array A



b. Sub-array B



c. Sub-array C

Figure 37. Rate of detection versus magnitude for the ABT (AOGF) and standard STA/LTA procedure applied to subarrays A, B and C (232 events from the ISN bulletin serve as a reference).

5.3 Improvements in Location: Precise Automatic Location of Regional Events.

5.3.1 Background and Data.

Within the general task of improving the monitoring capabilities of the CTBT in the Middle East, this research is focused on implementation of innovative, automatic and robust location procedures intended to improve the accuracy and enhance the efficiency of regional network performance using data collected by the Israel Seismic Network (ISN).

Automation of regional event location using ISN recordings is one of the tasks of our research program. This section describes continuation of research first reported by Pinsky & Shapira (1998), which presents the main aspects of our approach, and the initial results of the prototype automatic location procedure further reported by Pinsky (1999, 2000).

Routine source location of regional and local events is based on picking the onsets of P (first) and S (second) phases on the seismogram. These are then converted into the corresponding geographical source coordinates, depth and time, using a given travel time model determined by velocity structure. In doing this, we need to remove noise, spikes and sporadic simultaneous events. In such cases, analysts must rely on their view of the seismogram and previous experience. Our task was to imitate the performance of the analyst.

In the first stage of our investigation, we simplified the problem by picking not first arrivals, but maxima of energy of the corresponding phases as having a better signal-to-noise (SNR) relation. The physical basis for this is that the energy of the P and S seismic phases obeys the law of diffusion and propagates in the stratified medium at a constant velocity. Based on this, Ryzhikov et al. (1996) derived a theoretical function over the observed envelopes of seismic phases which has a maximum pointing to the source epicenter.

Further to this premise, and in parallel with Shoubik et al. (1997) and Husebye et al. (1998), we developed a procedure for estimating source epicenters, X,Y (no depth) and time, T, using specific envelopes of the seismogram (Pinsky and Shapira, 1998). This procedure utilized automatic picking of maxima Pmax and Smax from the envelopes and a robust search inversion method. The automatic algorithm yielded an accuracy for X,Y of ~6 km (local coordinates) and T ~1 sec for a data set of pre-selected seismograms with clear seismic phases from the ISN data base of 150 earthquakes and quarry blasts. However, it did not achieve the location accuracy (~2 km for X,Y; ~3 km for H and T ~0.3 sec) in the bulletin. This is probably due to the relatively large variation in Pmax and Smax times around the theoretical values, while the P and S first arrivals seem to be more stable, at least for earthquakes.

In view of this, we returned to the location method based on first arrival time estimation, but with reasonable preliminary estimates of X,Y and T from the envelope location procedure. There is a variety of automatic methods for finding first phase arrivals on seismograms. We tested one method based on maximum likelihood ratio (Pisarenko, et al., 1987) which was shown convincingly by Kushnir (1996) to be equivalent to, or even better than, manual picking, and another inspired by the envelope processing algorithm of Fedorenko and Husebye (1999). Both require a specified time interval, assumed to contain the phase arrival. We estimated this from the preliminary X,Y,T and theoretical travel time computations for P and S phase first arrivals. Finally, source coordinates, time and depth are estimated through a grid search using a robust optimization procedure based on M-estimates developed by Huber (1972) and tested for seismic location by Andersen (1982).

The data used in this study are short period seismograms (50 Hz sampling rate with effective bandwidth 0.5-12 Hz) of the Israel Seismic Network (~30 stations) telemetered to a Hub via radio FM link. The data include 61 earthquakes, $M_L=1.0-2.8$ at distances of 15-310 km. Event epicenters and station locations are presented in Figure 38. The location results for the three Dead Sea test explosions and four calibration quarry blasts exploded in the Arad quarry are presented in Section 4.1.7 and 4.1.10.

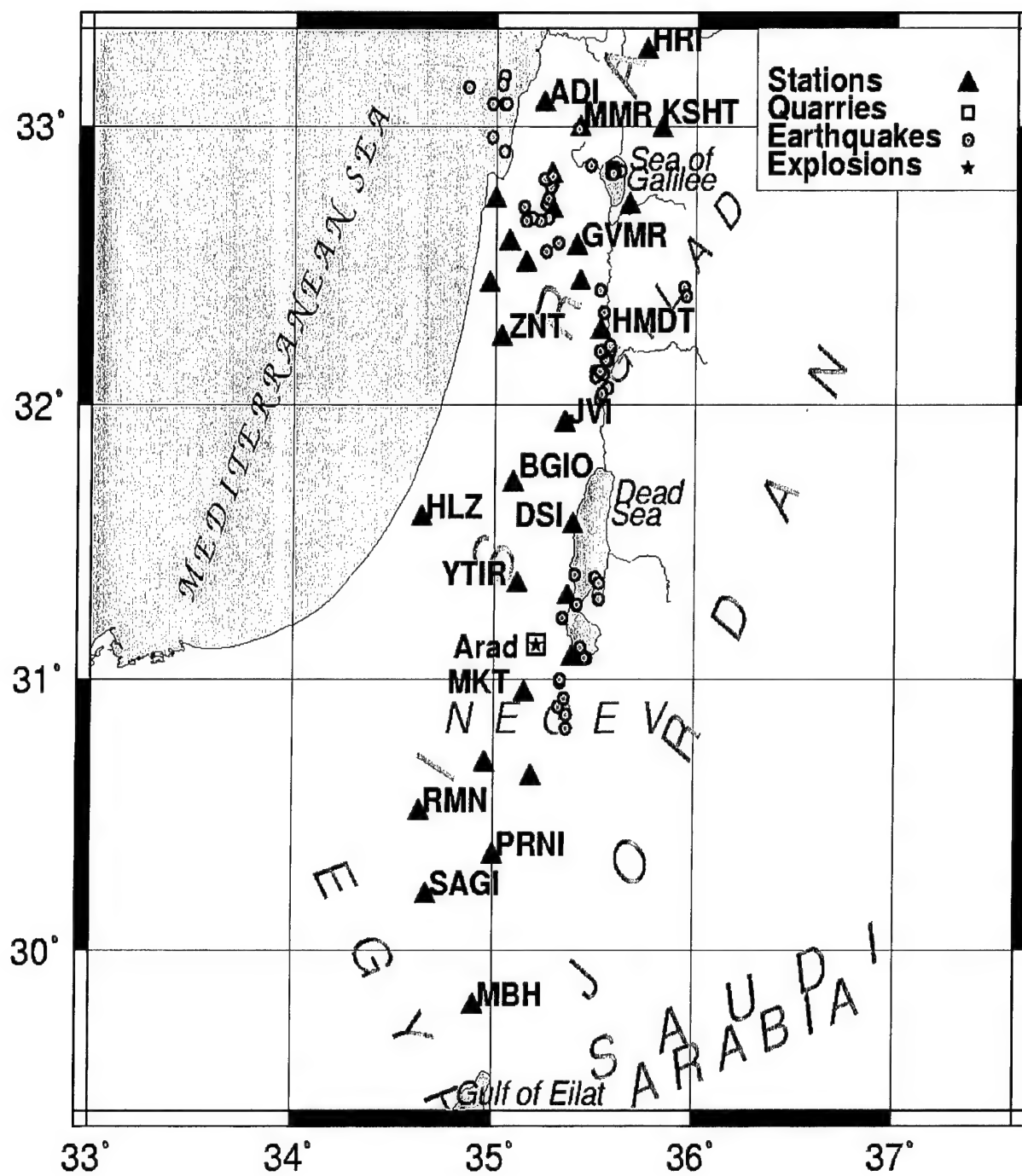


Figure 38. Map showing earthquake epicenters, quarry blasts and the ISN stations

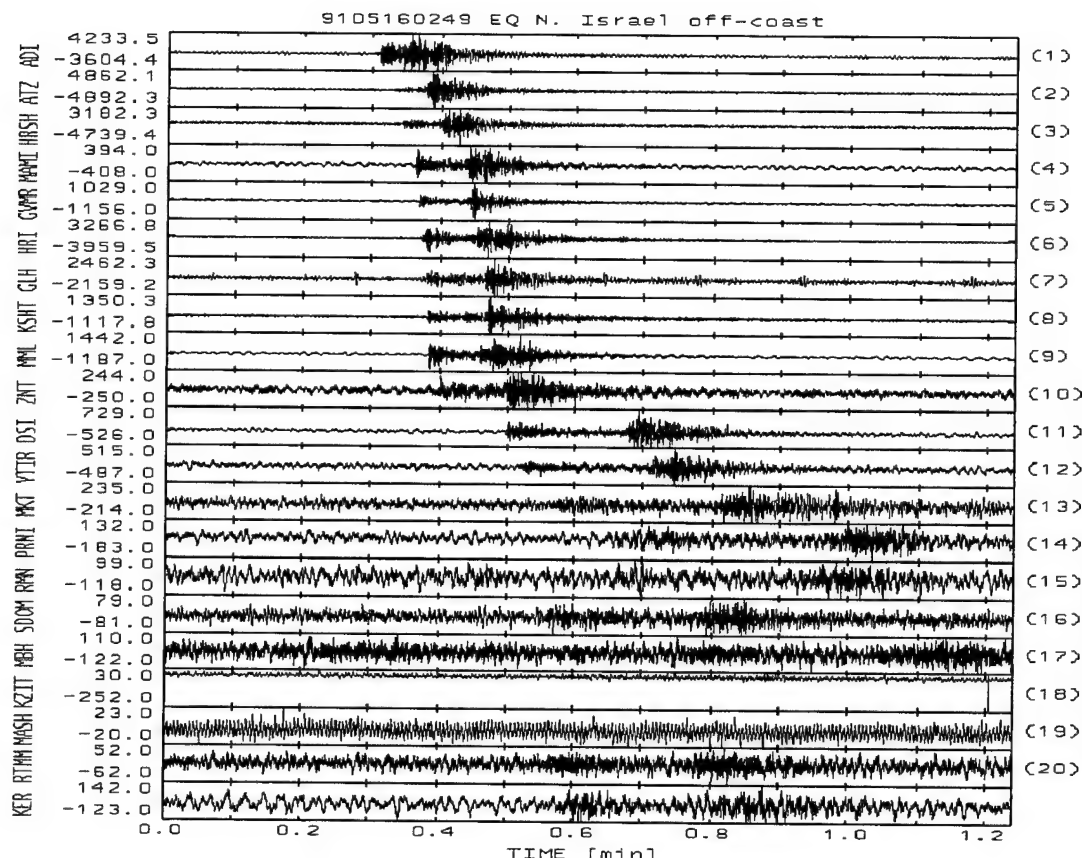


Figure 39. Example of typical earthquake recording by different ISN stations. Clear and noisy, steep and slow P and S phase arrivals are observed. Channels with bad SNR and un-removable spikes will be discarded by the automatic procedure.

5.3.2 Method.

The method used comprises four main stages: (i) preprocessing; (ii) preliminary epicenter location; (iii) P and S onset picking and (iv) final hypocenter location.

Preprocessing includes de-spiking and band pass filtering of the seismograms in an appropriate frequency band and automatic selection of the traces with appropriate signal-to-noise ratio (SNR). The records used are often marred by spikes or noise outbursts caused by radio pulses or industrial and micro-seismic noise that cause inaccurate interpretation (see Figure 39). It is crucial to the success of a procedure based on detecting seismic signals, that records are clean. A spike is assumed to be “thin” and “high”, thus we perform a simple de-spiking by cutting the whole trace into a series of intervals (2 sec. each) and comparing average noise level with its current value inside the interval. Some of the channels may suffer partial distortion of the signal as a result of this procedure.

The next step is to calculate seismogram envelopes for each station, which are used for preliminary epicenter location by the envelope location method (Pinsky, 1999). Two different types of envelope are computed, both characterized by abrupt onsets and sharp energy maxima, even for weak seismic phases; thus providing, in most cases, a clear separation between P and S phases even at short distances. The envelopes have local maximums P_{max} , S_{max} at time points T_p and T_s , which are coincident with P and S arrivals in the original non-transformed records. The quality of a trace is characterized by the $SNR = P_{max}/NL$ ratio, where NL is the noise level of the envelope. The traces with low SNR are omitted to give a clearer result, thus providing automatic selection of channels for further processing. Those traces that are left after trace selection as described above, are arranged according T_p time, the first having the minimum T_p among M channels, having the largest SNR. In this way it is possible to estimate the station which is (probably) closest to the source.

Preliminary epicenter location is provided by the envelope location method, based on fitting time-distance (T_p, R), (T_s, R) pairs to the travel time curves defined in this case by two lines: $T_p = T_{0p} + R/V_p$, $T_s = T_{0s} + R/V_s$, which characterize propagation of the maximum of energy for the regional P and S seismic phases (see Figure 40).

The parameters of the two equations, estimated through a least squares fitting for a set of earthquakes and quarry blasts, are $V_p = 6.0$ km/sec, $V_s = 3.5$ km/sec, $T_{0p} = 2.5$ sec, $T_{0s} = 3.5$ sec. The T_p and T_s estimates found by triggering on the envelopes at the maximum are not especially reliable. However, for the case where we have sufficient stations ($NS > 10$) with good SNR, true T_p and T_s are in the majority and a robust optimization that ignores false observations can provide a satisfactory source location. An optimization procedure for such a class was presented by Huber (1972) as M-estimators.

The task is to maximize (minimize) target function:

$$F(\theta) = \sum_r w_r f(\Delta_r(\theta)) \quad (5.1)$$

with a gain (loss) function $f(\Delta)$ of residuals $\Delta = (\text{observation} - \text{model})$. The usual and, in many cases, efficient procedure for location is a least-squares technique in which the solution is found by minimization of a sum of squares of the residuals $\Delta_{ai} = T_a - T_a(R_i) - T_0$, where a denotes P or S for a number of stations, and T_0 is the origin time. If, however, the observations include random outliers of the time T_a then this procedure is inefficient and, besides, may cause large errors in location. We observe that many P identifications have S travel times and vice versa; thus a random T_a variable for fixed a should belong to bi-modal or even multi-modal distribution. This feature should be taken into account in a specialized location scheme since the conventional least-squares procedure is not applicable in this case.

In such cases residuals appear as

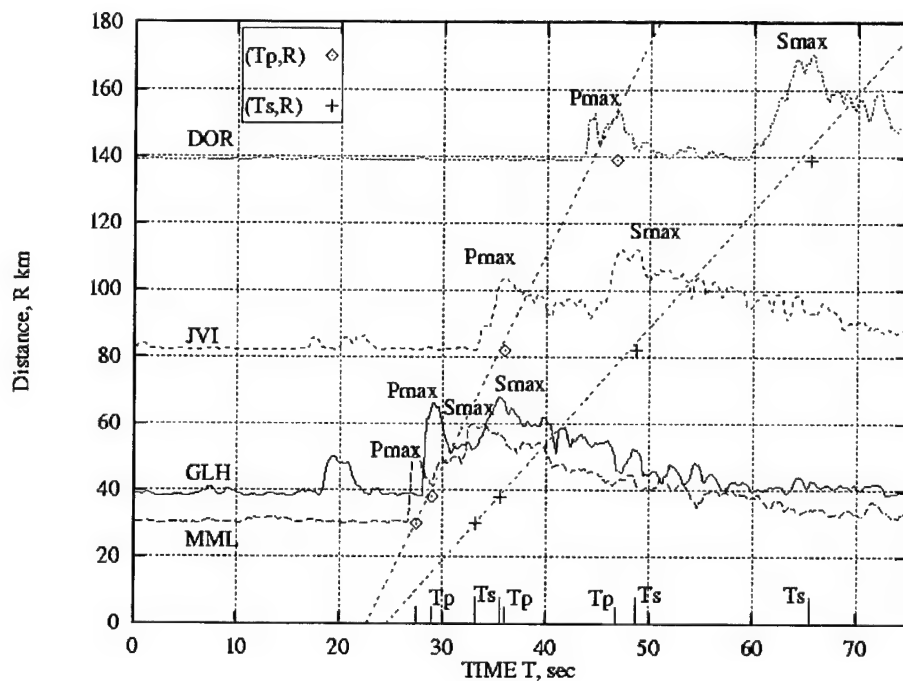
$$\Delta_{aci} = T_a - T_c(R_i) - T_0 \quad (5.2)$$

Next, instead of one station's residuals Δ_{aci} we shall consider two station residuals $\Delta_{abcij} = \Delta_{aci} - \Delta_{bcj}$, $i, j = 1, \dots, N$, $a, b, c = P, S$, which do not depend on origin time T_0 , thus, reducing the number of unknown variables from 3 to 2. From the "picker" above we obtain two time picks T_p and T_s for each channel, but the "picker" is not aware to which phase, P, S, or Rg they belong. To distinguish between correct and incorrect identifications we use a gain function in Equation 4

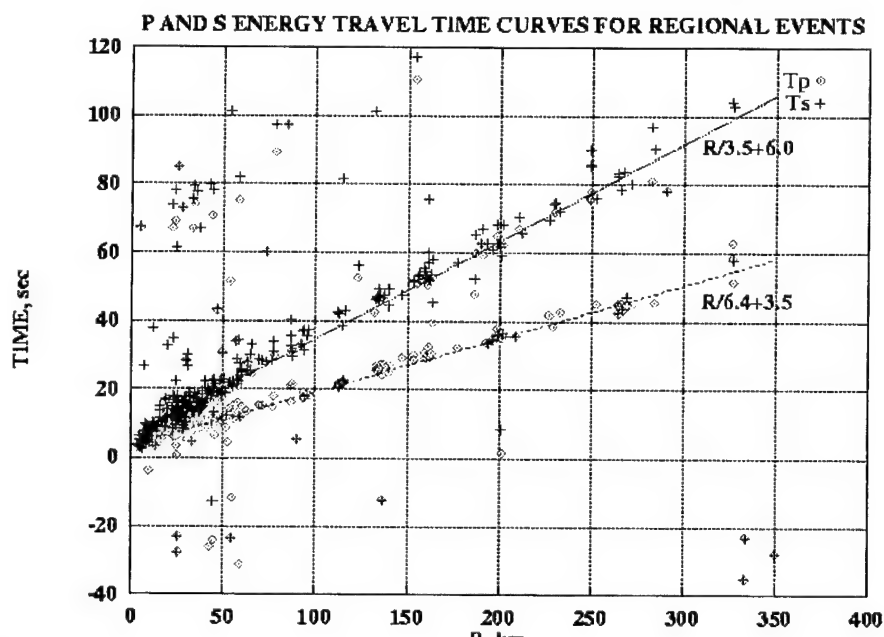
$$f(\Delta) = (|\Delta| + \epsilon)^{-1} \quad (5.3)$$

of deviations Δ (instead of the usual $f(\Delta) = \Delta^2$), "voting" for true pickings with large values and against false pickings with small values respectively. Then it is reasonable to estimate the epicenter X, Y by maximization of the $F(\theta)$ function (4) by computing the $F(\theta)$ value at grid points (i.e., 60x60 km, step 1 km).

The procedure unites two tasks, location and phase identification, where the majority of "good" picks, close to P or S travel time guarantee a successful solution. The control parameter $\epsilon > 0$ helps to avoid possible zeroes of the residuals Δ_{abcij} , thus providing robustness of the X_{\max} , Y_{\max} estimator, which maximizes the $F(\theta)$. After that we estimate origin T_0 providing a maximum to $F(\theta)$ with $f(\Delta)$ defined in (6), fixed $X = X_{\max}$, $Y = Y_{\max}$, and Δ determined by (5). The parameter ϵ is selected automatically as $\epsilon = 0.1 + k \cdot 2^{-k}$, $k = 1, \dots, 5$ according to the empirical criterion that for more than $N/2$ stations there is at least one combination of a, b, c, i and j that $(|\Delta_{abcij}| + \epsilon) < 3$.

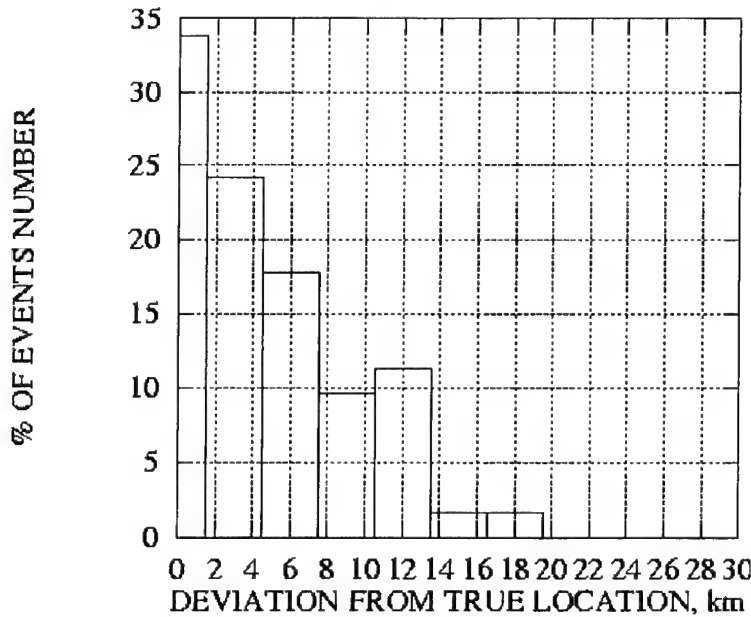


a.



b.

Figure 40. Initial epicenter location. (a) Envelope Location Scheme: the envelopes Pmax and Smax are fitted to the linear travel time model. (b) T_p and T_s time picks vs. distance R for 30 earthquakes from Galilee. Best fitting lines T_{pm} , T_{sm} : $T = R/6.4 + 3.5$ and $T = R/3.5 + 6.0$ are shown.



c.

Figure 40. Initial epicenter location (continued). (c) Distribution of preliminary location error for the 61 local earthquakes. 95% of the events are within 15 km error range

P and S Onset Pickings are provided by estimating P and S first arrivals Z_p and Z_s , which seem more stable than T_p and T_s for good SNR conditions. For the automatic Z_p and Z_s estimation we chose a statistically optimal algorithm proposed by Kushnir (1994) and shown to be efficient for seismic phase picking. The procedure is based on statistical testing of the hypothesis that the time series before and after signal arrival are two different autoregressive time-series in the chosen time interval $[T1, T2]$, possibly containing the point of interest T_0 . The two autoregressive models are approximated using “noise” and “signal” recordings corresponding to the opposite edges of the interval. The point T_0 is estimated as a maximum likelihood ratio (MLR) by scanning through the interval (see Figure 41a).

A very similar method with high picking accuracy is demonstrated by Leonard (2000), who combined the autoregressive Akaike information criteria (AIC) with an autoregressive prefiltering (AR-AIC method).

Another approach, published in Fedorenko and Husebye (1999) (FHM) is to look for the point where signal energy starts to grow. This comprises two steps: (1) linear regression of the envelope front in the neighborhood of a trigger point Tr and (2) computation of the intersection point Ti of the line obtained with the noise level, which provides us with an estimate of a seismic phase onset time (see Figure 41a) and the inclination angle A .

The time interval $[T1, T2]$, where the onset time T_0 is expected, is computed as $T1=T(R)-dt1$, $T2=T(R)+dt2$, where $T(R)$ denotes P or S travel time, determined by the preliminary epicenter location and by the local velocity model (Figure 41b). The values of $dt1$ and $dt2$ are set at 5 sec and 4 sec, correspondingly for both P and S phases.

Hypocenter location is a robust grid search procedure based on maximization of a type function (4) equal to the linear combination of the “bell-like” gain functions $f(\Delta)$ (equal to 1 when the discrepancy is 0 and equal to ~ 0 at infinity). The algorithm is comprised of two steps: first, the P arrivals Z_p provided previously by the two onset estimators, MLR and FHM, are used in computing:

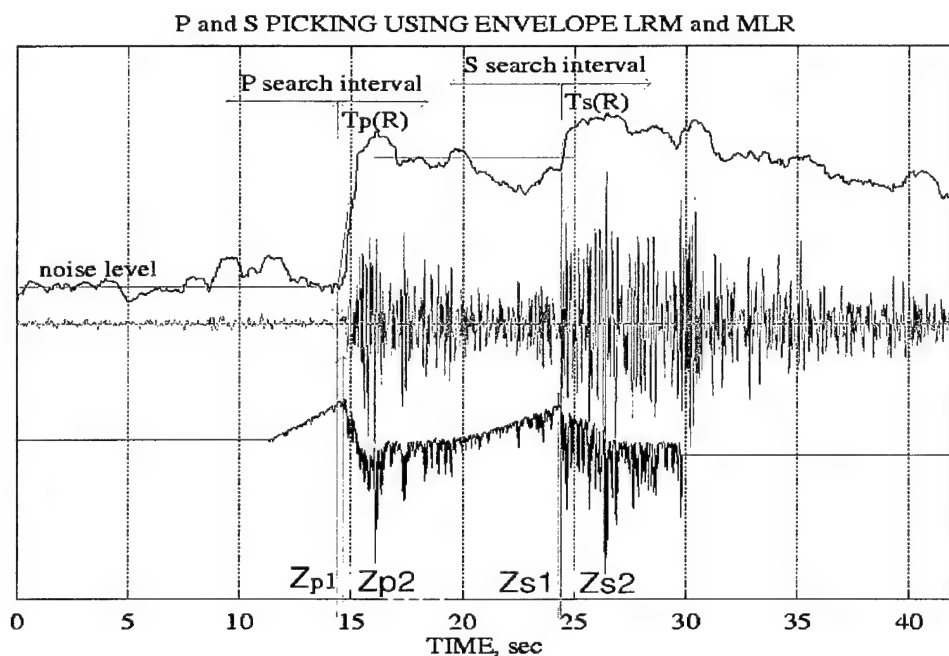
$$\Delta_{ip} = Z_p - Z_p(R_i, H) - T_0 \quad (5.4)$$

where $i=1, \dots, N$ is a channel index, $Z_p(R_i, H)$ – is a local travel time model for the first P phase arrivals at station number i , T_0 -origin time,

$$\begin{aligned}
 f(\Delta) &= \exp(-|\Delta|), & |\Delta| < 0.5 \\
 f(\Delta) &= 0 & |\Delta| > 0.5
 \end{aligned}
 \tag{5.5}$$

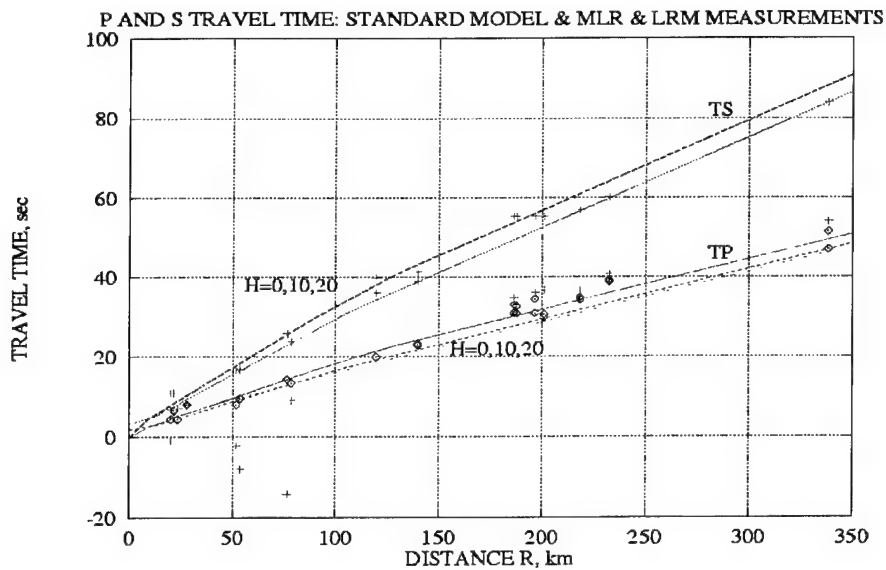
The scanning grid is $(60 \times 60 \times 25 \text{ km}^3, \pm 10 \text{ sec})$ with a relatively large step $dx, dy, dh = 2 \text{ km}, dt = 0.5 \text{ sec}$. The algorithm, using the gain function (8), ignores all observations Z , deviating more than 0.5 seconds from the model. When the optimum is found, it continues computations on a finer grid $(5 \times 5 \times 25 \text{ km}^3, \pm 3 \text{ sec})$, $dx, dy = 0.3 \text{ km}, dh = 1 \text{ km}, dt = 0.1 \text{ sec}$, using (7) for computation of Δ_{ip} and Δ_{is} (with index s substituting p), but using a gain function

$$\begin{aligned}
 f(\Delta) &= \exp(-|\Delta|^2), & |\Delta| < 0.7 \\
 f(\Delta) &= 0 & |\Delta| > 0.7
 \end{aligned}
 \tag{5.6}$$

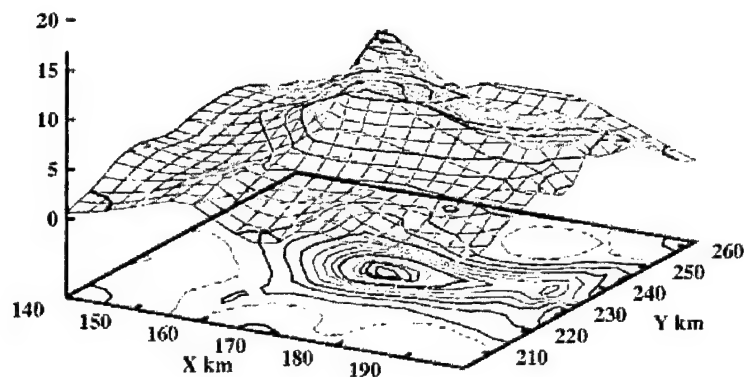


a.

Figure 41. Final automatic hypocenter location for a local earthquake.



b.



c.

Figure 41. Final automatic hypocenter location for a local earthquake (continued).

(a) The P and S on-set points are looked for in the intervals, specified for each station by the preliminary X_{max} , Y_{max} , T_{max} envelope estimates. The on-sets (Z_{p1} and Z_{s1}) of the MLA (bottom curve) and (Z_{p2} and Z_{s2}) of the FHM (upper curve) are used jointly in the optimization procedure, which compares: (b) the network MLA (Z_{p1} - , Z_{s1} +) and FHM (P - , S - \times) on-sets with P and S model travel-time curves: $T_p(R, H)$ and $T_s(R, H)$ (shown for $H = 0, 10, 20$ km). A number of outliers are seen, but these are discarded by our locator, yielding: (c) $X = 173$, $Y = 233.1$, $H = 16$ km, $T = 21.19$ sec, compared to bulletin results: $X = 173.8$, $Y = 230$, $H = 12$ km, $T = 21.28$ sec. Target function $F(X, Y, H1, T1)$ is evaluated using equations (1), (3) and (4), $H1 = 16$ km, $T1 = 21.19$ seconds.

Weighting coefficients w_r in (1) are set $w_r=1 \cdot \exp(-Tg(A_r))$, where A_r is the envelope inclination angle determined above. Thus, abrupt onsets are highlighted and very slow onsets neglected. Reliability of location is estimated from the maximum value of the $F(\theta)$ function close to the number of donating channels. Accuracy of location is determined by the $F(\theta)$ peak sharpness in the R space, or by the usual error ellipsoid.

5.3.3 Results

Under the supervision of the Geophysical Institute of Israel a series of four calibration explosions was performed at the Arad quarry (see Figure 38) and three underwater explosions in the Dead Sea. All of them had controlled source parameters: coordinates, time of ignition, charge, delays etc. The seismograms of the explosions were recorded by the ISN stations and processed by analysts. The automatic location algorithm was applied to the ISN seismograms of the events. The results, presented in the Sections 4.1.7 and 4.1.10 for the different travel time models and network configurations are very close to the analysts' solutions and, in several cases, somewhat better.

We applied the automatic algorithm to a data set of 61 small earthquakes $1.5 < M_L < 2.5$ in from the Galilee, Gilad and Dead Sea areas (Figure 40). Our epicenter location results are presented in Figures 40c and 42 by 1D histograms of deviations R from X_0, Y_0 and by 2D plots of points $(X-X_0, Y-Y_0)$. Here X_0, Y_0 are presumed true source coordinates as reported in bulletins. The 80% and 90% error ellipsoids are presented on the corresponding plots. From Figure 40c we see that preliminary epicenter estimates provided by the envelope processor STA+OD are sometimes rather rough. Nevertheless, epicenters demonstrated in Figure 42 are significantly improved by the MLR+RLM procedure and in many cases are equivalent to the bulletin solutions, showing 80% of epicenter "mislocation" $dR < 3$ km (assuming bulletin solution true) and standard deviation $\sigma(dR)=2.1$ km. Figure 42c depicts 2D estimates of origin time T_0 and depth by MLR+RLM procedure and shows that T_0 is well estimated; the depth estimates, however, often deviate considerably from those in the bulletin.

The above results appear promising for automation of local seismicity monitoring. Our new procedure performed well providing robust and accurate solutions for earthquake epicenters in the different geological regions of Israel; the Galilee, Gilad and Dead Sea areas, as well as for the four calibration explosions in the Arad quarry.

There are some locations which deviate from the results of standard processing, but usually these events are qualified in the bulletin as having "low reliability" and, as such, are difficult to judge as ground truth. The same remark is true for the depth estimates which are known to be poor in the bulletin due to the low resolution of the existing system of surface observations. We also tried to apply this technique to the local quarries. For many of them the results were very accurate, but almost 10% of the events proved problematic for analysis, most of them due to failure in the preliminary location stage. The reason is that this kind of signal source causes strong excitation of the R_g surface waves, propagating with low velocities in the range of 1-3 km/sec. This may, in turn, result in late picks of the true P and S phases. Another factor is scattering and multi-pathing due to heterogeneity of the uppermost part of the crust. The local seismicity is 99.9% represented by quarry blasts and earthquakes, hence our suggestion is that earthquakes/quarry blast automatic discrimination be carried out before the automatic location as shown in Gitterman et al. (1998) with around 98% reliability. If an event is classified as an earthquake it can be located automatically by the procedure developed. On the other hand, if it is a quarry blast, it is possibly easier to identify the source quarry among the set of known quarries using pattern recognition approaches as in Joswig (1990) or Fedorenko et al. (1998).

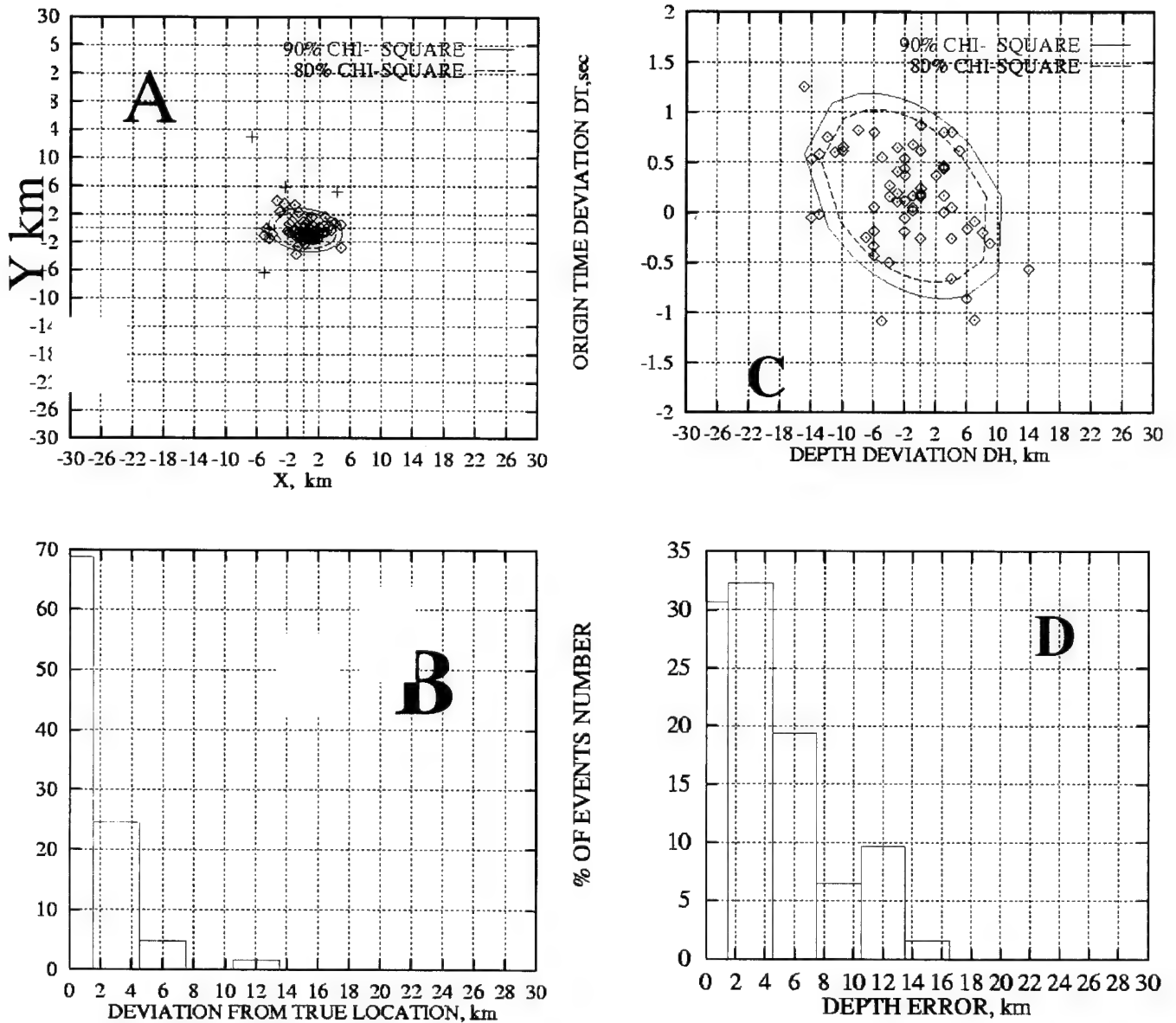


Figure 42. Automatic location results for 61 local earthquakes. Distribution of (a) automatic minus bulletin solutions for epicenters, (b) origin time and depth and histograms (c) for deviation of epicenter and (d) depth.

5.4 Characterization and Identification of Seismic Sources.

5.4.1 Spectral features of seismic waves and waveform characterization for controlled quarry blasts, correlation between blast parameters and signal characteristics, and discrimination analysis.

Four routine controlled ripple-fired explosions at the Arad phosphate quarry in the Negev desert were recorded by Israel seismic stations, at distances of 28-245 km. The stations used in the analysis and the explosion locations are presented in Figure 1, the summary of the explosion parameters is presented in Table 2 (Section 3.1.1). The explosions were located a few hundred meters apart, Example 3 and 4 were adjacent on the same bench. Two 3C accelerometers (A-800 by Geotech, USA) were also installed in close vicinity to the explosions (within few hundred meters) for better source characterization.

Seismic strength. Local magnitudes based on coda duration measurements and peak amplitudes (as an indication of seismic signal strength) of the blasts are presented in Table 26. The total yield of Example 3 was only 19% more than that of Example 4, however, it produced far more seismic energy (Figure 43). The peak amplitude ratio for the two explosions showed a factor of 2 at short distances (i.e., MZDA, $r=28$ km), increasing with distance to 3 at more remote stations (i.e., BB EIL, $r=161$ km, see Table 26). We attribute this effect to the role of delay times in the detonation process. Example 3 with small delays of 12 msec seems to be similar to instantaneous blasting with the strongest seismic effect.

We tried to collect and analyze seismograms of the blasts at neighboring seismic stations in Cyprus and Turkey. At our request Cypriot seismologists from the Geological Survey Department (courtesy of Mr. K. Solomi) supplied continuous recordings (20 samples/sec) of the Broad Band station CSS, located in 475 km from the explosions. We analyzed recordings of the strongest explosion Ex.3 ($M_L=2.9$). After strong filtering in the 6-8 Hz band, a possible signal can be observed at the EW component (Figure 44), which corresponds to the calculated arrival of P-waves. Nevertheless due to the absence of a similar signal on the vertical component we cannot consider this observation reliable.

We asked our Turkish colleagues to examine recordings of their southern stations, and to search for a visible signal from explosion No.3. A number of stations have been checked (Mr. Ekrem Zor, personal communication): Southeastern stations: Diyarbakir (SSR short period), Malatya, Gaziantep; Mediterranean region stations: Silifke, Isparta (GEOFON BB station). No signal was found at these remote stations located 600-800 km from the explosion site.

Example 4 with large delays of 80 msec showed decreased seismic energy due to destructive interference phenomenon and corresponds approximately to the one-row blast. The effect of delay times is observed also for Example 1 and 2 with intermediate delays of 40 msec. These blasts have much lower total yields than Example 4, but produced similar amplitudes (Figure 45).

Compared to those of EIL, signal amplitudes for Example 3 and 4 are enhanced at MRNI (Figure 43). EIL is located closer to the quarry at the opposite azimuth (see a map in Figure 1). Such an "azimuthal effect" was not observed at the SP stations, i.e., HRI and YASH. It cannot, therefore, be attributed to the source effect like direction of blast sequencing or orientation and position of the free face; however, it is likely to be associated with path and site effects.

Local duration magnitudes correlate well with peak amplitudes and correspond approximately to the upper limit of the yield-magnitude relationship of ripple-fired quarry blasts (Gitterman, 1998, Khalturin et al., 1998). Records of Example 3 (with delays of 12 msec) are exceptional, as this explosion has a source function more similar to instantaneous blasts.

Table 26. Local magnitudes and peak amplitudes of the analyzed quarry blasts.

Expl. No.	Mag. M_L	Peak amplitudes at different stations (vertical component), micron/sec					
		MZDA r=28 km north	YTIR r=29 km north	YASH r=170 km south	HRI r=245 km north	BB EIL r=161 km south	BB MRN r=212 km north
1	2.6	6.2	9.7	0.59	0.57	0.127	-
2	2.7	11.2	8.5	0.79	0.40	0.122	-
3	2.9	17.9	19.6	3.08	2.04	0.389	0.541
4	2.7	8.5	7.8	1.26	-	0.135	0.217

Waveform correlation. We studied waveform correlation for the explosions to check for similarity, i.e., that events from the same mine produce highly repeatable waveforms which, in turn, can be used for event clustering and source identification (i.e., Harris, 1997). Indeed, when comparing normalized seismograms at a specific station, one can observe conformity in the shape of some phases (see i.e., Figure 46). Table 27 shows cross-correlation maximum values between Example 1 and the other explosions at several close and remote stations for different time windows. The correlation values decrease significantly with distance (more complicated waveforms and lower signal-to-noise ratio) and increase for larger windows containing the whole wavetrain.

Table 27. Waveform correlation of the quarry blasts at different stations (relatively to Example1).

Station	Dist., km	Azim., deg	Time window, sec	Maximum of the cross-correlation function				Comments
				Ex.1	Ex.2	Ex.3	Ex.4	
MZDA	29	35	20	1	0.64	0.32	0.42	-
			35	1	0.63	0.31	0.40	whole signal
YTIR	31	348	10	1	0.39	0.43	0.33	P-waves
			35	1	0.81	0.52	0.37	whole signal
PRNI	84	192	64	1	0.73	0.48	0.61	
			15	1	0.42	0.20	0.20	P-waves
SAGI	110	206	35	1	0.28	0.17	0.25	whole signal
MBH	146	190	45	1	0.55	0.20	0.18	
			15	1	0.61	0.44	0.38	P-waves
			15	1	0.49	0.24	0.20	S-waves
YASH	170	190	15	1	0.41	0.14	0.14	P-waves
			40	1	0.34	0.30	0.22	whole signal

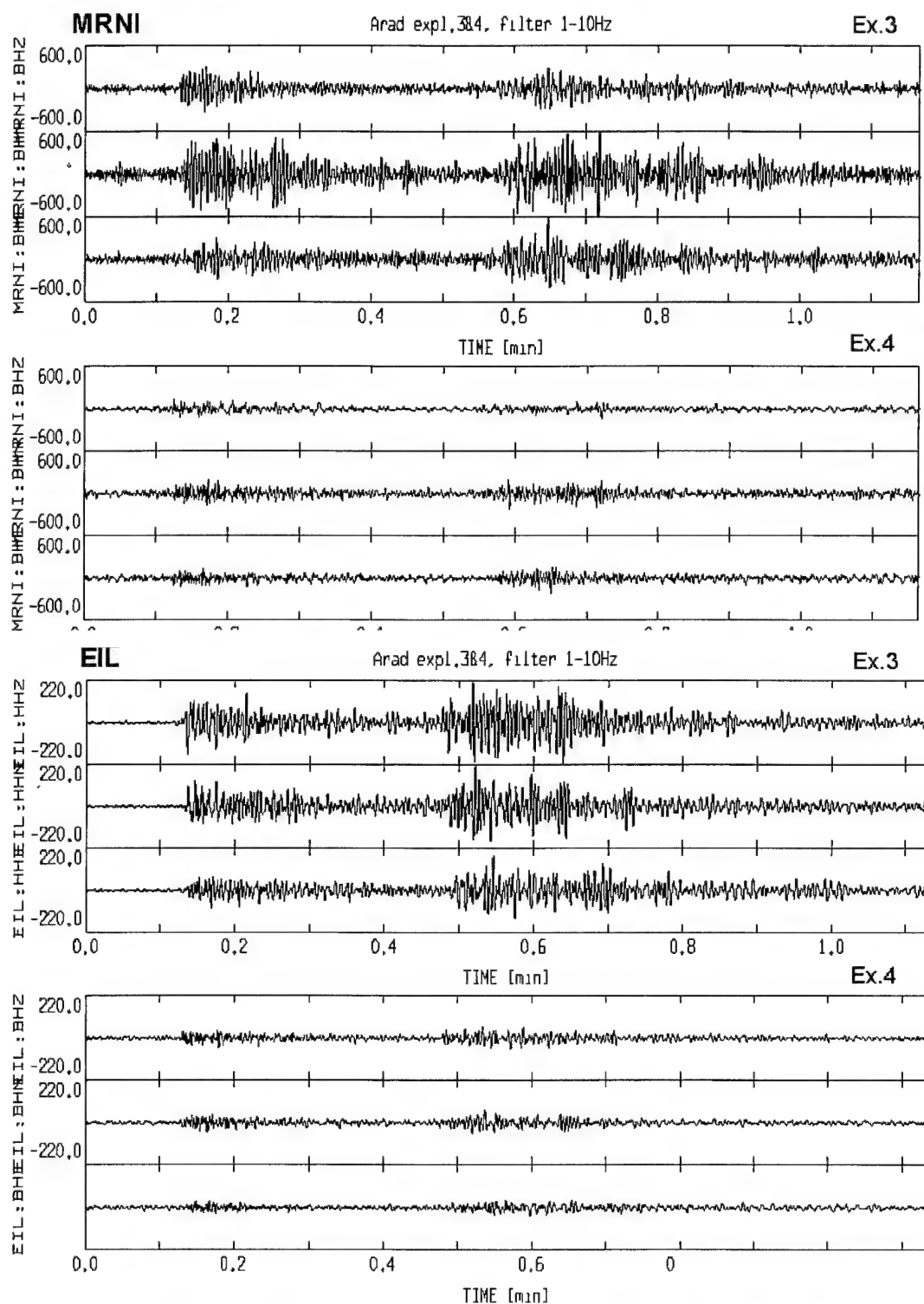


Figure 43. Seismograms (in the same scale) of Ex.3 and Ex.4 at BB stations EIL ($r=161$ km) and MRNI ($r=212$ km). Vertical units are counts.

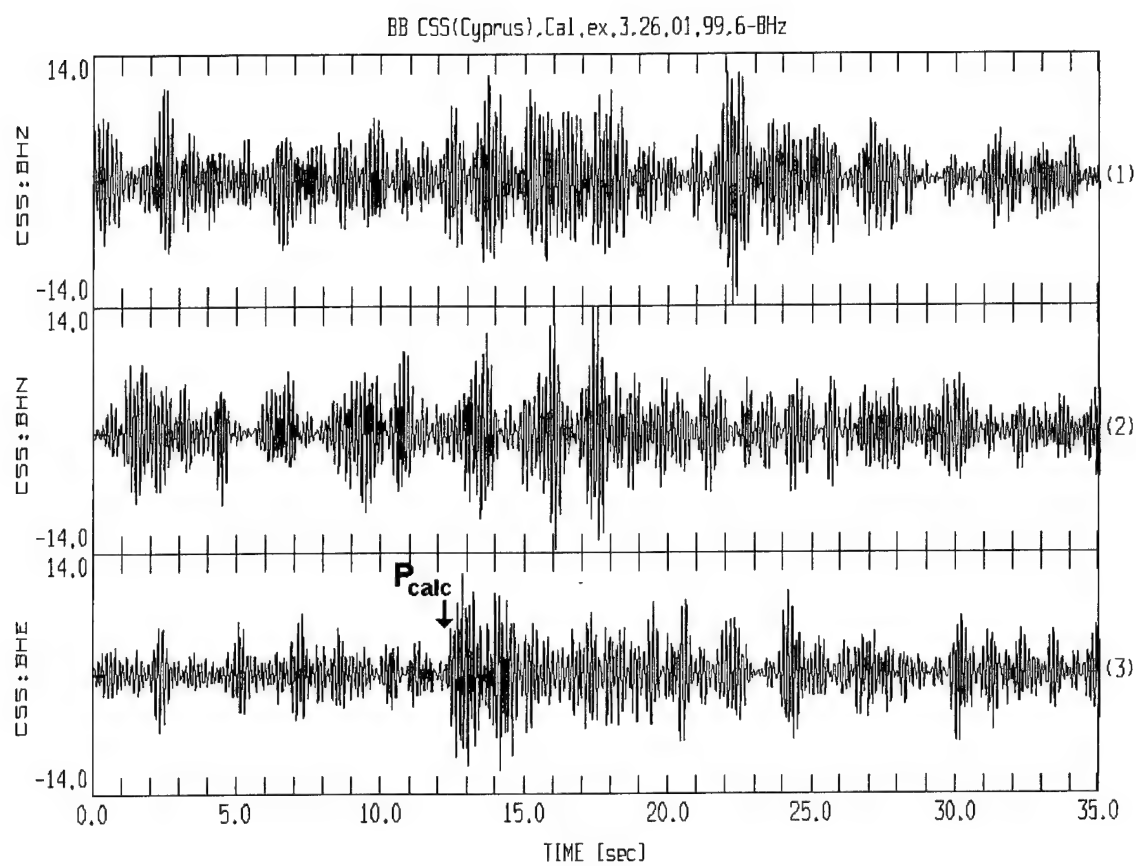


Figure 44. Expected arrival of P-waves from Example 3 at the BB station CSS (Cyprus), $r=475$ km.

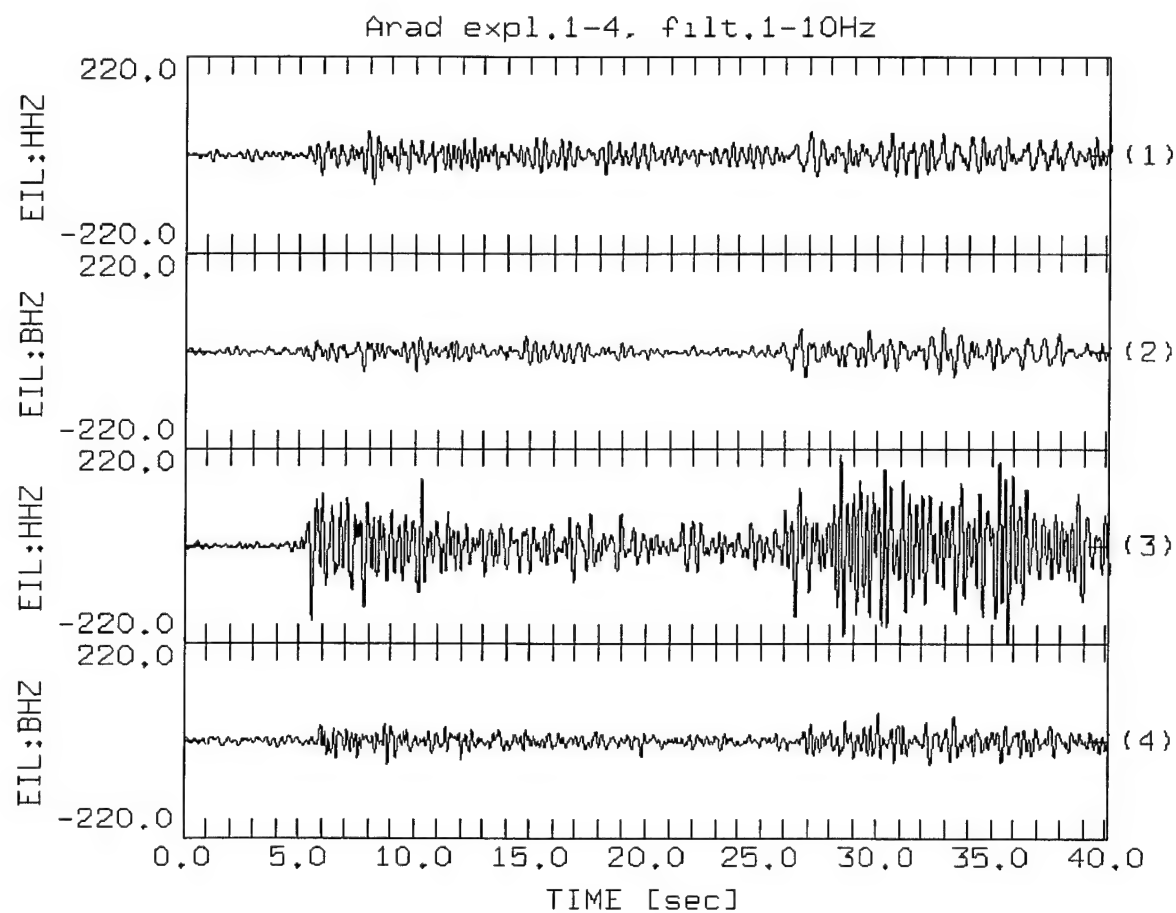


Figure 45. Comparison of amplitudes of the recorded blasts at the BB EIL station.

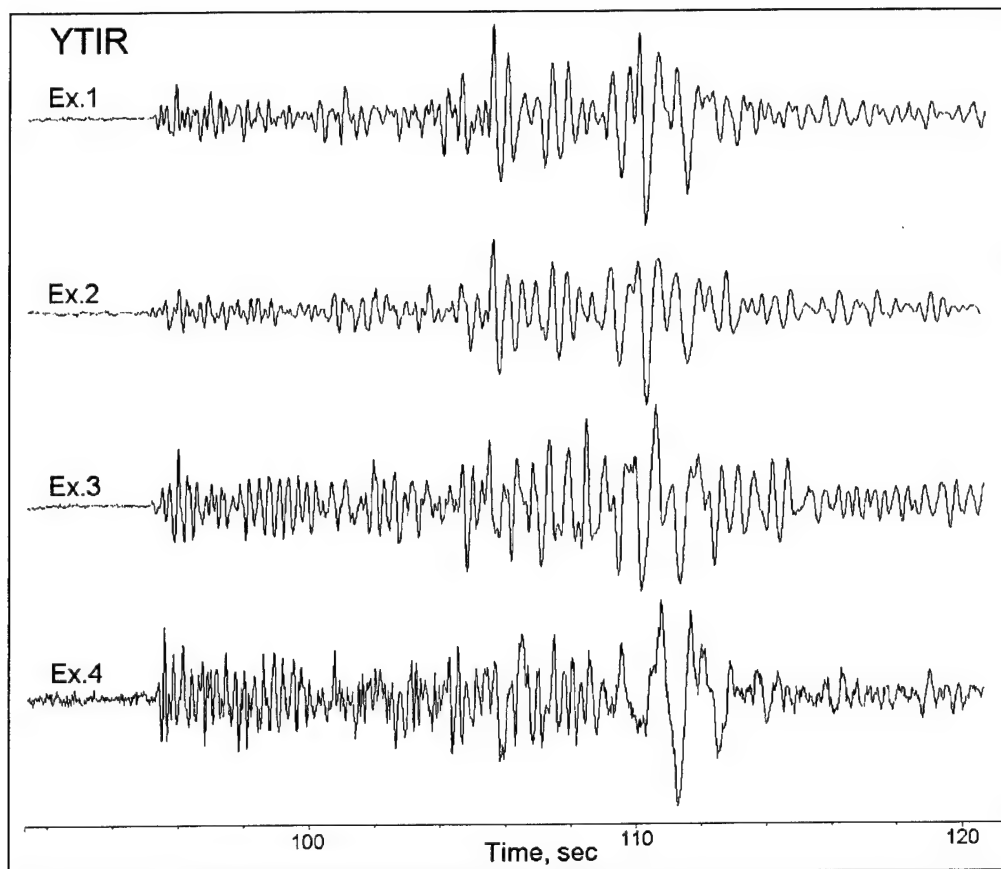


Figure 46. Comparison of waveform (normalized) at the short-period ISN station YTIR.

The results show rather low correlation, despite the fact that all the blasts were located in a small area of about 0.5 km radius. The highest correlation is between seismograms of Example 1 and Example 2, both having similar blast patterns and delays of 40 msec and spaced about 100 m apart. Example 3 and 4, with different delays and located a little further away (500 m), show very low correlation with Example 1, especially at distances greater than 100 km. Similar results were obtained recently by Stump et al. (1999) where regional waveforms from single-fired explosions in a single mine separated by a few kilometers, lost coherency above 1 Hz. All these observations suggest limited applicability of the correlation analysis method for identifying blasts from a large-scale mine (Harris, 1997), as well as the pattern recognition discrimination technique using a bank of master events (Joswig, 1990).

Spectral modulation. A characteristic feature of ripple-fired explosions is the spectral modulation in all wave phases (see Stump and Reinke, 1988, Chapman et al., 1992, Gitterman and van Eck, 1993). Availability of Ground Truth parameters for the quarry blasts analyzed and relatively simple blast patterns provide a good chance to check the correlation between blast parameters and seismic wave features. We also examine the correspondence between theoretical predictions, based on linear interference theory, and observations, for local mining practices and geological settings.

The main ripple-fired source features are explained by constructive (main maximum at f_m) and destructive (first spectral null at f_{01} and multiples f_{0k}) interference of seismic waves from inter-shots with millisecond delays, not by source finiteness in space or time, or total blast duration. For a regular blast pattern the frequencies depend on delays τ , and number of delays n (Gitterman, 1982, Gitterman and van Eck, 1993):

$$f_m = 1/\tau \quad (5.7)$$

$$f_{01} = 1/[(n+1) \times \tau] = f_m / (n+1); \quad f_{0k} = k \times f_{01}, \quad k = 1, 2, \dots, n \quad (5.8)$$

Any random variation of delay time or charge per delay, or any other non-regularity in the blast pattern or anelastic absorption of high-frequency energy with distance can distort, or even destroy, the spectral modulation features most significantly at high frequencies (greater than 10-15 Hz). The spectral null feature occurs at frequencies lower than the main maximum and so can be useful in identifying ripple-fired quarry blasts at regional distances. Based on numerous observations of quarry blasts in Israel and the simple theoretical analysis mentioned above, we found it better to analyze spectral modulation at low frequencies (<15 Hz) using smoothed spectra of the whole signal for several stations at different azimuths (Gitterman and van Eck, 1993). The advantage of the low-frequency approach is presented also in Hedlin (1998) and Carr and Garbin (1998).

Amplitude spectra of the whole signal (20-30 sec window) recorded at different SP and BB stations were smoothed in the 0.5-0.7 Hz window. The spectral shapes showed high coherency and clear modulation (except for Example 3 with small delays of 12 msec) for all stations, including the spectral null and main maximum features (Figures 47-50).

According to Equation (10), Example 4 with delays of $\tau=80$ msec should produce a main maximum at the frequency $f_m=12.5$ Hz. Spectral curves at different ISN stations, presented in Figure 47, show clear modulation and maximum at 14-15 Hz, highly coherent at different stations. From the average spectral curve we estimated value $f_m^*=14.6$ Hz. The maximum is rather strong, in spite of:

- a) non-regularity of the blast pattern (different number of hole charges in rows),
- b) strong attenuation of high-frequency seismic energy in the region ($Q=50-100$) due to widespread unconsolidated sediments in the upper crust,
- c) the restricted recording frequency band (0.5-12.5 Hz) at ISN stations.

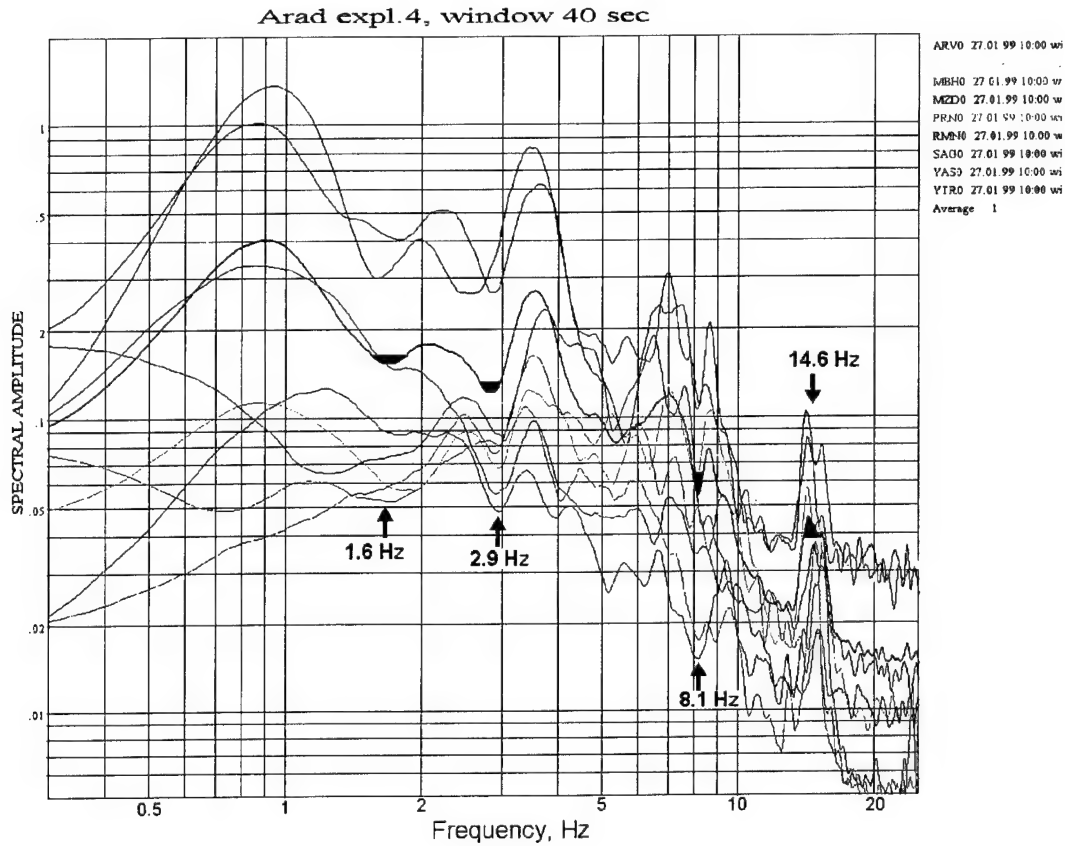


Figure 47. Spectral modulation and the main maximum feature for Ex.4 at ISN stations. The average spectral curve (thick line) is also shown.

This f_m measurement is the first observed for quarry blasts in the region, because existing mining practices in Israel and Jordan usually use delays of $\tau < 50$ msec. These delays produce main maxima at $f_m > 20$ Hz which cannot be observed at local seismic stations for reasons (b) and (c) mentioned above. In some geological settings such as crystalline shields, i.e., in the eastern USA, with low anelastic absorption, main maxima have been observed at frequencies up to 40 Hz (Kim et al., 1994).

The 2 Hz-shift of f_m from the theoretical value cannot be explained by a Doppler-like effect caused by the specific orientation of charge rows and azimuth to a station (Chapman et al., 1992), because the estimate f_m^* is obtained through averaging of several stations covering the whole azimuth range (see Figure 38). The most likely reason for the shift is well-known in mining practice, i.e., variability of delay systems where actual delays can differ from nominal values by 10-20%. Inverse calculations from Equation (10) give a reasonable value of the actual delay: $\tau^* = 1/f_m^* = 68.5$ msec (i.e., about 34 msec on average for a separate delay device was doubled for this explosion). Moreover, application of the measured delay for estimation of the first spectral null by Equation (11), results in a value of $f_{01}^* = 1/[(n+1) \times \tau^*] \approx 1.5$ Hz, which corresponds well to the observed minimum at this frequency on the average spectral curve (Figure 47), where the second (~ 2.9 Hz), and the fifth (~ 8.1 Hz) spectral nulls can also be identified.

In the case of Ex.1 ($\tau = 40$ msec, $n = 5$) a distinct first spectral null is observed for ISN stations at $f_{01}^* = 5.2$ Hz (Figure 48) as compared to the theoretical value of $f_{01} = 4.2$ Hz in Eq. (11). Supposing reduced (as in the case of Ex.4) delays, we estimated actual values $\tau^* = 1/[(n+1) \times f_{01}^*] \approx 32$ msec.

Broad band EIL records (sampling rate 80 Hz) from Example 1 were also analyzed. All three components showed the same low-frequency spectral modulation features (Figure 48b), and the spectra average corresponds well to the average based on ISN stations. The high-frequency modulation and the potential main maximum at $f_m \approx 25$ -30 Hz (which would be expected in seismograms filtered in the 0.5-40 Hz band). There is a steep descent in spectra above 10 Hz associated with local strong attenuation of high frequency energy of the signal. The modulation features for Example 2 were also observed in ISN records, but are less obvious than for Example 1 owing to the non-regularity of the blast pattern.

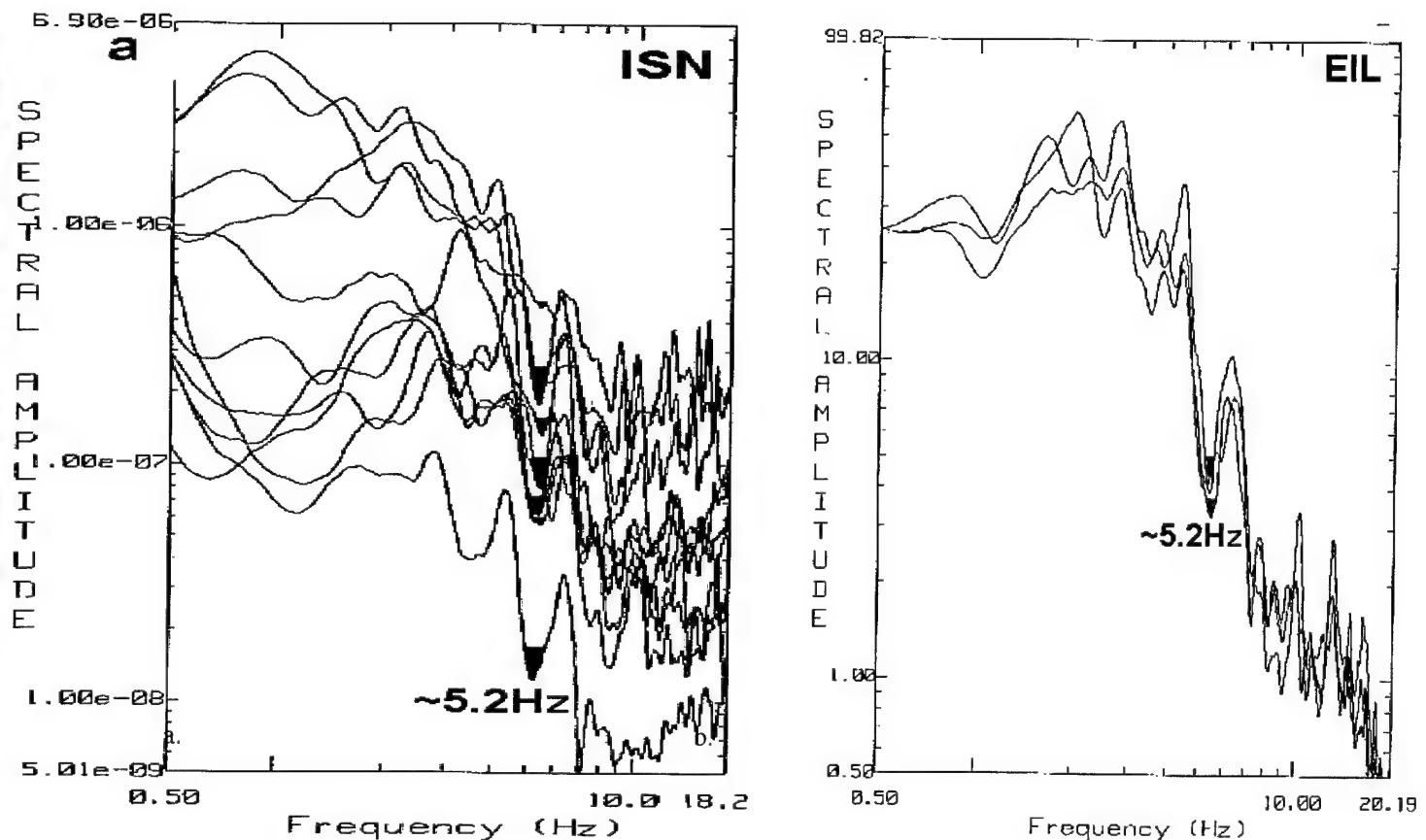


Figure 48. Spectral modulation and the first spectral null feature for Example 1 at ISN stations (a) and at BB EIL 3C station, band-pass filter 0.5-40 Hz (b).

Near-Field Observations. Strong motions of Example 2-4 were recorded by two A-800 accelerographs at distances of 200-500 m (Table 28). Example 3 and Example 4 yielded approximately equal horizontal Peak Ground Accelerations of 0.3g at about 360 m (Figure 49). At remote seismic stations, however, amplitudes and magnitude for Example 3 are much higher (see above). Analysis of the blast patterns and accelerograph locations showed that during Example 3, the PGA value was recorded at the free face of the quarry and away from the detonation sequence direction. During Example 4 the accelerometer was placed along the bench in an azimuth perpendicular to the detonation direction.

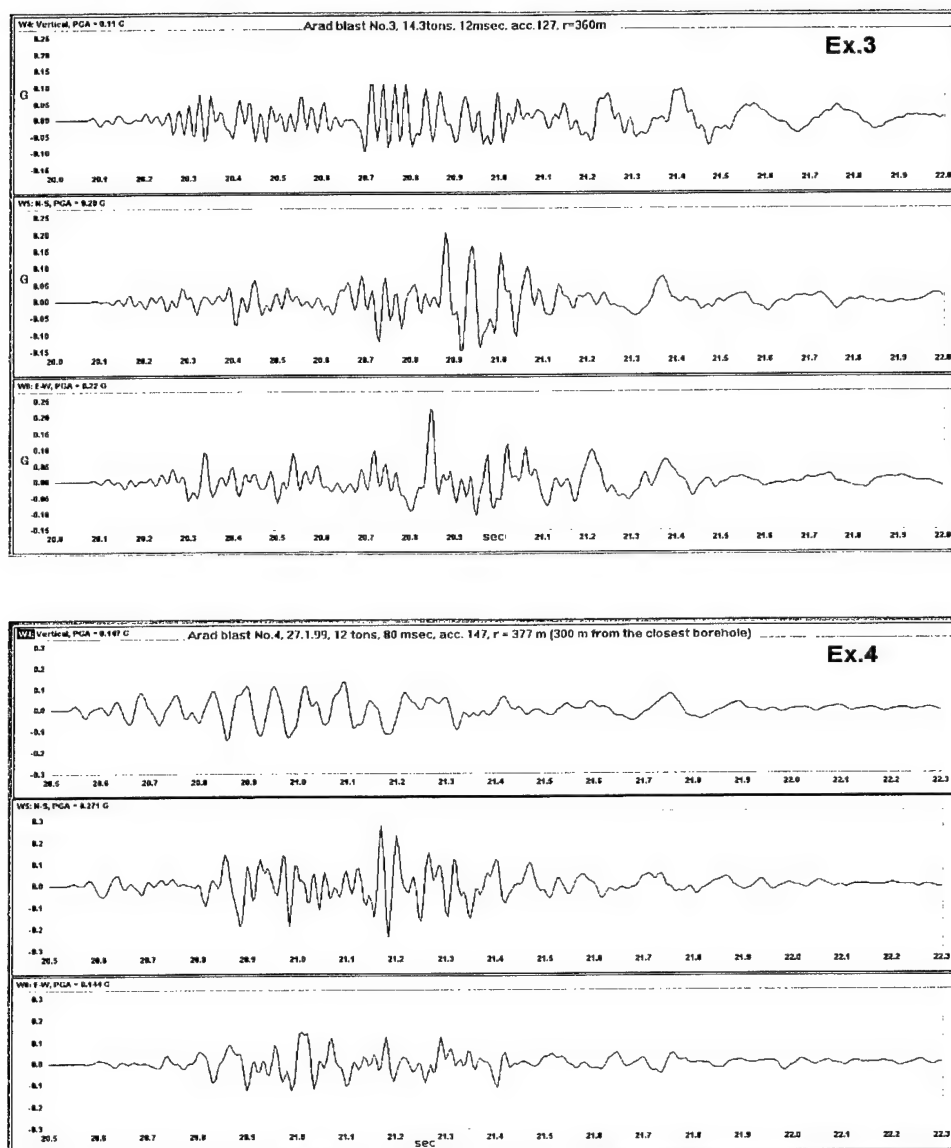


Figure 49. 3-component accelerograms of near-field observations of the blasts.

Accelerogram spectra demonstrated some high-frequency source features, which are not available in seismic station recordings with limited frequency band. Using accelerograms we can observe a main maximum $f_m \approx 26$ Hz for Ex.2 (Figure 49a) and multiple main maxima at about 30 Hz and 45 Hz for Example 4 (Figure 491b), which could not be found in the recordings of the ISN stations.

Table 28. Calibration and ground motion measurements by A-800 accelerometers during controlled quarry blasts.

Expl. No.	Acc No.	Comp.	Calibr. 2(max-min), counts	Dist. to init. point, m	PGA, g	PGA, cm/sec ²	PGV, cm/sec	PGD, cm
2	147	V	3822	340	0.0876	86.0 (85.6*)	0.563 (0.58*)	0.008 (0.01*)
		NS	3960		0.0736	72.2 (72.1*)	0.512 (0.56*)	0.0082 (0.008*)
		EW	4000		0.0873	85.6 (85.3*)	0.488 (0.51*)	0.0086 (0.012*)
3	127	V	4168	360	0.110	107.6	1.88	0.058
		NS	4128		0.200	198.7	2.03	0.056
		EW	4160		0.220	217.4	1.96	0.054
	147	V	4146	493	0.045	44.5	1.08	0.041
		NS	4130		0.079	60.8	1.54	0.044
		EW	4140		0.059	57.8	0.96	0.029
4	127	V	4180	207 (130**)	0.312	305.8	3.40	0.065
		NS	4120		0.392	384.8	4.90	0.073
		EW	4200		0.425	417.2	4.41	0.080
	147	V	4146	377 (300**)	0.147	144.1	2.36	0.055
		NS	4130		0.271	266.0	1.92	0.042
		EW	4140		0.144	141.5	2.09	0.046

* - measured by the SMA program for the 0.5 Hz corner frequency

** - distance to the closest borehole

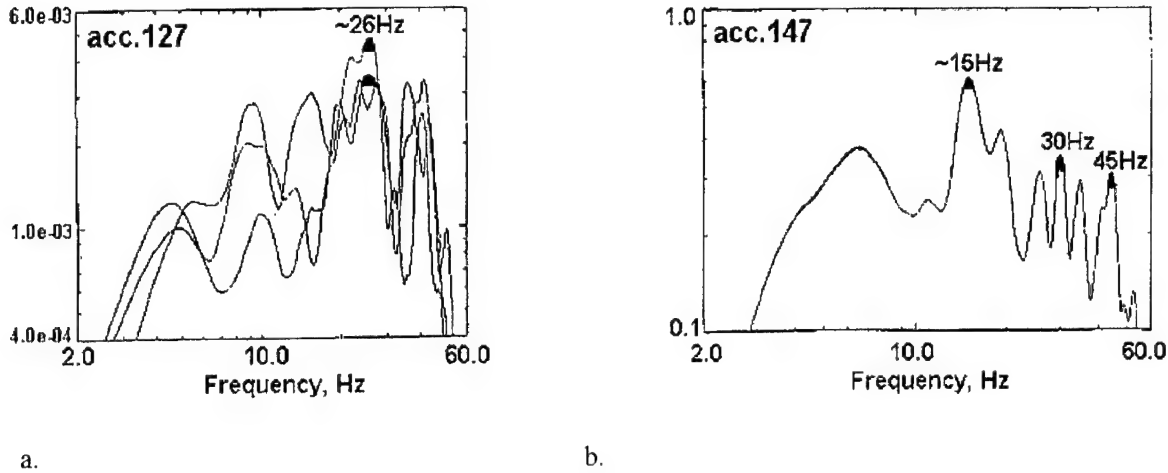


Figure 50. Spectral analysis of accelerograms: (a) spectra of three components for Example 2 ($r=340\text{m}$); (b) average over three components for Example 4 ($r=377\text{m}$).

Discrimination analysis. Multi-channel spectral discriminants, namely Energy Ratio and Semblance (Gitterman et al., 1996, Gitterman et al., 1998) were applied to amplitude spectra obtained in time windows containing the whole signal for the quarry blasts in Table 2.

The Ratios of seismic energy of low- (1-3 Hz) to high- (6-8 Hz) frequency bands are calculated for each single station (channel) and then averaged over several stations.

The Semblance statistic, commonly used in seismic prospecting for phase correlation of seismic traces in the time domain (e.g. Neidell and Taner, 1971), was modified to assess the coherency S_f of smoothed spectral shapes for different stations (channels) in a frequency band $[F_1, F_2]$ (for local distances 1-12 Hz):

$$S_f = \frac{1}{N} \sum_{F_1}^{F_2} \left[\sum_{k=1}^N (S_{ki} - \bar{S}_k) \right]^2 / \sum_{F_1}^{F_2} \sum_{k=1}^N (S_{ki} - \bar{S}_k)^2 \quad (5.9)$$

where $S_{ki} = \log_{10} S_k(f_i) - \log_{10}(\text{spectral amplitude at the } k\text{-th station})$, \bar{S}_k is the average spectral level and N is the number of used stations (channels).

For a given event, the discriminants were applied to a subset of ISN stations (covering a broad azimuth range) or to three components of a single BB (or short-period) station (see Table 29). In the case of the BB continuous recording with sampling 20 Hz the frequency band is restricted to 10 Hz, therefore the semblance was calculated in the range 1-10 Hz or 1-8 Hz.

Both multi- and single-station estimates verified the results previously obtained from the Galilee and Negev local data sets (Gitterman et al., 1996): the new quarry blasts also demonstrated higher values of energy ratio and spectral semblance than nearby earthquakes and corresponded to the explosion population. Relatively low energy ratios and semblance values for Example 4, estimated from ISN records, could be the result of suppression interference of low frequency energy due to large time delays.

We found that, for a given explosion, semblance estimates from a single 3C station are higher than those obtained from ISN stations. Such a relation is also found for earthquakes. For an earthquake from the Galilee dataset (April 15, 1994, 01:20, $M_L=2.4$), a multi-station ISN semblance estimate was 0.45 (see Gitterman et al., 1996), and for the single 3C ISN station ZNT we obtained a value of 0.776, still much lower than for explosions.

Table 29. Discrimination results for the controlled (calibration) ripple-fired quarry blasts.

Exp. No.	Seismic system	Energy ratio (1-3Hz)/(6-8Hz)	Semblance in range (1-12 Hz)	Number of stations (ISN), comments
1	ISN Vert.	41.0	0.89	11 (ATR, EIL, KER, MBH, MSH, MZDA, PRNI, RMNI, SAGI, YASH, YTIR)
	BB EIL 3C	56.3	0.98	trigger at 80 Hz, filter 0.5-40 Hz
2	ISN Vert.	63.3	0.81	11 (DRGI, ENGI, KER, MSH, PRNI, RMNI, RTMM, SVTA, SZAF, YTIR, ZFRI)
	BB EIL 3C	179.4	0.98 (1-10 Hz)	continuous recording at 20 Hz, filter 0.5-10 Hz
3	ISN Vert.	15.8	0.78	15 (ATR, DRGI, EIL, ENGI, HMDT, HRI, JVI, MSH, MZDA, PRNI, SAGI, SVTA, SZAF, YASH, ZFRI)
	BB EIL 3C	28.3	0.97	trigger at 80 Hz, filter 0.5-40 Hz
	BB MRNI 3C	10.3	0.90 (1-8 Hz)	continuous recording at 20 Hz, filter 0.5-10 Hz
4	ISN Vert.	5.6	0.64	9 (ARVI, DSI, MBH, MZDA, PRNI, RMN, SAGI, YASH, YTIR)
	BB EIL 3C	11.2	0.93 (1-8 Hz)	continuous recording at 20 Hz, filter 0.5-10 Hz
	BB MRNI 3C	3.9	0.89 (1-8 Hz)	continuous recording at 20 Hz, filter 0.5-10 Hz
5	ISN Vert.	3.89	0.86	11 (ATR, EIL, MBH, MSH, MZDA, PRNI, RMNI, SZAF, YASH, YTIR, ZFRI)
	BB EIL 3C	5.02	0.89	trigger at 80 Hz, filter 0.5-40 Hz

5.4.2 Waveform Characterization of Surface Single Explosions.

On-surface single explosions at the Sayerim site were recorded in the range 3 - 50 km by short-period portable stations, ISN stations, and the BB station EIL; the explosions at the Parran site were recorded by ISN stations in the range 12 - 180 km (see Table 3, Section 3.1). Sample seismograms are presented on Figures 51-53. Loudspeakers were used as acoustic sensors for registration of infrasound waves ("Barograph" channel on the figures).

Seismograms show relatively small P-wave amplitudes, compared with significant energy of S and S-coda waves (Figure 51-53). This effect is possibly explained by the specific seismic source of a contact (surface) explosion, like the vertical force. The only exception is the recording at station EIL, short-period (Figure 52) and broad-band (Figure 53), where strong P first motions are observed, as well as a low-frequency (~1 Hz) wavetrain of surface waves with a group velocity of about 1 km/sec.

Seismic signals are characterized by high-frequency content ($f > 3$ Hz) and, consequently, by strong attenuation with distance. This feature can be explained by the relatively small size of the surface seismic source in terms of the area where explosive energy is transferred to seismic energy. Most of explosion energy is released into the air, yielding shock (acoustic) waves, that are also registered on the seismic channels (Figure 51-52). In some cases the amplitudes of the acoustic waves on seismograms are much larger than amplitudes of seismic waves (Figure 52). The absence of an acoustic wave at EIL is explained by the sensor being inside a tunnel. A wavetrain preceding the acoustic wave is observed at some distant stations (i.e., at PRNI, Figure 52, denoted as a "seismo-acoustic wave"), possibly related to energy, propagating mostly through air, then transferred to the ground in the final portion of the path.

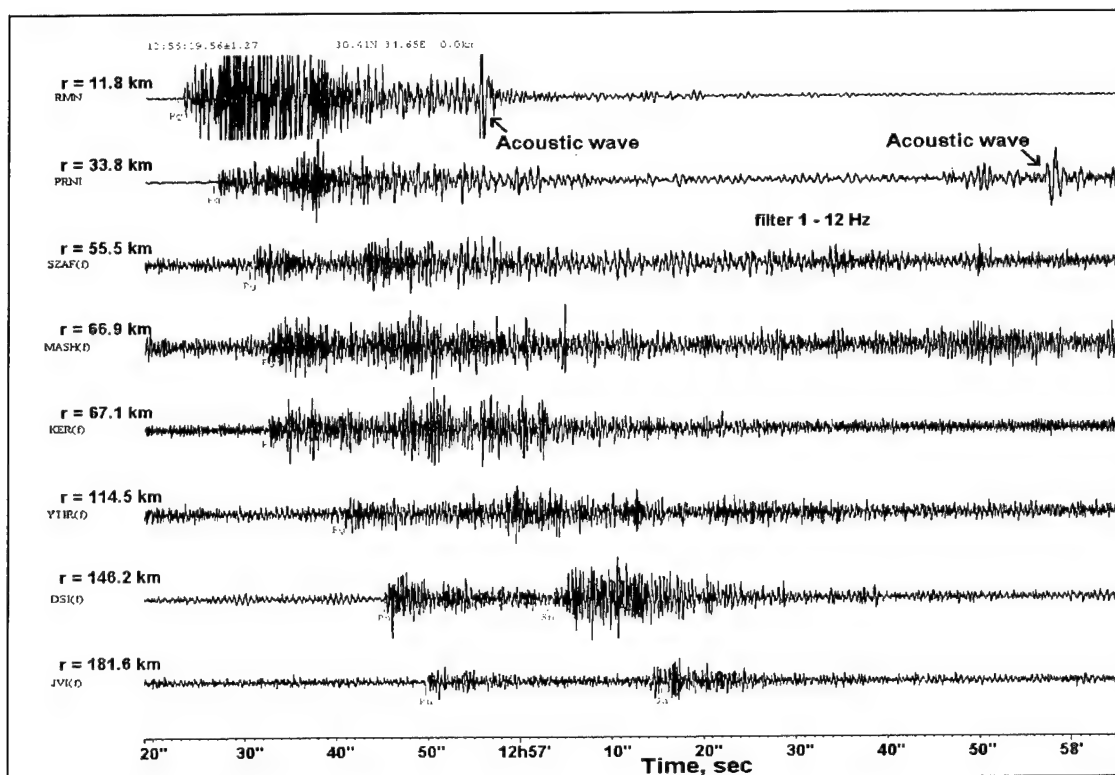
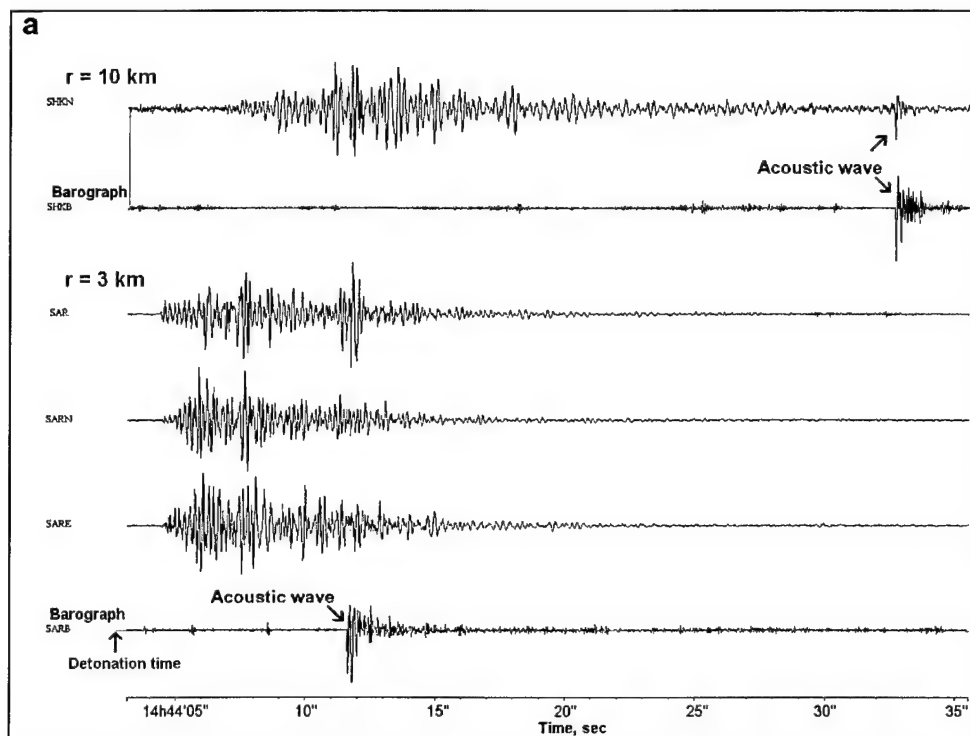
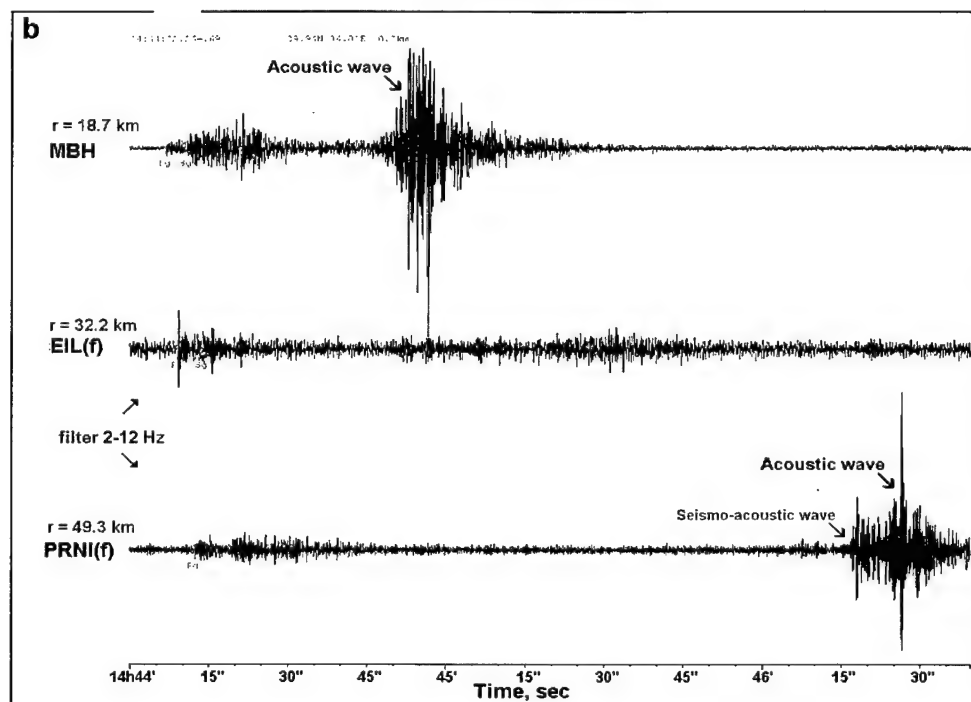


Figure 51. Seismograms of Example 16, recorded at ISN stations.

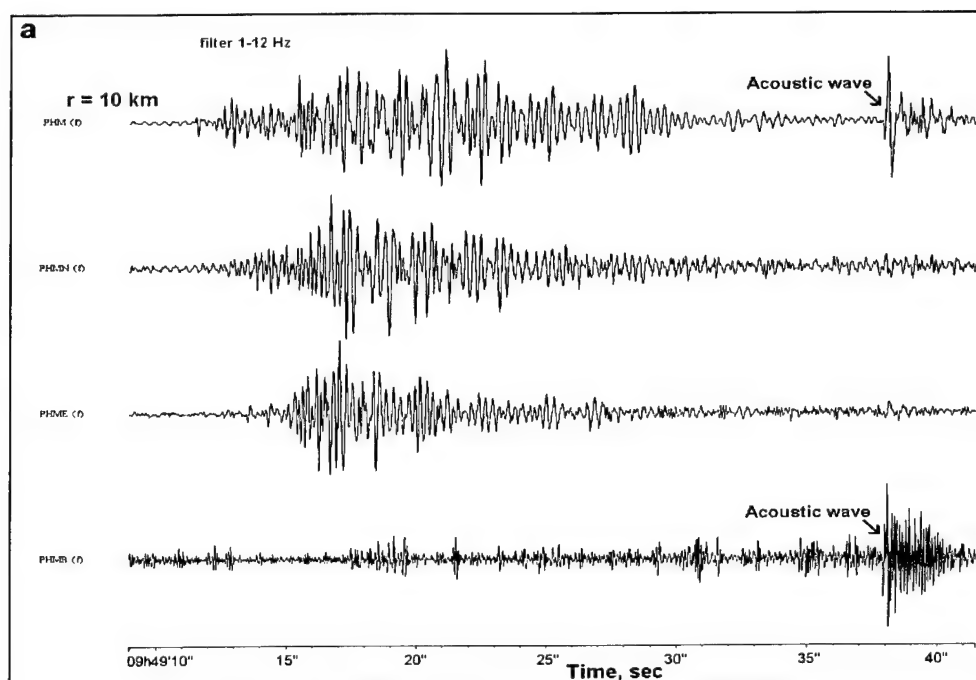


a. Portable stations

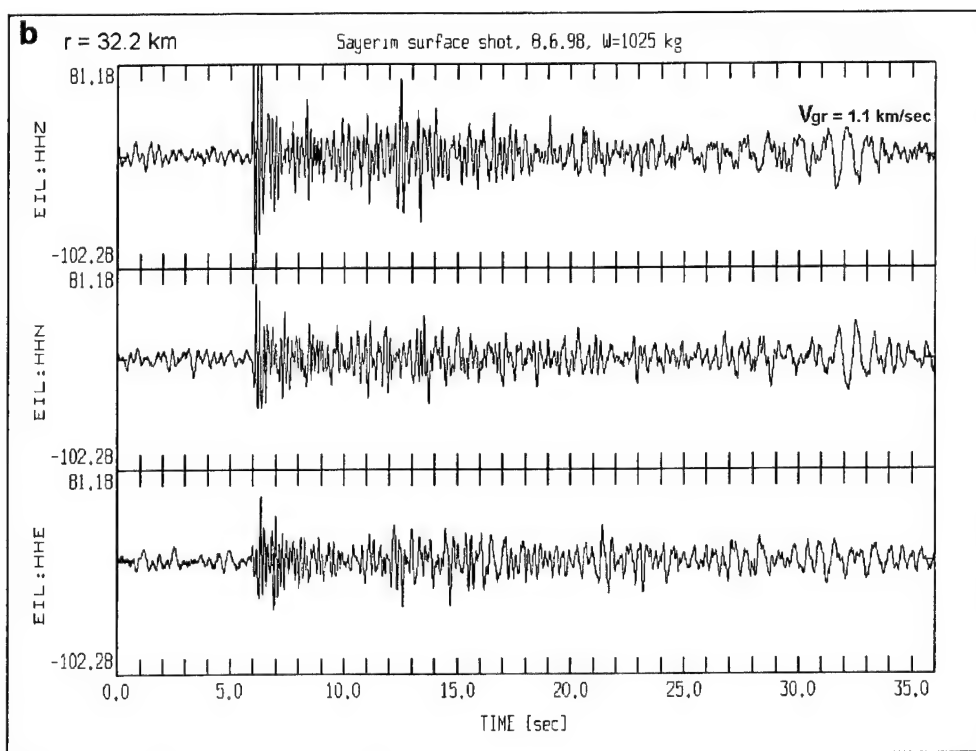


b. ISN stations

Figure 52. Seismograms of Example 3.



a. Portable stations



b. BB EIL station

Figure 53. Seismograms of Example 13.

5.4.3 Spectral features and discrimination analysis for recent nuclear tests, recorded by Israel stations.

We analyzed seismograms from the recent nuclear tests in India and Pakistan (see Sections 3.1.4, 5.1), observed by the short period ISN stations and broad band stations EIL, MRNI and JER. In order to provide a discrimination analysis we added several recordings of earthquakes occurring near the explosion sites in Pakistan (see Table 24, Figures 27-28 and Figure 54).

Spectral null feature. We calculated P-wave spectra from seismograms (after removing instrument response) of the test on May 28, 1998, the only one that triggered short-period ISN stations (see Figures 28 and 54). All spectra were computed using a ~15 sec time window at vertical recordings, including P and P-coda waves, and smoothed by a 0.5 Hz triangular window (Figure 55).

The spectra at all stations showed a pronounced coherent spectral minimum (null) at about 1.7 Hz, which may be interpreted as interference of P and pP phases, possibly complicated by non-linear surface effects, like spall (Lay, 1991). Kulhanek (1971) reported similar observations of 1 Hz spectral nulls for Nevada nuclear tests, interpreted as an interference effect. The relatively high null frequency of 1.7 Hz possibly corresponds to the reported shallow depth of the test, placed in a horizontal shaft of a steep mountain (Wallace, 1998), compared with deeper Nevada tests. The same 1.7 Hz coherent spectral null was also observed on all three components of the BB EIL station for the May 28 explosion, but not for the Indian test. The same spectral analysis was done for a nearby earthquake in Pakistan with similar magnitude and waveforms (Figure 54).

The earthquake spectra (Figure 55b) obtained at the same short-period stations do not show coherent nulls (similarly spectra at BB EIL), thus rejecting site-effect as an explanation. Wallace (1998) notes much more complex waveforms for the May 28 Pakistan test than for the Indian explosion (see also Figure 29), possibly explained by wave scattering from the complex topography in the test region.

Nevertheless, Gitterman et al. (1999), based on ISN observations of Semipalatinsk (STS) and Chinese nuclear tests and nearby earthquakes, showed that this spectral null feature, considered separately, cannot serve as a reliable identification characteristic of nuclear explosions, due to its non-stability over the whole nuclear test population, and its presence in recordings of some earthquakes.

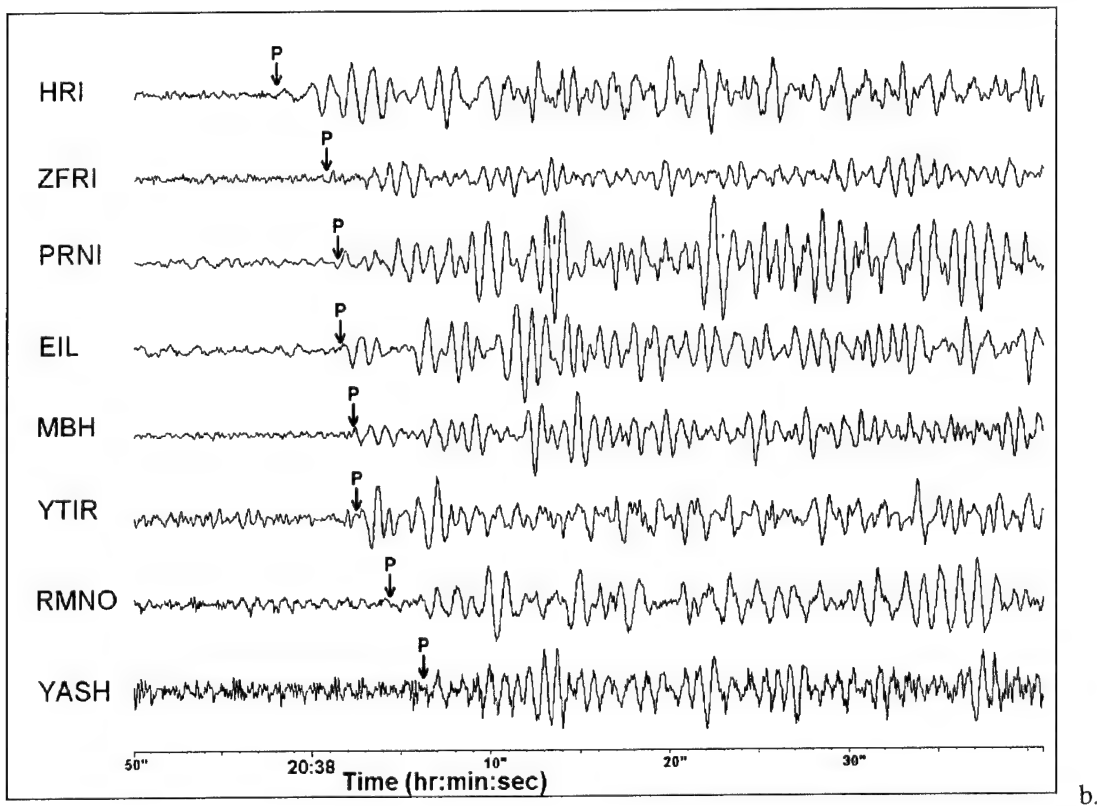
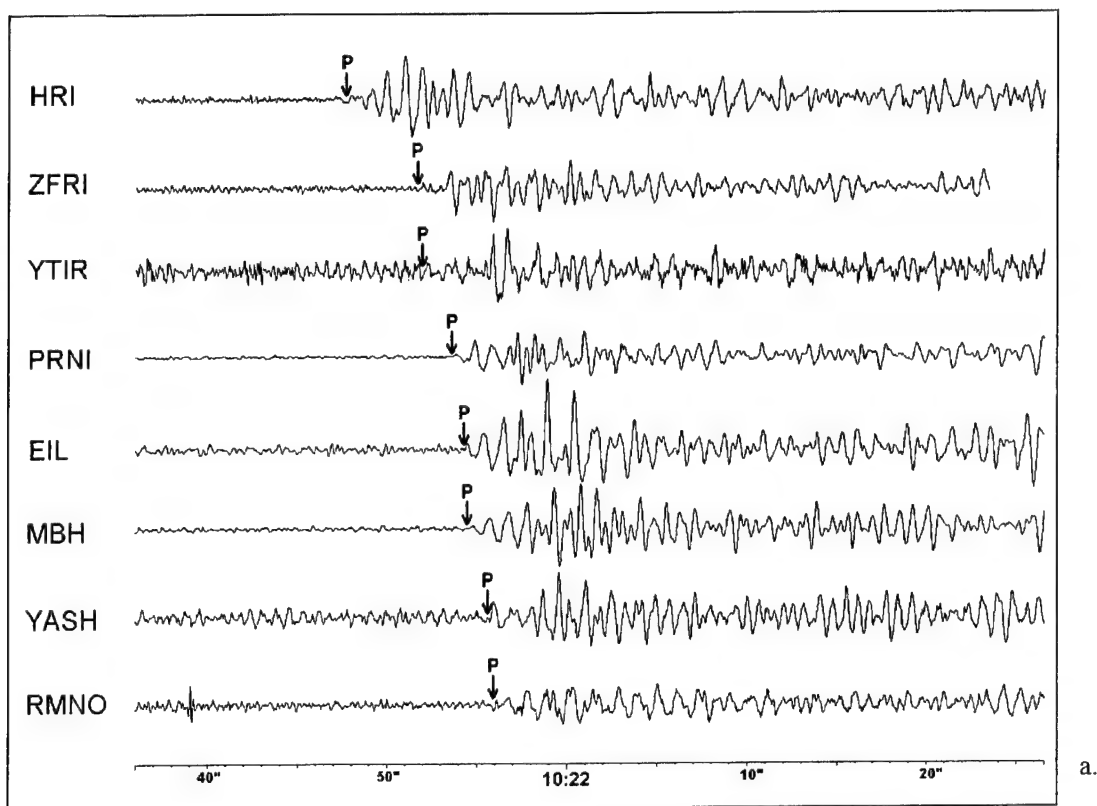


Figure 54. Sample seismograms of different types of seismic events: short-period vertical records of the first Pakistan test (28.5.98) (a), and the same day nearby earthquake in Pakistan (b).

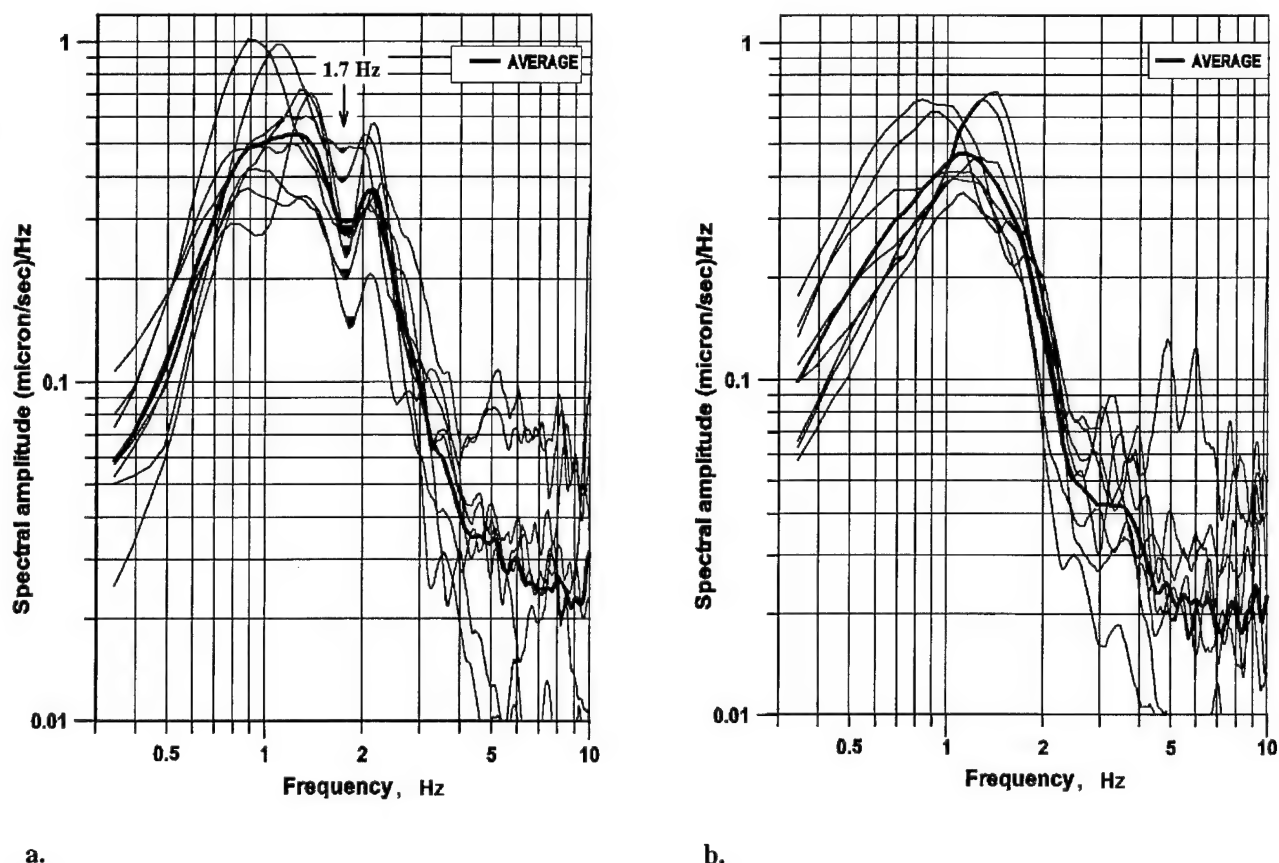


Figure 55. Spectra of the first Pakistan test, observed at short period stations, showing a spectral null source feature at 1.7 Hz (a), compared with the same day nearby Pakistan earthquake of a similar magnitude (b).

Spectral discrimination. Taylor and Marshall (1991) applied spectral ratios for discrimination between Soviet (STS) nuclear tests and earthquakes, recorded at the United Kingdom short-period teleseismic arrays. Using 5 sec windows including P-waves, the spectral ratios from an array beam in the 0.5-1 Hz and 2-3 Hz frequency bands provided the best discrimination performance. It was concluded that the explosions are characterized by more high-frequency energy (resulting in lower spectral ratios), than shallow Central Asia earthquakes.

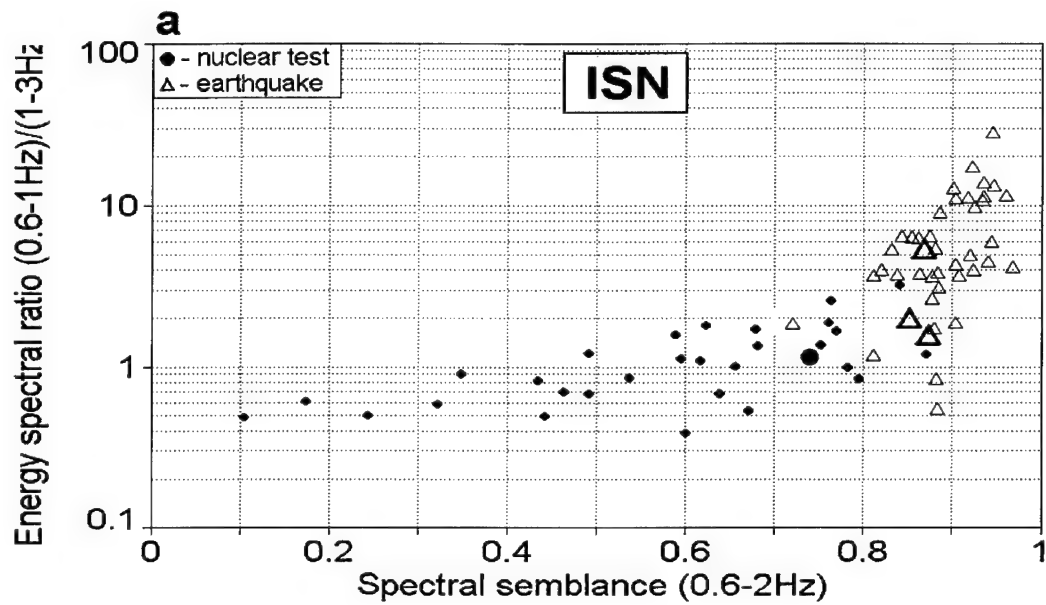
Similar results were obtained by Gitterman et al. (1999), using slightly different processing parameters, with higher ratios (low-to-high frequency energy) for teleseismic earthquakes, compared to nuclear explosions. The database included tests from STS, Novaya Zemlya and Lop Nor (China), recorded by the short-period Israel Seismic Network. A 15 sec window, comprising P- and P-coda waves, was selected for computation of spectral ratios of energy in low- (0.6-1 Hz) and high- (1-3 Hz) frequency ranges, providing the best performance. This study included the application to the same spectra of the spectral semblance discriminant (see Section 5.3.1). The network-based spectral semblance estimates showed higher coherency for teleseismic earthquakes than for nuclear explosions (Gitterman et al., 1999).

For the selected recent events in Table 24, the two discrimination statistics were estimated for a sub-set of 9 short-period vertical ISN stations (shown in Figure 28), and also for three components (channels) of the EIL broad band station; the ratios were then averaged for a given event over the stations, or over the three BB components. The second Pakistan nuclear test did not trigger the short-period and broad band stations. Both signals on the 20 Hz continuous recording are weak and comparable with the noise level (see Figure 29), therefore the spectral ratio and semblance were not calculated for this event.

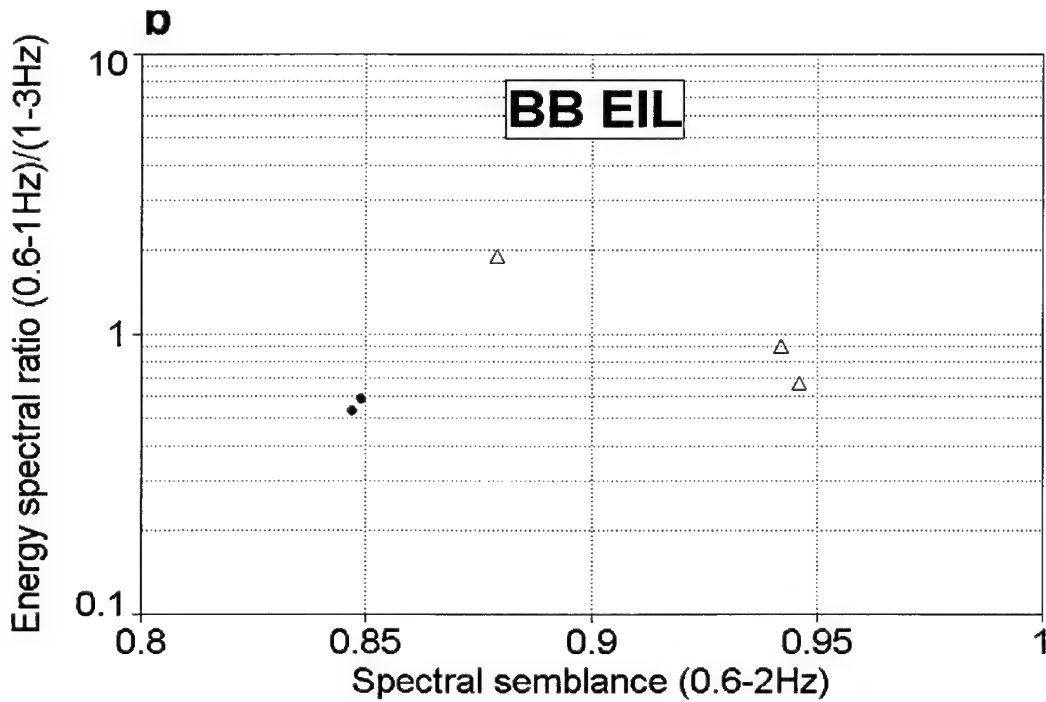
Both multi- and single-station estimates agree with the successful discrimination results obtained for the former Semipalatinsk and Chinese nuclear tests (Gitterman et al., 1999). The new nuclear tests also demonstrate lower values of energy ratio and spectral semblance than nearby earthquakes (Table 30, Figure 54). The waves analyzed (P and P-coda) of teleseismic earthquakes have relatively more low-frequency energy as predicted from source physics phenomena and more coherent spectral shapes than nuclear explosions. The short-period explosion signals (including scattered waves in the P-coda) are more influenced by inhomogeneities in the upper crust beneath the ISN stations, with varying site structure, thus leading to a decrease of spectra coherency and associated semblance values. The results show that both types of the discriminants, using the short period (Figure 56a) or broad band records (Figure 56b), provide reliable separation of nuclear explosions and earthquakes.

Table 30. Average spectral discrimination results for India and Pakistan tests based on ISN and BB EIL station records.

No	Date	energy ratio (0.6-1)/(1-3Hz)		semblance (0.6-2Hz)		Region, event
		ISN	EIL	ISN	EIL	
1	97/12/04	1.98	0.903	0.840	0.942	Pakistan earthquake
2	98/01/05	5.39	1.890	0.876	0.879	Pakistan earthquake
3	98/05/11	-	0.532	-	0.847	India nuclear test
4	98/05/28	1.248	0.588	0.737	0.849	Pakistan nuclear test
5	98/05/28	1.591	0.666	0.866	0.946	Pakistan earthquake



a.



b.

Figure 56. Application of semblance and energy ratio discriminants to the recent nuclear tests and nearby earthquakes: (a) multi-station ISN estimates (large symbols), compared with the results for old Eurasian events (small symbols) (Gitterman et al., 1999); (b) single-station, three component estimates for the EIL BB station.

5.5. Conclusions and Recommendations.

1. We investigated detectability at the two IMS auxiliary stations EIL and MRNI, and the cooperating station JER, using 20 Hz recordings sampled at 20 Hz of the Indian ($m_b=5.2$) and the two Pakistan nuclear tests ($m_b=4.6, 4.8$). In addition the detection of the Kazakh chemical test ($m_b=3.7$) was tested. Three detection procedures were compared: STA/LTA, Murdock-Hutt and Adaptive Statistically Optimal Detector (SOD). All nuclear tests were detected at EIL, while at MRNI we succeeded only with the first Pakistan NT, and at JER with the second one. Station detectability is determined by the maximum frequency dependant SNR, therefore the SOD proved to be the most efficient procedure due to more accurate adaptation to ambient noise spectra.

We cannot state detection of the Kazakh explosion at EIL with certainty, whereas it was clearly observed at IMS stations NOA (37.7°) and ILAR (60.6°). The EIL detectability may be due to unfavorable propagation conditions for the Asian events, approximated by the magnitude threshold $m_b=4.0-4.5$, within $25^\circ-38^\circ$ distance range. The magnitude threshold for MRNI and JER should be higher for similar events.

The case of the second Pakistan test simulates to a degree the scenario of a clandestine test masked by two other events: a strong earthquake in Afghanistan and a local earthquake near EIL. In spite of poor SNR the explosion signal was detected by the SOD at both IMS stations EIL and MRNI.

For these tests and nearby earthquakes we observed consistent delays of P-arrivals of about 4 sec relative to the IASPEI91 model at the EIL stations. Slightly smaller delays of about 3.7 seconds in average were found for old STS explosions recorded at the ISN station MBH situated a short distance from EIL. The similar residuals for MBH imply that only a few tenths of this effect are site related. P-arrival lags of 3.5-4 sec were also observed for the IMS station MRNI and the BB station JER. The similar delays at different stations indicate a path- rather than site-effect.

The results obtained will contribute to calibration of the IMS auxiliary stations EIL and MRNI regarding Asian seismic events. Events from Africa, Europe and other areas may have different station corrections relative to IASPEI91 and this should be checked when Ground Truth events from these areas become available at Israel stations.

2. Direct improvements in detectability of the ISN were obtained by application of the Statistically Optimal Detector technique compared with the STA/LTA algorithm. The SOD technique applied to the beams of the ISN subarrays enhanced the probability of true detection by a factor of 1.2-2 depending on magnitude and the subnetwork chosen.

3. A new automatic location method, based on a combination of the optimal statistical time series analysis and robust statistical phase identification, was designed. The method was applied to GT0 calibration explosions in the Dead Sea and the Arad quarry, and more than 60 GT5 earthquakes, demonstrating high performance.

4. Low waveform correlation observed for controlled blasts from the same quarry suggests limited applicability of the correlation analysis method for identifying blasts from a specific mine, as well as for the pattern recognition discrimination technique using a bank of master events.

Spectral modulation features (spectral nulls, maxima) were examined based on Ground Truth information for the quarry blasts. In some cases actual blast design parameter values (time delays) were derived from the spectral analysis. The theoretical predictions, based on linear interference theory, were confirmed for local mining practices and geological settings.

Some specific waveform features were observed for surface explosions: high-frequency content and strong attenuation with distance, strong acoustic waves and preceding seismo-acoustic waves recorded on seismic channels.

5. The spectra of the first Pakistan nuclear test showed a pronounced spectral null at 1.7 Hz for all three components of the broad band EIL station, as well as at the vertical component of the short period ISN stations. For this ground truth explosion with a reported shallow source depth (Wallace, 1998), the interference of P and pP phases seems the most reasonable explanation for this phenomenon. Other possible reasons, namely the spallation process (Lay, 1991) and wave scattering from the complex topography in the source zone, also relate to surface effects from very shallow seismic events, i.e., explosions.

However, the spectral null feature, considered separately, cannot serve as a reliable identification characteristic of nuclear explosions, because not all tests produce the nulls, whereas some earthquakes show this effect. Multi-channel spectral discrimination analysis, based on the spectral ratio of low-to-high frequency energy and semblance of spectral curves, provided reliable discrimination between the recent NT and several nearby Pakistan earthquakes. The results were in agreement with previous analyses of Soviet and Chinese NT recorded at seismic stations in Israel, where nuclear tests demonstrated lower values of energy ratio and spectral semblance than earthquakes (Gitterman et al., 1999).

It should be noted, that both spectral discriminants were originally successfully applied to small local quarry blasts, underwater explosions, and earthquakes (Gitterman et al., 1998), where the semblance (in the 1-12 Hz band) and the ratio (for 1-3 Hz and 6-8 Hz bands) showed higher values for explosions, contrary to the teleseismic case. The higher ratio is explained by path effects due to local geological settings (thick soft sediments). The higher semblance is related to specific source features of quarry blasts (ripple-firing) and underwater explosions (bubble pulse), producing azimuth-independent spectral modulation, as against earthquakes having less spectral similarity (at local distances) due to radiation pattern and directivity effects.

The spectral discriminants applied to the new quarry blasts also showed high performance - both multi-station statistics (calculated for a subset of ISN stations) and single-station estimates (calculated for three components of a single BB or short-period station).

The spectral energy ratio is similar to the $M_s:m_b$ discriminant used by the IDC for event screening, but can be applied (as well as the spectral semblance) to small local events where $M_s:m_b$ technique is not possible; whereas for teleseismic events the spectral discriminants can provide an additional independent check.

Section 6

Task 4 Field Experiments: Land Explosions.

6.1 Collection of Detailed Information about Mining Practices and Blasting Patterns in Israeli Quarries.

Four quarry blasts at the Arad phosphate quarry were conducted under our control; the summary of the explosion parameters is presented in Table 2, Section 3.1.1). The explosions were located a few hundred meters apart, Example 3 and 4 were adjacent at the same bench.

Routine blasts at this quarry (and at other Israel quarries) are usually conducted with 40 msec delays between rows of holes, as in the case of Example 1 and 2. At our request, two other explosions were conducted with blast patterns different from routine techniques, i.e., with smaller (12 msec for Ex.3) and larger (80 msec, consisting of two 40 msec devices, for Ex.4) time delays. Special efforts had to be made to obtain permission to decrease time delays in a ripple-fired blast from a routine value 40 msec to 12 msec, providing a stronger seismic effect. These delay values are nominal. As discussed before (Section 5.3.1), spectral analysis of seismograms showed that actual quantities were lower ($\sim 15\%$). In the case of Ex.3&4 Nonel PETN down-hole delays of 500 msec were used, which can introduce an additional ± 3.5 msec scatter in the delay times between rows (Rohay, 1999). Seismic efficiency for the quarry blasts as magnitude (amplitude) dependence on blast pattern parameters is discussed in Section 5.3.1.

Sample photos of the field work and detonation moments are presented in Figures 57-59.



Figure 57. Field measurements at the Arad quarry.

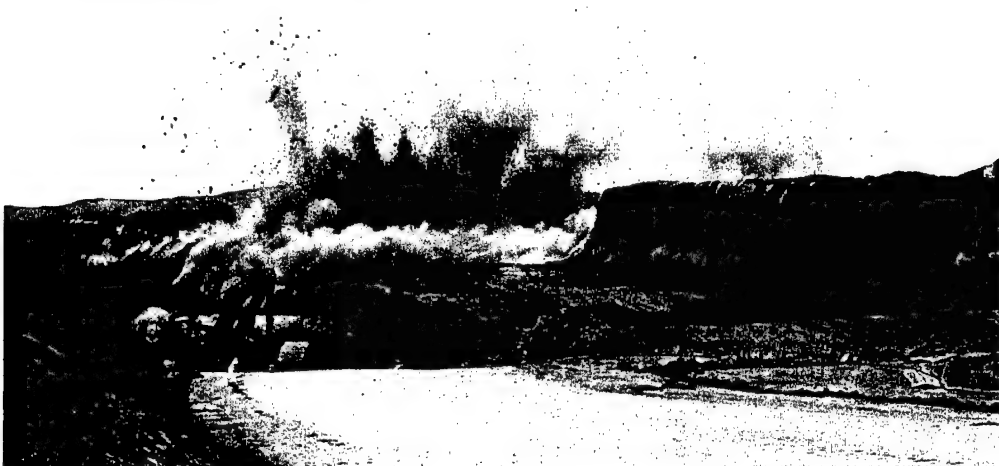


Figure 58. Detonation of Example 3 on 26.01.1999.



Figure 59. Detonation of Example 4 on 27.01.1999

6.2 Measurements of Ground Truth Data (Location and Origin Time).

A PC-based System Data Acquisition (SDA) was designed, including a zero time recording unit, combined with the GPS system, transducers for telemetric data communication, and analog/digital converter. The system provides accurate measurements of GMT time of the Origin Time and coordinates of an explosion. The small seismic sensor connected to the zero time recording channel, was located in 2-3 m away from the borehole initiated first, so the Origin Time relates to the detonation moment of this borehole charge (see an example in Figure 60).

The equipment for field seismic measurements was calibrated and tested during field recording of a joint Israel/US series of experimental explosions at the Sayerim site north of Eilat (see Sections 2.1.2 and 4.3.2). Coordinates of the explosions were accurately measured by GPS system, and for most explosions we obtained exact origin times by the zero time recording channel of the PC-SDA.

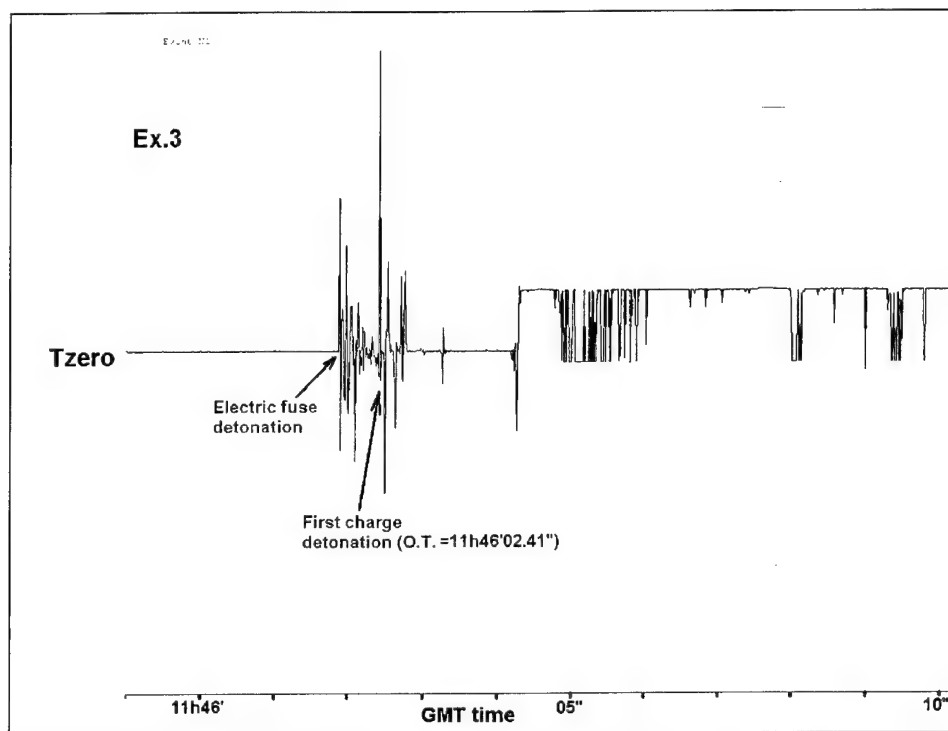


Figure 60. Measurement of Origin Time for Example 3. Time interval about 0.5 sec between the electric fuse detonation and the first borehole charge detonation corresponds to the down-hole delays of 500 msec used for this explosion.

Section 7

Task 4 Dead Sea Calibration Experiment.

7.1 Introduction.

A unique seismic and hydro-acoustic experiment involving large-scale underwater chemical explosions was conducted in the Dead Sea during November 8-11, 1999, thanks to its rare, unequalled setting. The collaborative efforts of several bodies provided this creative, cost-efficient venture, improving monitoring and verification of the Comprehensive Test Ban Treaty (CTBT) in the Middle East. The explosions were carried out by the Seismology Division of the Geophysical Institute of Israel (GII). This experiment is part of the project research to provide calibration sources lacking in the region.

The goals of the experiment were to calibrate the regional travel times and propagation paths of seismic waves across the Middle East and the Eastern Mediterranean region and thus improve location accuracy of seismic events; to calibrate local, regional and International Monitoring System (IMS) stations; and to provide data for source characterization to improve IMS detection, location and discrimination capabilities.

Based on a series of small-scale underwater shots in 1993 (Gitterman et al., 1998), it was estimated that a 5-ton explosion would correspond to an event of magnitude about 4.0 on the local Richter scale. It was expected that events of this order of magnitude would be recorded by seismic stations at local and regional distances, i.e., within 20° from the Dead Sea.

Apart from the well-known enhancement effect of underwater explosions, the lack of fish, etc. of the Dead Sea was one of main reasons for this choice of site. Moreover, the unique properties of super-saline Dead Sea water (density 1.236 gr/cm³ and acoustic velocity 1770.6 m/sec. (Anati, 1997), much higher than in the ocean) further enhance the seismic effect of an underwater explosion.

Although there is no aquatic life in the Dead Sea, it is unique with its many natural phenomena such as mineral springs, desert oasis, wild life reservations, etc., nearby. The explosion point was located a few kilometers from local spas, settlements and an important engineering installation, the Dead Sea Works dam. Consequently all safety conditions were analyzed and defined before the experiment took place and presented in the Safety Report (Gitterman and Shapira, 1999). In addition, in response to inquiries by the Israel Ministry for the Environment, an independent report was prepared by the Geological Survey of Israel regarding the potential environmental impact of the planned explosions (Abelson, 1999). The Safety Report showed no hazard to the people, property and local environment (fully confirmed after the shots). However, in order to verify the assumptions upon which the safety analysis is based, GII began the experiment by detonating 0.5-ton and 2-ton explosions prior to the main 5-ton shot.

7.2 Preliminary Test Small Explosions.

Five small (25 kg) detonations were conducted on October 28-29, 1999 in the Dead Sea (~150 m south the planned site of the large explosions). at depths 70-100 m, to test different procedures and provide necessary data for the main series of explosions.

The main goals of this experiment were:

- a) to conduct a small explosion under conditions similar to the planned large calibration shots;
- b) to select the explosives and detonation method to be used during the main shot series.

During the test explosions we planned to check:

- 1) the effectiveness at different depths (70-100 m) of the explosives “henamon” (ANFO -like) and two detonation techniques: electric fuse and detonation cord;
- 2) procedures for determining the GPS zero time of the explosions with the PC data acquisition system and GPS coordinates by different devices (GARMIN-II and Magellan);
- 3) recording hydroacoustic waves, using two Geospace hydrophones submerged near the boat;
- 4) measuring ground motions using a 3C seismometer station at the closest seashore site (near a jetty) to be used for verification of our safety estimates of peak seismic amplitudes.

Two Geospace hydrophones were placed near the ship “Lot’s Wife” which was the base for all sea operations, including the deployment of systems for measuring the origin time and coordinates using GPS systems. A third hydrophone was placed near the jetty at a water depth of about 1.5 m. Two short-period (SP) Mark Products L4C seismometers (vertical and radial) were deployed on shore, a few meters from the water line. The sampling rate for both PC-based data acquisition systems (ship and jetty) was 500 sps.

Parameters of the detonations are presented in Table 31. Thus, only two out of five attempts were successful, producing seismic signals, which were strong enough to cause triggering of the Israel Seismic Network.

Results of seismic measurements and analysis of recordings of two successful explosions are presented in Tables 32-33. Measured peak amplitudes and estimated local magnitudes are compared with values estimated from the empirical relationships developed beforehand (Gitterman, 1998).

Table 31. Design parameters and details of the test explosions (31.536N, 35.444E).

#	Date	Measured Origin Time (GMT)	Depth m	Charge design and initiation method	Work of charge components		
					Electric Fuses (EF)	Doubled Detonation Cord (DC)	Accelerator and Main Explos. (ME)
1t	28.10	14:30:01.7	100	EF inside an explosive accelerator (EA)	exploded	absent	not exploded
2t	28.10	15:20:01.6	100	EF inside EA	exploded	absent	not exploded
3t	29.10	09:35:01.47	70	EF attached to DC on the depth near the charge, DC inside ME	exploded	exploded	exploded
4t	29.10	10:45:01.37	100	EF attached to DC on the depth near the charge, DC inside ME	exploded	a surface part exploded	not exploded
5t	29.10	11:55:01.84	70	EF attached to DC on the water surface, DC inside ME	exploded	exploded	exploded

Table 32. Comparison of predicted and observed Peak Ground Velocity for the two test underwater explosions in the Dead Sea, W = 25 kg, H = 70 m, October 29, 1999.

Station	Dis- tance, km	Exp.#	Peak amplitude, micron/sec					Comments
			Measured			Estimated (vertical component)		
			Horiz.		Vertic.	Average curve	Maximum (upper limit level)	
			NS	EW				
SP Jetty	9	3t	46.0 (Rad.)		29.4	15.6	81.2	PGV measured by the program SEIS in the UNIX workstation seis1
SP DRGI	7.9	3t	-		45.4	18.5	96.1	
		5t	-		41.7			
SP ENGI	8.7	3t	-		42.6	16.3	84.8	
		5t	-		31.3			
SP MZDA	26.5	3t	2.6	3.4	2.6	3.8	19.9	
		5t	1.8	2.8	2.1			
SP YTR0	36.3	3t	-		3.9	2.6	13.2	
		5t	-		3.4			
BB JER	35.0	3t	0.86	1.52	0.93	2.7	13.9	Filter 1-10Hz
		5t	0.70	1.09	0.78			
BB MRNI	163.7	3t	0.38	0.30	0.18	0.36	1.87	
		5t	0.28	0.21	0.16			
BB EIL	211.0	3t	0.028	0.027	0.036	0.26	1.34	Filter 2-10Hz
		5t	0.018	0.022	0.027			

Table 33. Comparison of predicted and observed local magnitudes and fundamental frequencies of the two underwater explosions in the Dead Sea, W = 25 kg, H = 70 m, October 29, 1999.

#	Local magnitude M_L		Bubble frequency f_b , Hz	
	estimated	measured	Theory, for the normal barometric pressure	Measured average (ISN spectra maxima)
3t	1.7	1.9	7.3*	6.5
5t		1.7		6.5

Figure 62 shows a classic shock wave recorded by hydrophones near the ship from Example 1 when only electric fuses were exploded. Recordings by seismometers on the shore and the jetty hydrophone of the successful Example 3 are presented on Figure 63.

Results of the test explosions and conclusions:

a) Explosion technique.

- Electric fuses worked well on all attempts, at depths of 70 and 100 m.
- The detonation cord worked well at a depth of 70 m, and when initiated by electric fuses from the water surface, transferred the detonation wave to a charge placed at the depth of 70 m.
- Charges at the depth of 70 m were successfully exploded twice. Observed magnitudes and amplitudes of seismic waves verify that the whole charge was properly detonated and that caps are an appropriate explosive.
- Charges at a depth of 100 m did not explode. This can be explained by several factors:
- degradation of initiation properties of the explosive accelerator red caps) and the main explosive due to the high pressure (~ 13 bar) and the specific water media in the Dead Sea (this explanation is in agreement with the manufacturer's warning that the explosive may not detonate at 100 m);
- Detonation of electric fuses only was insufficient to initiate accelerator and main explosives under the high pressure.

Unfortunately, lack of time prevented us making additional attempts to conduct an explosion at a depth of 100 m with initiation by detonation cord.

Main conclusions for the planned large calibration explosions were:

- Use electric fuses and detonation cord jointly for detonation of charge;
- Intensify the detonation process by using tripled detonation cord and TNT as additional accelerator explosive;
- Place all three calibration charges at a depth of 70 m.

According to previous experience and the new obtained data, limiting the explosion depth to 70 m should not significantly decrease the seismic energy of the explosions as compared to a depth of 100 m (confirmed later during the large calibration explosions).

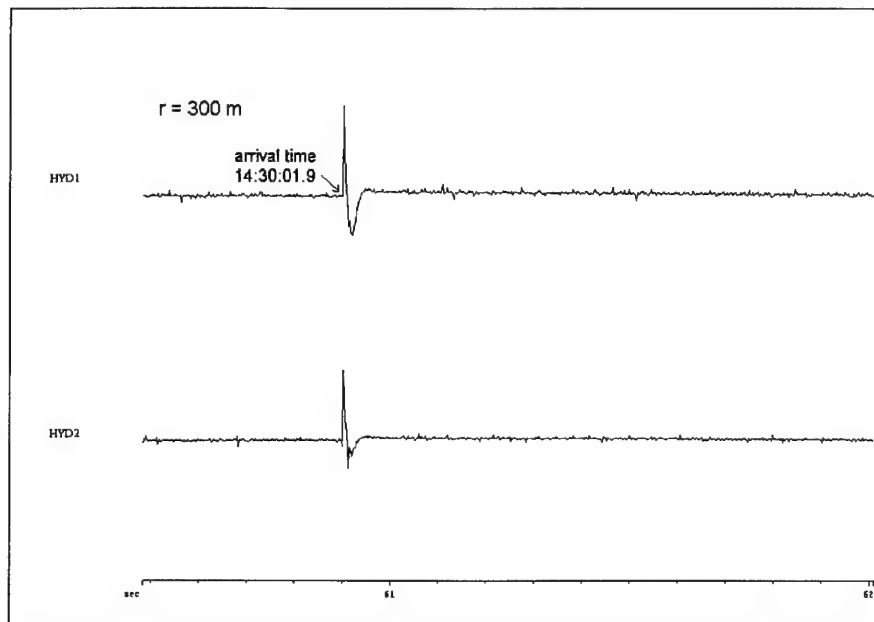


Figure 61. Classic shock wave shape recorded by a Geospace hydrophone near the ship from Example 1 t when only electric fuses were exploded.

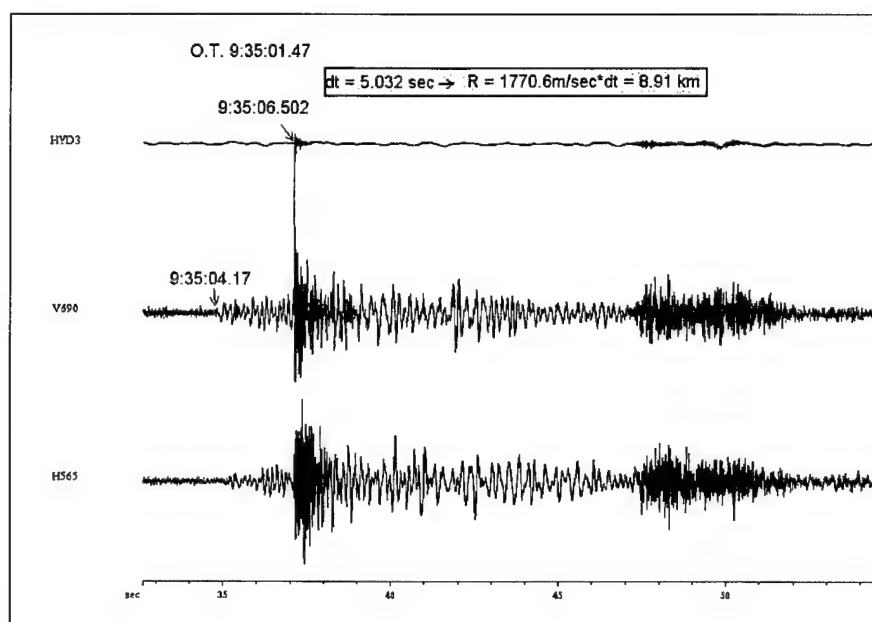


Figure 62. Recordings of the successful Ex.3t (W=25 kg) by seismometers on the shore and by a hydrophone near the jetty.

b) Measurement systems:

- Observed local magnitudes and peak amplitudes were in good agreement with the predicted values (see Tables 32 and 33). Peak amplitudes, including the closest temporary station at the jetty (near Kibbutz Ein-Gedi), are usually much lower than the predicted maximum values, and support the estimates of safety conditions presented in the Safety Report (Gitterman and Shapira, 1999). Nevertheless, it was concluded that we should increase measurements of ground shaking during the large explosions, enable on-site data analysis after each explosion, and verify the safety assessment before the next explosion.
- Average frequencies, measured from ISN spectra maxima (Table 33), are somewhat lower than calculated from the bubble frequency equation (corrected for the high water density 1.236 gr/cm^3 in the Dead Sea). We suspect that the charges drifted owing to underwater currents and the actual detonation depth was smaller.
- Measurements by a small seismic sensor attached to the charge or detonation cord provided accurate determination of the origin time. The time of the recording system is continuously synchronized with GPS and thus provided an accuracy better than 10 msec.
- The “Magellan” differential GPS system provides an accuracy of a few meters in determining the location coordinates. Nevertheless, strong variable underwater currents and winds in the Dead Sea cause **actual accuracy of about 30-50 m for epicentral coordinates of an explosion** at the depth of 70 m. Only the measured Dead Sea level: -414.7m can be considered as a very accurate estimation. The simpler, nondifferential GPS device GARMIN-II provides too low accuracy about 100 m which is too low.
- Joint recordings of a hydrophone and seismometers located near the jetty provided a clear identification of the high-frequency and high-amplitude seismic waves generated by the impact of the strong hydroacoustic waves on the sea shelf (see Figure 61).
- Geospace hydrophones provided arrival times of the direct hydroacoustic waves (Figures 61-62), thus enabling estimation of the distance between the explosion and the sensor. However, the system cannot record the actual high pressure and the shock waveforms. Consequently we invited an expert to provide reliable water shock wave measurements and subsequent estimation of explosion energy and TNT equivalent.

Based on the results of the test explosions we planned to deploy different measuring systems for monitoring the calibration explosions, and to perform on-site analysis of the recorded data from close-in stations (Table 34).

Table 34. Measurement systems and on-site data analysis at the Command Center during the calibration explosions on November 8-11, 1999.

System	Location	Expected results (estimations)	Goals	Hardware	Software	Data transfer to the Center	Comments
Existing BB stations	EIL, MRNI, JER	Peak velocity amplitudes, waveforms, frequencies	Checking station performance	Workstation SUN	PITSA or SAC	Event binary files (dta and SEED) prepared in GII and placed on the server with modem - by a telephone line - to the Center PC and to the workstation	Workstation and the PC should be connected by a local network.
Planned CNF BB stations	Malkishua, Amazia, Dimona	Peak velocity amplitudes, waveforms		PC desktop with a modem 56.6	GIIL_SDP		
Short-period ISN stations	All working stations (satellite and radio-telemetry)	Peak velocity amplitudes, waveforms, frequencies, location and O.T. estimation		PC desktop with a modem 56.6	GIIL_SDP		Measurements and analysis are provided by the GII personnel.
Temporary seismic stations	Ein-Bokek, 2 sites, two 3C stations at each site; Mineral Beach, one vertical seismometer	Peak velocity amplitudes, waveforms	Correction of preliminary amplitude estimations, decision about conducting larger shots			ZIP disks to the PC	
3 temporary A800 accelerom.	Mizpe Shalem, Ein Gedi, Mineral Beach	Peak accelerations		PC Compaq	DADISP	In the PC	
7 vibrometers	Ein Gedi, dam, Mizpe Shalem, Mineral Beach	Peak velocities and accelerations		Specific system		In the system recorder	
2 hydrophones Geospace	1 hydr. near the ship, 1 hydr. near Mineral Beach	Relative peak pressure amplitudes, waveforms	Checking expl. performance	PC Toshiba	PC SDA	In the PC	
Origin Time measurement	On the ship	O.T. value	Exact time				
GPS system MAGELLAN	On the ship and the basis on the shore	Coordinate measurements	Exact location				
Two special high pressure hydroacoustic sensors	Near the ship	Peak pressure, Explosion energy	Estimation of TNTequivalent and source characteristics	PC Laptop		In the system PC	Measur. are provided by expert Mr. Lipa Sadwin

7.3 Observers and Public Relations.

Conducting large-scale explosions in this politically sensitive area, just a few kilometers from the Israel-Jordan border, required serious long-term diplomatic efforts, supported by the Israel Ministry of Defense, and the Defense Threat Reduction Agency (DTRA) of the U.S. Department of Defense (DoD). The agreement of the Jordanian authorities was obtained through contacts at the highest government levels.

A number of international observers were invited to participate in the experiment and inspect the weighing and preparation of charges before the explosions:

- LTC James W. Nichols and Dr. Karl Veith (DTRA, USA);
- Colonel Sergei Kovalev and Dmitri Smirnov (Embassy of Russia in Israel);
- Gen. Naser Al-Majali, Mr. Hamed Al Mahagde, and Mr.Orwa Masawa (the Royal Eng. Corps, Jordan);
- Dr. Petr Firbas (CTBTO, Vienna);
- Dr. Jalal N. Al-Dabbeek and Mr. Radwan El-Kelani (An-Najah University, the Palestinian Authority).

The observers were given full information about the charges, detonation techniques, observational systems and measurement results after every explosion. They were allowed to observe the weighing of charges before the explosions and obtain the weight documents. A photocopy of the weight certificate for the 5000 kg charge is shown in Figure 63.

מס' תעודת שקילה/הערת משלוח/חשבונית מס/קבלה מס' 14530

מס' חומר: 11-11-99

מס' חומר: 11-11-99

מס' חומר: 11-11-99

מס' חומר: 11-11-99

מס' חומר: 11-11-99

<p>מס' חומר: 11-11-99</p> <p>מס' חומר: 11-11-99</p> <p>מס' חומר: 11-11-99</p>	<p>מס' חומר: 11-11-99</p> <p>מס' חומר: 11-11-99</p> <p>מס' חומר: 11-11-99</p>
---	---

GROSS 18230

TARA 12880

NET W. 5350 kg

EMPTY BOX W = 6x40 = 240 kg

DRIVEN 2

NET CORD

350 kg

Figure 63. Photocopy of the weight certificate of the 5000 kg charge.

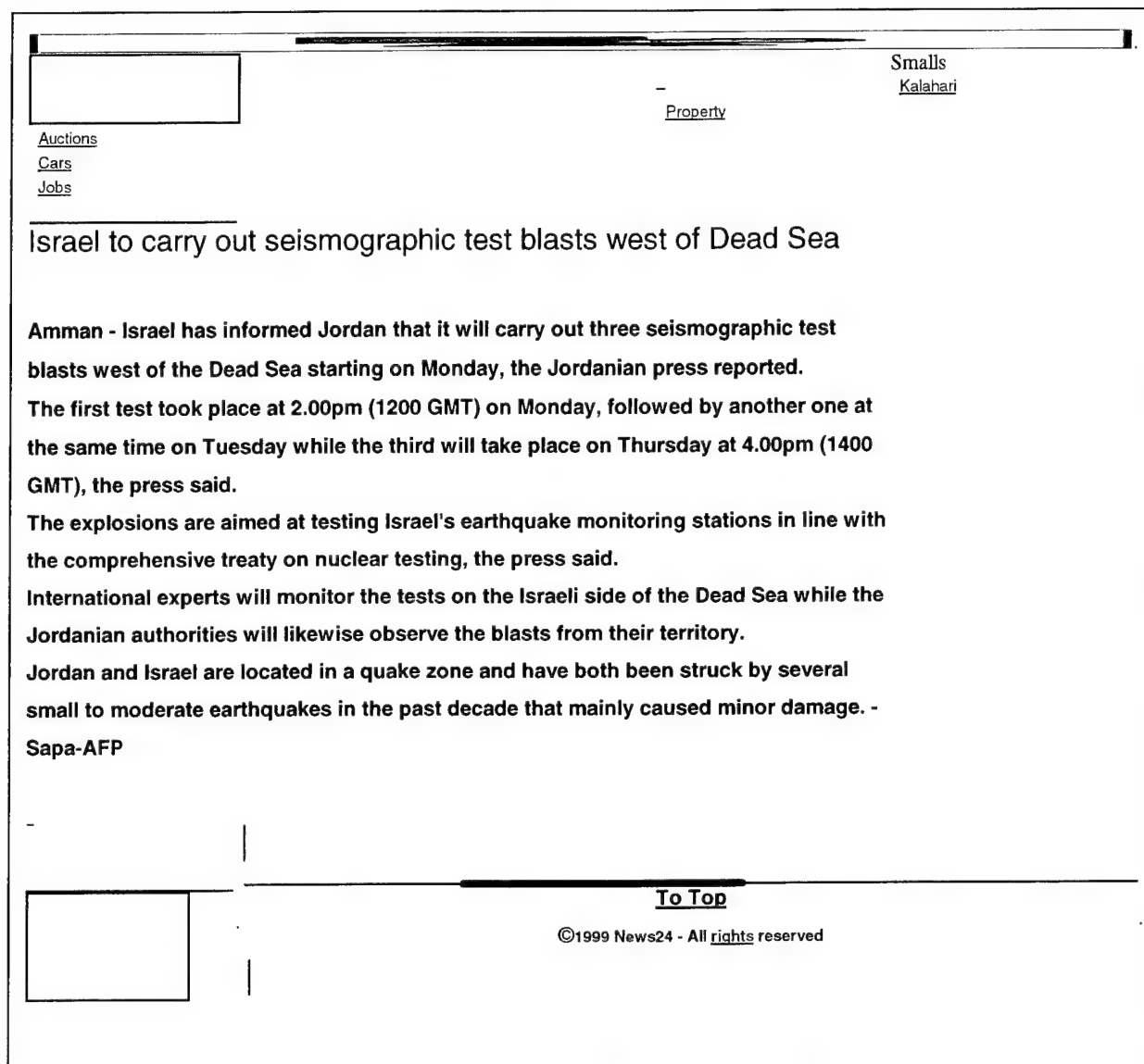


Figure 65. Information about the Dead Sea experiment on the Website NEWS24.

7.4 Explosion Design.

Based on the results of small test explosions, it was decided to use a combined detonation technique, electric fuses and detonating cord (fuse) with multiple initiation points, and to limit the charges to a depth of 70 m. The design, assembling charges and conducting the explosions were carried out by ELITA Security Ltd. (Mr. Shimon Kobi), supported by Explosives Manufacturing Industries (1997) Ltd. (Eng. Emanuel Hausirer). The experiment configuration is shown in Figure 66. Parameters of the explosions are presented in Table 35.

The charge unit design and sample photographs are shown in Figures 67-68. The primary blasting agent, CHEN AMON explosive (detonation velocity 5500 m/sec, energy 900 cal/gr), based on Ammonium Nitrate, has a density of 1.3-1.4 gr/cm³, which is higher than the Dead Sea water density, and therefore no ballast was used to sink the explosives. Rotex detonating fuse (cord) 10.5 was used, which detonates at a velocity higher than 6500 m/sec.

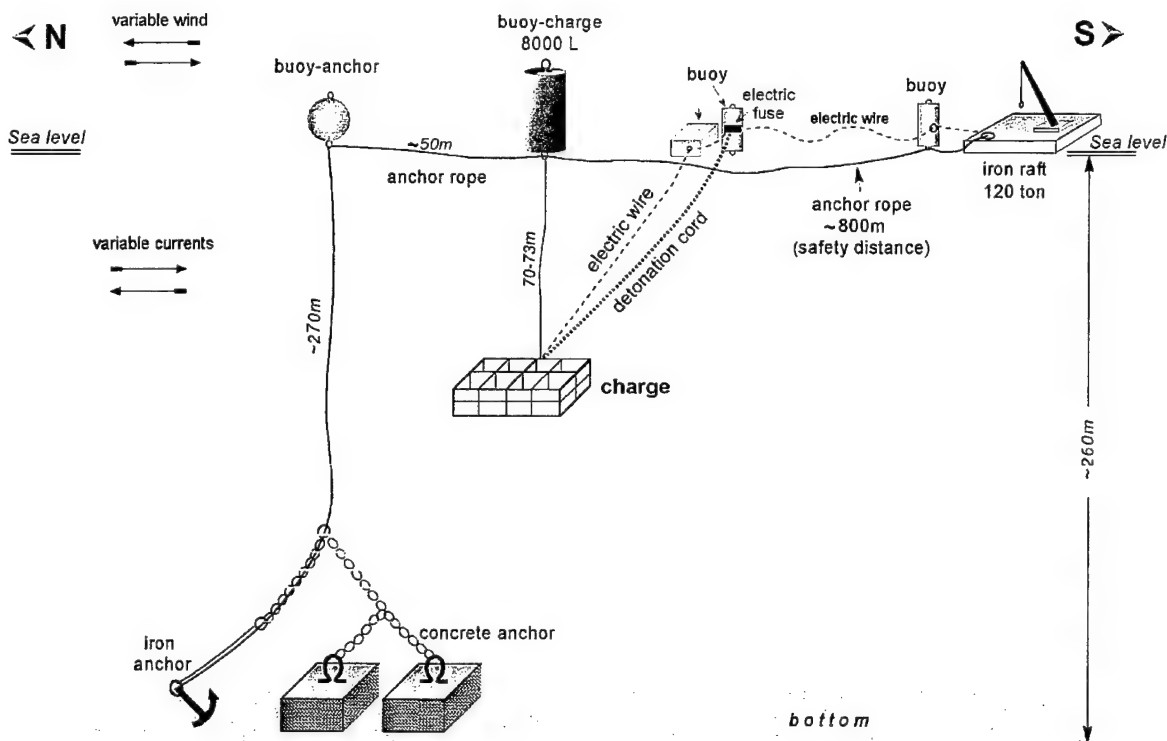
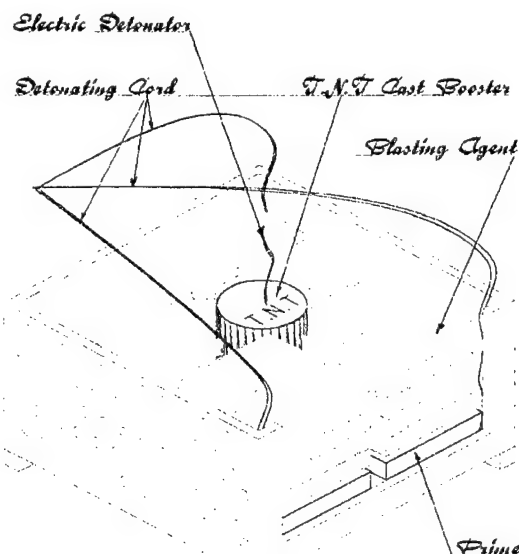


Figure 66. Details of marine operations and experiment configuration (courtesy of Mr. M. Gonen).



500 KG - Charge



מכיל זכרון יעקב, ת.ד. 17 מיקוד 30900, ס"ל 04-6390555, פקס: 04-6390520, 04-6390520
P.O.B. 17, ZICHRON JACOB, ISRAEL 30900 - Tel. 972-0-6390555, Fax: 972-0-6390520



Figure 67. Design of charge unit (courtesy of Eng. E. Hausirer).

Table 35. Parameters of calibration underwater explosions in the Dead Sea, charge depth H=70-73m, sea depth ~260 m (Ground Truth Information rank GT0).

Date Origin time, GMT	Location, GPS Magellan	Total charge kg	Charge components, kg		Initiation of the charge (using electric fuse - EF, and detonating cord - DC)	Comments
			Main agent CHEN AMON	Accelerator (red CH-AM, TNT, PETN)		
08.11.99 13:00:00.33	31.5330°N 35.4406°E	500	410	90	EF connected to DC on the water surface and at depth near the charge	-
10.11.99 13:59:58.21	31.5338°N 35.4400°E	2060	1640	420	EF connected to DC (length about 70-75 m) on the water surface	After detonation failure on 9.11, two additional TNT units were added
11.11.99 15:00:00.80	31.5336°N 35.4413°E	5000	4460	540	EF connected to DC (length about 70-75 m) on the water surface	Water uplift about 15 m was observed 5-7 sec after the detonation

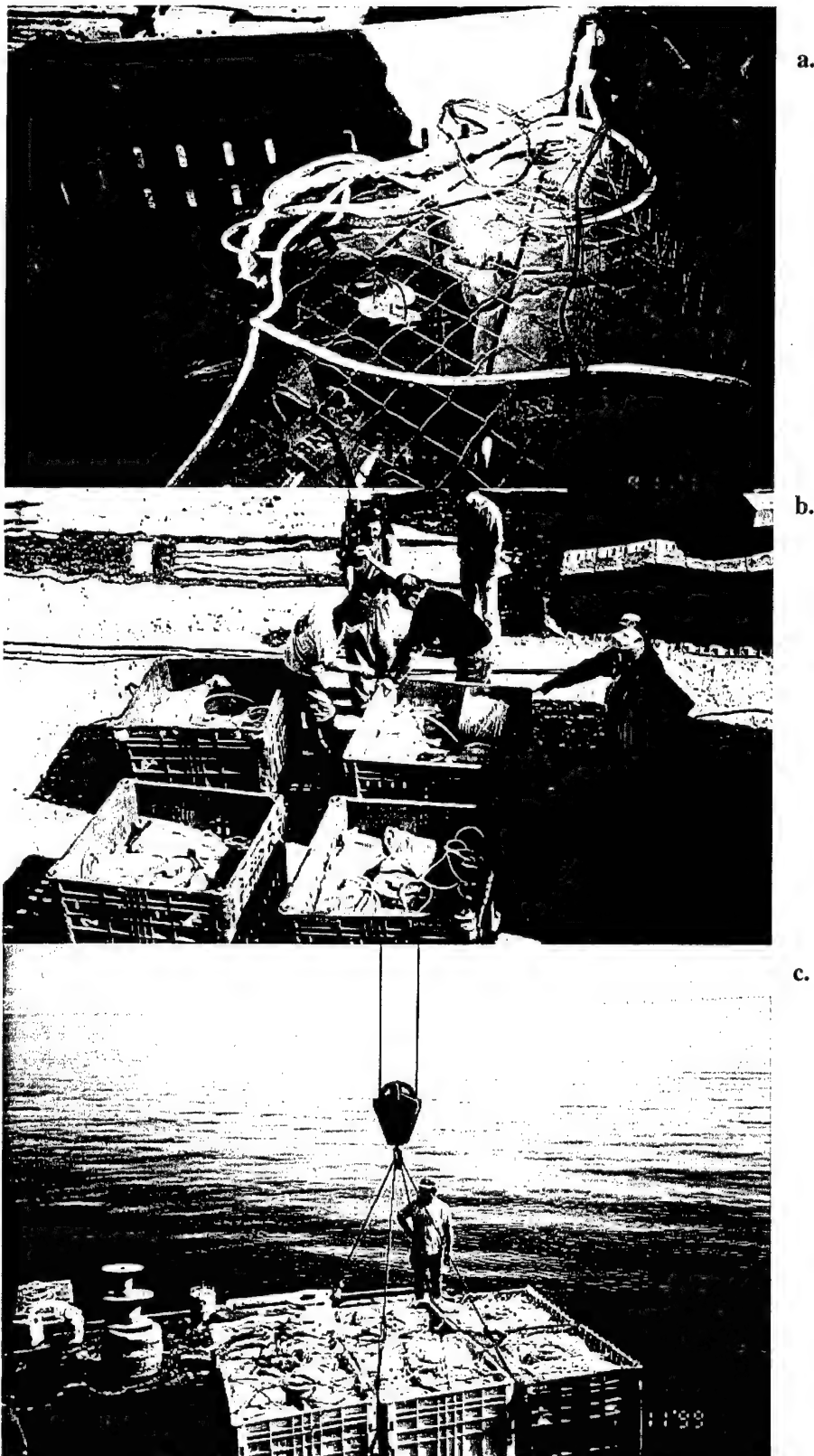


Figure 68. Sample photographs of the charges of the three explosions. The 0.5-ton charge unit (a) was used also for the 2-ton charge (b); the 5-ton charge consisted of six units of about 833 kg each (c).

An iron raft (dead weight 120 tons) was built especially to transport the charges and a 12-ton crane which was used to download the largest charge to the explosion site. The site was located about 9 km from the jetty. A detailed bathymetric map of the Dead Sea (Hall, 1993) shows that the sea depth in the experiment area was $H=260\text{--}265$ m (Figure 69). The raft was towed by a wooden boat ("Lot's Wife", Gonen Marine Works Ltd., Israel). Transportation time was about 2.5 hours (Figure 70).

During the first explosion, 0.5-ton, the measurement systems (GPS coordinates and origin time, hydroacoustic) were placed on the boat at distance of about 900 m. During the two last shots the systems were deployed on the raft which is more resistant to the shock wave impact. Consequently, the distance to the shot-point could be shortened to 600 m.

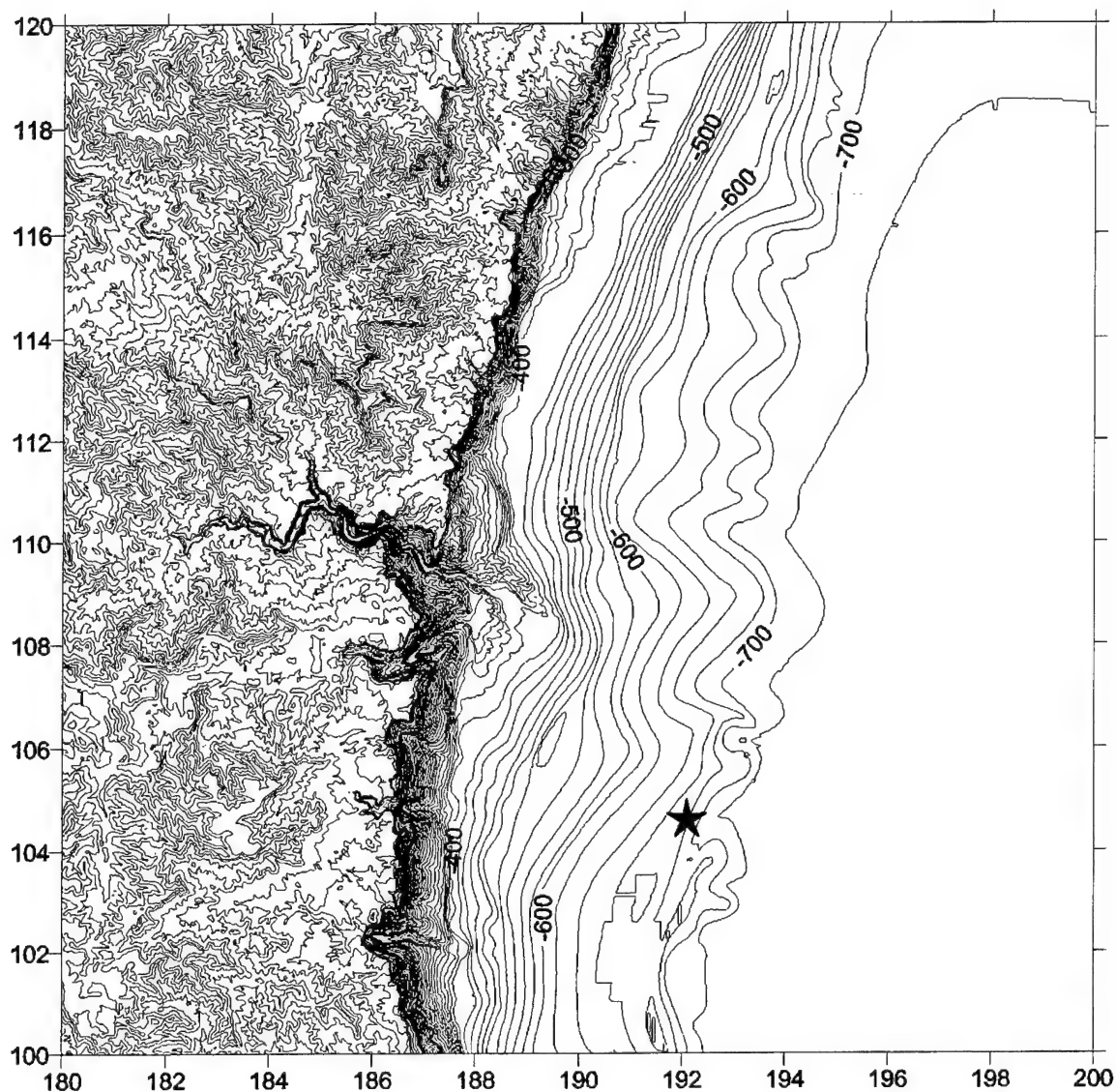
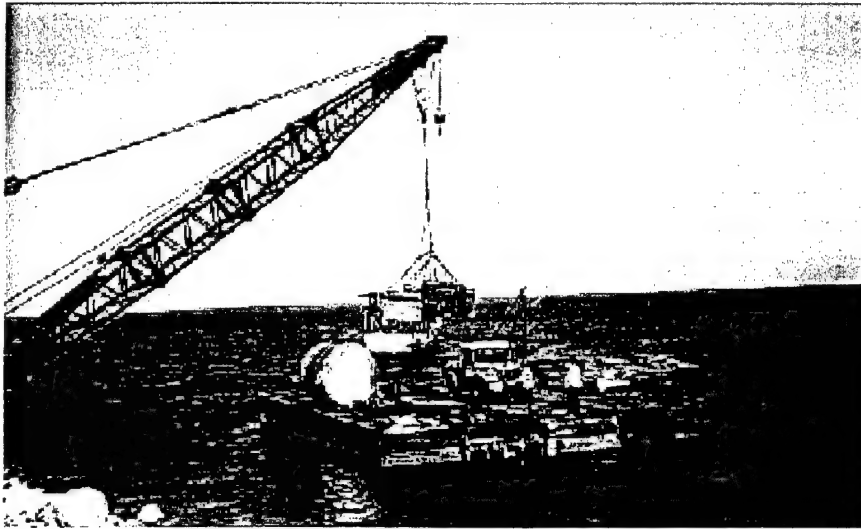
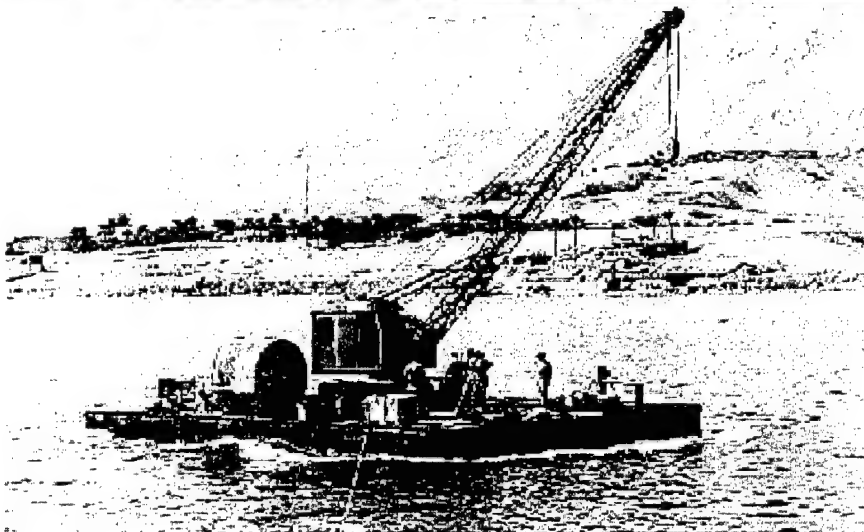


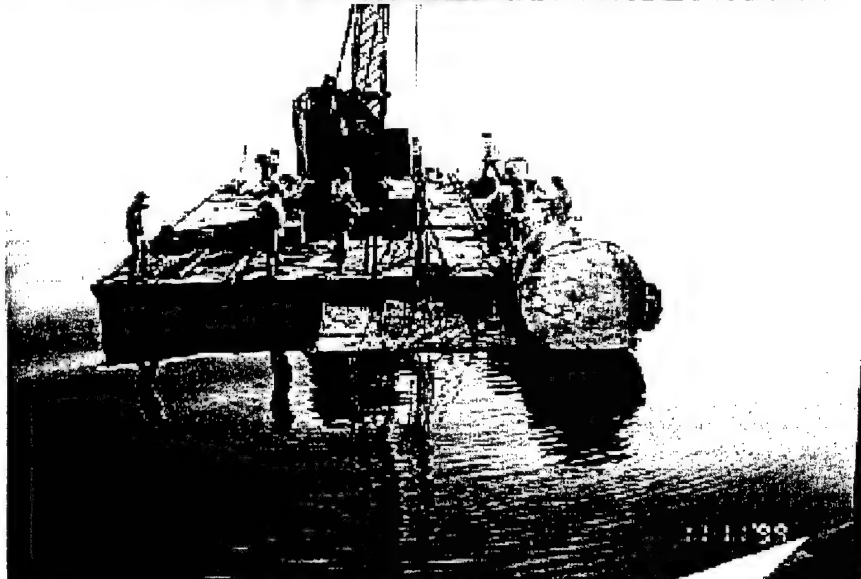
Figure 69. Bathymetric chart of the Dead Sea near the shot point (H). The water surface level is -415 m (November 1999). Axes are local coordinates in km.



a.



b.



c.

Figure 70. Sample photographs of marine activities during the experiment: (a) - loading of the 2-ton charge to the raft (9.11.99), (b) towing the raft, 5-ton charge and a steel buoy (8000 liters) to the explosion site (11.11.99), (c) submerging the 5-ton charge.

7.5 Measuring Origin Times and Coordinates.

For the first shot (500 kg), a small seismic sensor was attached to the charge and provided accurate determination of the origin time (Figure 71). During the second shot (2060 kg), the sensor became disconnected from the recording system and the origin time is estimated based on the relative propagation time of shock waves to piezoelectric sensors (see below Section 7.7, Figure 77) and the absolute GPS time of the wave arrival to a hydrophone co-located with the sensors. For the largest explosion (5000 kg) we recorded the exact moment of electric fuse detonation, connected to detonating cord, which initiated the charge. The finite detonation time of the 70-75 m long cord, estimated to be about 10 msec ($\sim 70\text{m}/7000\text{ m/sec}$), was also considered. The timing in the recording system was continuously synchronized with GPS. Using a 500 Hz digitizer, we obtained an accuracy better than 5 msec.

The differential GPS system "Magellan" provided an accuracy of a few meters in determining the location coordinates. Nevertheless, due to strong variable underwater currents and winds in the Dead Sea (especially during the second shot), we estimated the actual accuracy to be about 50 m, corresponding to possible drifting of the charge around the anchor (see Figure 66).

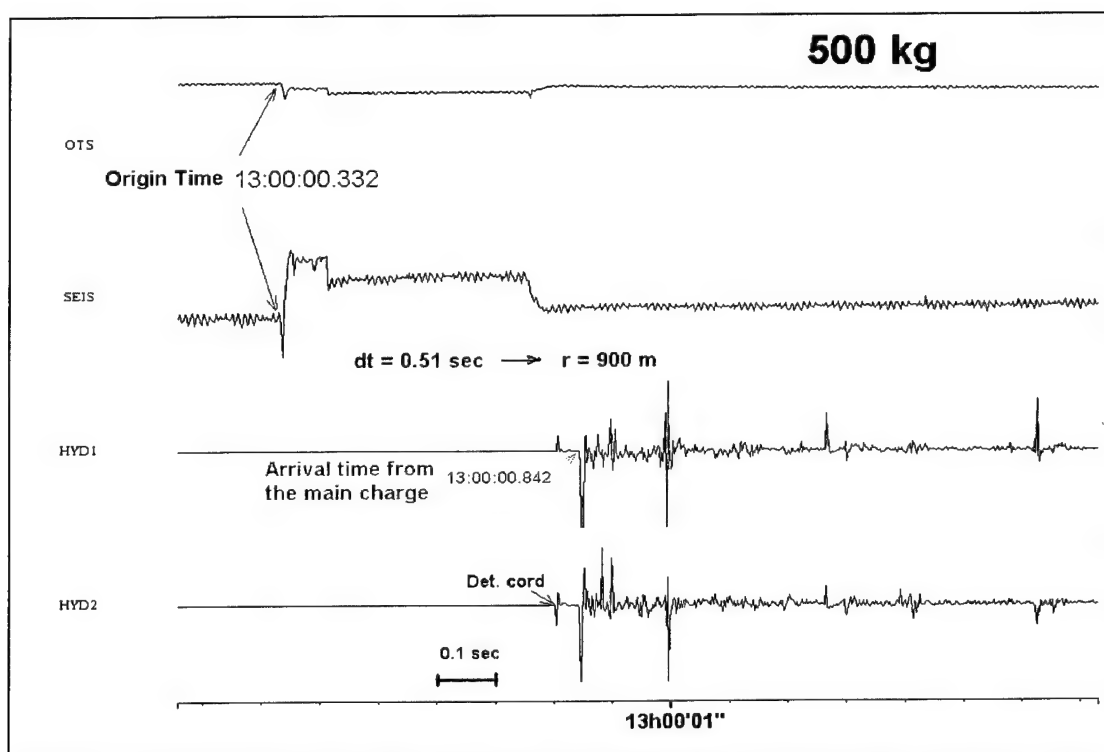


Figure 71. Measurements of the origin time for the 500 kg shot (two upper channels).

The shock wave arrival time, recorded by two hydrophones near the boat, was used to verify the distance to the explosion.

7.6 Audio-Visual Records of the Explosions.

The experiment was videotaped. A home camera was placed on the raft, at a distance of several hundred meters from the shot site. The video and audio tracks provided observations and rough time measurements of interesting physical phenomena, such as a "cavitation hat", arrivals of shock waves and bubble pulsations near the raft. The video clips also provided a rough estimation of the shock wave propagation time to the surface and the raft and contributed to verification of the charge depth and explosion-to-raft distance.

For the video-recording rate of 25 fps (frames per second) used, the time measurement accuracy can be considered as the time between two successive frames which is 40 msec. Figure 72 shows snapshots of the 2060 kg, where following phenomena can be observed:

- a) "Cavitation hat", created upon the direct shock wave arrival to the water surface. An initial sign of the cavitation strip can be revealed at about 40 msec, according to the propagation time $t_c = 70\text{m}/1770\text{m/s} = 0.0395\text{ sec}$, the frames 80, 120 and 200 msec show evolution of the cavitation process;
- b) the camera focus is disturbed by the shock wave impact on the raft at about 440 msec, yielding a raft distance from the shot $\sim 775\text{ m}$, which corresponds well to the estimate obtained from hydroacoustic recordings (see Section 7.7);
- c) the focus' distortion is repeated after $\sim 0.5\text{ sec}$ (at the 920 msec snapshot) due to the gas bubble pulsation, which is close to predicted and measured from seismic spectra bubble pulse periods;
- d) a water uplift by gases rising in the time window 9 - 14 sec;
- e) appearance of yellow gases - explosive detonation products, during 35-40 sec, in an area displaced to the right of the epicenter, evidence strong underwater currents in the Dead Sea, preventing location of the charge placed at a depth of 70 m more accurately than 50 m.

The video-record of the largest explosion 5000 kg (see Figure 73) has an impressive audio-track providing 2-3 specific audible signals, produced by the gas bubble pulsation, and repeating at intervals of about 0.8 sec (see Figure 74). It corresponds well to the estimate of the bubble pulse period 0.78 sec from seismic records (see Table 42 below).

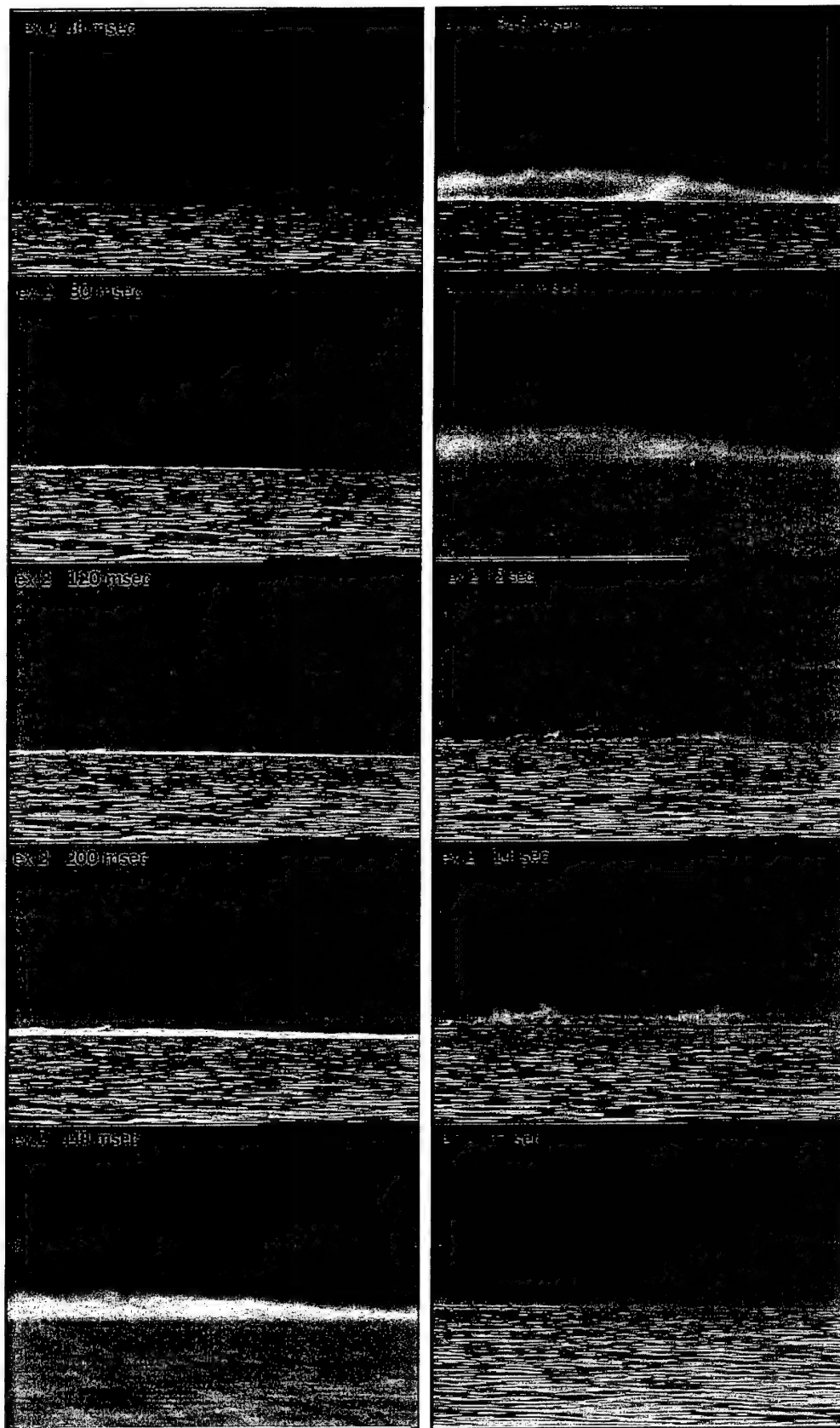


Figure 72. Sample video snapshots of the 2060 kg explosion taken on the raft from a distance of 770 m. Note the horizontal strip on the surface of the water at 0.08-0.2 sec (a "cavitation hat"), and the camera focus disturbance at 0.44 sec, caused by the shock wave. The camera speed is 25 frames/sec.

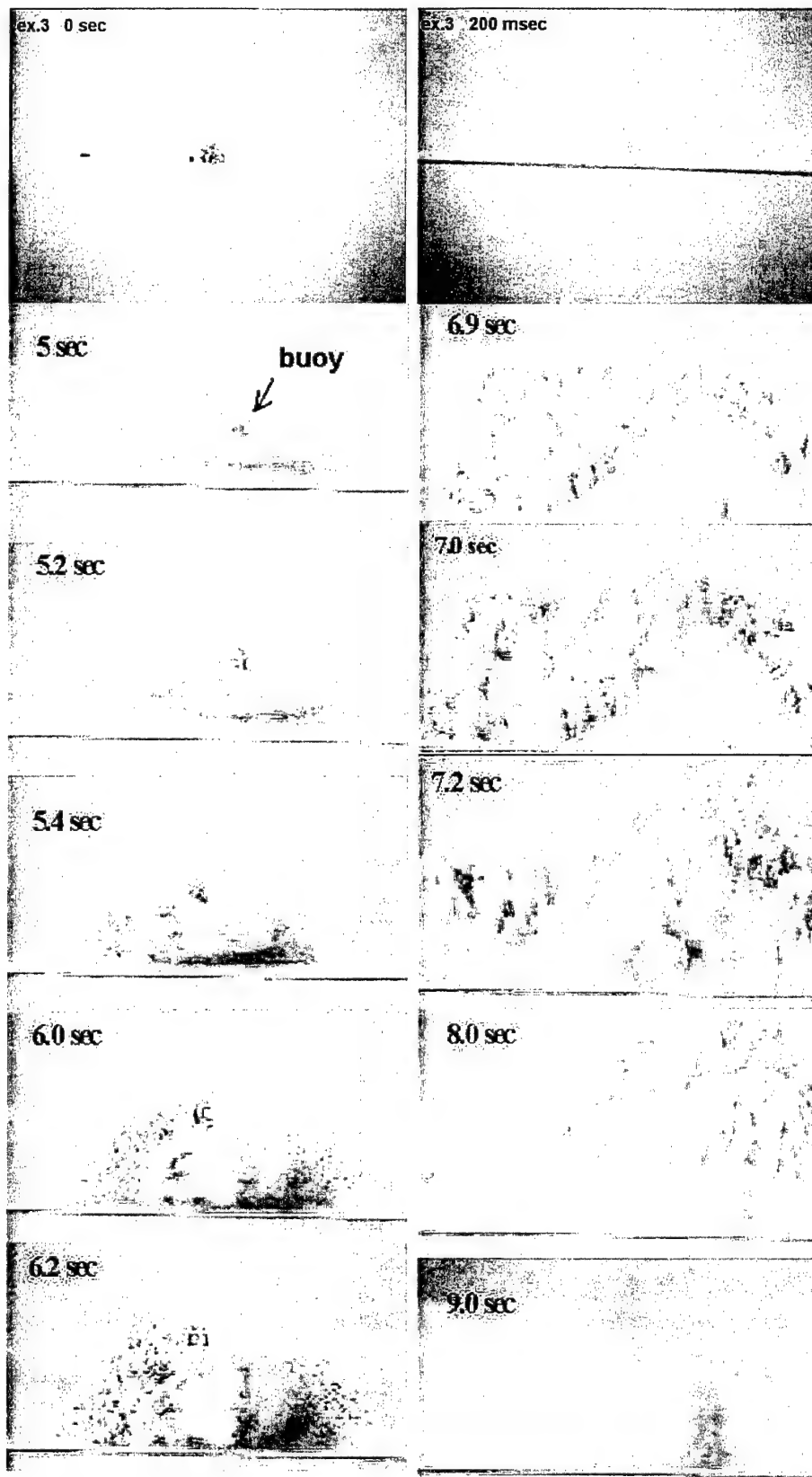


Figure 73. Sample video snapshots of the 5-ton explosion taken on the raft from a distance of about 620 m. Note the horizontal strip on the surface of the water at 0.2 sec (a "cavitation hat"). The spot on top of the water uplift is a steel buoy (height 2.2 m and length 2.4 m, shown at 0 sec), used to fix the charge to the depth of 70 m. The camera speed is 25 frames/sec.

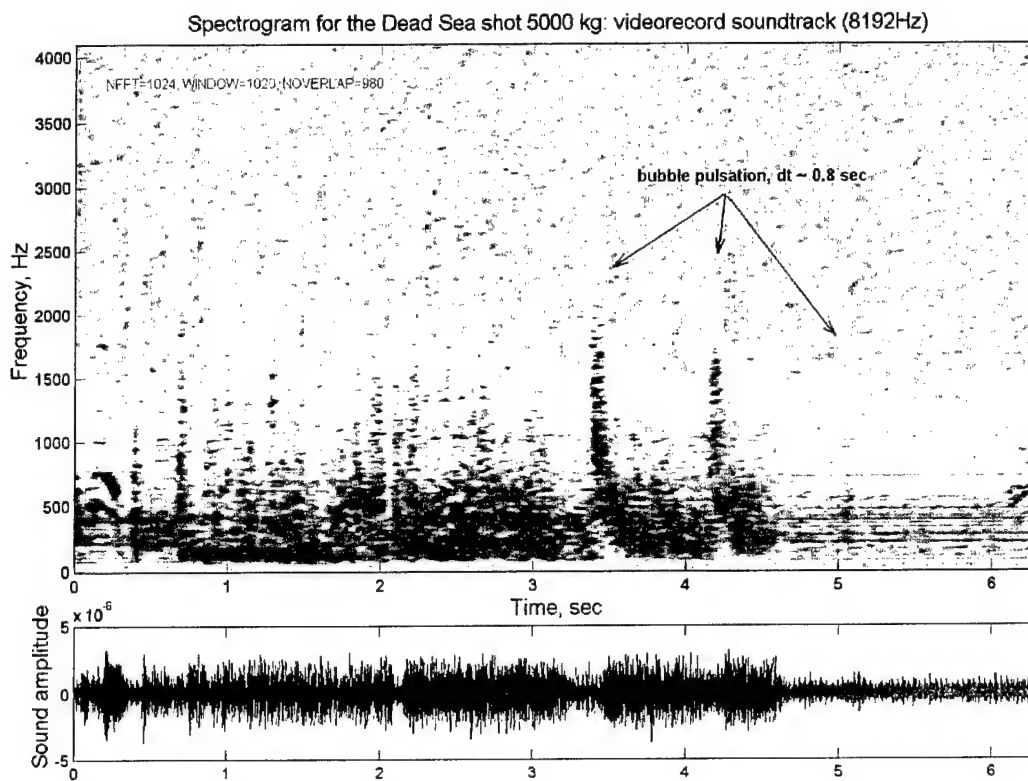


Figure 74. Spectrogram of the video-recording soundtrack for the 5-ton explosion, demonstrating clear bubble pulsations with an interval corresponding to the predicted bubble period and the measured from seismic spectra value.

7.7 Hydroacoustic Measurements.

Unique shock wave observations were taken for the two largest explosions. Such measurements have never been made before in super-saline water with unusual properties as in the Dead Sea.

7.7.1 Recording System; Estimation of Travel Times and Shock Wave Speed.

The water pressures were measured by piezoelectric underwater blast sensors (type 138A01 of PCB Piezotronics) by Sadwin Engineering Consultancy, Israel. Two measurement gages were located near the raft, at a distance of about 600-800 m from the explosions, at a depth of 25-30 m. The pressure-time history was recorded by a computer system with 250 kHz response for each channel used (see Figures 75-76). The record duration was only 0.7 sec due to restrictions of computer memory and disc space.

Accurate zero time (non-absolute) for triggering the computer recording was obtained by using an electric fuse parallel to the charge detonators. This arrangement has provided an accurate determination of the shock (acoustic) wave travel times between the charge and the sensors, and a confirmation of the high speed of the waves. Figure 75 shows the pressure-time history for the 2-ton explosion recorded by two gages spaced at about 25 m, which provides an estimate of the shock wave speed about $C^*=1794$ m/sec.

The expected 23 m/sec (1.4%) excess of the acoustic velocity ($C=1770.6$ m/sec) is possibly related to an error in measuring the gage spacing, or to extremely high pressures in the shock wave at short distances. Speed addition on the leading edge of the shock wave is given by:

$$\Delta C = \frac{\Delta P}{\rho C} \quad (7.1)$$

For measured peak pressure about 700 kPa at distance 770 m (Figure 75), density $\rho = 1236 \text{ kg/m}^3$ and acoustic velocity $C = 1770.6 \text{ m/sec}$, Equation 13 gives only $\Delta C = 3.2 \text{ m/sec}$. However, at 100 m, where the pressure is estimated as 5.2 Mpa (see Equation 16 below), the speed addition can reach 24 m/sec.

A minor measurement system based on Geospace hydrophones (provided by GII) was used for determining the absolute (GPS) arrival times of the shock waves, thus providing estimated travel times and distance (Figures 71, 77). Joint recordings of a hydrophone and seismometers located near the jetty provided clear identification of the high-frequency and high-amplitude seismic waves (see Figure 84) generated by the impact of the strong water waves arriving at the sea shelf.

7.7.2 Types of Water Shock Waves.

For the largest explosion only one gage record was obtained, plotted in Figure 76. The direct wave P1 and surface-reflected P2 waves can be easily identified, whereas interpretation of P3 and P4 is uncertain in a trade-off between bottom-reflected, bottom-refracted and surface-bottom-reflected phases (see details in Section 7.7.3).

The cepstral simulation and inversion algorithm for analysis of regional seismic recordings of underwater explosions, developed by Dr. D. Baumgardt, allows to separate out the band modulation of the surface reflection, and for the narrow band (20 Hz) EIL and MRNI data of the Dead Sea shots gives a negative cepstral peak at about 0.15 seconds period; the optimal search inversion program returned very low values of the best matching reflection coefficient, sometimes in the order of -0.3 to -0.4 (D. Baumgardt, personal communication).

Considering the high acoustic velocity in the Dead Sea $C = 1770.6 \text{ m/sec}$, we can easily interpret the 0.15 sec cepstral peak as really caused by the surface reflection. The fundamental frequency in this case is $f_r = C/(4 \cdot h) = 1770.6/(4 \cdot 70) = 6.32 \text{ Hz}$, and period is 0.158 sec, fitting very well to the cepstral peak (much better than for ocean acoustic velocity).

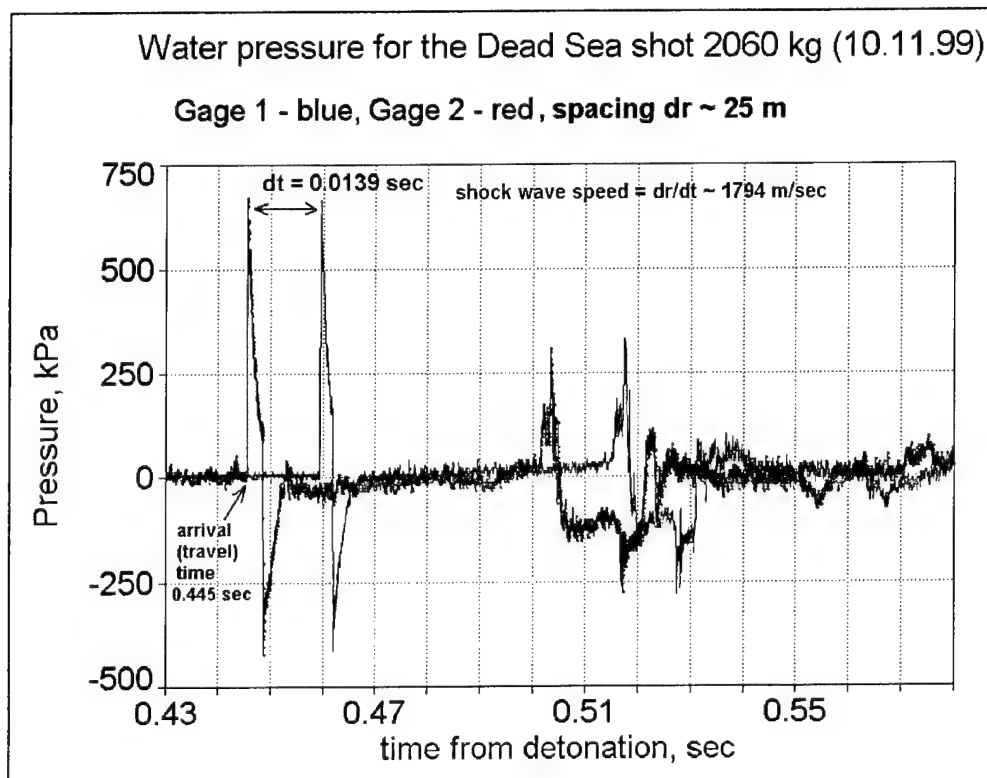


Figure 75. Water pressure-time history of the 2-ton explosion at distance of about 770 m. Spacing between two gages is about 25 m

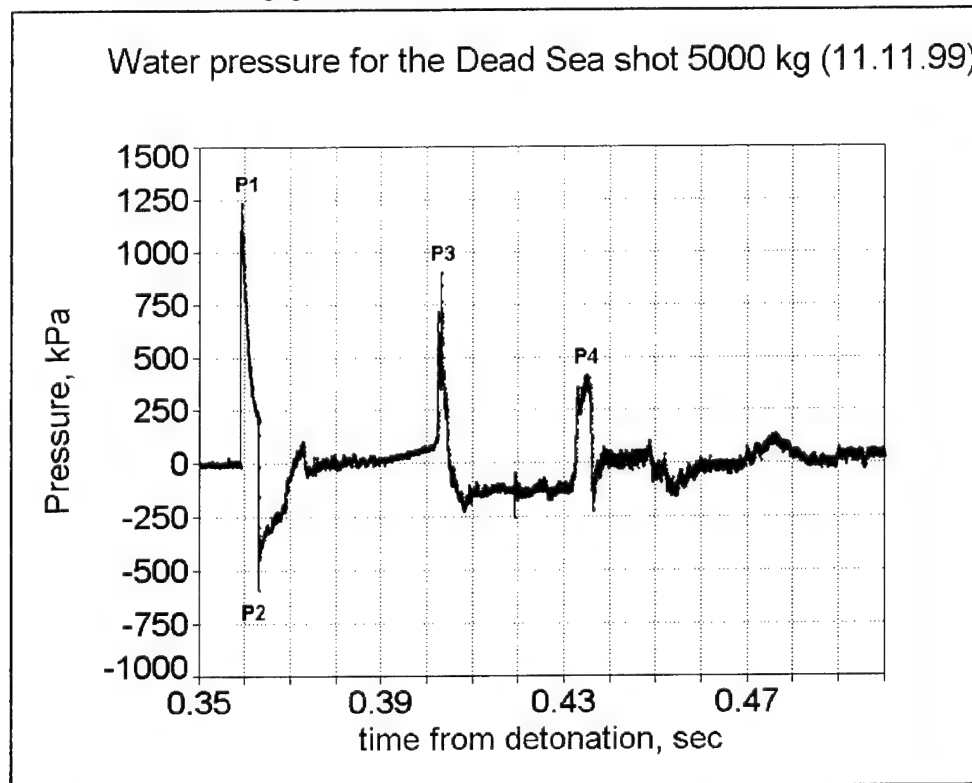


Figure 76. Water pressure-time history of the largest explosion at distance of about 620 m.

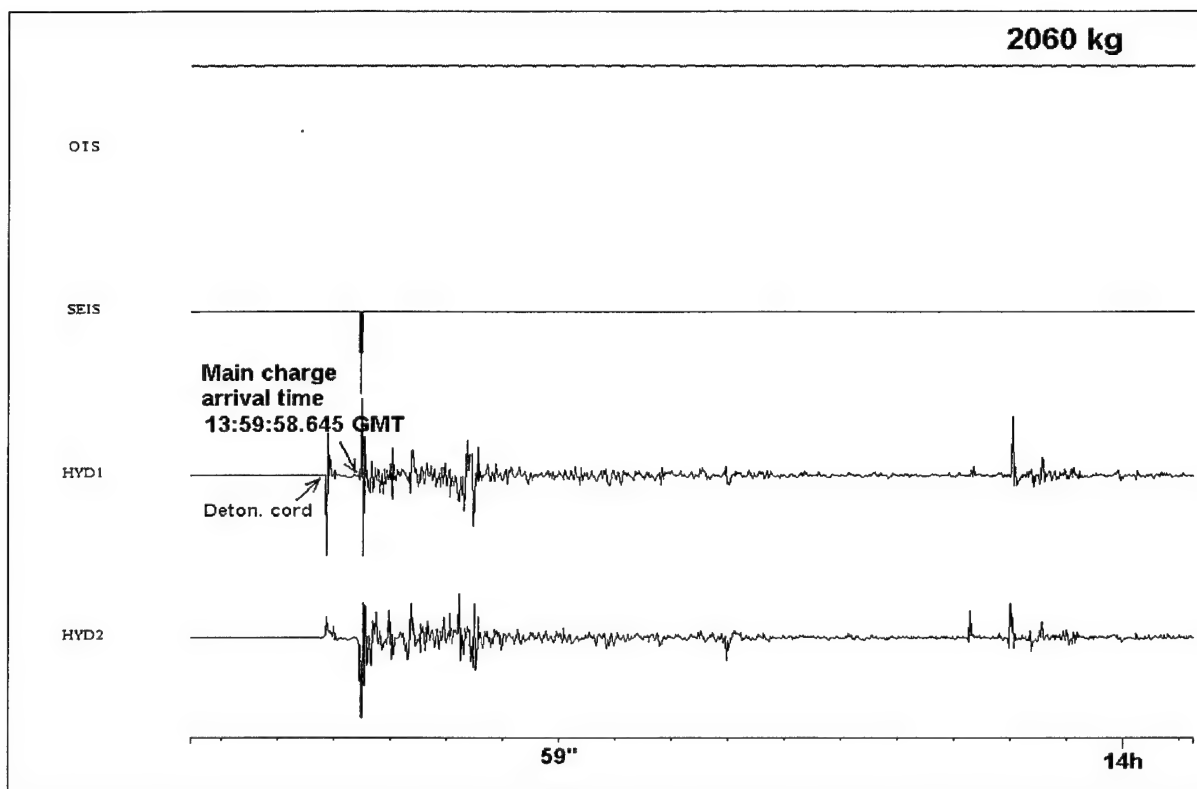


Figure 77. Measuring the absolute GPS time of the shock waves, arriving to hydrophones, co-located with the piezoelectric sensors. The shock wave arrival time is 0.445 sec (Figure 75). The detonation duration of the detonating cord is about 10 msec. The Origin Time is estimated as: $13:59:58.645 - (0.445 - 0.010) = 13:59:58.21$ GMT.

In the ISN spectra this surface reflection maximum is merged with the 5th harmonic of the bubble fundamental frequency $f_{b5} = f_b \cdot 5 = 1.28 \cdot 5 = 6.4$ Hz, causing enhanced maxima at about 6.46 Hz (see Figure 99 in Section 7.8.4).

Water pressure measurements (Figure 76) show that the amplitude of the surface reflected wave is about 0.5 of the primary shock wave amplitude. This observation corresponds in some way to the low reflection coefficient estimated from the inversion algorithm by Dr. Baumgardt.

7.7.3 Verification of Distance and Depths.

Based on the experiment configuration and arrival times of different phases measured from recordings of shock waves we tried to verify estimates of source-sensor distance r , charge depth h and sea depth H in the shot point area. Travel times of different phases as measured from recordings of piezoelectric sensors and hydrophones are presented in Table 36.

The required parameters were estimated from combinations of simple kinematic equations, under the assumption that the shock wave velocity is constant along the whole propagation path ($C = 1770.6$ m/s):

$$r_i/C = t_i - \Delta t \quad (7.2)$$

where index i corresponds to different waves, r_i is the propagation path depending on h and H , t_i is the arrival time (relative the initiation moment), and Δt is the delay of a shot caused by the detonation cord of unknown length and detonation velocity (>6500 m/sec), which connects the initiation point on the water surface and the charge on the depth.

Table 36. Measured arrival (travel) times of different water shock waves.

Charge kg	Sensor type	Sensor depth, h_s , m	Arrival time from the initiation moment, sec					
			P1, direct wave, t_d	P2, surface reflect., t_s	P3 t_3	P4 t_4	1 st bubble pulse	2 nd bubble pulse
500	hydro	2	0.510	-	-	-	0.931	1.289
2060	hydro	2	-	-	-	-	1.095	1.602
	piezoel.	30	0.44546	0.44854	-	-	-	-
		25	0.45933	0.46180	-	-	-	-
5000	hydro	2	0.349*	-	-	-	1.147	1.922
	piezoel.	30	0.35915	0.36304	0.40248	0.432	-	-

* - time from the charge detonation moment

The detailed bathymetric map of the Dead Sea (Hall, 1993) shows (see Figure 69), that the sea depth in the experiment area is $H=260-265$ m.

The phase analysis and interpretation results can be summarized as follows:

- 1) For both shots the delay Δt was estimated at about 0.010 sec, a reasonable value considering the detonation cord length of about 70-75 m and detonation velocity 7000-7500 m/s. This is confirmed by a similar difference in the direct wave arrivals to hydrophone and piezoelectric sensors for the shot 3 (see Table 36);
- 2) The interpretation of the phase P3 (see also Figure 78) as the bottom-transmitted wave and P4 as the bottom-reflected wave provide the sea depth estimate $H=265$ m, which corresponds well to the bathymetric map estimation. However very high amplitudes and short duration of phase P3 contradict the theoretical description of the bottom-transmitted wave as a slow-rising and low amplitude wave, and correspond much better to the bottom-reflected wave (see for example, USACE, 1991). Thus this interpretation is based only on kinematic features of the observed phases.
- 3) The interpretation of phase P3 as the bottom-reflected wave and P4 as the surface-bottom reflection provides a different estimate of the sea depth $H=212$ m. This interpretation is based on both kinematic and dynamic features of the observed waves, but there is significant disagreement with the bathymetric map (another discrepancy is that surface-bottom reflection should be negative due to reflection from the water surface). The difference cannot be related to estimation errors and, at the moment, we cannot provide any reasonable rationale for choosing between the two interpretations.
- 4) A somewhat increased depth estimation $h=73.5$ m for the 5000 kg shot seems to be reasonable, possibly due to a stretched rope and charge-center shift.

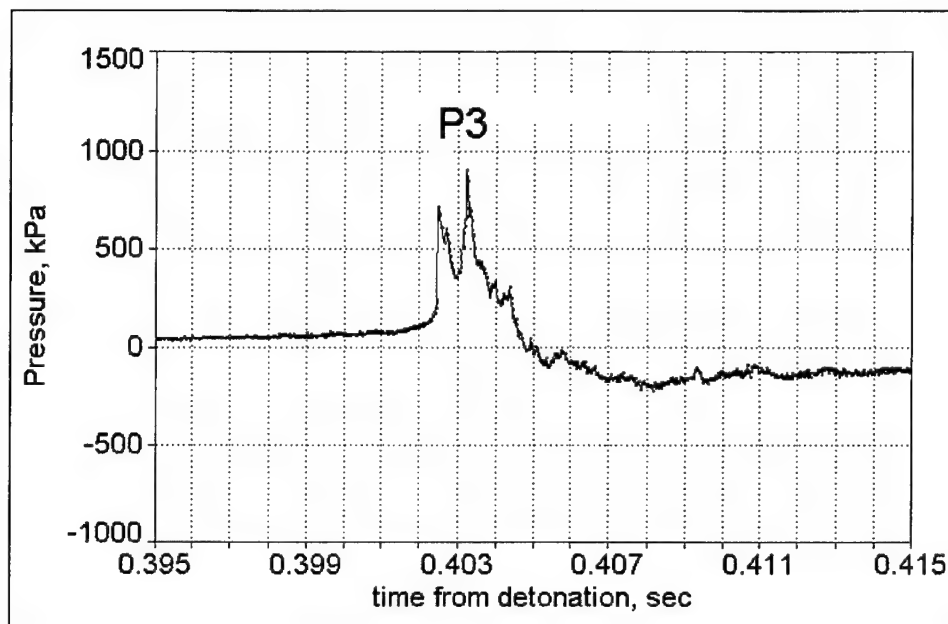


Figure 78. Complex form of the P3 phase for the shot 5000 kg.

Obtained estimates of the shot configuration parameters and the bubble period (as the average for arrivals of the 1st and 2nd bubble pulses) are presented in Table 37.

Table 37. Shot configuration parameters and bubble periods estimated from shock wave travel times.

Charge, kg	Shot depth h , m	Sea depth, H , m	Hypocentral distance r , m	Bubble period T_b , sec	Comments
500	-	-	900	0.390	no precise piezoelectric measurements
2060	70	*	770, 795	0.578	r is for two gages separated by 25 m
5000	73.5	265 (212)	618	0.782	H estimate depends on phase interpretation

* The full records for shot 2 with phases P3 and P4 are not yet available, and H estimation cannot be conducted.

At our request Dr. Mariana Eneva of Maxwell Technologies/Systems Division provided a preliminary analysis of the observed shock wave phases, showing that interpretation #2 presented before is apparently the correct one and not #3 (M.Eneva, personal communication). According to this analysis P4 is the bottom reflection. The terminology used in REFMS (code for modeling of surface reflections, and bottom reflections and refractions due to sound-velocity gradients, Eneva et al., 2001) for waves like P3 is "precursory arrival", which is used for any shock ray that appears before a shock wave obeying Snell's reflection laws (seismologists refer to these as "head" waves propagating along the interface). The bottom velocity V_b that fits best the width of P3 is 3500 m/s (if $V_b < 3200$ m/s, P3 becomes too wide; if $V_b > 3600$, then P3 disappears). Some estimates were made regarding a second, higher-velocity layer in the bottom, beneath the sediments. In this case density and thickness of the sediment layer and velocity of the underlying layer become more important in the phase analysis. P3's width fits best with sediments 5-m thick, density 1800 gr/cm³, velocity 3500 m/s, and velocity for the layer beneath the sediments ~6000 m/s. The lowest bottom layers are by default considered of infinite thickness in the REFMS version used.

7.7.4 Enhanced Peak Pressures.

For the largest shot of 5000 kg, the main blasting agent CHEN AMON was about 97% of the total charge weight (see Table 35). According to the manufacturer's estimate the explosive energy is about 80% of TNT. Nevertheless, the measured peak pressures significantly exceeded the expected values from an equal TNT charge in ocean water (Table 38, Figure 79).

USACE (1991) and Joachim and Welch (1997), in a form similar to that provided by Cole (1948), give the relationships:

$$P(t) = P_m e^{-(t-t_a)/Q} \quad (7.3)$$

$$P_m \text{ (MPa)} = 53.1 R_s^{-1.13} \quad (7.4)$$

$$t_a = r/C_w \quad (7.5)$$

$$Q_{(s)} = 9.2 \cdot 10^{-5} W^{1/3} R_s^{0.18} \quad (7.6)$$

$$R_s \text{ (m/kq}^{1/3}) = r/W^{1/3} \quad (7.7)$$

where P_m is the peak pressure, t_a is the arrival time, Q is the time constant, W is the equivalent weight, in kg, of TNT, detonated in ocean/lake water, r is the lateral distance in m, R_s is the scaled distance, C_w is the sonic (acoustic) velocity in water, m/sec.

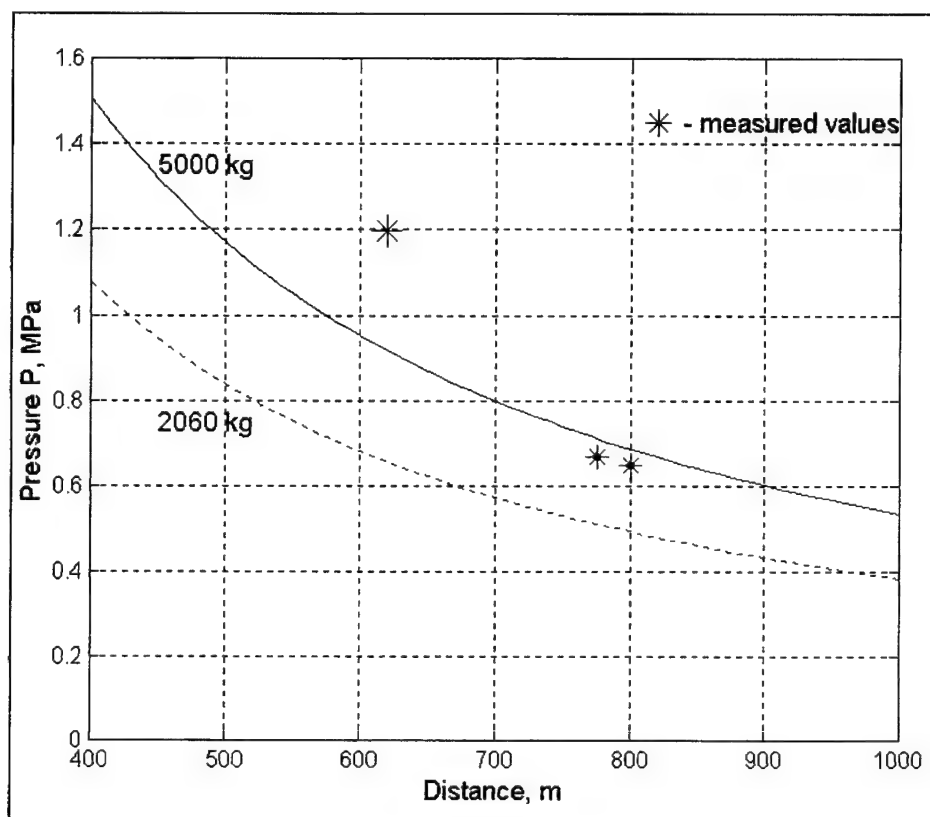


Figure 79. Peak water pressure vs distance for underwater explosions of TNT in the ocean water and measurements of the Dead Sea shots.

Table 38. Measured peak pressures in the shock waves.

Explosive weight, kg	Distance R, m	Sensor depth, m	Peak pressure, kPa		
			Estimated from Equation(16)	Measured	Ratio measured/estimated
2060	770	30	515	672	1.30
	795	25	496	654	1.32
5000	618	30	922	1230	1.33

The peak pressure values in Figure 79 are calculated from the equation (16). This observation of the enhanced pressures for the Dead Sea shots can be attributed to the acoustic impedance of the supersaline Dead Sea water being about 40% higher than in the ocean and, thus, yielding a much stronger shock wave impact (see Equation 20 below).

7.7.5 Estimation of the Shock Wave Energy.

Shock wave energy flux density is calculated as (Cole, 1948):

$$E_{DS} = Z_{DS}^{-1} \int P^2(t) dt \quad (7.8)$$

where Z_{DS} is the Dead Sea water acoustic impedance, $Z_{DS} = \rho_{DS} \cdot C_{DS} = 1236 \text{ kg/m}^3 \times 1770 \text{ m/sec}$, and $P(t)$ is the curve-fit equation (Figure 81) with estimated time constant $Q_{DS} = 0.0018458 \text{ sec}$:

$$P_{DS}(t) = 1.23 \cdot \exp[-(t - 0.3592)/Q_{DS}] \quad (\text{in MPa}) \quad (7.9)$$

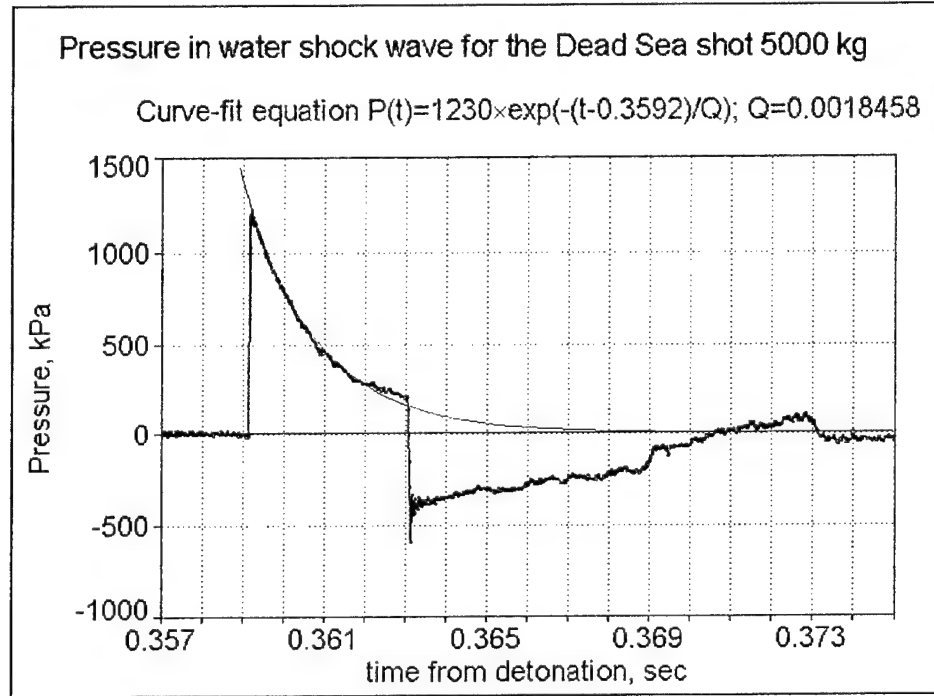


Figure 80. Primary and surface-reflected shock waves and the curve-fit equation.

Integral in Equation 20 is calculated from the arrival time $t_a = 0.3592 \text{ sec}$ to $t = t_a + 6.7Q$ (Cole, 1948).

$$E_{DS} = \frac{1}{Z_w} \int_{t_a}^{t_a + 6.7Q} (10^3 \times 1230 \times \exp(-(t - 0.3592)/Q))^2 dt = 1219 \text{ joule / m}^2$$

The full shock wave energy can be calculated (at distance $r = 618 \text{ m}$) as:

$$E_s = E_{DS} \times 4\pi r^2 = 0.585 \times 10^{17} \text{ erg}$$

Specific energy of the explosive CHEN AMON, used in the experiment, according to the manufacturer specifications: $900 \text{ cal/gr} = 3.8 \times 10^{13} \text{ erg/kg}$, and the full explosive energy is: $E_e = 1.9 \times 10^{17} \text{ erg}$. Then the share energy estimate for the primary shock wave is:

$$E_s/E_e = 30.8\%$$

This value seems to be reasonable although it slightly exceeds the free-water estimate 23-24%, from shallow reservoir research (Eneva et al., 2000), and a 25% estimate at distances more than 15 charge radii by Pritchett (1971).

7.7.6 Estimate of the TNT Equivalent.

It is assumed that the primary shock wave energy flux for the Dead Sea shot ($W=5000$ kg of CHEN AMON) E_{DS} equals the shock wave energy flux E_{OC} for the "equivalent" TNT charge W_T exploded in the ocean water:

$$E_{DS} = E_{OC} \quad (7.10)$$

The value E_{OC} is calculated from Equations (16-20):

$$E_{OC} = Z_{OC}^{-1} \int [53.1 R^{-1.13} \exp(-t/Q_{OC})]^2 dt \quad (7.11)$$

where the impedance for the ocean water is $Z_{OC}=1030 \text{ kg/m}^3 * 1536 \text{ m/sec}$, and Q_{OC} depends on W_T , as in Equation (18). The value E_{DS} is calculated from Equation (20,21):

$$E_{DS} = Z_{DS}^{-1} \int [1.23 * \exp(-t/Q_{DS})]^2 dt \quad (7.12)$$

Finally, the TNT equivalent to the 5000 kg charge of CHEN AMON exploded in the Dead Sea is determined from Equations (22-24) as:

$$W_T = 4010 \text{ kg}$$

This value corresponds to the manufacturer's estimate of the explosive CHEN AMON energy as about 80% of TNT.

7.8 Seismic Observations.

Temporary short-period seismic stations and accelerographs (A-800) were placed along the Dead Sea coast. as shown on Figure 81.

7.8.1 Accelerograph Records.

The station coordinates are presented in Table 39, and PGA measurements are shown in Table 40. Spectral content of accelerograms was analyzed; results are presented on Figures 82-83.

Table 39. Coordinates of the accelerograph stations.

Station	DMS		ITM	
	Latitude N	Longitude E	X, km	Y, km
N8/Mitzpe-Shalem	31°34'12.32" 31.57009	35°24'2.07" 35.40058	188.05	108.05
P8/Pump Station	31°19'43.73" 31.32881	35°24'8.57" 35.40238	188.28	81.81
HOF/Mineral Beach	31°33'19.41" 31.55539	35°24'17.3" 35.40481	188.54	106.92

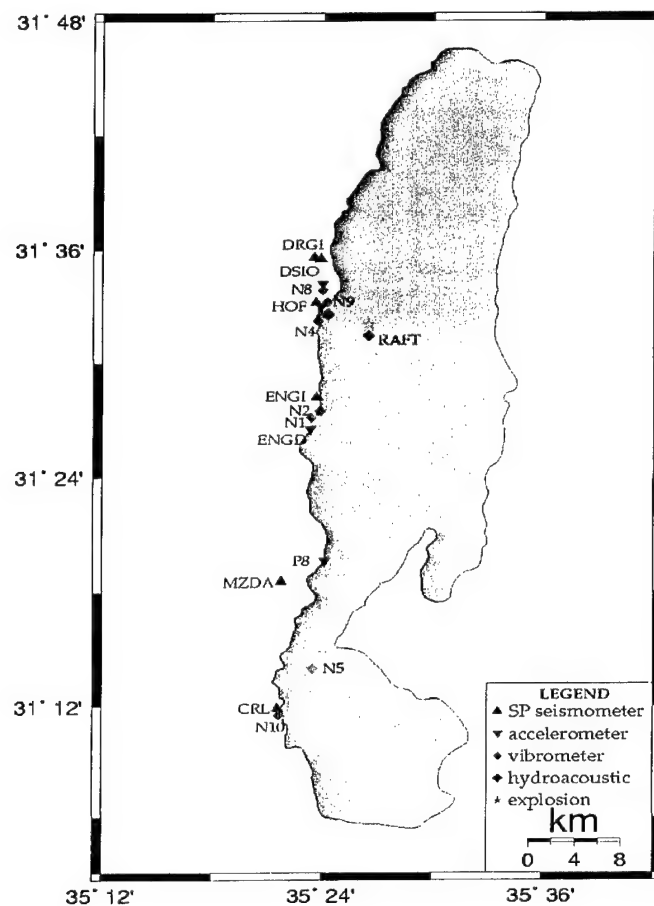


Figure 81. Location of nearby stations recorded the explosions.

Table 40. Recorded Peak Ground Accelerations

Location	Coordinates			direction	Expl. 2060 kg		Expl. 5000 kg	
	X [km]	Y [km]	Distance [km]		PGA (1/g)	PGV (m/s)	PGA (1/g)	PGV (m/s)
Mitzpe Shalem	188.053	108.053	5.3	V	0.0066	0.00062	0.0129	0.0033
				NS	0.0068	0.00061	0.0115	0.0034
				EW	0.0078	0.00071	0.0117	0.0023
Mineral Beach	188.454	106.920	4.3	V	0.0652	0.0023	0.073	0.0038
				NS	0.0479	0.0032	0.0769	0.0029
				EW	0.0591	0.0033	0.063	0.004
Pump Station /P8/	188.275	81.810	23.3	V	-	-	0.005	0.000771
				NS	-	-	0.0065	0.002088
				EW	-	-	0.0085	0.003227

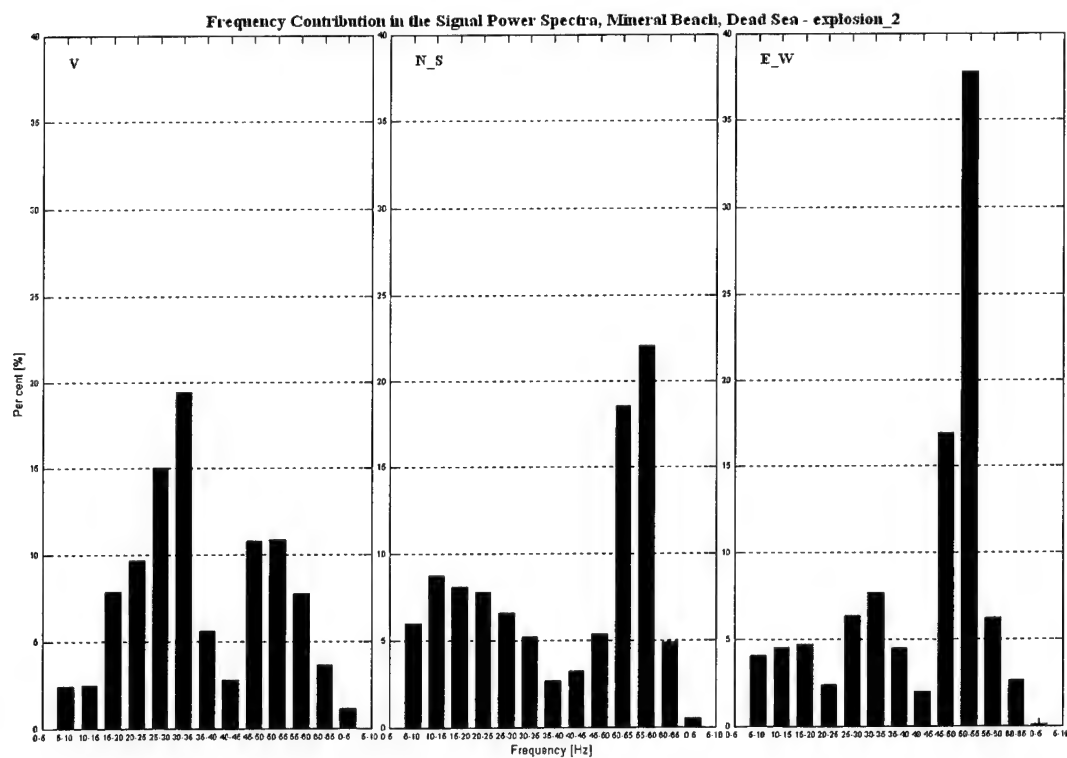
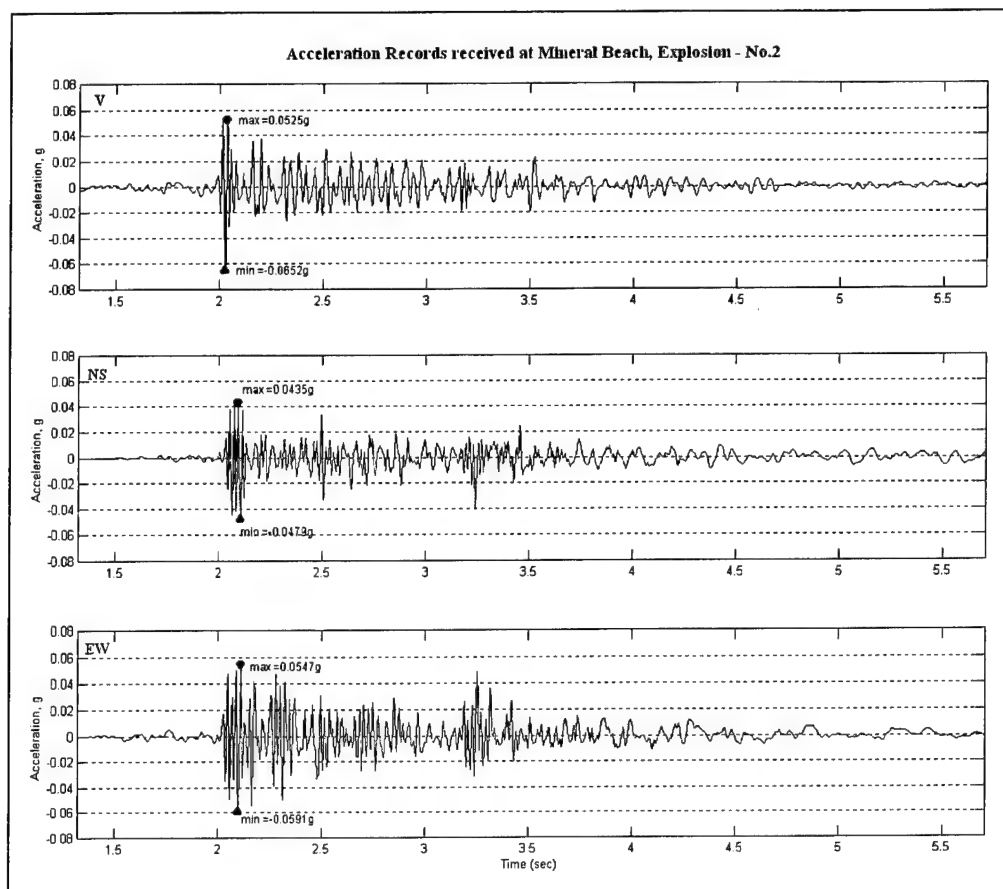


Figure 82. Accelerograms and power spectra observed at the closest station at Mineral Beach from the shot 2060 kg.

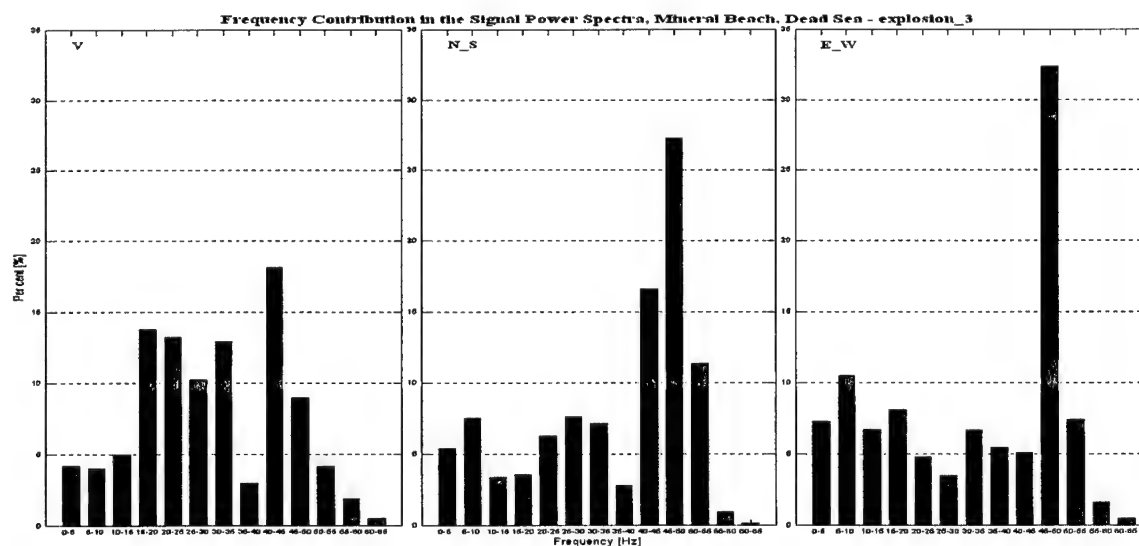
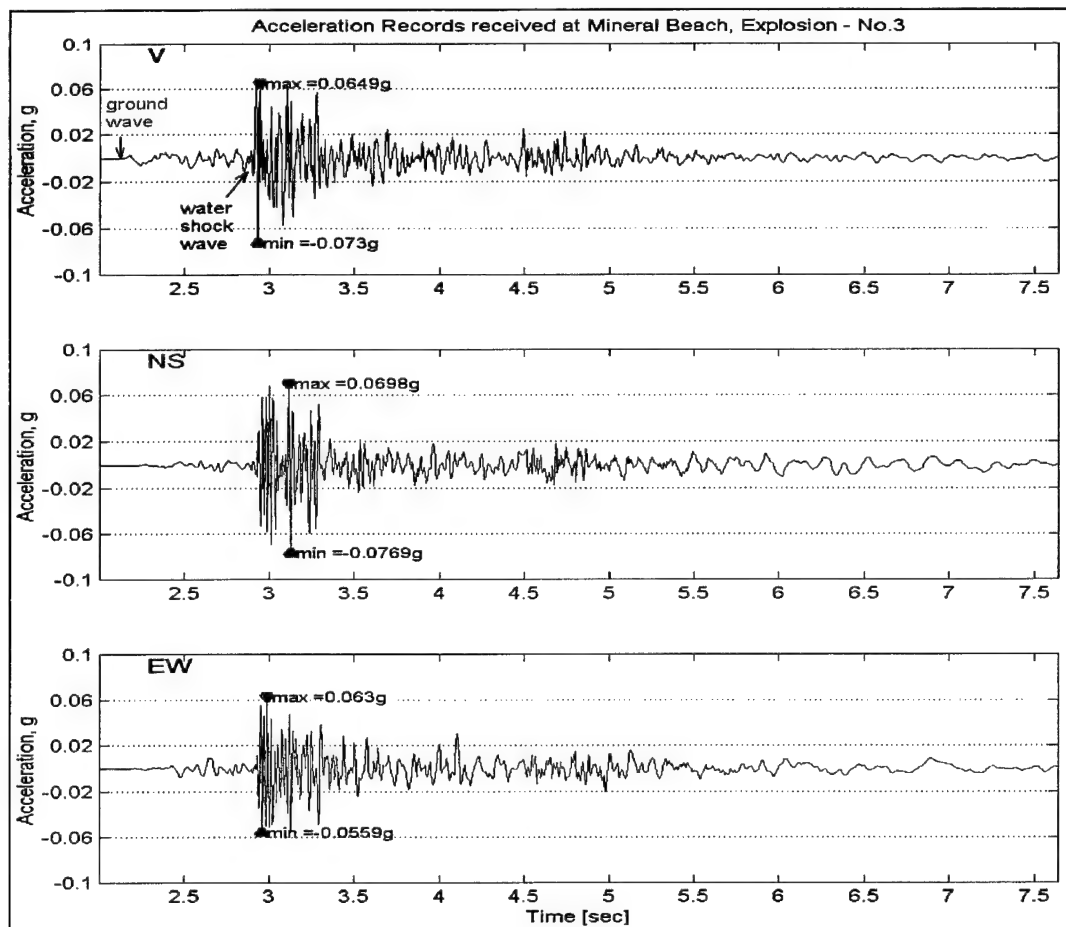


Figure 83. Accelerograms and power spectra observed at Mineral Beach from the 5-ton shot

The high-frequency and high-amplitude accelerations at the station at Mineral Beach (HOF on the map in Figure 81) closest to the explosion, located a few meters from the shore, were generated by the impact on the sea shelf by the water shock waves (Figure 83). This is evident from the joint recording of a seismometer, co-located with the A-800 and a nearby hydrophone placed in water, shown in Figure 84.

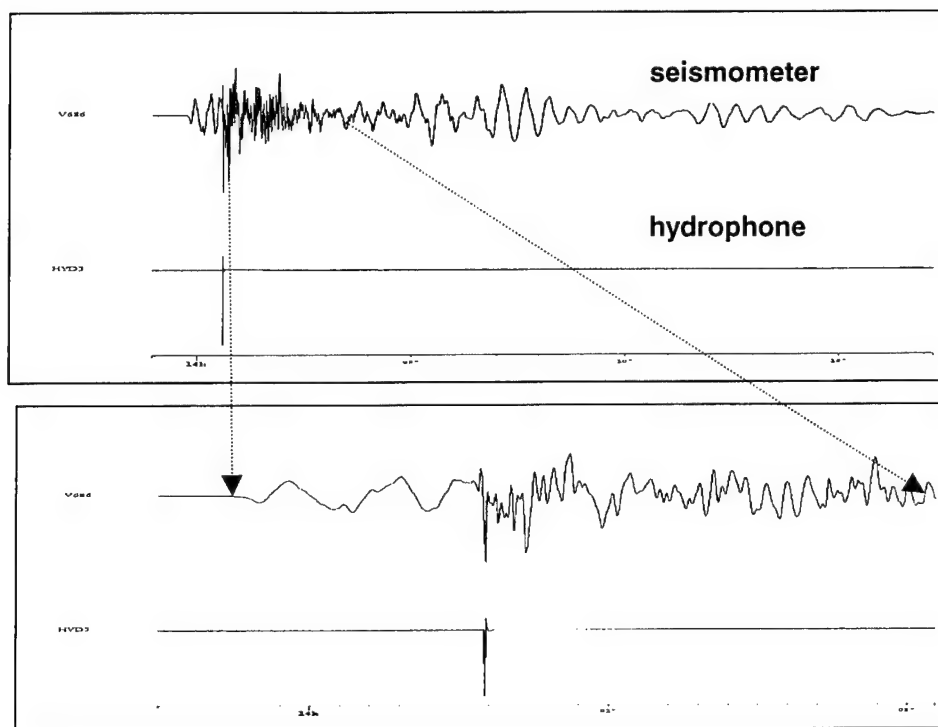


Figure 84. Seismometer and hydrophone recording of the 2060 kg explosion at Mineral Beach.

The high frequency (about 40-55 Hz) energy, generated by the shock wave-sea shelf interaction, is observed in the power spectra (Figure 85). It is most pronounced on the E-W component, which was close to the radial direction.

However, comparing seismic effects for the two explosions (2060 and 5000 kg), more significant enhancement of peak amplitudes (see Table 40), as well as seismic energy (see Figure 85) at the N-S (near transversal) component, may be observed. A little surprising is the small decrease of ground motion energy observed at the E-W (radial) component for the larger shot (Figure 85).

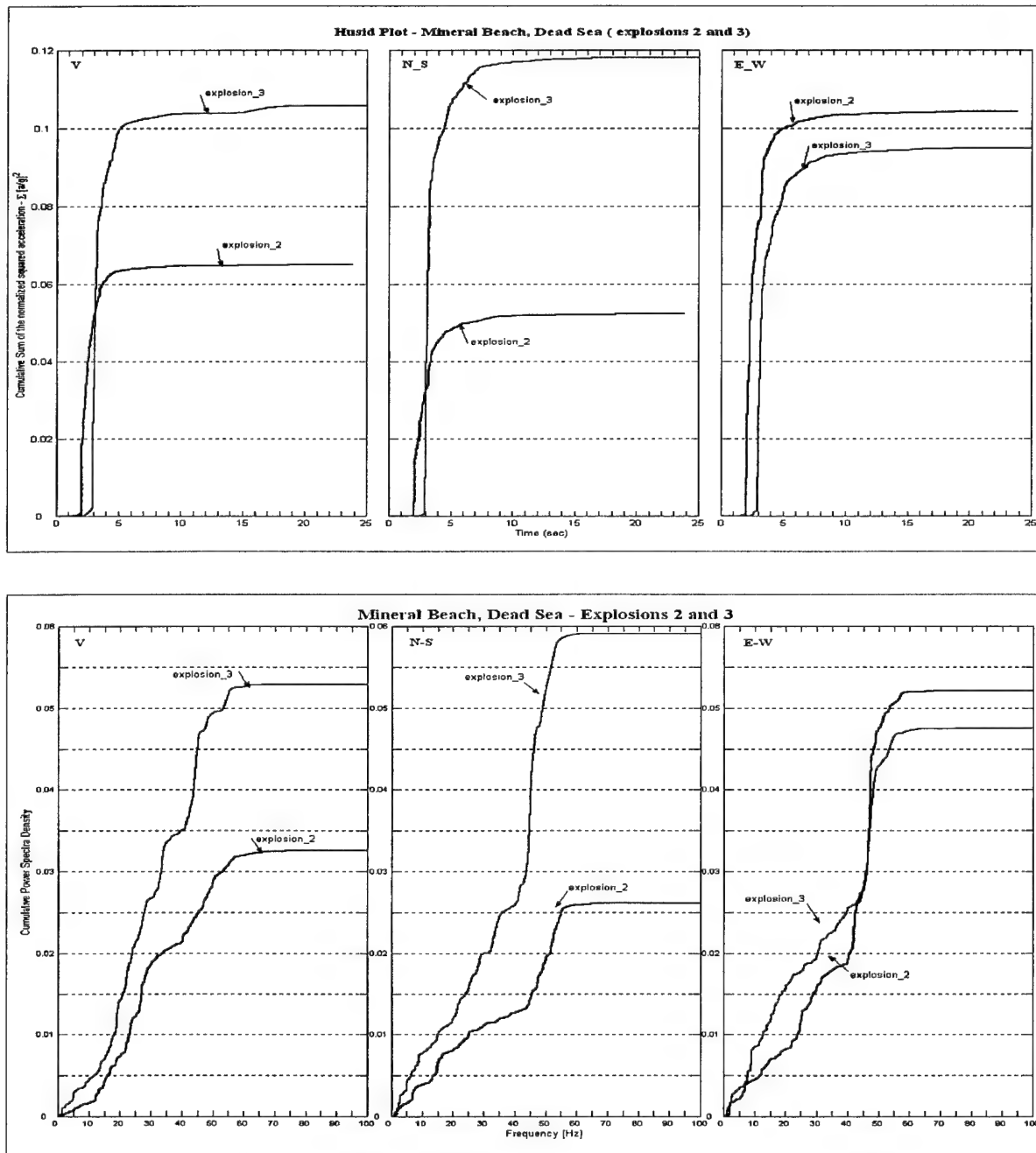


Figure 85. Cumulative Sum of the normalized squared acceleration and Power Spectra Density of accelerograms recorded at Mineral Beach from two 2-ton and 5-ton explosions.

7.8.2 Ground Motions in the Hotel Area.

For monitoring safety conditions during the experiment two stations with horizontal components (N-S and E-W) were placed on the roof of the 7-story "Carlton" Hotel (Ein-Boqeq area, see station CRL on the map in Figure 81), and two short-period 3C stations were deployed on the ground near the hotel at distances of 20 and 54 meters from the building (free field). Sample seismogram of the 2060 kg explosion is shown on Figure 86. Maximal ground velocity amplitudes are presented in Table 41.

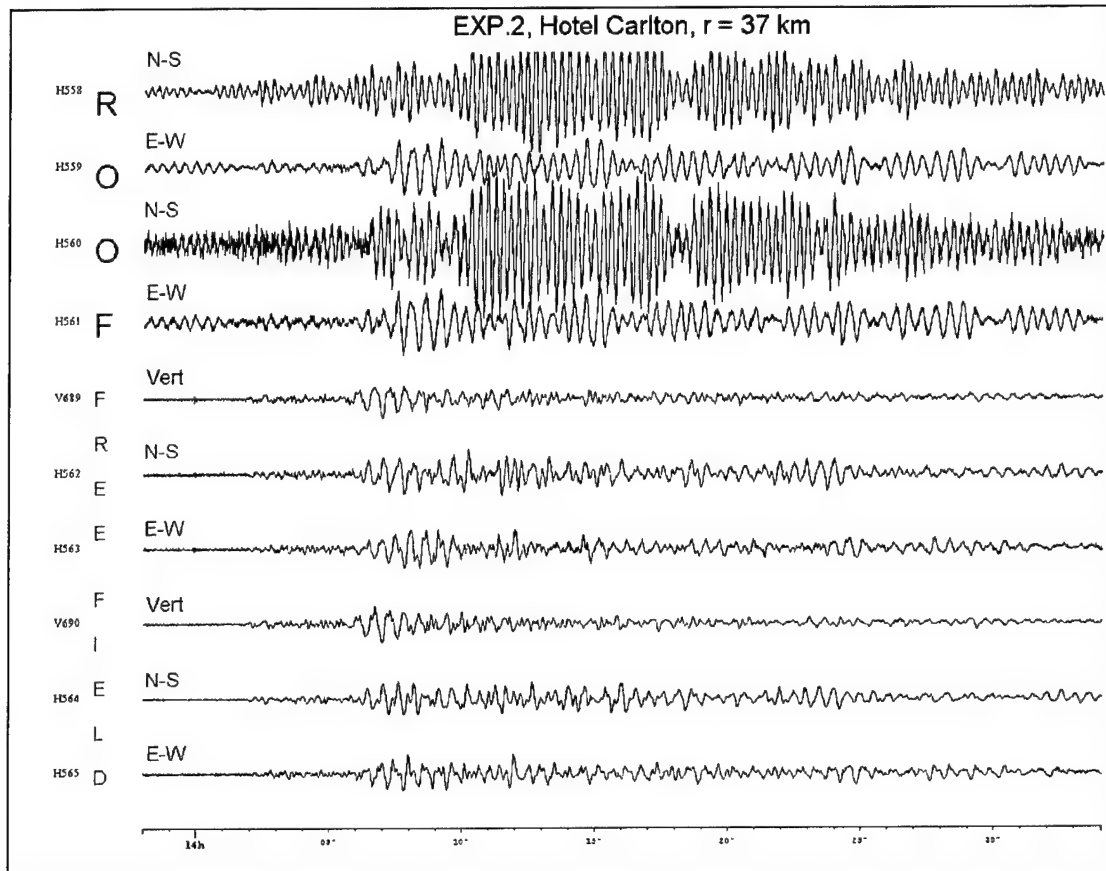


Figure 86. Seismometer recordings of the 2060 kg explosion. Note differences in building and ground seismograms which are plotted in the same scale.

Table 41. Peak-to-peak amplitudes (micron/sec) of ground motions near the Carlton Hotel.

Direction	Station 3 (20 m from the Hotel)			Station 4 (54 m from the Hotel)		
	500 kg	2060 kg	5000 kg	500 kg	2060 kg	5000 kg
Vertical	56.6	78.5	96.2	34.6	90.2	87.0
N-S	74.0	106.0	181.0	67.0	88.7	169.0
E-W	66.5	96.5	167.7	57.9	93.4	139.9

Smoothed amplitude spectra of ground and building motions (Figure 87) demonstrate common spectral bubble modulation as well as specific features of natural (resonance) frequencies in the building spectra which are different in E-W (building long dimension) and N-S (short dimension).

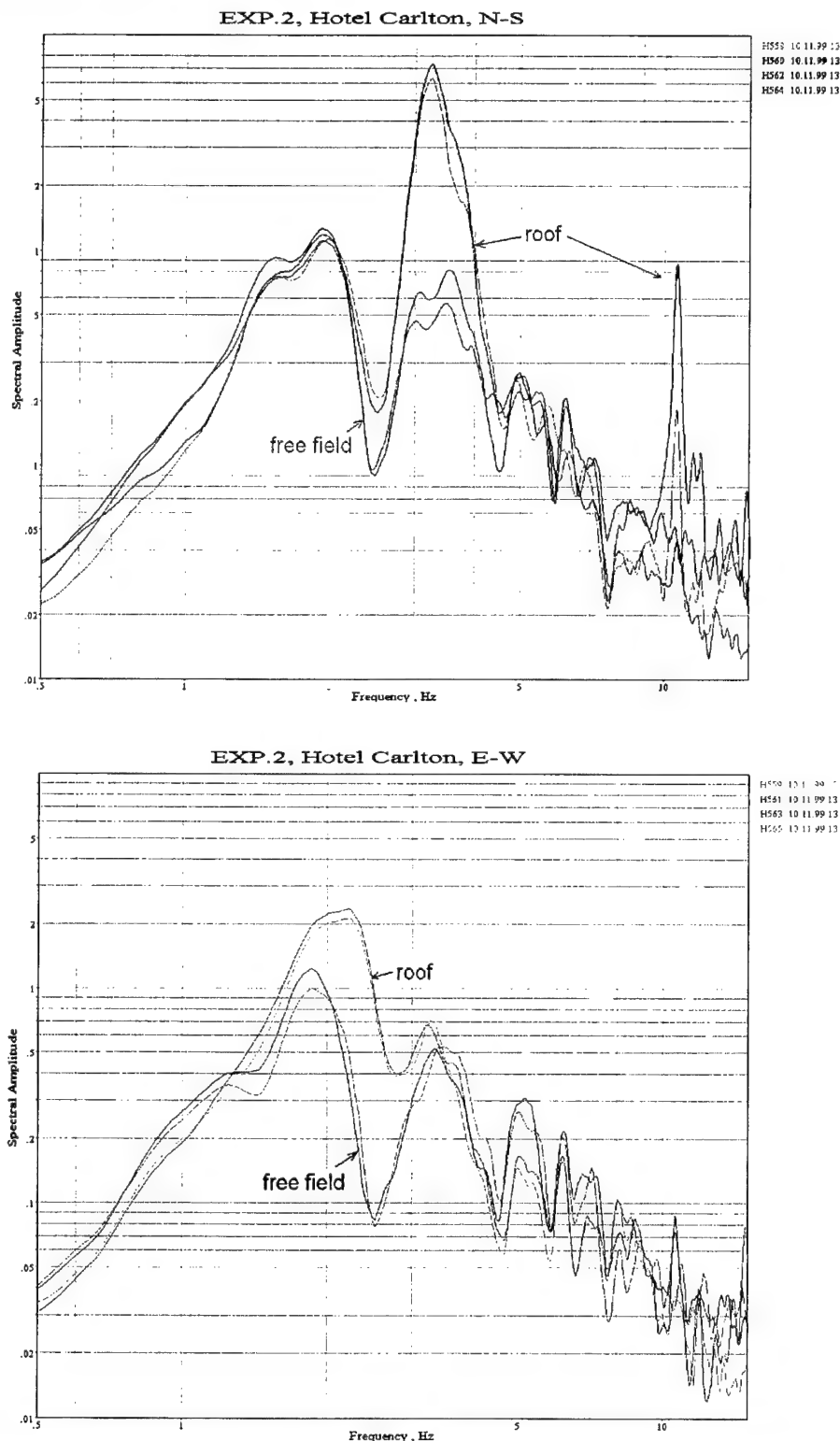


Figure 87. Smoothed spectra of the whole seismogram ($t = 40$ sec) of the Dead Sea explosion 2060 kg, recorded on the building and at nearby ground.

7.8.3 Observations at Local Distances and Seismic Efficiency.

The explosions were recorded by the Israel Seismic Network (ISN), consisting of 23 SP stations (Figure 88), two auxiliary IMS stations MRNI (Figure 89) and EIL (recorded the 2-ton and 5-ton explosions, Figure 90), and Contributing National Facility (CNF) station, JER (Figure 91). The short-period small-aperture microarray EILESA north of Eilat recorded all the explosions (Figure 92). Data were also obtained at three temporary (surrogate) BB stations AMZI, DIMI and MMLI (Figure 93), which were deployed at sites of planned CNF stations. Data from several Jordanian stations, also presented on the map, were obtained on-line at the Geophysical Institute of Israel (see station AQBJ in Figure 88); data for other stations (see, for example, Figure 94) were supplied by our Jordanian colleagues (Dr. Abdel-Qader, NRA). Station locations are shown on Figure 1 (Section 3.1). Two small test shots (25 kg), conducted two weeks before the main series at the same location and depth, are also considered in the analysis.

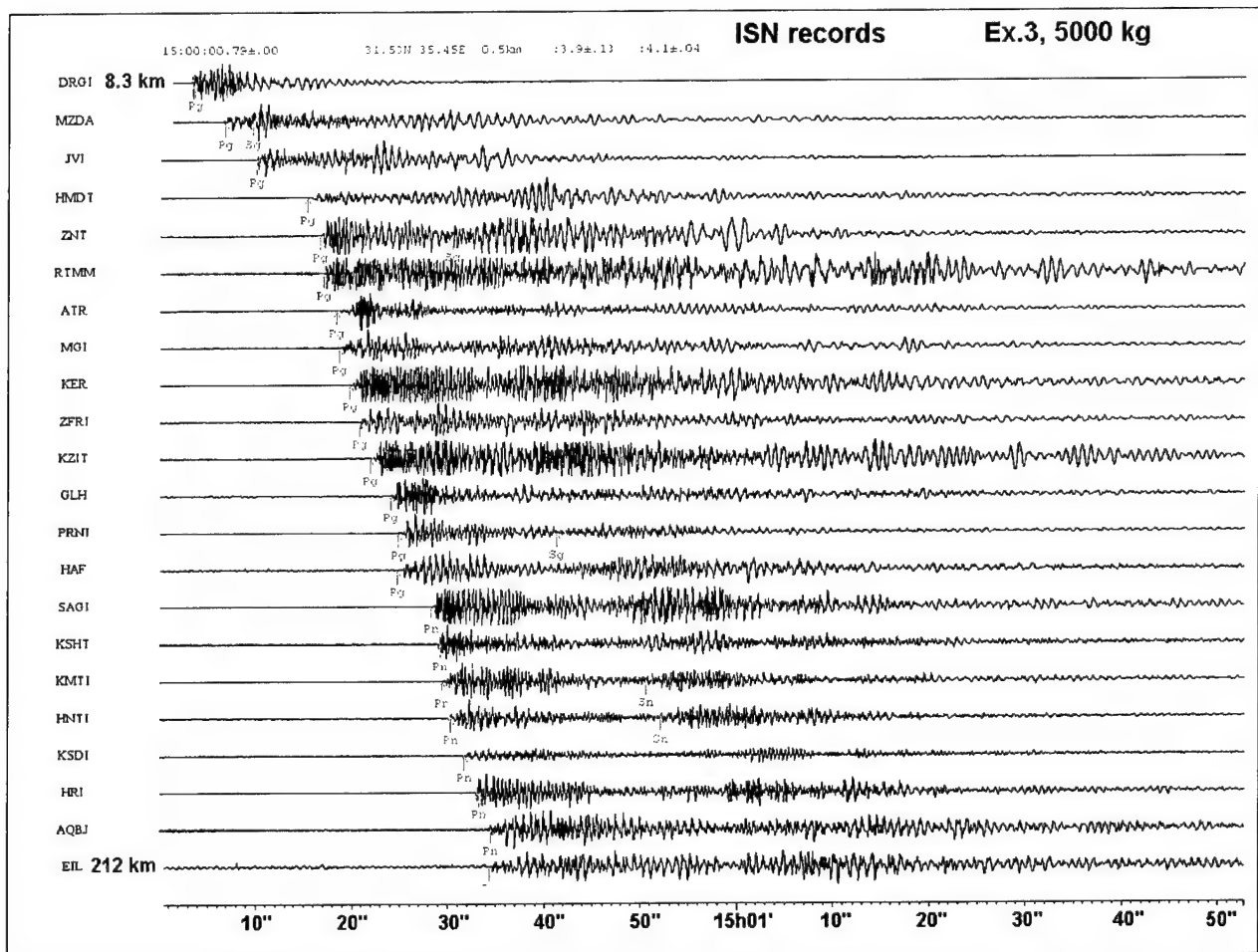


Figure 88. ISN recording of the largest explosion.

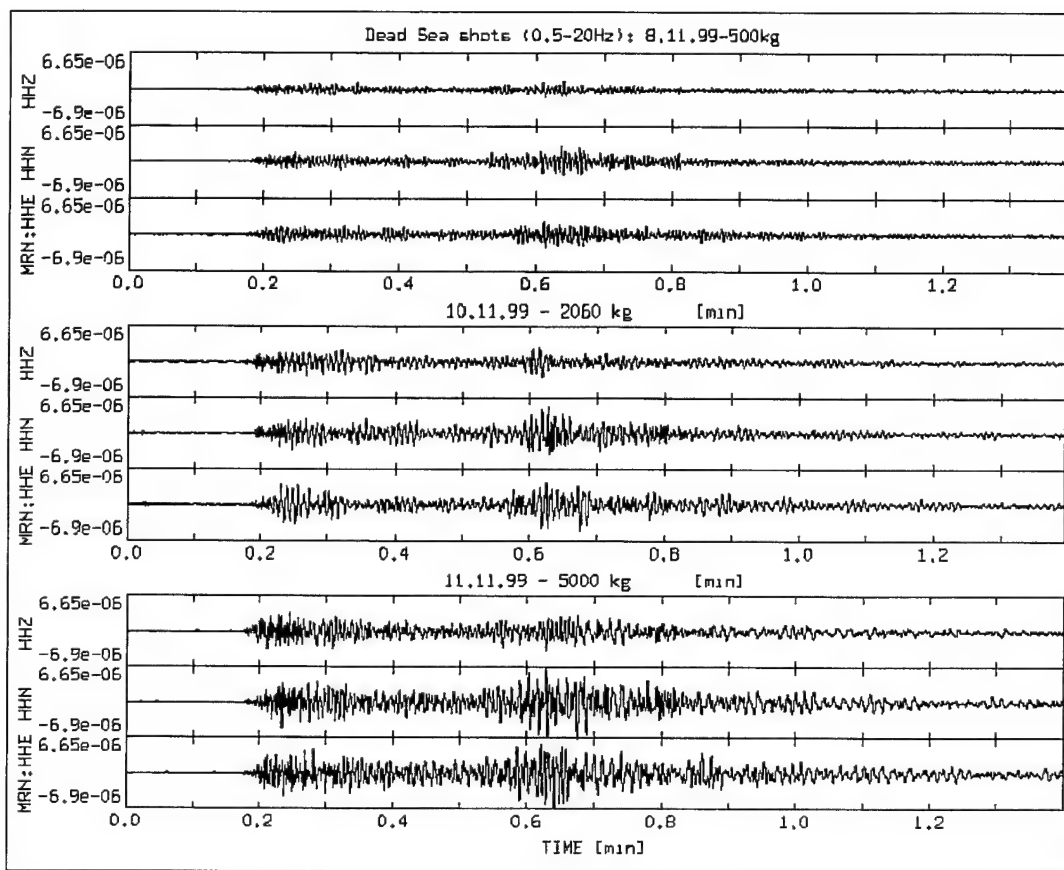


Figure 89. Records (the same scale) of the three explosions at IMS station MRNI (164 km).

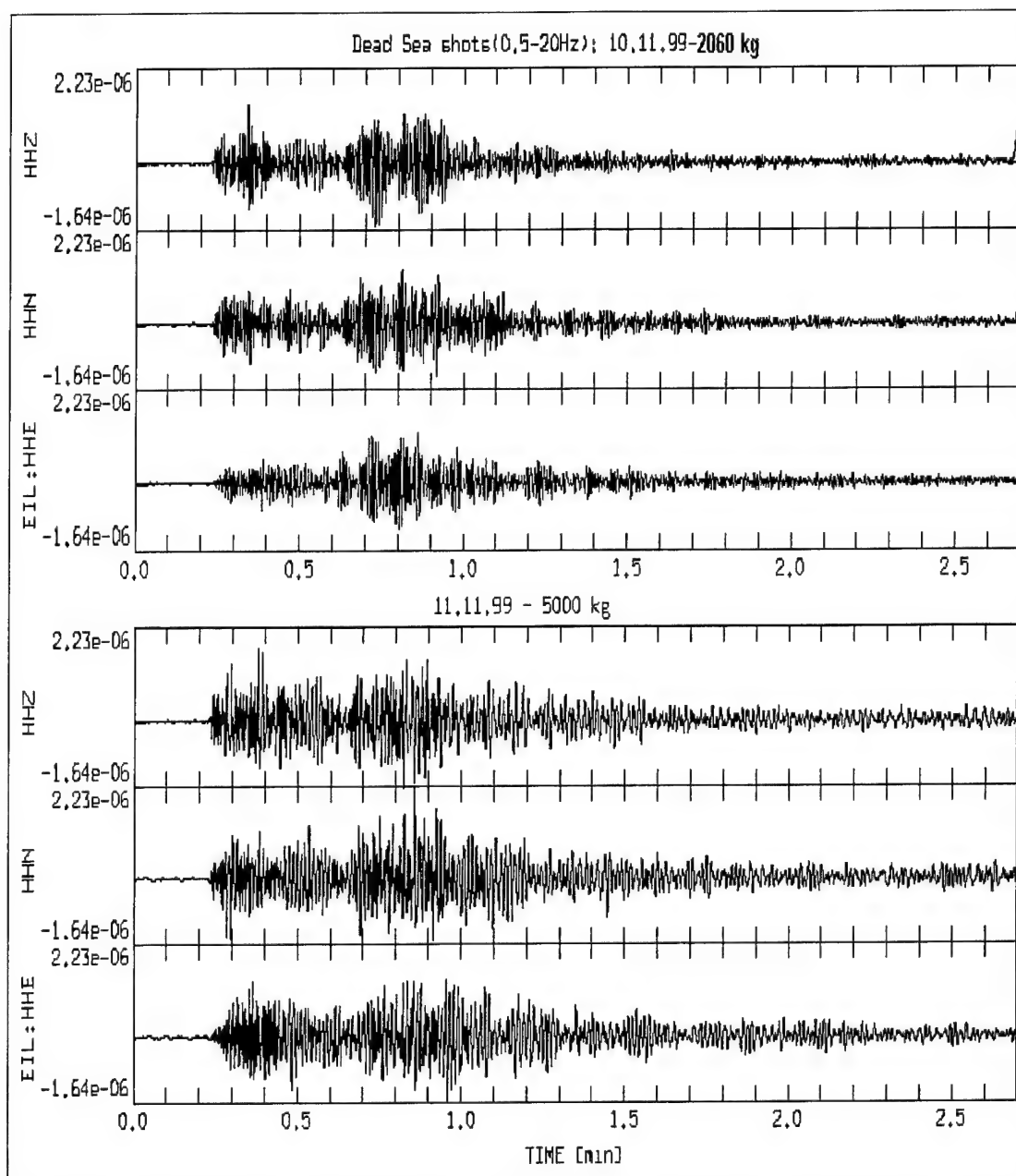


Figure 90. Records (the same scale) of the two explosions at IMS station EIL (212 km).

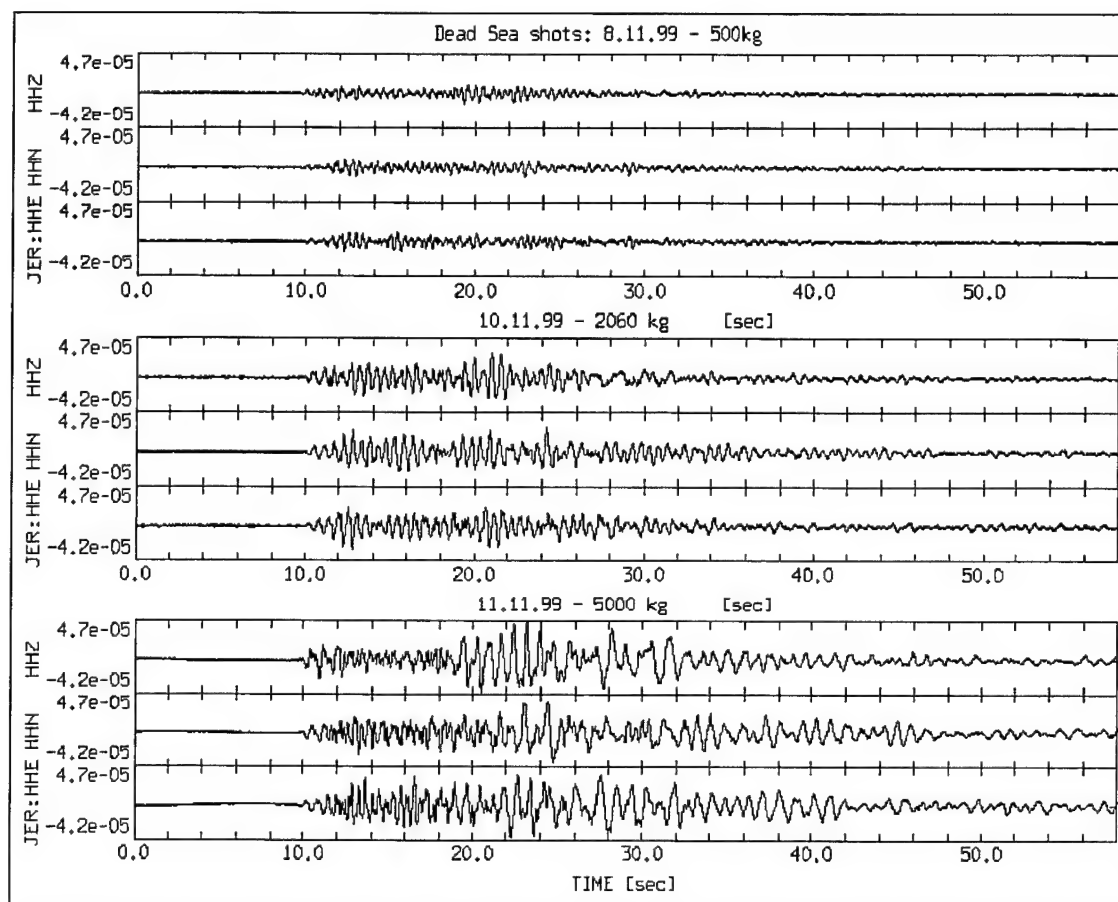


Figure 91. Records (in the same scale) of the three explosions at BB station JER (35 km).

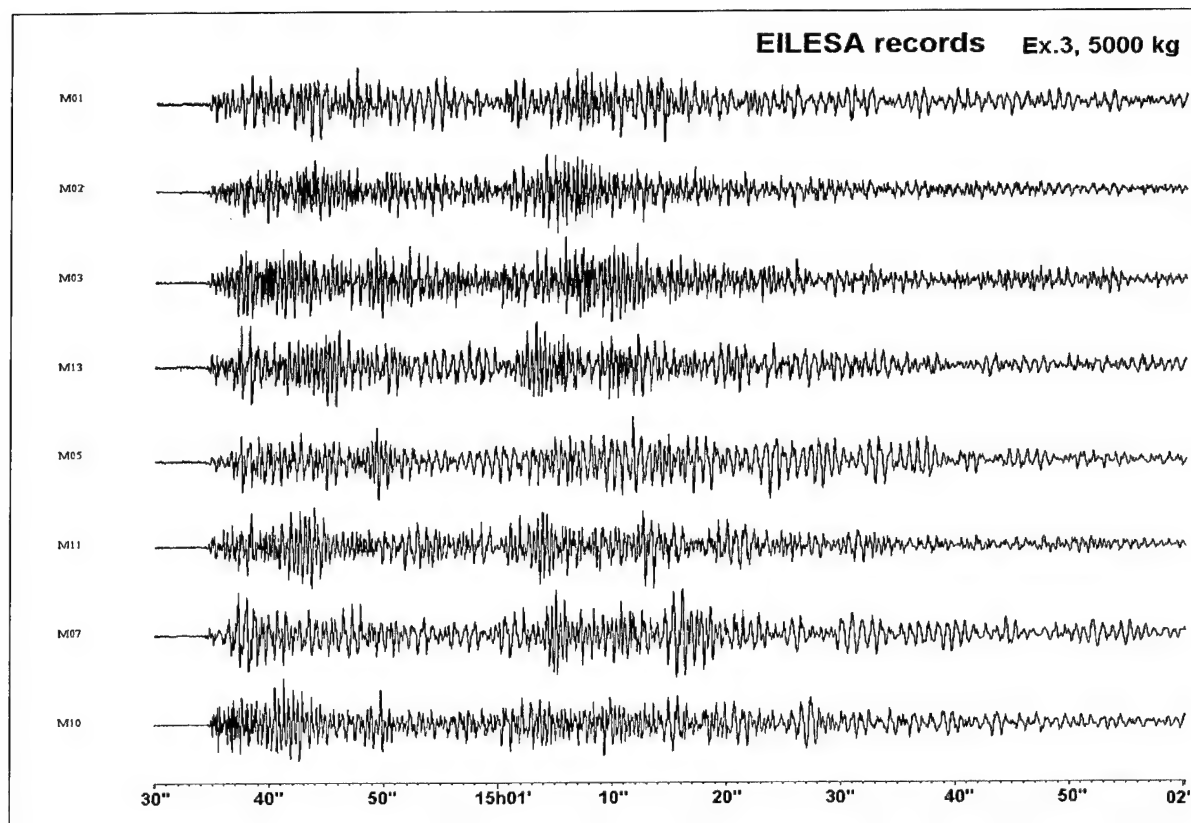


Figure 92. Records of the largest explosion at EILESA array (211 km).

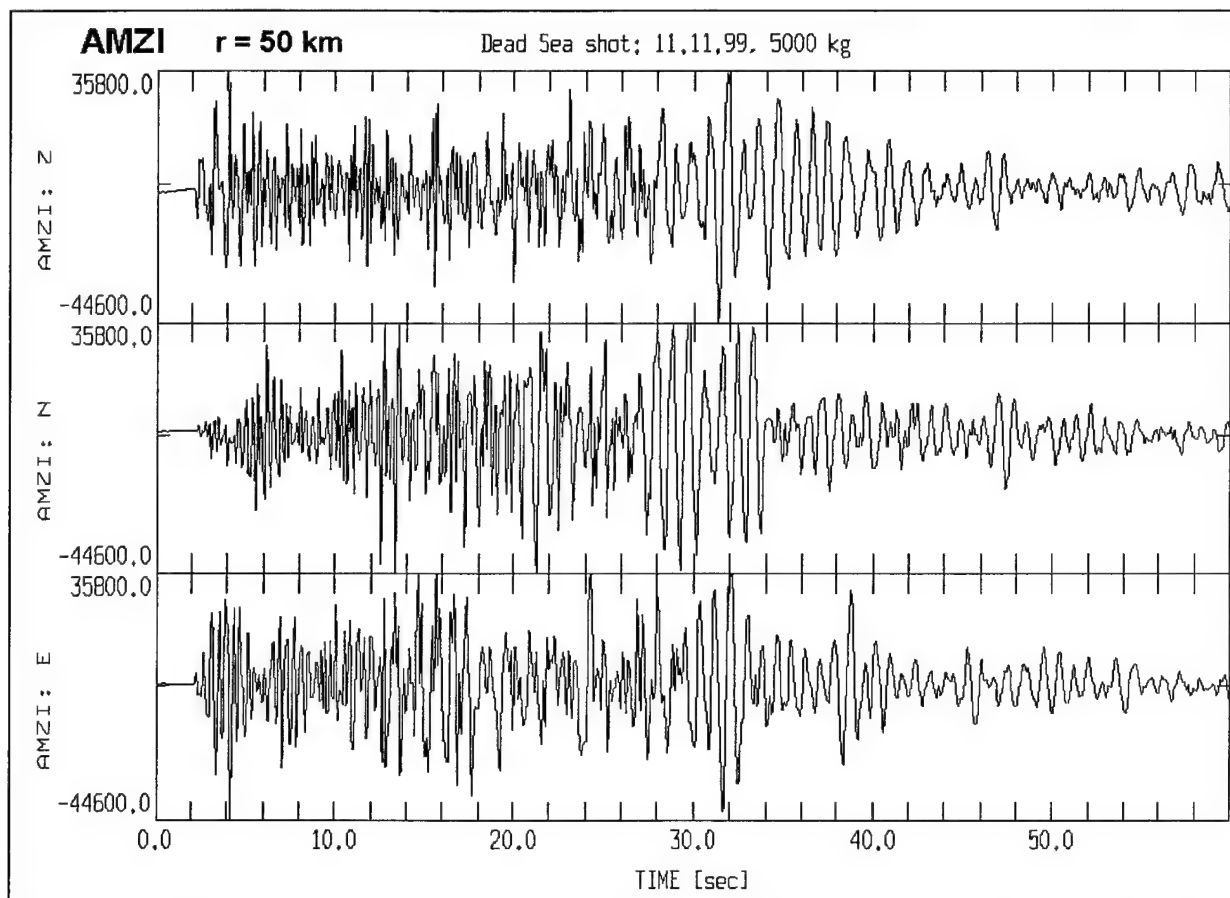


Figure 93. Records of the largest explosion at CNF station AMZI.

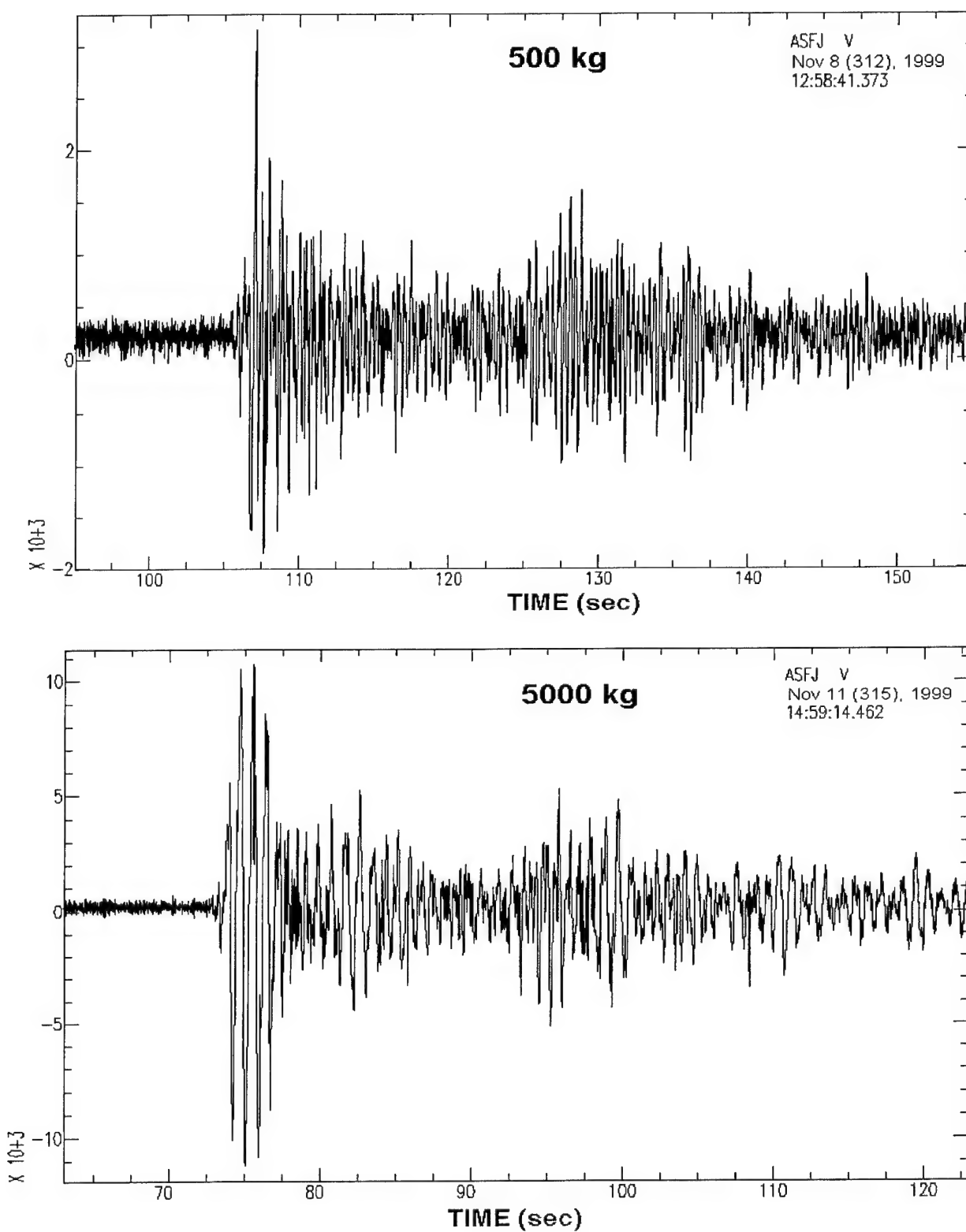


Figure 94. Seismograms (normalized) of the Jordanian station ASFJ (vertical component).

Increase in the explosion charge weight caused an appropriate rise of radiated seismic energy and corresponding magnitudes and signal amplitudes (Figures 89-91, 94), as well as signal periods and wavelengths. Observed local (duration) magnitudes (Table 6.12, Figure 95), determined from short-period ISN recordings, correspond well to the values predicted at the design stage of the experiment by the empirical relationship (Gitterman, 1998):

$$M=0.285+\log_{10}(W, \text{ kg}) \quad (7.13)$$

based on the 1993 series of small scale Dead Sea shots (Gitterman et al., 1998).

Table 42. Comparison of predicted and observed local magnitudes and fundamental frequencies of underwater explosions in the Dead Sea (Oct.-Nov. 1999).

Charge W, kg	Local (ISN based) magnitude M_L		Frequency f_b , Hz / Bubble period T_b , sec		
	Predicted (Equation 25)	Measured	Predicted (Equation 27) shot depth $d=70\text{m}$	Measured	
				average from ISN spectral maxima	from autocorrelation analysis of IMS stations (CMR event Report, 1999)
25 (two shots)	1.7	1.7 1.9	7.20/0.139	6.50/0.154	-
500	3.0	3.1	2.72/0.367	2.61/0.383	2.70/0.37
2060	3.6	3.6	1.70/0.589	1.78/0.561	1.82/0.55
5000	4.0	3.9	1.26/0.791	1.28/0.782	1.30/0.77

The high magnitudes with relatively low charge weights confirm the high seismic efficiency of underwater explosions in the Dead Sea, significantly exceeding the upper limit curve for all known chemical and nuclear explosions in hard rock (Khalturin et al., 1997), presented on Figure 95. The observed magnitudes and amplitudes of seismic waves verify that the whole charge was properly detonated in all cases.

The explosion seismic efficiency was estimated by determination of seismic waves energy recorded at local seismic stations relative to the explosives energy. The energy release of an earthquake is an important physical quantity that describes the earthquake. Kanamori et al. (1993) presented a method for the estimation of seismic energy, based on time-domain integration, of local and regional velocity-squared seismograms observed at TERRAscope in Southern California. They were able to obtain reliable energy estimations, since the propagation effect is of minor importance at short distances. Recently, Mayeda and Walter (1996) proposed to estimate the energy from coda envelopes using broad band data at different frequency ranges. The Mayeda and Walter (1996) method seems to be better than that of Kanamori et al. (1993). Calibration of the region is now in progress and once achieved, a refinement of the results is expected when applying the Mayeda and Walter method. In the presented research we used the Kanamori et al. (1993) method to estimate the seismic energy of the Dead Sea explosions.

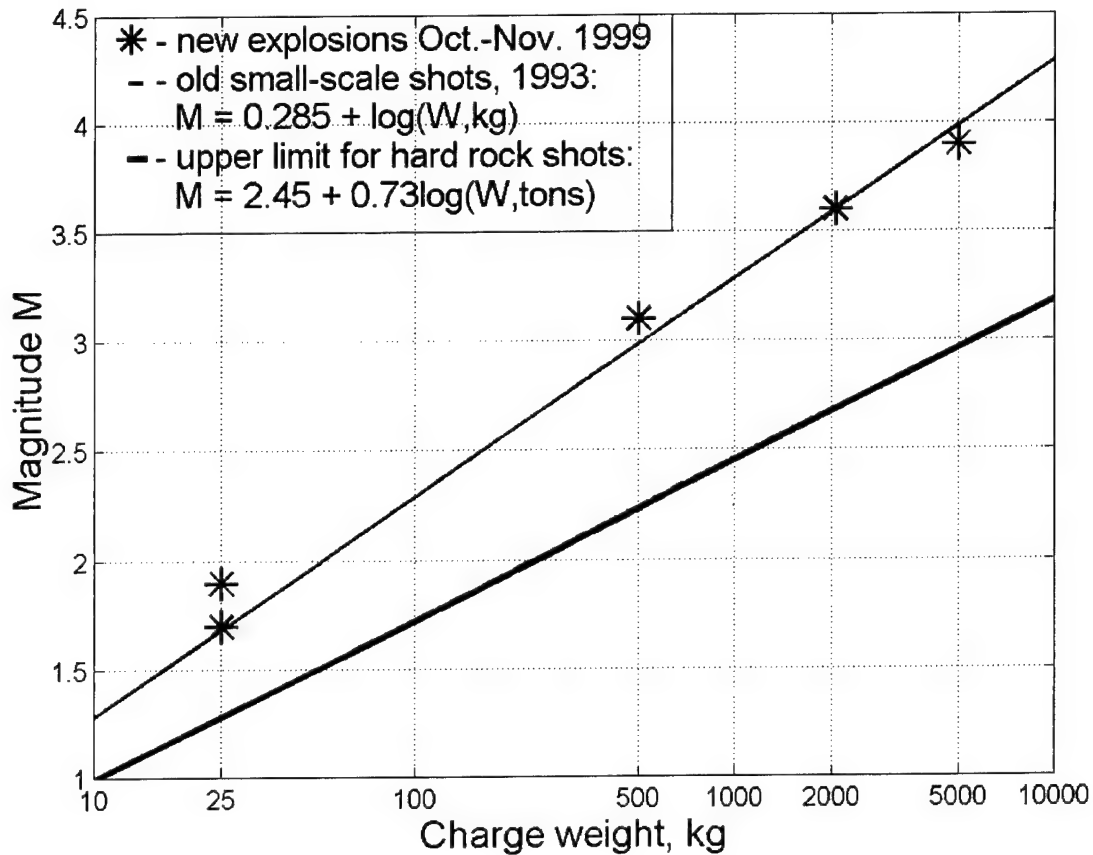


Figure 95. Magnitude versus charge weight for the Dead Sea explosions.

Hofstetter and Shapira (2000) estimated the attenuation function in the short period frequency range (0.5 Hz to 10 Hz)

$$A(R) = (1.850 \pm 0.005) \log R + (0.00460 \pm 0.00005) R \log e + 0.05 \quad (7.14)$$

where R is the hypocentral distance $R^2 = \Delta^2 + h^2$ in the distance range of $50 \leq R \leq 1500$ km, Δ is the epicentral distance, h is the source depth (close to zero in our case). The standard deviation is 0.24 (or uncertainty factor of 1.7). The function (26) was utilized for estimation of the seismic energy for the Dead Sea shot, observed at several 3C short period and broad band stations of the Israel Seismic Network, including IMS and CNF stations (see Figure 1), located at various distances (range 50-211 km) and azimuths. Figure 96 shows the seismic efficiency, estimated as:

$$Efficiency = \frac{seismic\ energy}{Explosives\ energy}$$

where, according to the manufacturer's specifications, the energy of the Chen Amon explosives used is given as 900 cal/gr = 3.8×10^{13} erg/kg. The efficiency values for different stations are averaged, and the variance is shown for different shots.

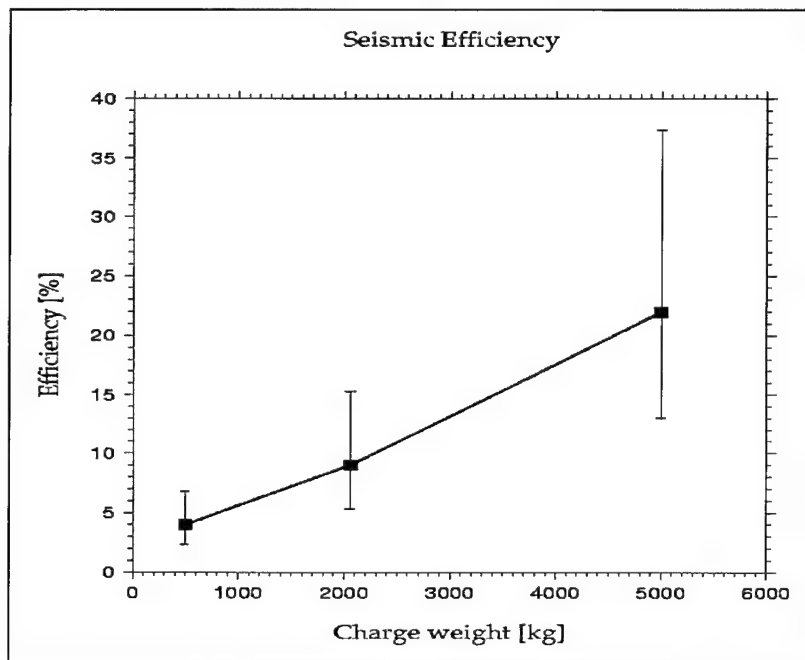


Figure 96. Seismic efficiency of the Dead Sea explosions estimated from seismograms of local short period and broad band stations, located in the distance range 50-200 km.

Evidently, a large part of the explosives energy was released in hot gases in the detonation vicinity, and the energy of initially radiated seismic waves was either absorbed or scattered in the media along the propagation path to a station. It is clear, however, that the efficiency of the underwater explosions in the Dead Sea (especially for the largest explosions 5000 kg), is much higher than for similar hard-rock shots, which reaches a few percents only (see also Figure 96).

The efficiency values for the 500 kg and 2060 kg shots are possibly underestimated, as well as the value for the 5-ton shot which seems to be a little overestimated (if compared with about 30% for the shock wave energy, see Section 7.7.5). Nevertheless the increasing trend corresponds to a lesser scattering of seismic energy in the crust at inhomogeneities and a lower intrinsic dissipation of seismic energy for longer wavelengths from larger shots.

7.8.4 Signal Features: Spectral Modulation.

The prominent azimuth and distance independent spectral modulation caused by the bubble pulse effect is evident in all SP and BB seismograms, especially for the 5-ton explosion. A clear frequency banding is observed in the smoothed amplitude spectra of the whole signal (50-60 sec) and in spectrograms (see examples on Figures 97 and 98).

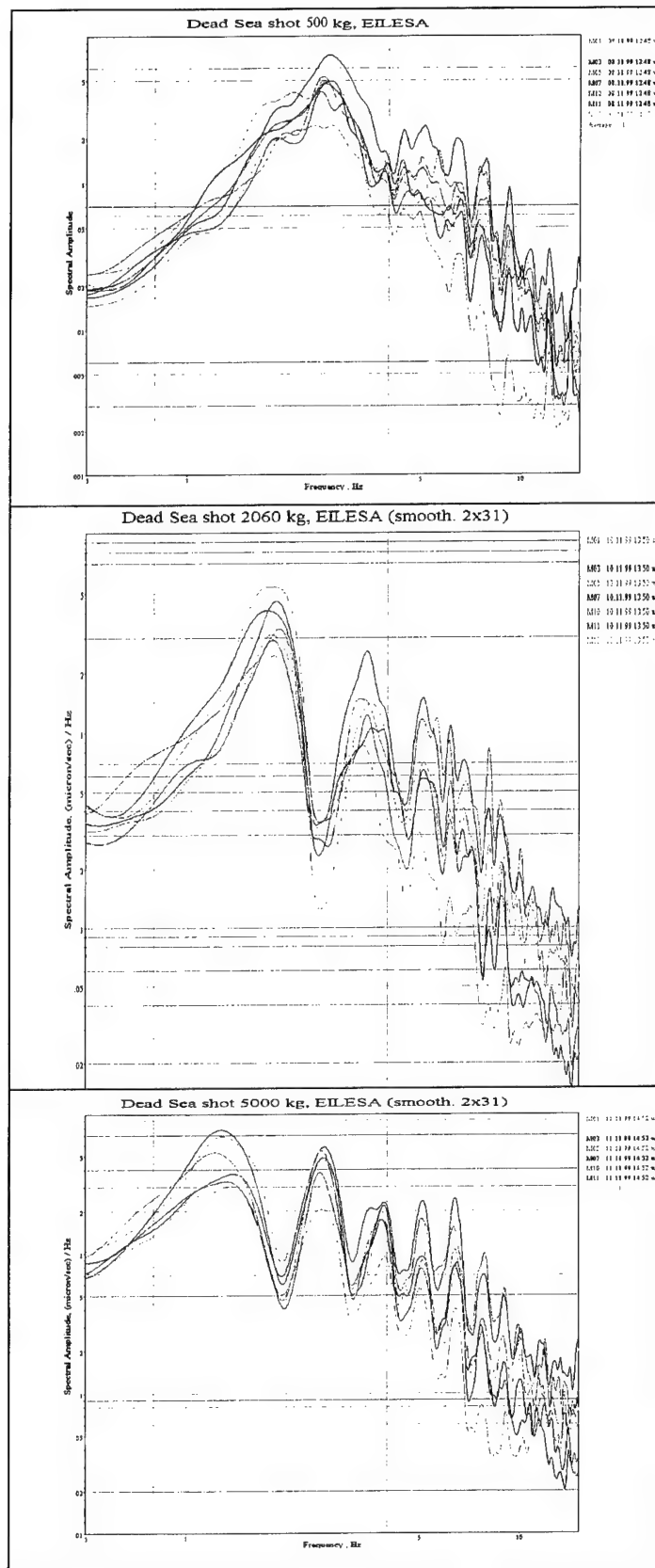
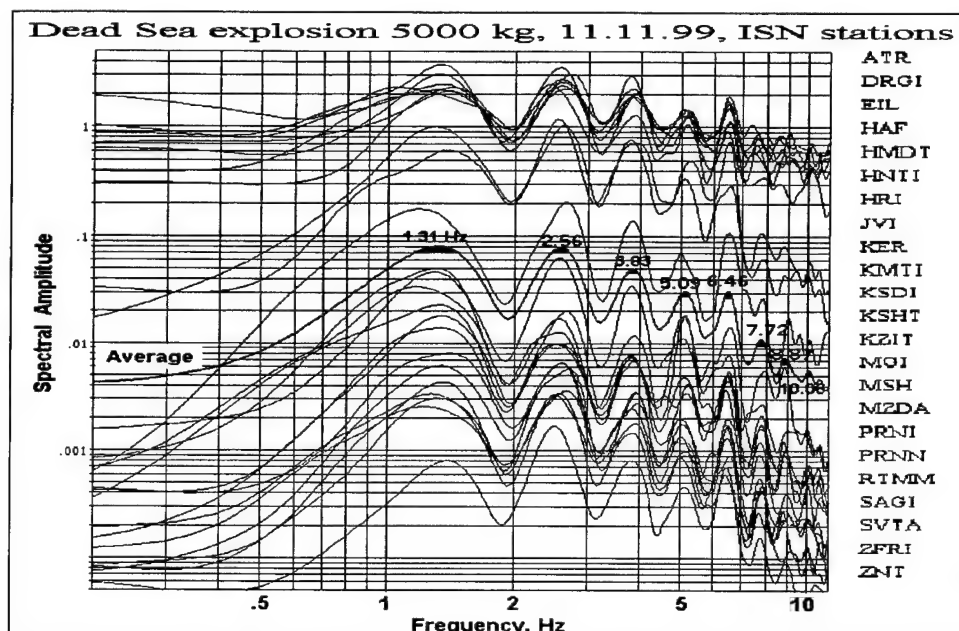
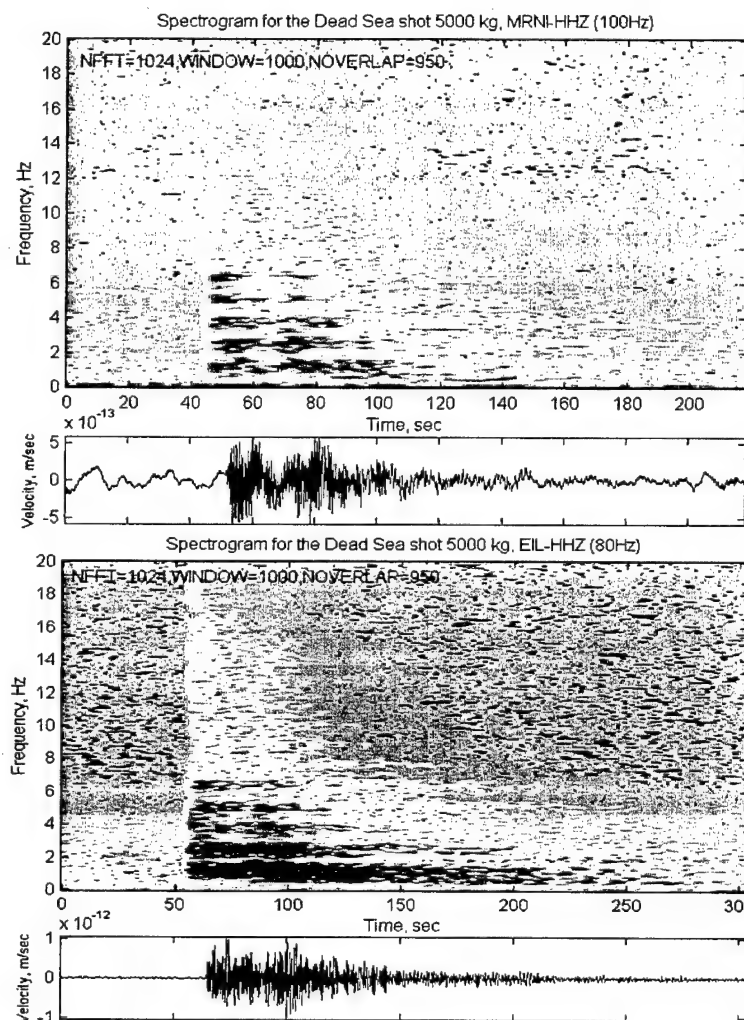


Figure 97. Amplitude spectra for the three explosions at the microarray. For larger charges the “bubble” modulation becomes more distinct.



a.



b.

Figure 98. Amplitude spectra at short-period ISN stations (a) and spectrograms at BB stations MRNI and EIL (b) showing the "bubble" spectral modulation for the 5-ton shot.

Spectrograms demonstrate time-independent spectral modulation with at least eight harmonic strips observed in the initial part of seismogram. The high-frequency strips disappear as time increases due to non-elastic attenuation of high-frequency energy along the propagation path. The low-frequency (less than 1 Hz) energy belongs to the coda of an earthquake in Turkey preceding the explosion.

The fundamental bubble periods (and bubble frequencies) determined from the harmonic series in smoothed spectra of ISN seismograms (Figure 98) are in good agreement with the modified Willis (1963) empirical equation (see Table 42):

$$T_b = 2.1 * W^{1/3} / (P_0 + d * \rho)^{5/6} \quad f_b = 1/T_b \quad (7.15)$$

where P_0 is the barometric pressure at the level of the Dead Sea (792 mm mercury or 10.778 m of water column during the experiment), d is the shot depth, ρ is the water density. The observed periods are also consistent with estimations obtained from auto-correlation analysis of IMS stations (CMR Event Report, 1999).

In contrast to the complete harmonic series caused by the bubbling effect, water reverberations produce two odd harmonic series with fundamentals f_H and f_d (Weinstein, 1968):

$$f_H = V_0/4H; \quad f_{nH} = (2n-1)*f_H, \quad n = 1, 2, \quad (7.16)$$

$$f_d = V_0/4d; \quad f_{nd} = (2n-1)*f_d, \quad n = 1, 2, \quad (7.17)$$

where V_0 is the sound velocity (m/sec), H is the water depth (m), d is the detonation depth (m). For velocity 1770.6 m/sec, detonation depth about 70 m and the sea depth (at the explosion site) about 260 m:

$$f_H = 1.7 \text{ Hz}, \quad f_d = 6.3 \text{ Hz}$$

The spectral modulation patterns of the largest explosion (Figure 98) do not show distinctly any of the estimated reverberation frequencies. The bubble effect modulation is dominant and suppresses (or hides) the reverberation modulation. Nevertheless the frequency f_d can be identified for the two smaller shots in the band 6.0-6.5 Hz. Even the odd harmonic f_{2d} can be supposed at about 18 Hz, for the considered local (small) distances. For the 5-ton shot the frequency f_d overlaps with $f_{5b} = 6.4$ Hz, resulting in an enlarged maximum in the band 6-7 Hz (see Figures 98 and 99).

The frequency f_H overlaps the f_b maximum for all three shots, and is vaguely seen only for the smallest explosion being shifted to 1.8-1.9 Hz (Figure 99). Two harmonics can be identified for 0.5-ton and 2-ton shots in the band 8-9 Hz (f_{3H}) and at about 12 Hz (f_{5H}), when the frequency f_{3H} for the 2-ton shot overlaps with $f_{4b}=8.1$ Hz, resulting in an enlarged maximum (see Figure 99).

7.8.5 Discrimination Analysis.

We attempted the spectral classification method (Gitterman et al., 1998a), which includes application to seismograms at different network stations of two spectral statistics: a) energy ratio in low and high frequency windows, averaged for several stations; b) semblance, characterizing coherency of spectral curves at network stations (see also Sections 5.3.1, 5.3.3).

The method was applied to vertical ISN and 3C Broad Band (EIL, JER and MRNI) records of the three calibration explosions in the Dead Sea and of four earthquakes close in magnitude, location and time to the explosions. The earthquake parameters are presented in Table 43, and all analyzed events and recording stations are shown on Figure 99.

Table 43. List of earthquakes of October-November 1999, close in location and magnitude to the Dead Sea calibration shots.

Date year/month/day/hour/min/sec	Magn. M_L	X, km	Y, km	Depth, km	Latit.	Long.	Region
1999 10 04 02 04 37.6	2.8	192.4	80.2	22	31.31	35.45	Arad
1999 10 07 03 50 26.8	2.9	179.8	-0.6	9	30.58	35.31	Arava
1999 11 16 02 39 15.5	3.4	192.3	87.7	21	31.38	35.45	Arad
1999 11 16 16 57 45.0	2.7	183.0	21.7	15	30.79	35.35	Arava

Time windows of 30-40 sec, containing the whole signal, were used. The spectra are smoothed in frequency windows about 0.7 Hz, while the energy ratio was calculated for the (1-3 Hz)/(6-8 Hz) ranges, and semblance for the (1-12 Hz) range. For BB data the semblance is calculated in the 1-9 Hz range, because only 20 Hz records are available for some earthquakes.

Identification of underwater explosions is based on spectral features of recordings: spectra coherency at different stations, due to the bubble modulation and low-frequency seismic energy. Figures 97-101 show coherent and relatively low-frequency spectra for the explosions, and non-regular and high-frequency spectra for the earthquakes. The different spectral patterns provided clear separation of the two populations of seismic events in the two-parameter space, shown on Figure 102.

The spectral methods for discrimination between earthquakes and underwater explosions provided reliable automated identification of the Dead Sea explosions. These observations correspond well to the results from the previous series of smaller underwater explosions (16-304 kg) conducted along a profile in the Dead Sea in 1993 (Gitterman et al., 1998b).

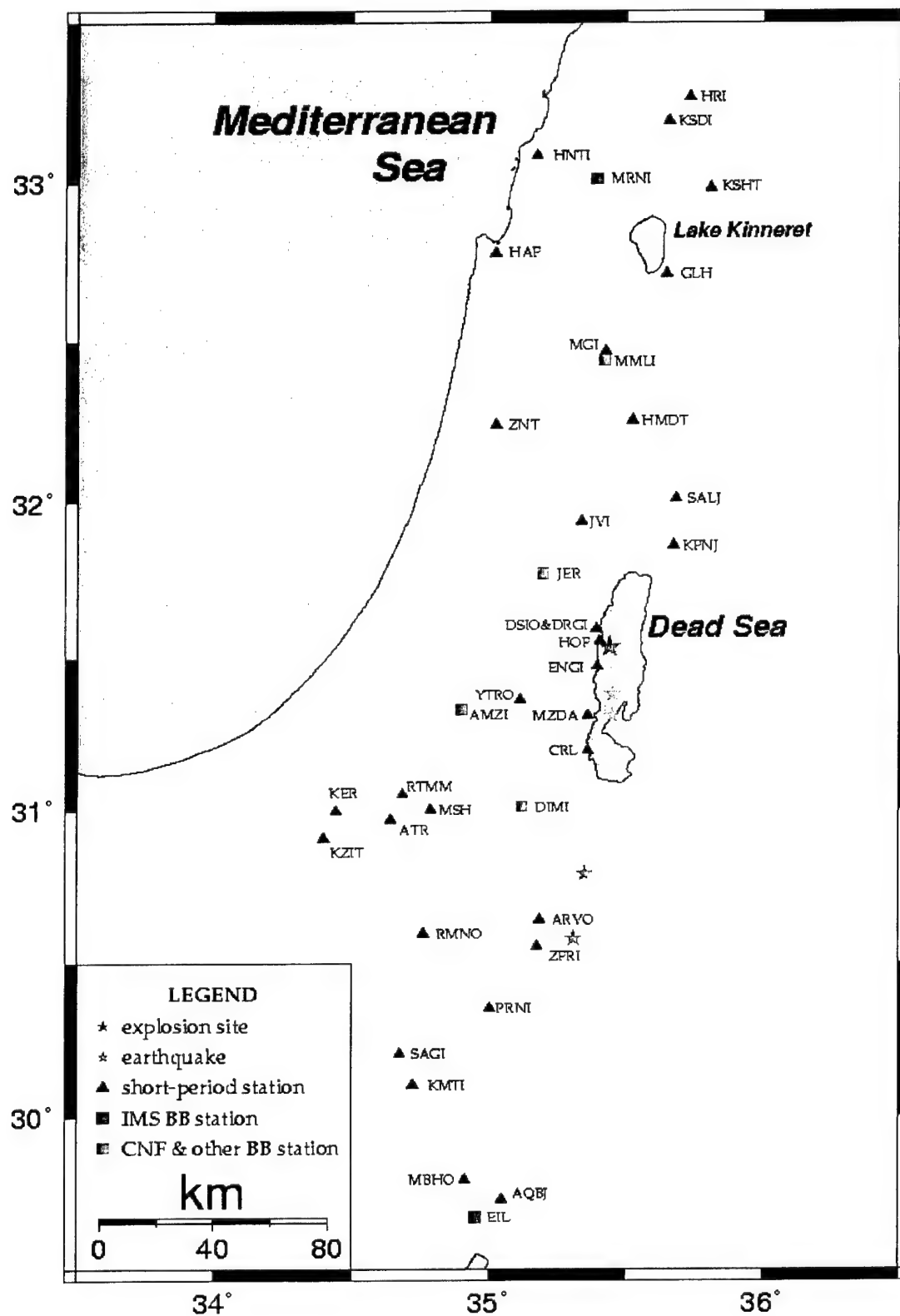


Figure 99. Dead Sea explosions, earthquakes and recorded stations used for the discrimination analysis.

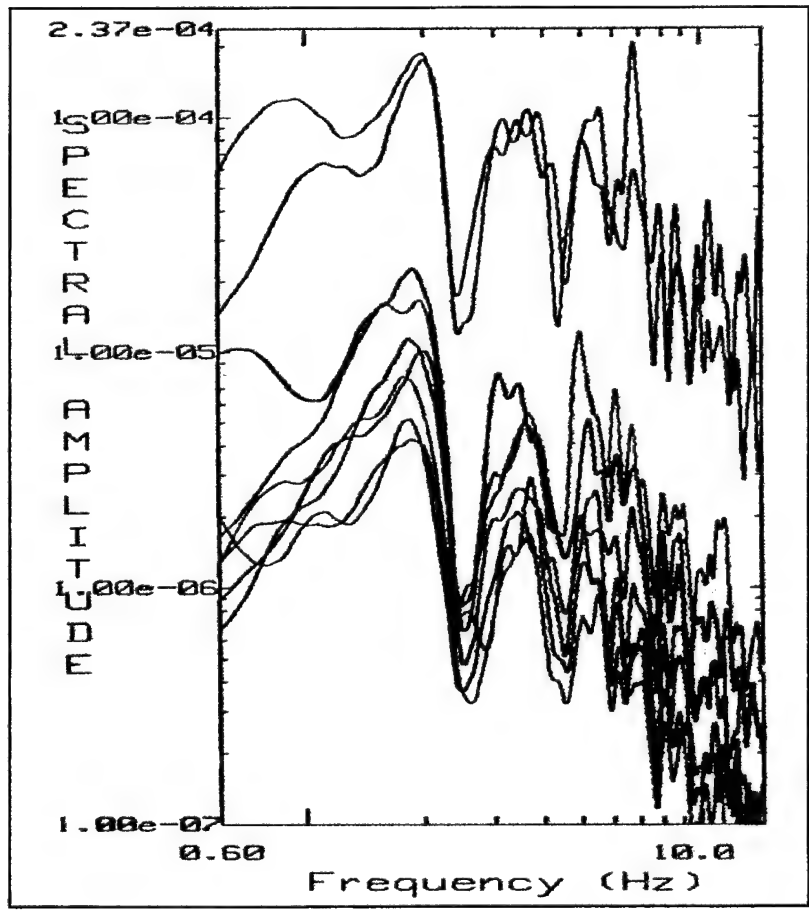
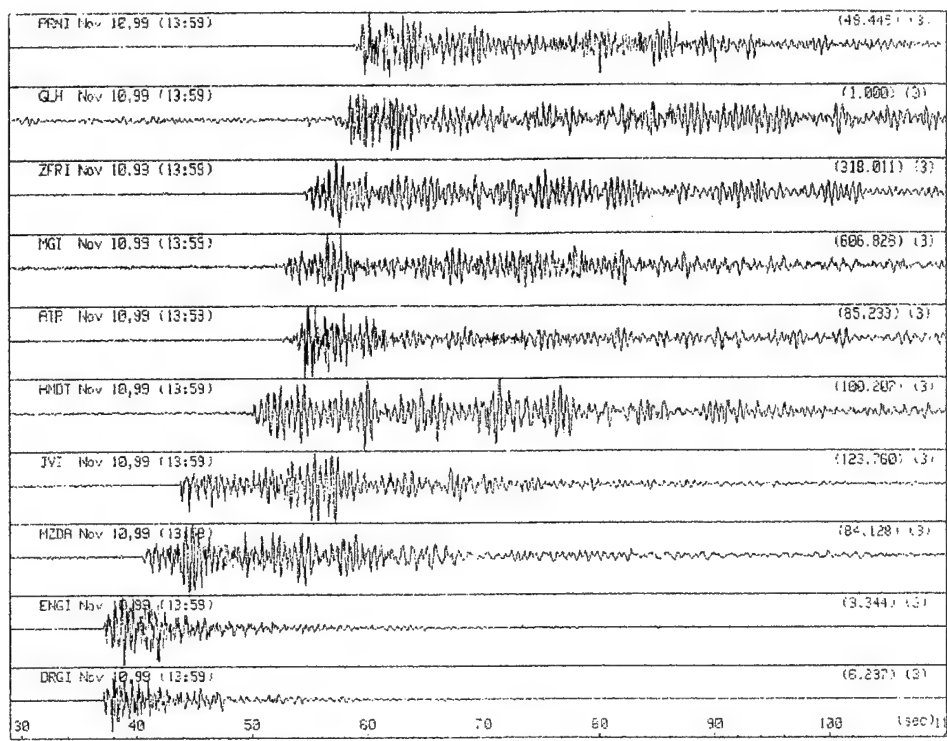


Figure 100. Sample seismogram and spectral patterns at ISN stations for the 2-ton shot.

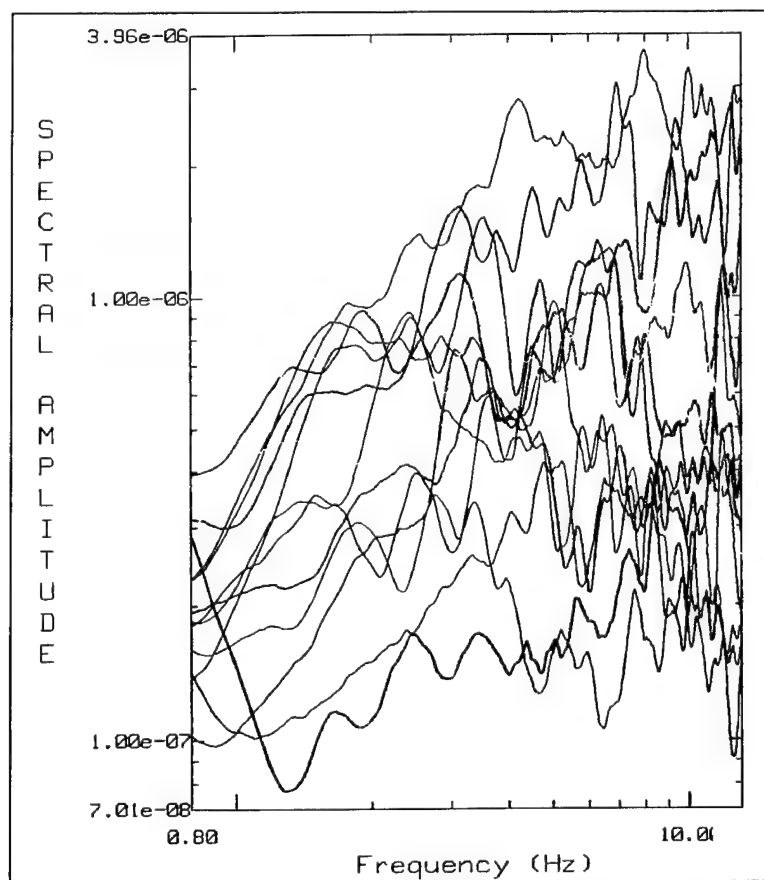
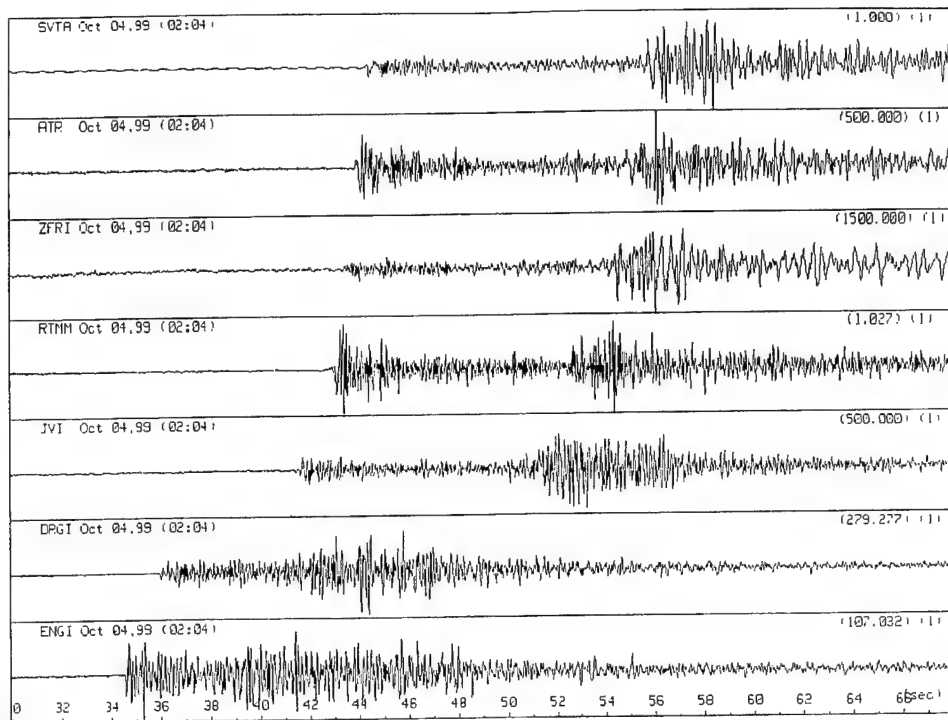


Figure 101. Sample seismogram and spectral patterns at different ISN stations for the closest to the explosion site earthquake on 4.10.99.

Spectral discrimination of seismic events:

Dead Sea shots in 1999 (0.5-5 ton) (•) and in 1993 (16-304kg) (◊) and close earthquakes (Δ)

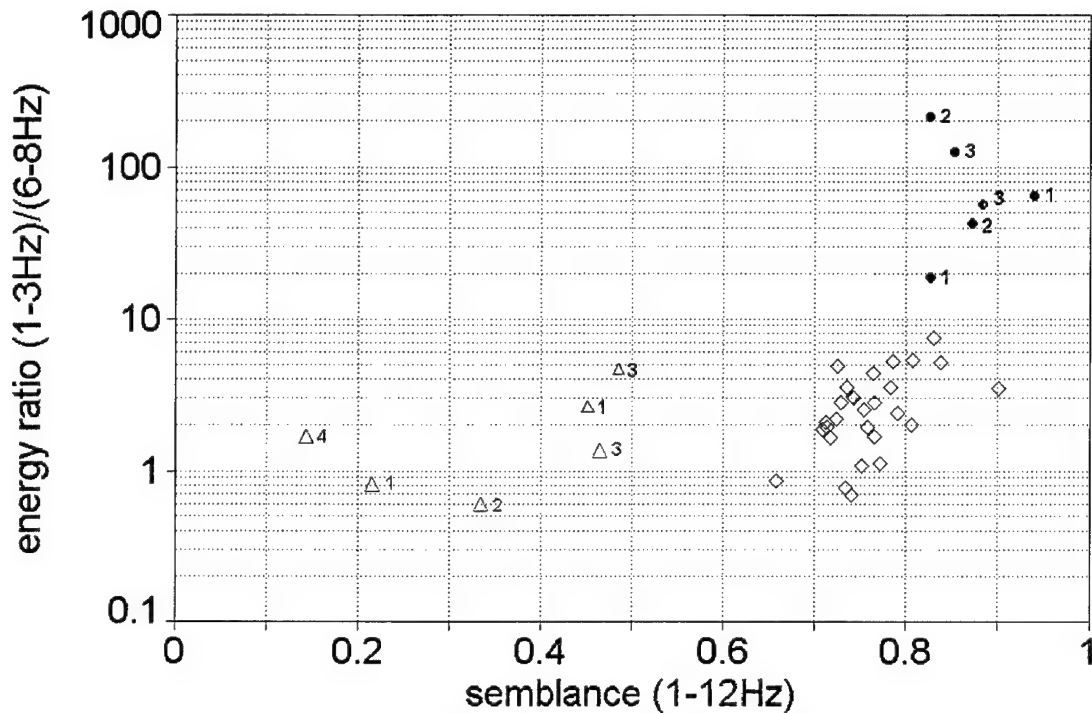


Figure 102. Discrimination results for the Dead Sea explosions (•) and nearby earthquakes (Δ), based on ISN short-period recordings, and BB stations EIL, JER and MRNI (shown by red color, where semblance is calculated in 1-9 Hz range, because for some earthquakes only 20Hz records were available).

7.8.6 Calibration of TT Models at Regional and Teleseismic Distances.

The explosions were also recorded at seismic stations as far away as 30° (see Figure 103). The differences between observed and calculated (using the IASPEI91 model) travel times were estimated and are presented in Table 44. The time residuals are within the measurement uncertainty.

All three shots were observed by Cypriot stations (CSN). Records of the BB station CSS show an increase of the S/P ratio for the larger charges (Figure 104). The Cypriot station ALFC ($r=481$ km) shows exceptionally high amplitudes of the low-frequency surface waves from the 5-ton shot (Figure 105).

After narrow band-pass filtering of the seismograms of the 5-ton explosion, clear P-signals can be observed at some stations located in Greece: the German operated stations SKD and KRIS (data provided by Dr. W. Hanka, Figure 106), the Swiss operated stations APER and KOUM (project MIDSEA, data provided by Dr. S. van der Lee, Figure 107).

The 2 and 5-ton explosions are observed at the LDG network (France) (phase data were provided by Dr. B. Feignier, see Table 44), and a signal from the 5-ton shot was seen (after record processing) at the EKA, Eskdalemuir Array, Scotland, United Kingdom (data provided by Dr. J. Young).

There is information that the explosions were observed at Saudi Arabian stations, out to distances of nearly 500 km, but the data are not available to us.

The two 0.5-ton and 2-ton shots were recorded only at the two IMS stations located in Israel (EIL and MRNI), but the largest 5-ton explosion was observed at 8 IMS stations (including GERESS, Germany, about 2500 km (Figure 108), and PDYAR in Russia (Figure 103), more than 5000 km away). The pIDC located this explosion at 2.3 km from ground truth, and assigned a magnitude of $m_b=3.9$ (CMR event report, 1999, see Figure 109). These results agree with our pre-experiment assessment of a local magnitude of about 4 and a maximum observable range of about 2000 km. On the other hand it should be noted that the explosion was not observed at much closer stations, such as the IMS array BRAR in Turkey. This observation must be investigated in the future.

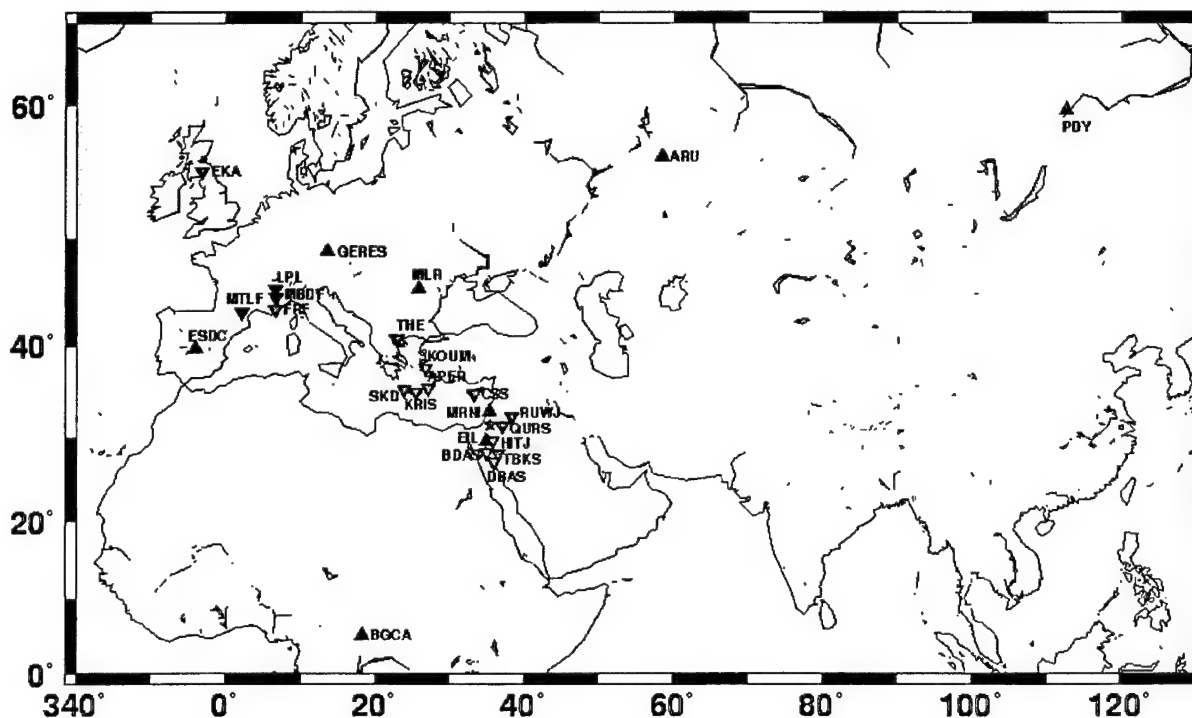


Figure 103. IMS stations and national/international stations reported observations of the Dead Sea explosions.

Table 44. Observations of the Dead Sea calibration shots at different seismic stations.

Station	Country	Exp #	Distance	Phase	Observed arrival time	Obs.-calc. (IASPEI 91)	Peak Vert. Amp., nm/s	Filter (Hz)
			deg.					
CSS	Cyprus	1	3.85	Pn	13:01:01.34	0.60	211	1-5
CSS		2		Pn	14:00:59.10	0.48	526	
CSS		3		Pn	15:01:01.88	0.67	462	0.5-5
CSS		3		Sn	15:01:48.20	2.6	-	
SKD	Greece	3	10.36	Pn	15:02:28.91	-1.66	126	1.2-5
KRIS	(Germany)	3	9.07	Pn	15:02:11.52	-1.37	98	
APER	Greece	3	7.98	Pn	15:01:56.70	-1.24	-	1.5-10
KOUM	(Switzerland)	3	9.39	Pn	15:02:16.90	-0.38	-	
MBDF	France (LDG network)	2	26.2	Pn	14:05:33.94	-0.51	3.7	
FRF		3	25.9	Pn	15:05:31.55	-2.77?	55.1	
MBDF		3	26.2	Pn	15:05:37.15	0.11	23.1	
LPL		3	26.5	Pn	15:05:39.76	0.01	-	
MTLF		3	29.0	Pn	15:06:01.33	-0.80	18.2	
EKA	Scotland, UK	3	36.06	Pn	15:07:04.04	0.24		

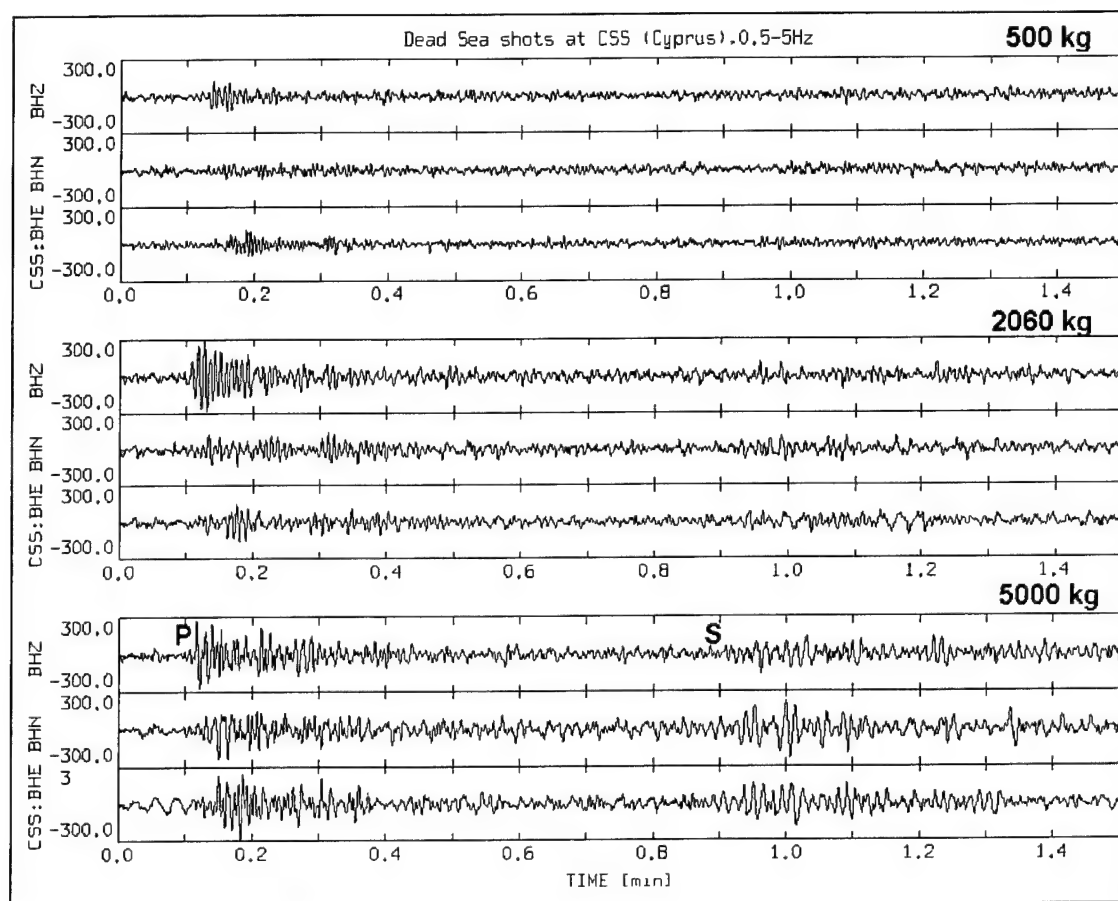


Figure 104. Seismograms of the explosions recorded at the BB station CSS, Cyprus, $r=428$ km.

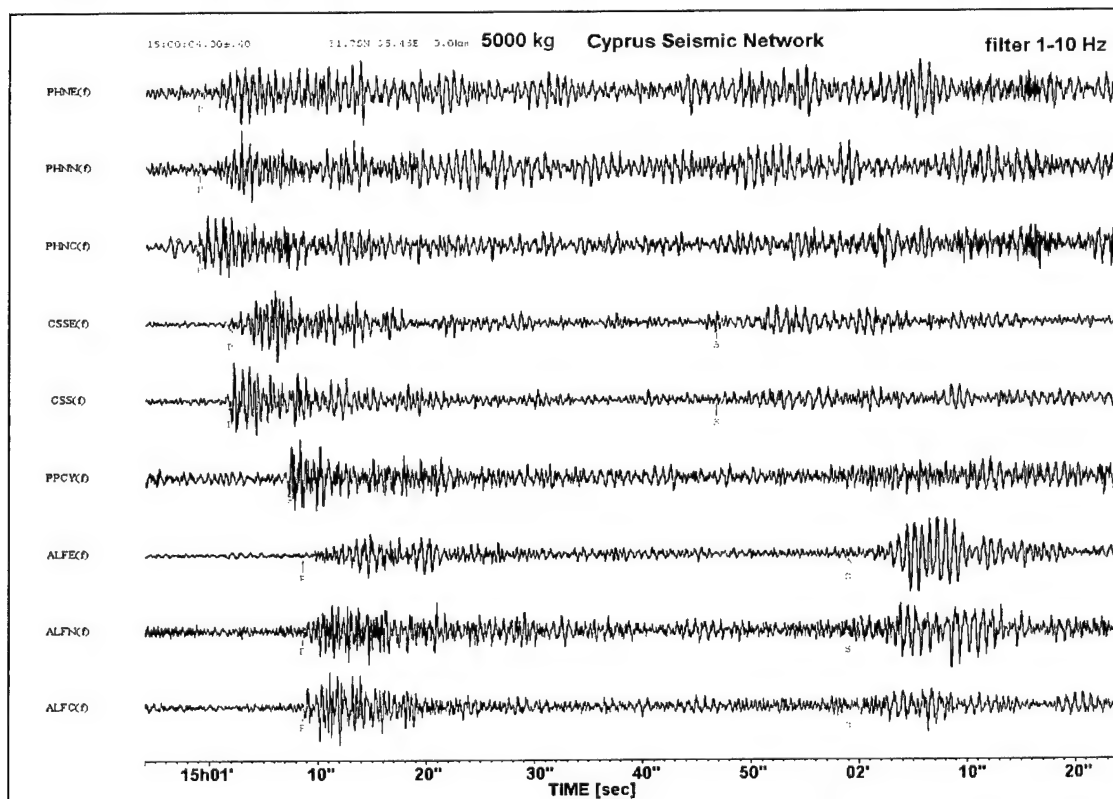


Figure 105. Seismograms of the 5-ton explosion recorded by the Cyprus Seismic Network.

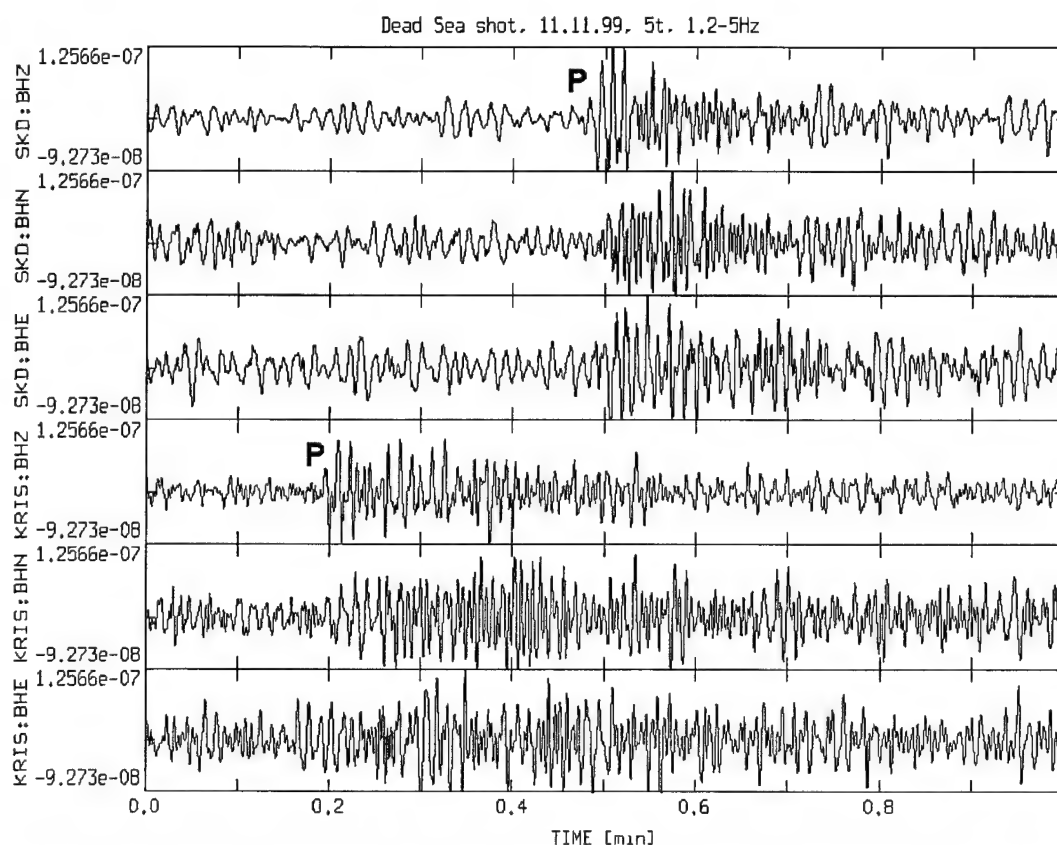


Figure 106. Seismograms of the 5-ton explosion recorded at the German operated stations SKD and KRIS in Greece.

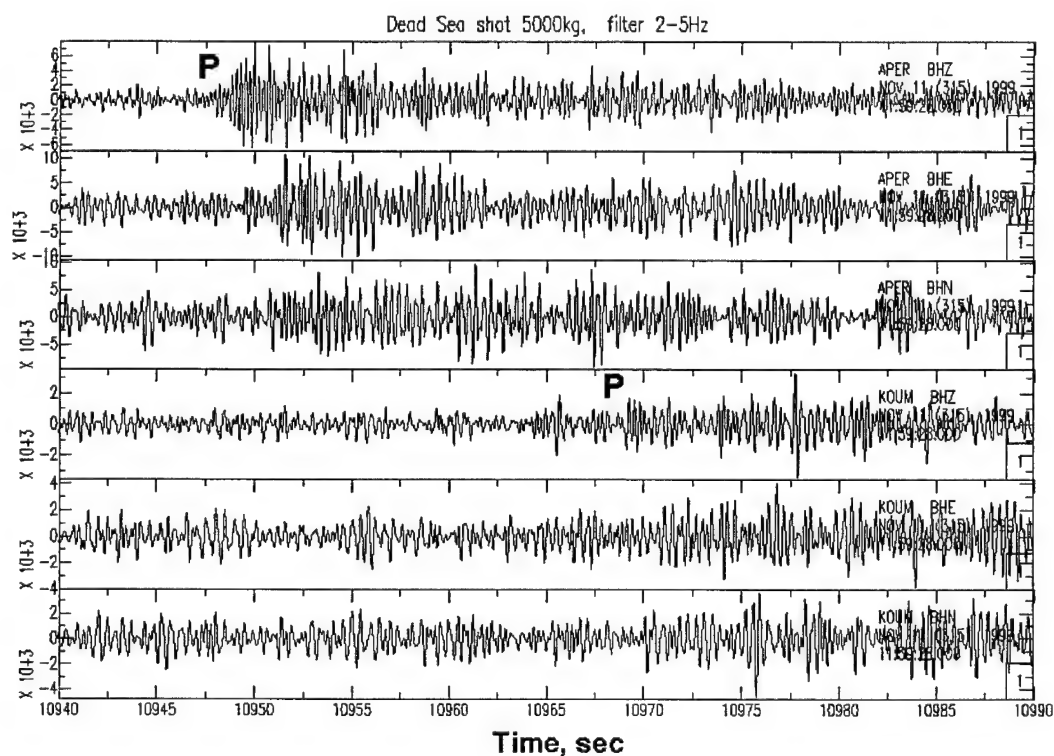


Figure 107. Seismograms of the 5-ton explosion recorded at the Swiss operated stations APER and KOUM in Greece.

Dead Sea ex.3, GERESS, time window start - after 160 sec, filter 0.8-1.5 Hz

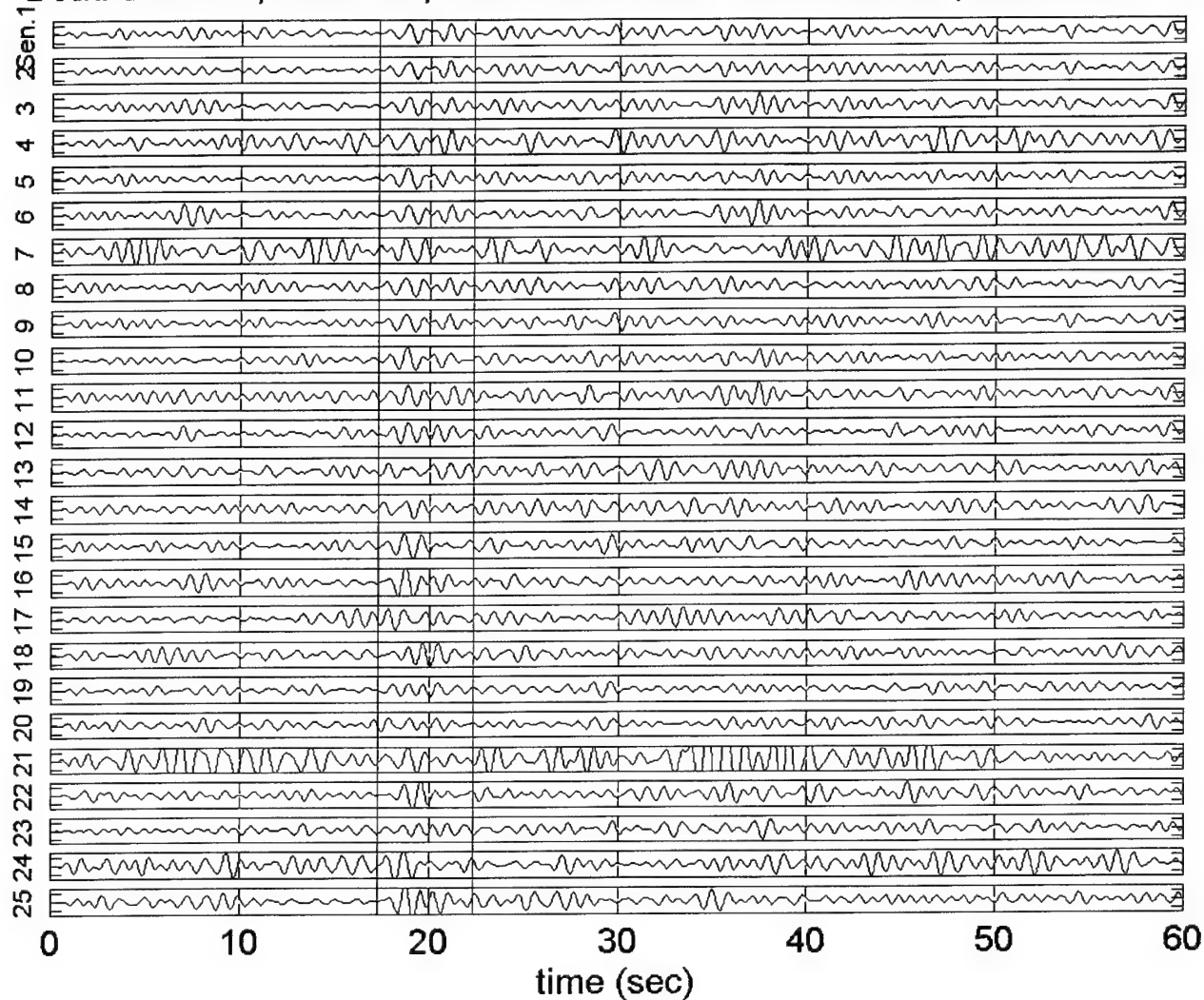


Figure 108. Recording of the 5-ton explosion at the IMS primary station – GERESS array. First P-arrivals are observed in the frame (after a strong filtering).

CMR source information for event on 1999/11/11

Origin time

1999/11/11 15:00:00.8 +- 0.0 GMT.

Location

REB:

Epicenter: 31.52 o N 35.46 o E

Error coverage ellipse (90% confidence):

Semi major axis: 34.7 km

Semi minor axis: 10.4 km

Strike: 97.7 degrees clockwise from North

JHD:

Epicenter: 31.55 o N 35.43 o E

Error coverage ellipse (90% confidence):

Semi major axis: 39.1 km

Semi minor axis: 14.9 km

Strike: 90.2 degrees clockwise from North

Depth

0.0 km

Constrained by analyst.

No defining depth phase for this event.

Magnitudes

mb: Average=3.86+-0.24, based on 5 stations.

MLE =3.27+-0.09, based on 31 stations. (Maximum Likelihood Estimation)

ML: =4.05, based on 1 station.

Ms: No LR detected.

Upper-bound (95% confidence)=3.28, based on 29 stations. (Maximum Likelihood Estimation)

Event Reference Information

The results in this report relate to:

Event notification number: 1999315-01

Bulletin: REB

Orid: 20610545

Bulletin Issued: 99/11/11 17:14:22.

Supporting station detections for event on 1999/11/11

10 defining phases from 8 stations were used in the location.

Phase associations:

Dist	EvAz	Sta	Phase	SNR	Time	TRes	Slow	SRes	Azim	AzRes	Def	mb	ML	Ms
1.5	357	MRNI	Pg	82.7	15:00:28.3	0.3	15.7	1.0	348		T			
			Lg	10.0	15:00:48.5	0.3	19.9	-9.9	300		T			
1.9	193	EIL	Pn	36.5	15:00:34.6	0.2	12.6	-1.2	25	12	T			
			Lg	3.4	15:01:00.9	-0.1	14.2	-18.2	20	7	T			
15.8	334	MLR	Pn	1.4	15:03:45.9	1.2	11.2	-1.8	23		T	4.0		
23.9	322	GERES	P	4.6	15:05:16.3	0.5	11.1	1.4	127	-1	TSA	3.4		
29.7	26	ARU	P	3.1	15:06:06.1	-1.8	10.7	1.8	202	-20	TSA	4.6		
30.7	214	BGCA	P	2.5	15:06:18.1	0.5	13.5	4.7	355	-33	T	3.5		
32.9	295	ESDC	P	5.3	15:06:35.3	-1.0	7.3	-0.8	98	17	TSA	3.8		
56.9	36	PDYAR	P	3.6	15:09:48.2	0.9	8.5	1.4	267	-8	TSA	3.9		

Dist: station to event distance (degrees).

EvAz: event to station azimuth (degrees).

SNR: signal-to-noise ratio.

TRes: time residual (sec).

Slow: observed slowness (sec/degree).

SRes: slowness residual (sec/degree).

Azim: observed station to event azimuth (degrees).

AzRes: azimuth residual (degrees)

Def: T= time defining; A=azimuth defining; S=slowness defining.

Figure 109. Information of the IDC about the 5-ton Dead Sea explosion (CMR report, 1999).

7.9 Geophysical Observations.

We collected data from measurements of the Total Electron Component (TEC) at the GPS network of Israel (Figure 110) during the Dead Sea 2-ton (10.11.99) and 5-ton (11.11.99) explosions (Figure 111). The data were supplied by Dr. E. Ostrovsky of the Survey of Israel.

The TEC measurements are based on a radio-signal from the satellite network (24 US satellites), which is received continuously at the GPS stations. Propagation of the signal through the ionosphere causes modifications of signal parameters due to the reflection and absorption effects. The modifications depend on the TEC concentration in the ionosphere. After computer processing of the received radio-signal the TEC values are estimated.

The data show a peak in the TEC curves for several GPS stations, starting 2.5 hours after the 2-ton shot, and a much stronger peak 1.5 hours after the 5-ton shot (Figure 111). These features may suggest a possible correlation between the explosions and the ionosphere effects. Nevertheless the available data (for a relatively short time period) seems insufficient for a reliable conclusion about a straight influence of the Dead Sea underwater explosions on the concentration of electrons in the ionosphere.

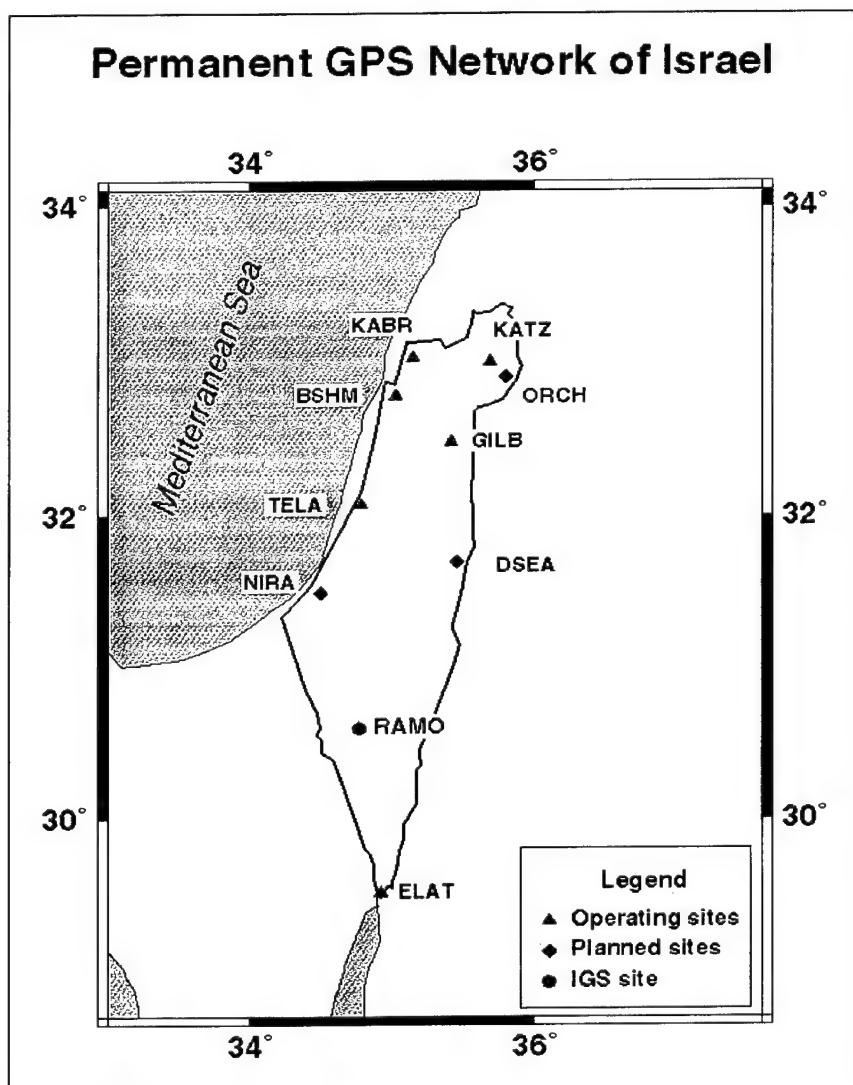


Figure 110. GPS stations of Israel.

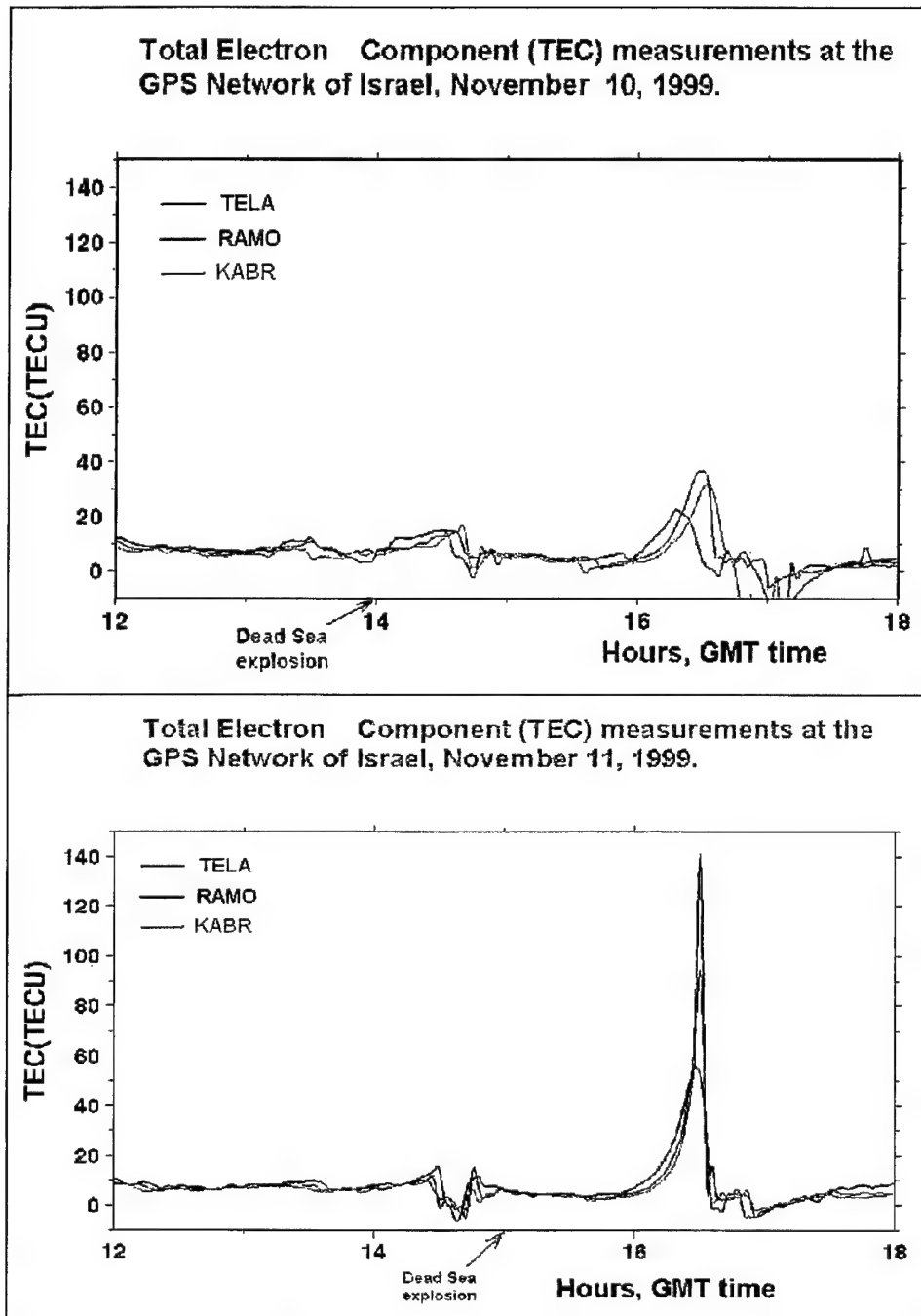


Figure 111. Observations of the Total Electronic Component during the Dead Sea experiment (courtesy of Dr. E. Ostrovsky, Survey of Israel).

Additional measurements and observations were made by different institutions. These include (Abelson, 2000): 1) aerial photographs displaying unstable structures on the nearest coasts, before and after the explosions; 2) monitoring of ground water level in the vicinity of the explosion site; 3) monitoring the stability of rock blocks on the cliff of Massada (distance about 25 km); 4) radon emanation. Analysis of the observations showed that no effect was recorded.

7.10 Conclusions.

The Dead Sea calibration experiment provided a variety of unique data. The video and audio tracks present interesting phenomena such as the “cavitation hat”, arrivals of the shock waves and the bubble pulsations at the raft and water uplift at the detonation point. The video clips also provide a rough estimation of the shock wave propagation time to the surface and to the raft and contribute to verification of the charge depth and explosion-to-raft distance.

The measured peak pressures significantly exceed the expected values from an equal TNT charge in ocean water due to enhanced acoustic impedance of the supersaline Dead Sea water. Analysis of different phases and arrival times on the records facilitates the identification of surface (“ghost”) and bottom reflections and contributed to the verification of the experiment configuration. The shock wave energy was calculated utilizing the wave energy flux density equation, recorded pressure-time functions and specific properties for the Dead Sea water. These observations could also provide preliminary estimations of the shock energy share relative to the explosive energy, and the TNT equivalent of the shots.

The high magnitudes under relatively low charge weights confirmed the high seismic efficiency of underwater explosions in the Dead Sea, significantly exceeding the upper limit curve for all known chemical and nuclear explosions in hard rock. The observed magnitudes and amplitudes of seismic waves verify that the entire charge was properly detonated in all cases. Our prior estimations of the seismic efficiency were justified, and the expected magnitude (about 4) was reached.

A prominent spectral modulation (azimuth- and time-independent), caused by the bubble pulse effect, was observed in all SP and BB seismograms, manifested by clear frequency banding in smoothed amplitude spectra of the whole signal and in spectrograms. The bubble periods, determined from the harmonic series on smoothed spectra of ISN seismograms, are in good agreement with the empirical equation.

A preliminary discrimination analysis based on spectral energy ratio and semblance characteristics, using local short-period stations recordings of the explosions and nearby earthquakes with comparable magnitudes was carried out. Due to the specific features of seismic waves from the underwater explosions (spectra coherency at different stations, caused by the bubble modulation, and low-frequency seismic energy), the analysis provided reliable separation between earthquakes and explosions in the Dead Sea region.

Precise travel times were obtained for network stations in Israel, Jordan, Cyprus and Saudi Arabia, providing verification of existing local propagation models, their correction and improvement, and estimates of the accuracy of measuring arrival times for the three explosions at the same place (see Section 4.1).

From a seismologist’s point of view, the main 5-ton explosion exceeded expectations, when the maximal observable range of about 2000 km was estimated before the experiment. Except for the near field and local stations, it was also clearly recorded on single regional stations of up to 1100 km distance away. The blast was observed at 8 IMS stations, at distances up to 5000 km, with the estimated location only 2.3 km from ground truth, and the event magnitude of $m_b=3.9$, corresponding to the predicted local magnitude of about 4.

Various observations and surveys in the vicinity of the explosion site showed the absence of irreversible environmental impact by the explosions, as it was predicted by the safety analysis conducted before the experiment.

This is not the first time that underwater shots have been carried out in the Dead Sea; however the explosions conducted are the first large-scale artificially generated calibration events in the area, having precise source information (Ground Truth of the rank GT0). The results of the experiment will improve monitoring and verification of the CTBT in the Middle East by the IMS and regional stations.

Section 8

References

- Abelson, M., "Review of environmental impact: conducting underwater explosions for seismic calibration experiment in the Dead Sea," Report GSI/17/99, Jerusalem, (in Hebrew), 1999. (UNCLASSIFIED)
- Abelson, M., "Calibration tests in the Dead Sea: environmental impact of the underwater explosions," Report GSI/26/2000, Jerusalem (in Hebrew), 2000. (UNCLASSIFIED)
- Anati, D.A., "The hydrography of a hypersaline lake, in: The Dead Sea: the lake and its setting," (Oxford Monographs on Geology and Geophysics, No.36), Edited by T.M. Niemi, Z. Ben-Avraham and J.R. Gat, New York, Oxford, Oxford University Press, 89-103, 1997. (UNCLASSIFIED)
- Andersen K.R., "Robust earthquake location using M-estimates," Phys.Earth.Plan.Inter., 30, 119-130, 1982. (UNCLASSIFIED)
- Baker, G. Eli and T. Barker, "Source and propagation characterization for network performance simulations in the Middle East," Proceedings of 19th Annual Seismic Research Symposium on Monitoring a CTBT, 201-210, 1997. (UNCLASSIFIED)
- Barazangi, M., D. Seber, M. Vallve, and B. Isacks, "A geological and geophysical information system for Eurasia, the Middle East and North Africa," Final Report, PL-TR-95-2168, Cornell University, Ithaca, NY, ADA305455, 1995. (UNCLASSIFIED)
- Barker, B., M. Clark, P. Davis, M. Fisk, M. Hedlin, H. Israelsson, V. Khalturin, W.Y. Kim, K. McLaughlin, C. Meade, J. Murphy, R. North, J. Orcutt, C. Powell, P.G. Richards, R. Stead, J. Stevens, F. Vernon and T. Wallace, "Monitoring Nuclear Tests," Science, 281, 1967-1968, 1998. (UNCLASSIFIED)
- Baumgardt, D.R., "Characterization of regional-phase propagation and seismic discriminants for the Middle East," Proceedings, 18th Annual Seismic Research Symposium on Monitoring a CTBT, 4-6 September, 1996, 474-483, 1996. (UNCLASSIFIED)
- Carr, D.B and H.D. Garbin, "Discriminating ripple-fired explosions with high-frequency (>16 Hz) data," Bull. Seis. Soc. Am., 88, 963-972, 1998. (UNCLASSIFIED)
- Chapmen, M.C., G.A. Bollinger, and M.S. Sibol, "Modeling delay-fired explosions spectra at regional distances," Bull. Seis. Soc. Am., 82, 2430-2447, 1992. (UNCLASSIFIED)
- Center for Monitoring Research, "CMR Event Report - Dead Sea Calibration Explosions, 1999/11/08-1999/11/11," Issued: November, 1999, Arlington, VA, 29 pp., 1999. (UNCLASSIFIED)
- Cole, R.H., "Underwater explosions," Princeton University Press, 1948. (UNCLASSIFIED)
- CTBTO, "Preliminary IDC reviewed event solution for the announced Pakistan underground nuclear test 30-May-1998," Preparatory Commission for the CTBTO, Provisional Technical Secretariat, Vienna, 1998a. (UNCLASSIFIED)
- CTBTO, "Preliminary IDC reviewed event solution for the announced Kazakhstan Calibration Explosion 22-August-1998," Preparatory Commission for the CTBTO, Provisional Technical Secretariat, Vienna, 1998b. (UNCLASSIFIED)
- El-Isa, Z., "Lithospheric structure of the Jordan-Dead Sea transform from earthquake data," Tectonophysics, 180, 29-36, 1990. (UNCLASSIFIED)

El-Isa, Z., J. Mechie, C. Prodehl, J. Markis, and Rih., "A crustal structure study of Jordan derived from seismic refraction data," *Tectonophysics*, 138, 235-253, 1987. (UNCLASSIFIED)

Eneva, M., J.L. Stevens, J. Murphy, B.D. Khristoforov, "Effect of charge depth in Russian hydroacoustic data from nuclear and HE explosions," *Proc. 22nd Annual DoD/DoE Seismic Research Symposium: Planning for Verification of and Compliance with the Comprehensive Nuclear-Test-Ban Treaty (CTBT)*, September 12-15, 2000, New Orleans, LA, 2000. (UNCLASSIFIED)

Fedorenko, Yu., E.S. Husebye, B. Heincke and B.O. Ruud, "Recognizing explosion sites without seismogram readings: Neural network analysis of envelope transformed multistation SP recordings 3 – 6 Hz," *Geoph. J. Int.*, 133, F1, 1998. (UNCLASSIFIED)

Fedorenko, Yu.V., E.S. Husebye, "First breaks - Automatic pickings of P- and S- onsets in seismic records," *Geoph. Res. Lett.*, submitted for publication, 1999. (UNCLASSIFIED)

Ginzburg, A., J. Makris, K. Fuchs, C. Prodehl, W. Kaminski, and U. Amitai, "A seismic study of the crust and upper mantle of the Jordan-Dead Sea rift and their transition toward the Mediterranean Sea," *J. Geophys. Res.*, 84, 1569-158, 1979a. (UNCLASSIFIED)

Ginzburg, A., J. Makris, K. Fuchs, B. Perathoner, and C. Prodehl, "Detailed structure of the crust and upper mantle along the Jordan-Dead Sea rift," *J. Geophys. Res.*, 84, 5605-5612, 1979b. (UNCLASSIFIED)

Ginzburg, A. and Y. Folkman, "The crustal structure between the Dead Sea rift and the Mediterranean Sea," *Earth Planet. Sci. Lett.*, 51, 181-188, 1980. (UNCLASSIFIED)

Ginzburg, A., J. Makris, K. Fuchs, and C. Prodehl, "The structure of the crust and upper mantle in the Dead Sea rift," *Tectonophysics*, 80, 109-119, 1981. (UNCLASSIFIED)

Gitterman, Y., "Assessment of dynamic parameters of seismic and air shock waves from multiple shot systems," Ph.D. Thesis, Institute of Mining, Academy of Sciences of the USSR, Novosibirsk, 1982. (UNCLASSIFIED)

Gitterman, Y. and T. van Eck, "Spectra of quarry blasts and micro-earthquakes recorded at local distances in Israel," *Bull. Seis. Soc. Am.*, 83, 1799-1812, 1993. (UNCLASSIFIED)

Gitterman, Y., V. Pinsky, and A. Shapira, "Discrimination of seismic sources using Israel Seismic Network," *Scientific Report No. 1, PL-TR-96-2207*, Phillips Lab., MA, 98pp., 1996. (UNCLASSIFIED)

Gitterman, Y., V. Pinsky and A. Shapira, "Spectral classification methods in monitoring small local events by the Israel seismic network," *J. of Seismology*, 2, 237-256, 1998a. (UNCLASSIFIED)

Gitterman, Y., Z. Ben-Avraham and A. Ginzburg, "Spectral analysis of underwater explosions in the Dead Sea," *Geophys. J. Int.*, 134, 460-472, 1998b. (UNCLASSIFIED)

Gitterman, Y., "Magnitude-yield correlation and amplitude attenuation of chemical explosions in the Middle East," in: *Proceedings of the 20th Annual Seismic Research Symposium on Monitoring a CTBT*, 302-311, 1998. (UNCLASSIFIED)

Gitterman, Y., V. Pinsky and A. Shapira, "Spectral discrimination analysis of Eurasian nuclear tests and earthquakes recorded by the Israel Seismic Network and the NORESS array," *Physics Earth and Planet. Inter.*, 113, 111-129, 1999. (UNCLASSIFIED)

Gitterman, Y. and A. Shapira, "Safety analysis for calibration explosions in the Dead Sea. Progress Report No. 19 on the project 'Improvements in Monitoring the CTBT in the Middle East by the Israel Seismic Network'," *Contract Number DSWA01-97-C-0151, GII Report No. 591/61/97(19)*, 1999. (UNCLASSIFIED)

Hearn, T.M., and J.P. Ni, "Pn velocities beneath continental collision zones: the Turkish-Iranian Plateau," *Geophys. J. Int.*, 117, 273-283, 1994. (UNCLASSIFIED)

Harris, D. B., "Waveform correlation methods for identifying population of calibration events,": in: *Proceedings of the 19th Annual Seismic Research Symposium on Monitoring a CTBT*, 604-613, 1997. (UNCLASSIFIED)

Hedlin, M.A.H., "Identification of mining blasts at all regional distances using low-frequency seismic signals," in: *Proceedings of the 20th Annual Seismic Research Symposium on Monitoring a CTBT*, 335-344, 1998. (UNCLASSIFIED)

Hall, J.K., "The GSI Digital Terrain Model (DTM) completed," in: R. Bogoch and Y. Eshet (eds.), *GSI Current Research: V.*, Jerusalem, 47-50, 1993. (UNCLASSIFIED)

Hofstetter, A. and Shapira, A., "Determination of earthquake energy release in the Eastern Mediterranean region," *Geophys. J. Int.*, in press, 2000. (UNCLASSIFIED)

Huber, P.J., "Robust statistics: a review," *Ann. Math. Stat.*, 43, 1041-1067, 1972. (UNCLASSIFIED)

Husebye, E. S., B.O. Ruude and A.M. Dainty, Fast, "Robust and Reliable Epicenter Determinations: Envelope Processing of Local Network Data," *Bul.Seism.Soc.Am*, 88, 284-290, 1998. (UNCLASSIFIED)

Johnson, C.E., "CEDAR - An approach to the computer automation of short period local seismic networks," Ph.D. Dissertation, California Institute of Technology, Pasadena, CA., 1979. (UNCLASSIFIED)

Joswig, M., "Pattern recognition for earthquake detection," *Bul.Seism.Soc.Am.*, 80, 170-186, 1990.

Kanamori, H., J. Mori, E. Hauksson, T. Heaton, K. Hutton, and L. Jones, "Determination of earthquakes energy release and ML using TERRAScope," *Bull. Seism. Soc. Am.*, 83, 330-346, 1993. (UNCLASSIFIED)

Khalturin, V., T. Rautian and P. Richards, "The seismic signal strength of chemical explosions," *Bull. Seis. Soc. Am.*, 88, 1511-1524, 1998. (UNCLASSIFIED)

Kim, W.Y., D.W. Simpson and P.G. Richards, "High-frequency spectra of regional phases from earthquakes and chemical explosions," *Bull. Seis. Soc. Am.*, 84, 1365-1386, 1994. (UNCLASSIFIED)

Kulhanek, O., "P wave amplitude spectra of Nevada underground nuclear explosions," *Pure Appl. Geophys.*, 88, 121-136, 1971. (UNCLASSIFIED)

Kushnir, A.F., V.M. Lapshin, V.I. Pinsky and J. Fyen, "Statistically optimal event detection using small array data," *Bull. Seis. Soc. Am.*, 80, 1934-1947, 1990. (UNCLASSIFIED)

Kushnir, A.F., "Algorithms for adaptive statistical processing of seismic array data," in: *Monitoring Comprehensive Test Ban Treaty*, E.S. Husebye and A.M. Dainty (Eds.), NATO ASI Series, Series E: Applied Sciences - Vol. 303, 1995. (UNCLASSIFIED)

Lay, T., "Teleseismic manifestations of pP: problems and paradoxes," in: *Explosion Source Phenomenology*, in: S.R. Taylor, H.J. Patton and P.G. Richards (Eds.), *Geophysical Monograph* 65, 109-125, 1991. (UNCLASSIFIED)

Leonard, M., "Comparison of Manual and Automatic Onset Picking," *Bull. Seis. Soc. Am.*, 90, 1384-1390, 2000. (UNCLASSIFIED)

Makris, J., Z. Ben-Avraham, A. Behle, A. Ginzburg, P. Giese, L. Steinmetz, R. Whitmarsh, and S. Eleftheriou, "Seismic refraction profiles between Cyprus and Israel and their interpretation," *Geophys. J. R. Astr. Soc.*, 75, 575-59, 1983. (UNCLASSIFIED)

- Mayeda, K. and R. Walter, "Moment, energy, stress drop, and source spectra of Western United States earthquakes from regional coda envelopes," *J. Geophys. Res.*, 101, 11195-11208, 1996. (UNCLASSIFIED)
- Murdock, N.J and C.R. Hutt, "A new Event Detector Designed for the Seismic Research Observatories," USGS Open-File Report 83-785, 1983. (UNCLASSIFIED)
- Neidell, N.S. and M.T. Taner, "Semblance and other coherency measures for multichannel data," *Geophysics*, 36, 482-497, 1971. (UNCLASSIFIED)
- Pinsky, V. and A. Shapira, "Regional Events Location Using Seismic Energy Time-Space Distribution," *Proceedings of the 20th Annual Seismic Research Symposium on Monitoring a CTBT*, Santa Fe, 265-274, 1998. (UNCLASSIFIED)
- Pinsky, V.I., "An Approach to Automatic Location of Regional Events" *Phys. Earth. and Planet. Interiors*, 113, 293-303, 1999. (UNCLASSIFIED)
- Pinsky, V., and A. Shapira, "Robust Procedures For Automatic Precise Location of Regional Seismic Events," *Proceedings of the 21st Seismic Research Symposium: Technologies for Monitoring the Comprehensive Nuclear-test-Ban-Treaty*, 21-24 September 1999, Las Vegas, Nevada, v.1, 579-588, 1999. (UNCLASSIFIED)
- Pinsky, V., "Prototype Autonomous Earthquake Locator for Regional Networks," *Geophysical Research Letters*, Vol. 27, No. 21, 3549-3552, 2000. (UNCLASSIFIED)
- Pisarenko, V.F., A.F. Kushnir and I.V. Savin, "Statistically adaptive algorithms for estimations of onset moments of seismic phases," *Phys. Earth. Planet. Interior*, 47, 888-900, 1987. (UNCLASSIFIED)
- Pritchett, J.W., "An evaluation of various theoretical models for underwater explosion bubble pulsation," *Rep. IRA-TR-2-71*, Information Research Associates Inc., Berkeley, Calif., 1971. (UNCLASSIFIED)
- Rodgers, A., J.P. Ni and T. Hearn, "Propagation characteristics of short period Sn and Lg in the Middle East," *Bull. Seism. Soc. Amer.*, Vol. 87, 396-413, 1997. (UNCLASSIFIED)
- Rohay, A.C., "Modeling ripple fired explosions from the Centralia mine, Southwestern Washington," *Abstracts of the 94th Annual Meeting of SSA*, *Seism. Res. Lett.*, 70, 228, 1999. (UNCLASSIFIED)
- Ryzhikov, G.A., M.S. Birulina and E.S. Husebye, "Automatic event location using local network data," *Proceedings of the 17th Annual Seismic Research Symposium on Monitoring a CTBT*, 12-15 September 1995, 393-399, 1995. (UNCLASSIFIED)
- Sandvol, E, D. Seber, Al- K. Damegh, and M. Barazangi, "Regional Seismological Research in The Middle East in Support of CTBT Monitoring," *22nd Annual Seismic Research Symposium CTBT*, 04-09, 2000. (UNCLASSIFIED)
- Shapira, A., "T-phases from underwater explosions off the coast of Israel," *Bull. Seis. Soc. Am.*, 71, 1049-1059, 1981. (UNCLASSIFIED)
- Shapira, A., "Measurement arrival times of seismic waves," IPRG report Z1/567/79(73), (in Hebrew), 8pp, 1990. (UNCLASSIFIED)
- Shapira, A., "Detectability of regional seismic networks: analysis of the Israel Seismic Networks," *Isr. J. Earth Sci.*, 41, 21-25, 1992. (UNCLASSIFIED)
- Shoubik, B.M., A.F. Kushnir, L.M. Haikin, and A. Dainty, "SCANLOC: Automatic seismic event location based on local seismic network data," *Proceedings of the 18th Annual Seismic Research Symposium on Monitoring a Comprehensive test Ban Treaty*, 774-781, 1996. (UNCLASSIFIED)

Steer, D.N., D. Seber, E. Sandvol, C. Orgen and M. Barazangi, "Global-scale Geographical Information System (GIS) for the Prototype International Data Center (PIDC)," Proceedings of the 20th Annual Seismic Research Symposium on Monitoring a CTBT, 754-763, 1998. (UNCLASSIFIED)

Stump, B.W. and R.E. Reinke, "Experimental confirmation of superposition from small scale explosions," Bull. Seis. Soc. Am, 78, 1059-1073, 1988. (UNCLASSIFIED)

Stump, B.W., D.C. Pearson and V. Hsu, "Empirical scaling relations for contained single-fired chemical explosions and delay-fired mining explosions at regional distances," Abstracts of the 94th Annual Meeting of SSA, Seism. Res. Lett., 70, p.212, 1999. (UNCLASSIFIED)

Taylor, S.R. and P.D. Marshall, "Spectral discrimination between Soviet explosions and earthquakes using short-period array data," Geophys. J. Int., 106, 265-273, 1991. (UNCLASSIFIED)

U.S Army, Corps of Engineers (USACE), "Underwater blast monitoring," Engineer Technical Letter No. 1110-8-11 (FR), Washington, D.C., 9pp, 1991. (UNCLASSIFIED)

Vila, J., "The broadband seismic station CAD (Tunel del Cadi, Eastern Pyrenees): Site characteristics and Background Noise," Bull. Seis. Soc. Am., 88, 297-303, 1998. (UNCLASSIFIED)

Wallace, T.C., "The May 1998 India and Pakistan Nuclear Tests," Seism. Res. Lett., 69, 386-393, 1998. (UNCLASSIFIED)

Walter, W.R., A.J. Rodgers, K. Mayeda, S.C. Myers, M. Pasyanos and M. Denny, "Preliminary regional seismic analysis of nuclear explosions and earthquakes in Southwest Asia," Proceedings of the 20th Symposium on Monitoring a Comprehensive Test Ban Treaty, Santa Fe, 442-451, 1998. (UNCLASSIFIED)

Weinstein, M.S., "Spectra of acoustic and seismic signals generated by underwater explosions during Chase experiment," J. Geoph. Res., 73, No. 16, 5473-5476, 1968. (UNCLASSIFIED)

Willis, D.E., "Seismic measurements of large underwater shots," Bull. Seism. Soc. Am., 53, 789, 1963. (UNCLASSIFIED)

DISTRIBUTION LIST

DTRA-01-35

DEPARTMENT OF DEFENSE

DEFENSE INTELLIGENCE AGENCY
DIRECTORATE FOR SCIENTIFIC &
TECHNICAL INTELLIGENCE
WASHINGTON, DC 20340-6158
ATTN: DTIP

DEFENSE TECHNICAL INFORMATION CENTER
8725 JOHN J KINGMAN RD SUITE 0944
FORT BELVOIR, VA 22060 6218
2 CYS ATTN: DTIC/OCF

DEFENSE THREAT REDUCTION AGENCY
8725 JOHN J KINGMAN RD MAIL STOP 6201
FORT BELVOIR, VA 22060-6201
ATTN: TD, A.DAINTY
ATTN: TDND, MAJ T. CARTLEDGE, US

OFFICE OF THE SECRETARY OF DEFENSE
3030 DEFENSE PENTAGON
WASHINGTON, DC 20301-3030
ATTN: DDR&E, ROOM 3E808

OFFICE OF THE SECRETARY OF DEFENSE
NUCLEAR TREATY PROGRAMS OFFICE
1515 WILSON BOULEVARD, SUITE 720
ARLINGTON, VA 22209-2402
ATTN: DR. S. MANGINO

DEPARTMENT OF THE ARMY

US ARMY SMDC
P.O. BOX 1500
HUNTSVILLE, AL 35807-3801
ATTN: TC-YD, MR. B. ANDRE

DEPARTMENT OF THE AIR FORCE

AIR FORCE RESEARCH LABORATORY
29 RANDOLPH ROAD
HANSCOM AFB, MA 01731
ATTN: VSBL, MR. R. RAISTRICK

AIR FORCE TECHNICAL APPLICATIONS
CENTER
USAF AT USGS
NATIONAL CENTER MAIL STOP 951
12201 SUNRISE DRIVE
RESTON, VA 20192
ATTN: DR. R. BLANDFORD
ATTN: MR. R. JIH

AIR FORCE TECHNICAL APPLICATIONS CENTER
1030 SOUTH HIGHWAY A1A
PATRICK AFB, FL 32925-3002
ATTN: TTR, DR. D. CLAUTER
ATTN: TTR, DR. V. HSU
ATTN: TT, DR. D. RUSSELL

ATTN: TTR, DR. M. WOODS

DEPARTMENT OF THE NAVY

NAVAL RESEARCH LABORATORY
4555 OVERLOOK AVE SW
WASHINGTON, DC 20375-0001
ATTN: CODE 7643, DR. D. DROB

DEPARTMENT OF ENERGY

DEPARTMENT OF ENERGY
1000 INDEPENDENCE AVENUE, S.W.
WASHINGTON, DC 20585-0420
ATTN: MS. L. A. CASEY
ATTN: MS. FRANCES KEEL

UNIVERSITY OF CALIFORNIA
PACIFIC NORTHWEST NATIONAL LABORATORY
A DIVISION OF BATTELLE MEMORIAL
INSTITUTE
P.O. BOX 999 BATTELLE BOULEVARD
RICHLAND, WA 99352
ATTN: MS K5-12, DR. D. N. HAGEDORN

UNIVERSITY OF CALIFORNIA
LAWRENCE LIVERMORE NATIONAL LABORATORY
P.O. BOX 808
LIVERMORE, CA 94551
ATTN: MS-L 205, DR. D. HARRIS
ATTN: MS-L 205, DR. J. ZUCCA
ATTN: CEWES - SD

DISTRIBUTION LIST

DTRA-TR-01-35

LOS ALAMOS NATIONAL LABORATORY
P.O. BOX 1663
LOS ALAMOS, NM 87545
ATTN: MS C335, DR. S.R. TAYLOR
ATTN: MS D408, DR. S. PHILLIPS

SANDIA NATIONAL LABORATORIES
MAIL SERVICE
P.O. BOX 5800
ALBUQUERQUE, NM 87185-1363
ATTN: MS 0945, DR. E. CHAEL
ATTN: MS 1138, DR. C. YOUNG

OTHER GOVERNMENT

U.S. GEOLOGICAL SURVEY
12201 SUNRISE VALLEY DRIVE
RESTON, VA 20192
ATTN: DR. J. FILSON

U.S. GEOLOGICAL SURVEY
345 MIDDLEFIELD RD
MENLO PARK, CA 94025-3591
ATTN: MS 977, DR. W. MOONEY

U.S. DEPARTMENT OF STATE
2201 C STREET NW
WASHINGTON, DC 20520
ATTN: MR. R. MORROW, ROOM 5741
ATTN: DR. W. LEITH

UNIVERSITIES

BOSTON COLLEGE
INSTITUTE FOR SPACE RESEARCH
140 COMMONWEALTH AVENUE
CHESTNUT HILL, MA 02167
ATTN: MR. B. SULLIVAN
ATTN: DR. D. HARKRIDER

BROWN UNIVERSITY
DEPT OF GEOLOGICAL SCIENCES
75 WATERMAN ST
PROVIDENCE, RI 02912-1846
ATTN: PROF D. FORSYTH

CALIFORNIA INSTITUTE OF TECHNOLOGY
DIVISION OF GEOLOGICAL AND PLANETARY
SCIENCES
SEISMOLOGICAL LABORATORY
1201 EAST CALIFORNIA BOULEVARD
PASADENA, CA 91125
ATTN: PROF. D. HELMBERGER
ATTN: PROF. T. AHRENS

COLUMBIA UNIVERSITY
LAMONT DOHERTY EARTH OBSERVATORY
61 ROUTE 9W
PALISADES, NY 10964-8000
ATTN: DR. W. Y. KIM
ATTN: PROF. P. RICHARDS
ATTN: PROF. L. SYKES
ATTN: DR. J. XIE
ATTN: DR. MAYA TOLSTOY

CORNELL UNIVERSITY
INSTITUTE FOR THE STUDY OF THE
CONTENTS
3126 SNEE HALL
ITHACA, NY 14853
ATTN: PROF. M. BARAZANGI

HARVARD UNIVERSITY
HOFFMAN LABORATORY
DEPARTMENT OF EARTH, ATMOSPHERIC
AND PLANETARY SCIENCES
20 OXFORD STREET
CAMBRIDGE, MA 02138
ATTN: PROF. A. DZIEWONSKI
ATTN: PROF. G. EKSTROM

INCORPORATED RESEARCH INSTITUTIONS
FOR SEISMOLOGY
1200 NEW YORK AVENUE, N.W. SUITE 800
WASHINGTON, DC 20005
ATTN: DR. D. SIMPSON
ATTN: DR. G. VAN DER VINK

INDIANA UNIVERSITY
DEPT OF GEOLOGICAL SCIENCES
1005 10TH ST
BLOOMINGTON, IN 47405
ATTN: PROF. G. PAVLIS

DISTRIBUTION LIST

DTRA-TR-01-35

MASSACHUSETTS INSTITUTE OF
TECHNOLOGY
EARTH RESOURCES LABORATORY
34 CARLETON ST, E34-458
CAMBRIDGE, MA 02142
ATTN: DR. W. RODI
ATTN: PROF. N. TOKSOZ

MICHIGAN STATE UNIVERSITY
DEPARTMENT OF GEOLOGY
EAST LANSING, MI 48824
ATTN: PROF. K. FUNITA
ATTN: DR. K. MACKEY

NEW MEXICO STATE UNIVERSITY
DEPARTMENT OF PHYSICS
BOX 30001
LAS CRUCES, NM 88003
ATTN: DR. T. HEARN
ATTN: DR. J. NI

NORTHWESTERN UNIVERSITY
DEPARTMENT OF GEOLOGICAL SCIENCES
1847 SHERIDAN RD
EVANSTON, IL 60208
ATTN: PROF. E. OKAL

SAN DIEGO STATE UNIVERSITY
DEPARTMENT OF GEOLOGICAL SCIENCES
SAN DIEGO, CA 92182
ATTN: PROF. S. DAY

SOUTHERN METHODIST UNIVERSITY
STATISTICS DEPARTMENT
P.O. BOX 750302
DALLAS, TX 75275-0302
ATTN: PROF. H. GRAY

SOUTHERN METHODIST UNIVERSITY
DEPARTMENT OF GEOLOGICAL SCIENCES
P.O. BOX 750396
DALLAS, TX 75275-0395
ATTN: PROF. E. HERRIN
ATTN: PROF. B. STUMP
ATTN: PROF. P. GOLDEN

ST. LOUIS UNIVERSITY
DEPARTMENT OF EARTH & ATMOSPHERIC
SCIENCES
3507 LACLEDE AVENUE
ST LOUIS, MO 63103
ATTN: PROF. R. HERRMANN
ATTN: PROF. B. MITCHELL

THE PENNSYLVANIA STATE UNIVERSITY
GEOSCIENCES DEPARTMENT
403 DEIKE BUILDING
UNIVERSITY PARK, PA 16802
ATTN: PROF. C. LANGSTON
ATTN: DR. C. AMMON

UNIVERSITY OF ARIZONA
DEPARTMENT OF GEOSCIENCES
BUILDING #77
TUCSON, AZ 85721
ATTN: PROF. T. WALLACE

UNIVERSITY OF CALIFORNIA BERKELEY
EARTH SCIENCE DIVISION
479 MCCONE HALL, LBNL 90-2106
BERKELEY, CA 94720
ATTN: PROF. L. JOHNSON, MS 90-1116
ATTN: PROF. N. ROMANOWICZ,
MS 4760

UNIVERSITY OF CALIFORNIA DAVIS
DIVISION OF STATISTICS
1 SHIELDS AVENUE
DAVIS, CA 95616
ATTN: PROF. R. SHUMWAY

UNIVERSITY OF CALIFORNIA SANTA CRUZ
EARTH SCIENCES DEPARTMENT
EARTH & MARINE SCIENCES BUILDING
SANTA CRUZ, CA 95064
ATTN: PROF. T. LAY
ATTN: DR. R.S. WU

DISTRIBUTION LIST

DTRA-TR-01-35

UNIVERSITY OF MISSISSIPPI
COLISEUM DR
UNIVERSITY, MS 38677
ATTN: PROF. J. BASS

UNIVERSITY OF CALIFORNIA SAN DIEGO
SCRIPPS INST OF OCENOGRAPHY, IGPP,
9500 GILMAN DRIVE
LA JOLLA, CA 92093-0225
ATTN: PROF. J. BERGER
ATTN: DR. C. DEGROOT - HEDLIN
ATTN: DR. M. HEDLIN
ATTN: PROF. J. ORCUTT
ATTN: DR. F. VERNON

UNIVERSITY OF COLORADO
DEPARTMENT OF PHYSICS, CIRES
CAMPUS BOX 390
BOULDER, CO 80309
ATTN: PROF. C. ARCHAMBEAU
ATTN: DR. R. ENGBAHL
ATTN: DR. A. L. LEVSHIN
ATTN: PROF. M. RITZWOLLER

UNIVERSITY OF CONNECTICUT
DEPARTMENT OF GEOLOGY &
GEOPHYSICS, ROOM 207
BOX U-45
STORRS, CT 06268
ATTN: PROF. V.F. CORMIER

UNIVERSITY OF HAWAII - MANOA
P.O. BOX 1599
KAILUA-KONA, HI 96745-1599
ATTN: DR. M. A. GARCES

UNIVERSITY OF SOUTHERN CALIFORNIA
DEPT OF EARTH SCIENCES
LOS ANGELES, CA 90089-0740
ATTN: PROF. T. JORDAN
ATTN: PROF. C.G. SAMMIS

UNIVERSITY OF TEXAS - AUSTIN
INSTITUTE FOR GEOPHYSICS
4412 SPICEWOOD SPRINGS ROAD
BUILDING 600
AUSTIN, TX 78759-8500
ATTN: PROF. C. A. FROHLICH
ATTN: DR. J. PULLIAM

UNIVERSITY OF TEXAS - EL PASO
DEPARTMENT OF GEOLOGICAL SCIENCES
EL PASO, TX 79968
ATTN: DR. D. DOSER
ATTN: DR. R. KELLER

UNIVERSITY OF WYOMING
DEPARTMENT OF GEOLOGY AND
GEOPHYSICS
LARMIE, WY 82071
ATTN: DR. S. SMITHSON

UNIVERSITY OF WISCONSIN - MADISON
1215 W. DAYTON ST
MADISON, WI 53706-1600
ATTN: PROF C. THURBER

WASHINGTON UNIVERSITY IN ST LOUIS
DEPARTMENT OF EARTH AND PLANETARY
SCIENCES
CAMPUS BOX 1169
1 BROOKINGS DR
ST LOUIS, MO 63130
ATTN: DR. G. SMITH

FOREIGN

AUSTRALIAN GEOLOGICAL SURVEY
ORGANIZATION
CORNER OF JERRAGOMERRA &
NINDMARSH DRIVE
CANBERRA, ACT 2609
AUSTRALIA
ATTN: DR. D. JEPSON

AUSTRALIAN NATIONAL UNIVERSITY
RESEARCH SCHOOL OF EARTH SCIENCES
G.P.O. BOX 4
CANBERRA, ACT 0200
AUSTRALIA
ATTN: PROF. B. KENNETT

GEOPHYSICAL INSTITUTE OF ISRAEL
SEISMOLOGY DIVISION
P.O. 182,
LOD 71100, ISRAEL
ATTN: DR. Y. GITTERMAN
ATTN: DR. A. SHAPIRA

DISTRIBUTION LIST

DTRA-TR-01-35

INSTITUTE FOR GEOPHYSIC
PHUR UNIVERSITY BOCHUM
P.O. BOX 102148
4630 HOCUMUM 1,
GERMANY

ATTN: PROF. H.P. HARJES

MINISTRY OF DEFENSE
BLACKNEST, BRIMPTON
READING FG7 - FRS
UNITED KINGDOM

ATTN: DR. P. MARSHALL

ATTN: DR. D. BOWERS

NTNT/NORSAR
P.O. BOX 51
1007 KJELLER
NORWAY

ATTN: DR. T. KVAERNA

ATTN: DR. F. RINGDAL

SOCIETE RADIOMANA
27 RUE CLAUDE BERNARD
75005 PARIS
FRANCE

ATTN: DR. B. MASSINON

ATTN: DR. P. MECHLER

UNIVERSITY OF BEREGEN
INSTITUTE OF SOLID EARTH PHYSICS
ALLEGATEN 41
BERGEN N- 5007
NORWAY

ATTN: PROF. E. HUSEBYE

UNIVERSITY OF CAMBRIDGE
DEPARTMENT OF EARTH SCIENCES
MADINGLEY RISE, MADINGLEY ROAD
CAMBRIDGE CB3 0EZ
UNITED KINGDOM

ATTN: PROF. K. PRIESTELY

OBSERVATORIO SAN CALIXTO
INDABURO #0944
CASILLA 126546 LA PAZ
BOLIVIA

ATTN: ING. E. MINAYA

DEPARTMENT OF DEFENSE CONTRACTORS

BBN TECHNOLOGIES
1300 N 17TH ST, SUITE 1200
ARLINGTON, VA 22209

ATTN: DR. D. NORRIS

ATTN: DR. JAY PULLI

ATTN: DR. R. GIBSON

ENSCO INC
5400 PORT ROYAL ROAD
SPRINGFIELD, VA 22151

ATTN: DR. D. BAUMGARDT

ATTN: DR. ZOLTAN A. DER

ENSCO INC
CENTER FOR MONITORING RESEARCH
1300 N 17TH STREET, SUITE 1450
ARLINGTON, VA 22209 2308

ATTN: DR. V. RYABOY

ITT INDUSTRIES
ITT SYSTEMS CORPORATION
1680 TEXAS STREET SE
KIRTLAND AFB, NM 87117 5669
2 CYS ATTN: DTRIAC

JAYCOR
25 NORTH CASCADE AVE SUITE 300
COLORADO SPRINGS, CO 80903
ATTN: J. I. LUBELL

MISSION RESEARCH CORPORATION
8560 CINDERBED ROAD, SUITE 700
NEWINGTON, VA 22111-8560

ATTN: DR. M. FISH

ATTN: DR. R. BURLACU

DISTRIBUTION LIST

DTRA-TR-01-35

SCIENCE APPLICATION INTL CORP
CENTER FOR MONITORING RESEARCH
1300 N 17TH STREET, SUITE 1450
ARLINGTON, CA 22209-2308

ATTN: LIBRARIAN
ATTN: DR. K. MCLAUGHLIN
ATTN: DR. R. NORTH
ATTN: DR. R. WOODWORTH
ATTN: DR. X. YANG
ATTN: DR. T. J. BENNETT
ATTN: MR. J. MURPHY
ATTN: DR. I. BONDAR

SCIENCE APPLICATIONS INT'L CORP
10260 CAMPUS POINT DRIVE
SAN DIEGO, CA 92121

ATTN: DR. J. STEVENS
ATTN: DR. G. E. BAKER
ATTN: MR. D. ADAMS
ATTN: DR. M. ENEVA

SCIENCE APPLICATIONS INT'L CORP
1227 S. PATRICK DR. STE 110
SATELLITE BEACH, FL 32937

ATTN: DR. M. FELIX
ATTN: DR. H. GIVEN
ATTN: MS. A. HENSON

WESTON GEOPHYSICAL CORPORATION
57 BEDFORD STREET SUITE 102
LEXINGTON, MA 02420

ATTN: MR. J. LEWKOWICZ
ATTN: DR. R. REITER
ATTN: DR. A. ROSCA
ATTN: DR. I. TIBULEAC

WESTON GEOPHYSICAL CORPORATION
411 NW 26TH ST
GAINESVILLE, FL 32607
ATTN: DR. S. RUSSELL

URS CORPORATION
566 EL DORADO STREET, SUITE 100
PASADENA, CA 91101 2560

ATTN: DR. C. SAIKIA
ATTN: DR. B. WOODS
ATTN: DR. G. ICHINOSE